

# REPORT DOCUMENTATION PAGE

Form Approved  
OMB No. 0704-0188

Public reporting burden for this collection of information is estimated to average 1 hour per response, including the time for reviewing instructions, searching existing data sources, gathering and maintaining the data needed, and completing and reviewing this collection of information. Send comments regarding this burden estimate or any other aspect of this collection of information, including suggestions for reducing this burden to Department of Defense, Washington Headquarters Services, Directorate for Information Operations and Reports (0704-0188), 1215 Jefferson Davis Highway, Suite 1204, Arlington, VA 22202-4302. Respondents should be aware that notwithstanding any other provision of law, no person shall be subject to any penalty for failing to comply with a collection of information if it does not display a currently valid OMB control number. PLEASE DO NOT RETURN YOUR FORM TO THE ABOVE ADDRESS.

1. REPORT DATE (DD-MM-YYYY) 01-09-2009		2. REPORT TYPE Technical Paper		3. DATES COVERED (From - To)	
4. TITLE AND SUBTITLE  <b>A Study of Ignition Effects on Thruster Performance of a Multi-Electrode Capillary Discharge Using Visible Emission Spectroscopy Diagnostics</b>		5a. CONTRACT NUMBER			
		5b. GRANT NUMBER			
		5c. PROGRAM ELEMENT NUMBER			
6. AUTHOR(S) Anthony Pancotti (USC)		5d. PROJECT NUMBER			
		5e. TASK NUMBER			
		5f. WORK UNIT NUMBER 50260542			
7. PERFORMING ORGANIZATION NAME(S) AND ADDRESS(ES)  Air Force Research Laboratory (AFMC) AFRL/RZST 4 Draco Drive Edwards AFB CA 93524-7160		8. PERFORMING ORGANIZATION REPORT NUMBER  AFRL-RZ-ED-TP-2009-328			
9. SPONSORING / MONITORING AGENCY NAME(S) AND ADDRESS(ES)  Air Force Research Laboratory (AFMC) AFRL/RZS 5 Pollux Drive Edwards AFB CA 93524-7048		10. SPONSOR/MONITOR'S ACRONYM(S)			
		11. SPONSOR/MONITOR'S NUMBER(S) AFRL-RZ-ED-TP-2009-328			
12. DISTRIBUTION / AVAILABILITY STATEMENT  Approved for public release; distribution unlimited (PA #09402).					
13. SUPPLEMENTARY NOTES For USC Ph.D. Thesis Paper on 11 September 2009.					
14. ABSTRACT  This work examined the effect of ignition on thruster performance characteristics of a capillary discharge device. Early tests of the presented device, incorporating an exploding wire ignition, showed a strong dependence on the initial plasma conditions. The literature supported these findings for more basic laboratory capillaries, but the effect on a thruster device was unknown. An in-depth investigation of different ignition systems were conducted for a capillary discharge based pulsed plasma thruster. In addition to conventional wires, capillary discharges were ignited with low pressure gas and several different types of spark igniters. These methods were compared with each other and with newly developed computer models. The viability of a capillary discharge based electro thermal pulsed plasma thruster as an in-space propulsion system was examined. Thruster performance levels, and their ability to fill a desired niche, which has historically shown rather poor efficiencies, have been explored. This work contains a background literature study, experimental setup and testing of a capillary design, and a comparison to performance models created by others. New techniques have been coupled with proven plasma diagnostics to investigate the internal plasma properties of the device. Visible-light spectroscopy techniques were developed to examine the time-resolved electron number densities at the exit. Novel thrust stand techniques were demonstrated, measuring thruster performance characteristics with a high degree of accuracy.					
15. SUBJECT TERMS					
16. SECURITY CLASSIFICATION OF:		17. LIMITATION OF ABSTRACT  SAR	18. NUMBER OF PAGES  162	19a. NAME OF RESPONSIBLE PERSON Marcus Young	
a. REPORT Unclassified				19b. TELEPHONE NUMBER (include area code) N/A	
b. ABSTRACT Unclassified				c. THIS PAGE Unclassified	

A STUDY OF IGNITION EFFECTS ON THRUSTER PERFORMANCE OF A MULTI-ELECTRODE  
CAPILLARY DISCHARGE USING VISIBLE EMISSION SPECTROSCOPY DIAGNOSTICS

by

Anthony P. Pancotti

---

A Dissertation Presented to the  
FACULTY OF THE GRADUATE SCHOOL  
UNIVERSITY OF SOUTHERN CALIFORNIA  
In Partial Fulfillment of the  
Requirements for the Degree  
DOCTOR OF PHILOSOPHY  
(AEROSPACE ENGINEERING)

December 2009

Copyright 2009

Anthony P. Pancotti

Your vision is not limited by what your eyes can see,  
but by what your mind can imagine.

Many things that you take for granted were considered unrealistic dreams  
by previous generations.

If you accept these past accomplishments as commonplace  
then think of the new horizons that you can explore.

From your vantage point, your education and imagination  
will carry you to places which we won't believe possible.

Make your life count and the world will be a better place because you tried.

Ellsion S. Onizuka

*to my parents*

# Acknowledgments

AFRL, Marcus Young, E.P. Muntz, USC Faculty and Staff, Andrew Ketsdever, Andrew Smith, John Duncan, Matt Gilpin, Jairo Ascencio, Tailor Lilly, Ryan Downey, Sergey & Natasha Gimelshein, Leonid Pekker

# Table of Contents

<b>Epigraph</b>	ii
<b>Dedication</b>	iii
<b>Acknowledgments</b>	iv
<b>List of Figures</b>	vii
<b>List of Tables</b>	xi
<b>Abbreviations</b>	xii
<b>Abstract</b>	xiv
<b>Preface</b>	xv
<b>1 Introduction</b>	1
1.1 The Need for High Efficiency . . . . .	2
1.2 Other Capillary Discharge Pulsed Plasma Thrusters . . . . .	3
1.3 Other Capillary Discharge Applications . . . . .	6
1.4 Capillary Discharge Description . . . . .	6
1.4.1 Ablation Process . . . . .	7
1.5 Capillary Physics and Assumptions . . . . .	11
1.5.1 Pressure Ratio . . . . .	12
1.5.2 Local Thermodynamic Equilibrium . . . . .	13
1.5.3 The Non-Ideal Parameter . . . . .	15
1.6 Evaluation of Thruster Performance . . . . .	15
1.7 Ignition Methods . . . . .	16
1.7.1 Wire Ignition . . . . .	18
1.7.2 Paschen Ignition . . . . .	20
1.7.3 Coaxial and 3-Electrode Ignition . . . . .	20
<b>2 Experimental Setup</b>	23
2.1 Capillary . . . . .	23
2.1.1 Capillary Design V1.0 for Wire Testing . . . . .	23
2.1.2 Capillary Design V2.0 for Paschen Breakdown Testing . . . . .	25
2.1.3 Capillary Design V3.0 with Coax Ignitor . . . . .	28
2.1.4 Capillary Design V4.0 with 3-Electrode Ignitor . . . . .	29
2.2 Circuit . . . . .	31
2.2.1 Switches . . . . .	32

2.3 Facilities . . . . .	33
<b>3 Diagnostics</b>	<b>36</b>
3.1 Current . . . . .	36
3.2 Voltage . . . . .	37
3.3 Mass Loss . . . . .	37
3.4 Force Measurements . . . . .	37
3.4.1 Piezoelectric Force Sensors . . . . .	38
3.4.2 Thrust Stand . . . . .	39
3.5 Optical Diagnostics . . . . .	54
3.5.1 Temperature from Resistivity . . . . .	56
3.5.2 Electron Number Density . . . . .	60
3.5.3 Mach Disc diagnostics . . . . .	65
<b>4 Modeling</b>	<b>68</b>
4.1 Zero-Dimensional Model . . . . .	68
4.2 One-Dimensional Model . . . . .	69
<b>5 Results</b>	<b>71</b>
5.1 Circuit . . . . .	71
5.2 Wire Ignition . . . . .	72
5.2.1 Test Procedures . . . . .	73
5.2.2 Data . . . . .	73
5.3 Paschen Breakdown Ignition . . . . .	76
5.3.1 Test Procedures . . . . .	76
5.3.2 Data . . . . .	78
5.4 External Coaxial Ignition . . . . .	81
5.4.1 Test Procedure . . . . .	81
5.4.2 Data . . . . .	81
5.5 Internal Three Electrode Ignition . . . . .	83
5.5.1 Test Procedures . . . . .	83
5.5.2 Data . . . . .	84
5.6 Electron Number Density . . . . .	85
<b>6 Discussion</b>	<b>93</b>
6.1 Ignition Comparison . . . . .	93
6.2 Electrode Erosion . . . . .	97
6.3 Dual Mode Operation . . . . .	99
6.4 Ablation Effects . . . . .	101
6.5 Initial Discharge . . . . .	103
6.6 Material factors . . . . .	104
6.7 Background Pressure Effects . . . . .	104
<b>7 Conclusions</b>	<b>108</b>
<b>Reference List</b>	<b>110</b>

# List of Figures

1.1	Electrothermal and Ion Thruster Performance . . . . .	3
1.2	Electrothermal PPT Performance History . . . . .	4
1.3	Ablation Process within a Capillary Discharge . . . . .	7
1.4	Ablation Mechanisms . . . . .	9
1.5	PrismSpect Spectra of Various Capillary Materials . . . . .	11
1.6	Radiative Energy of Materials . . . . .	12
1.7	Photograph and X-radiograph of an Exploding Wire . . . . .	18
1.8	Paschen Curve . . . . .	21
2.1	Schematic of Capillary Discharge Design V1.0 . . . . .	24
2.2	Schematic of Capillary Discharge Design V1.1 . . . . .	25
2.3	Schematic of Capillary Discharge Design V2.0 . . . . .	26
2.4	Schematic of Capillary Discharge Design V2.1 . . . . .	27
2.5	Schematic of Capillary Discharge Design V2.2 . . . . .	28
2.6	Schematic of Capillary Discharge Design V3.0 . . . . .	29

2.7	Schematic of Capillary Discharge Design V4.0	30
2.8	Picture of Capillary Discharge Vacuum Chamber	34
3.1	Schematic of original Piezoelectric Force Sensor Setup	39
3.2	Data from Piezoelectric Force Sensors	40
3.3	Schematic of Capillary Discharge Thrust Stand	41
3.4	LVDT data showing Impulse Measurements	42
3.5	LVDT data showing Mass Loss Measurements	42
3.6	Picture of the Capillary Discharge Thrust Stand	43
3.7	LVDT Diagram	44
3.8	Michelson Interferometer Diagram	45
3.9	LVDT vs. Interferometer Data	46
3.10	Electrostatic Fin Validation Data	48
3.11	Hammer vs. ES Fin Data	49
3.12	Thrust Stand Deflection vs. $K$	50
3.13	Thrust stand Range vs. $I$	52
3.14	Thrust Stand Mass Loss Measurements	53
3.15	Diagram of Kinetics Mode Operation	55
3.16	$10\mu\text{m}$ Optical System	57
3.17	Plasma Resistivity	59
3.18	High Speed Video Still Frames	66

3.19 Corresponding Current Data for High Speed Video . . . . .	66
4.1 Energy Fluxes for a $5\text{cm}$ 2500V Capillary Discharge . . . . .	70
5.1 Circuit Parameters . . . . .	72
5.2 Voltage Dependence of Wire Ignition Current Data . . . . .	74
5.3 Inductance Dependence Wire Ignition Current Data . . . . .	74
5.4 Length Dependence of Wire Ignition Current Data . . . . .	75
5.5 Paschen Ignition Current Data . . . . .	78
5.6 Paschen Ignition Thruster Performance Data . . . . .	80
5.7 Coaxial Ignitor Capillary Discharge Current Data . . . . .	82
5.8 Coaxial Ignitor Capillary Discharge Thruster Preformance . . . . .	83
5.9 3-Electrode Capillary Discharge Current Data . . . . .	85
5.10 3-Electrode Capillary Discharge Thruster Performance Data . . . . .	86
5.11 Lorentzian Fit of Experimental Data . . . . .	87
5.12 Experimental and 1D Model Number Densities . . . . .	88
5.13 Number Density for Various Capillary Voltages . . . . .	90
5.14 Number Density for Various Capillary Lengths . . . . .	90
5.15 High Self-absorbtion Spectral Profile . . . . .	91
5.16 Comparison of FWHM and Shifts . . . . .	92
6.1 Current Comparison . . . . .	94
6.2 Thruster Performance Comparison . . . . .	96

6.3	Photos of Anode Erosion . . . . .	97
6.4	Diameter Change with Anode Erosion . . . . .	98
6.5	Capillary and Electrode Mass Loss for Paschen Ignition . . . . .	99
6.6	Capillary and Electrode Mass Loss for 3E Ignition . . . . .	100
6.7	Photo of Capillary Failure do to External Ablation . . . . .	102
6.8	Initial and Subsequent Current Traces . . . . .	103
6.9	Current Traces for Various Capillary Materials . . . . .	105
6.10	Current Traces for Various Background Pressures . . . . .	106
6.11	Thrust Stand Deflection vs. Background Pressure . . . . .	107

# List of Tables

3.1	Coeffecients for 1st interation & optimized CD thrust stand . . . . .	51
3.2	Ratio of conductivity in a Lorentz gas . . . . .	58
3.3	Fractional Intensity Widths . . . . .	64
5.1	Inductive Effects on Discharge Circuit Parameters . . . . .	75

# Abbreviations

CD - Capillary Discharge

$K$  - Spring Constant

$I$  - Moment of Inertia

$C$  - Dampening Coeff

LVDT - linear variable differential transformer

PE - Piezo-Electric

ES - Electro Static

CCD - Charged coupled device

CEE - Charge exchange efficiency

LED - Light emitting diode

$I_{sp}$  - Specific Impulse

PET - Pulsed electrothermal

HDPE - high-density polyethylene

LCR - Inductive, resistive, capacitive

PTFE -

UV - Ultra-violet

LTE -local thermodynamic equilibrium

$\beta$  - PressureRatio

$\mu_o$

$k$

$\varepsilon_o$

$\Gamma$  - Non-Ideal plasma parameter

OES - Optical EmissionSpectroscopy

EDM - Electric Discharge Machining

*T/C* - thermalcouple

# Abstract

This work examined the effect of ignition on thruster performance characteristics of a capillary discharge device. Early tests of the presented device, incorporating an exploding wire ignition, showed a strong dependence on the initial plasma conditions. The literature supported these findings for more basic laboratory capillaries, but the effect on a thruster device was unknown. An in-depth investigation of different ignition systems were conducted for a capillary discharge based pulsed plasma thruster. In addition to conventional wires, capillary discharges were ignited with low pressure gas and several different types of spark igniters. These methods were compared with each other and with newly developed computer models.

The viability of a capillary discharge based electrothermal pulsed plasma thruster as an in-space propulsion system was examined. Thruster performance levels, and their ability to fill a desired niche, which has historically shown rather poor efficiencies, have been explored. This work contains a background literature study, experimental setup and testing of a capillary design, and a comparison to performance models created by others. New techniques have been coupled with proven plasma diagnostics to investigate the internal plasma properties of the device. Visible-light spectroscopy techniques were developed to examine the time-resolved electron number densities at the exit. Novel thrust stand techniques were demonstrated, measuring thruster performance characteristics with a high degree of accuracy. The research conducted here has not only increased the understanding of ignition effects, but also the basic physics, of capillary devices.

# Preface

This thesis focuses mainly on the investigation of different ignition techniques involved in capillary discharges. In order to carry out this study a great deal of initial work was needed. Not only to design and build a capillary discharge, but also to set up: the vacuum facility, the high powered circuits, the computer control, and the data acquisition. When I began this project for my Ph.D research 5 years ago there was only a stack of journal articles on my desk.

The bulk of this work, like most other research experiments, is based on the diagnostics. I was introduced to several of the necessary tools early on in engineering, others took me years to perfect during my graduate studies at USC. A large section of this thesis is related to experimental setup and diagnostic techniques.

A.P. Pancotti

Los Angeles, California

December 2009

# Chapter 1

## Introduction

In order to appreciate the potential of a capillary discharge based propulsion system, it is important to look at existing technology. To justify and validate this research, there must be a need for it. The entire realm of electric spacecraft propulsion was examined and an apparent need was noticed. There are currently no flight qualified propulsion systems that have the capabilities of the proposed advanced electrothermally pulsed plasma thruster. These devices are not new and have been studied for many years, so an in-depth literature search was done to gather and use previous knowledge in this work. There are several major contributors, but none as influential as the work done by Burton. His work was guided by the same niche observed today, it is discussed further in Section 1.1. In addition to the work done in propulsion with coaxial electro thermal pulse plasma thrusters (PPTs), there are also a great number of other fields that use capillary discharge technology, as is discussed in Section 1.3. While not linked to the engineering challenge of a PPT concept, their respective works do provide useful insight into the physics of these devices.

From the literature it is possible to compose a general idea of how these devices work. Their basic design remains fairly consistent throughout the literature, and for different applications. Capillaries are sources of very high density plasma formed through an ablation process. By understanding the basic physics described in this section, a capillary discharge thruster was designed for the tests conducted here. Several different designs were tested before a suitable device could fire consistently and reliably. All the design iterations are discussed in detail in Section 2.1. The capillary was powered by a high power LRC circuit. A suite of diagnostics was developed to measure multiple discharge parameters ranging from current and voltage, to temperature and density, to thrust and Isp. Using such a wide variety of diagnostics, described in Section 3, yields a thorough, accurate understanding of the capillary discharge physics.

Early exploratory experiments were conducted to determine how capillary discharges operated under different voltages, inductances, and capillary lengths. From these initial tests, a strong dependence on ignition became apparent. Limited information on ignition conditions of capillary discharges were found in the literature, and no evidence of their effect on a thruster based system were found. Therefore, the

major effort of this work was the investigation of ignition characteristics and their effects on capillary discharge operation, and more specifically, thruster performance. This work examines, in detail, previously used ignition methods, as well as alternative ignition methods and their effect on the discharge. The Ignition methods tested are described in detail in section 1.7. The results of the tests are given in Section 5, with further discussion in Section 6. Zero dimensional and one dimensional models, described in Section 4, are compared to the experimental results. In addition to the ignition processes, other important observations were noted and analyzed. These range from confinement issues to electrode erosion.

## 1.1 The Need for High Efficiency

The field of electric propulsion has existed for over a century[25]. During that time a wide range of electric propulsion concepts have been investigated to satisfy spacecraft propulsion requirements, ranging from stationkeeping[41][102][101][63] to orbit insertion[6]. There are also proposed applications of drag compensation, formation flying[54], attitude control[69][23], and even planetary and deep space exploration[26][9]. Electric propulsion systems have successfully demonstrated system mass savings over traditional chemical propulsion systems for many non-time-critical applications. The optimal specific impulse for an individual mission can be approximately determined, by comparing the propellant mass savings with the added power supply mass for a representative total mission  $\Delta V$ . Optimal specific impulses are dependent on the specific mission, but they are almost always in the range of 1000 s to 3000 s for Earth orbiting spacecraft[46]. Individual missions often have different optimal specific impulses during the mission, depending on the time criticality of each individual maneuver. A thruster system capable of operating with a specific impulse ranging from 1000 s to 3000 s at high thrust efficiencies,  $\eta$ , would be very advantageous for Earth orbiting missions. Electric propulsion systems are commonly categorized into three classes: electrothermal, electrostatic, and electromagnetic according to their dominant acceleration mechanism[52]. The class of continuous electrothermal thrusters have, in general, demonstrated high thrust efficiencies at specific impulses somewhat less than 1000 s, but their thrust efficiency drops precipitously at specific impulses approaching 1000 s, this is due to material limitations and frozen flow loss[16]. It is not possible to maintain a continuous electrothermal thruster at the required high pressures and temperatures that would allow complete recovery of the input energy through full nozzle expansion. In contrast, electrostatic and electromagnetic thrusters have demonstrated high thrust efficiencies at specific impulses somewhat greater than 1000 s. Once again, however, as the specific impulse approaches

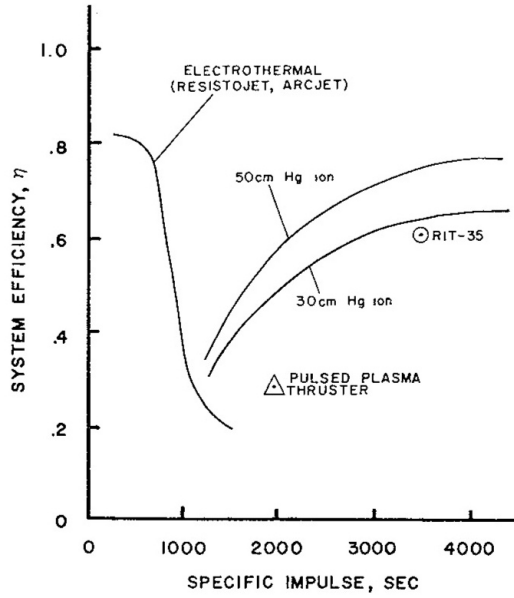


Figure 1.1: Electrothermal and Ion Thruster Performance[16]

1000  $s$  (this time from  $> 1000 s$ ) thrust efficiency continuously decreases due to the increasing relative importance of the ionization cost. These trends are depicted in Figure 1.1. A thruster system that operated at high thrust efficiency ( $\eta > 65\%$ ), only at a specific impulse of 1000  $s$ , would still be a useful technology. It has been shown, as in Figure 1.2, that an electro-thermal pulse plasma thruster (PPT) can work quite well in this area.

## 1.2 Other Capillary Discharge Pulsed Plasma Thrusters

A capillary discharge (CD) is a pulsed, ablative electro-thermal PPT, capable of efficiently producing high density plasma. These devices are characterized by their high aspect ratio. An arc is established in the center of the capillary, which results in ablated wall material that constitutes the high density plasma. In the case of PPT, one end is open, allowing the plasma to exit the capillary while at the same time creating thrust. The capillary discharge PPT not only exhibits high efficiency, but also has an excellent balance between high  $I_{sp}$  and high thrust. Some of the most important contributions to CD PPT's were made by Burton in the 1980s[19, 16, 17, 15, 13, 14] and are discussed in the next section.

While the field of pulsed plasma thrusters has been extensively studied, the work done on the specific high power ( $kJ$ ) electrothermal PPTs of interest here is limited. One of the major contributors to this field

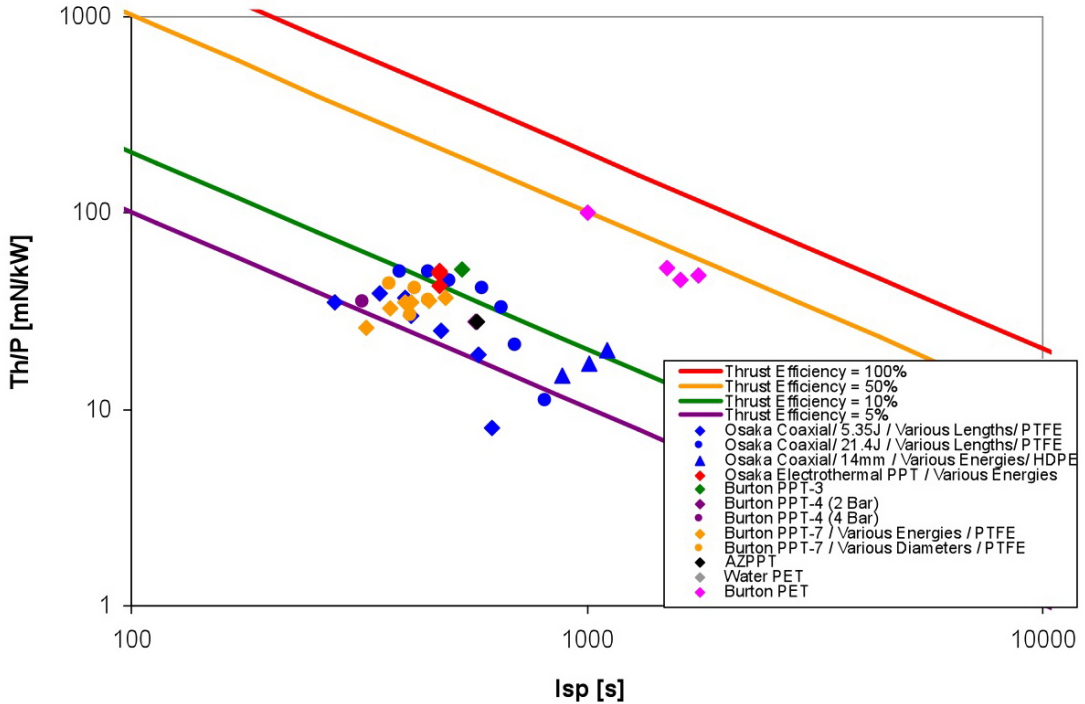


Figure 1.2: Electrothermal PPT Performance History

was Burton. Burton noticed a lack of high efficiency thrusters in the 750s to 3000s  $I_{sp}$  range as shown in Figure 1.1. His initial work, done at GT-Devices in 1982[19][16], investigated the predicted performance of a pulsed electrothermal thruster (PET) concept that operated in the  $1 - 10 \text{ kJ}$  energy range. The device dimensions were about  $4 \text{ mm}$  in diameter and a few centimeters long, with a pulse length of  $10 - 20 \mu\text{s}$  and a current of  $100 \text{ kA}$ . With this pulse mode Burton predicted a thruster efficiency as high as 80% in the  $1500 - 3000 \text{ s}$  range. The PET thruster had estimated plasma densities of  $5.7 \times 10^{27} \text{ m}^{-3}$  and temperatures of  $4 \text{ eV}$ . One of the most important points that Burton highlighted in this early work was the aforementioned efficiency. He looked at the 3-body ion combination rate[17] and calculated the mean free path for recombination for his given plasma conditions. At the exit he showed a mean free path of  $2 \times 10^{-11} \text{ m}$  which is much smaller than the length of the nozzle. Therefore, the flow should be in Saha equilibrium and the ionization cost should be nearly completely recovered. That is the primary reason why pulsed electrothermal devices in general, and capillary discharges in particular, boast such high potential efficiencies. Another reason for the PET Thruster's high predicted efficiency is the capillary's high dimensional ratio (*length/diameter*), which indicates that the majority of emitted radiation will strike the propellant walls. Assuming that the walls absorb all the radiation Burton[19]

goes on to show that of the  $16\text{eV}$  of energy it takes to evaporate, dissociate, and ionize one molecule of polyethylene ( $C_2H_4$ ) all but  $3.2\text{eV}$  can be recaptured into the directed flow by use of a nozzle. This leads to a predicted efficiency of 87% for polyethylene.

In 1984 Burton published experimental results on his PET thruster design. He operated his device in both an unsteady mode, with  $15\ \mu\text{s}$  pulses, and quasi-steady mode, with  $48 - 100\ \mu\text{s}$  pulses, and recorded efficiencies of 56% to 37%, respectively. Of interest in Burton's published work is the effect of pulse length. He showed the highest efficiencies for unsteady  $15\ \mu\text{s}$ , with a  $23\text{ kA}$  peak current. For the quasi-steady tests (the  $48\ \mu\text{s}$  and  $100\mu\text{s}$  shots) both had the same peak current ( $15\text{ kA}$ ), however, the efficiency was higher (42 % instead of 37%) for the longer pulse. It is possible that this improvement for longer pulse lengths is due to the minimization of the late time ablation mentioned earlier in Section 1.2. It is also important to note the trade-off in  $I_{sp}$  vs. impulse for the two operational modes. The unsteady test had a lower  $I_{sp}$  and higher impulse ( $1000\text{ s}, 0.2\text{ Ns}$ ), while the quasi-steady test had a higher  $I_{sp}$  and lower impulse ( $1600\text{ s}, 0.086\text{ Ns}$ ).

Burton continued his PET thruster development by focusing on developing a propellant feed mechanism instead of improving the thruster efficiency. Over the next 5 years (1984-1989) Burton tried water[15], hydrazine[13], and hydrogen[14] propellant. After these early publications, Burton's research moved towards smaller, much less efficient pulsed plasma research[21]. It is the long term goal of this project to continue with Burtons original PET thruster work, in an attempt to achieve thrust efficiencies in excess of 65%, like he first predicted. It is conceivable that by increasing the pulse length even longer than achieved in Burton's capillaries, the late time ablation effect can be limited. In addition, lower currents would cause less electrode erosion and also lower pressures, while still operating in a regime where ionization losses can be recovered. Hence the effects of capillary voltage, inductance, and geometry were all investigated in this work.

The capillary discharge designed for this experiment was predicted to operate at densities one or two orders of magnitude lower than Burton's work. Therefore, it is important to check the three-body recombination rate with predicted density to make sure that ionization energy can be recovered through the nozzle expansion. The three-body recombination rate is[4]

$$\nu_e = \alpha_3 n^2 = 8.75 \times 10^{-27} T^{-4.5} n^2 = 3.9 \times 10^{10} [\text{s}^{-1}] \quad (1.1)$$

Where  $T$  is the electron temperature in  $eV$ , and  $n$  is the number density in cubic centimeters. Assuming only the thermal velocity of the ion

$$u = \sqrt{\frac{8kT}{\pi M}} = 9.6 \times 10^5 [cm/s] \quad (1.2)$$

Where  $M$  is the average molecular weight, which for polyethylene is  $5.33 amu$ . It is then possible to calculate the mean free path at exit.

$$\lambda = \frac{u}{\nu_e} = 2.5 \times 10^{-5} [cm] \quad (1.3)$$

While this value is orders of magnitude larger than Burton's PET thruster it is still much smaller than the characteristic length of the nozzle and therefore the propellant is able to adiabatically expand though the nozzle.

### 1.3 Other Capillary Discharge Applications

Capillary discharges are efficient sources of high-density high-temperature pulsed plasmas which are being developed for a wide range of applications. Capillaries have been investigated as wake field accelerators and optical guides for high power lasers[108] They have been used as x-ray sources[65] for low pressure capillary discharges and electro-thermal-chemical guns[80, 110, 109, 38, 85] for high- pressure capillary discharges. Capillary discharges have been used as pre-injectors for electromagnetic rail systems that provide initial acceleration and the material needed for the plasma armature.[90] A similar discharge occurs in a devices called an ablation controlled arcs, which are essentially the same a capillary discharges but with two open ends. These devices are often studied for gas-blast circuit breakers[81].

### 1.4 Capillary Discharge Description

Capillary discharges can produce high-density ( $5 \times 10^{25} - 5 \times 10^{26} m^{-3}$ ), high-temperature ( $1 - 8 eV$ ) pulsed plasmas. They typically consist of a long capillary of a nonconductive material, usually high-density polyethylene (HDPE) or Teflon<sup>®</sup> with electrodes at both ends of the capillary as shown in Figure 1.3. The anode is typically inserted into one end of the capillary while the cathode is a hollow cylinder

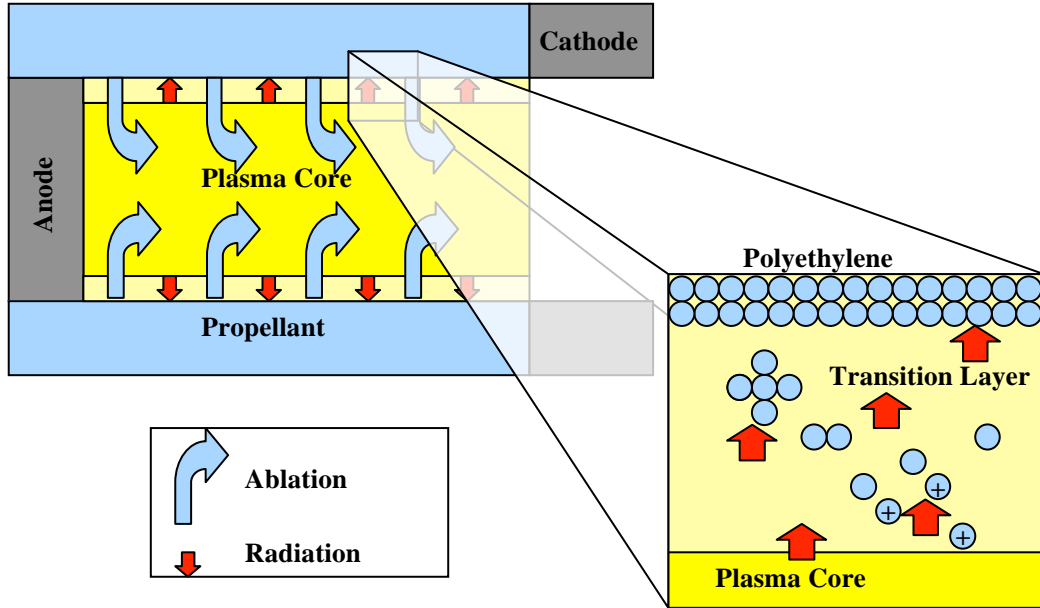


Figure 1.3: Ablation Process within a Capillary Discharge

on the opposite end of the capillary, although the reverse polarity also works. The capillary dimensions are such that the ratio of length to diameter is large ( $\approx 20$ ), giving it its name.

Capillary discharges are ignited by creating a predischarge plasma throughout the capillary using some ignition source, typically an exploding wire ignition system. A capacitive electrical energy source (either an LRC circuit or a more complicated pulse forming network) is connected across the electrodes. Once a conductive path has been created between the electrodes, current will begin flowing between them and the plasma will be heated by Joule heating. The heated plasma along the axis radiates, ablating material in the wall. The ablated material becomes dissociated and ionized during its transit through a thin (typically several  $\mu m$ ) transition layer, adding mass to the capillary discharge as shown in Figure 1.3. Mass is injected into the discharge from the entire capillary area while it is only lost from the discharge through the relatively small exit orifice in the cathode, which allows high-densities ( $> 1 \times 10^{25} m^{-3}$ ) to be achieved.

#### 1.4.1 Ablation Process

While ignition is the primary focus of this work, it is important to take a look at the overall operation of the device. As stated earlier, it is the overall goal of this project to demonstrate a device with high propulsion

efficiency in the  $750 - 3000\text{ s}$   $I_{sp}$  range. After the ignition tests were under way, low efficiencies were noted and will need to be addressed. The information in this section provides an in-depth view of capillary processes and possible methods for improving efficiency beyond the ignition techniques described here.

The ablation process that occurs at the surface of the capillary wall is a complicated one. Different ablation mechanisms have been isolated and studied, however, it is very difficult to understand how they all interact with each other. In this section, the major ablation mechanisms are considered in more detail to develop an understanding of the device, as well as to provide background information that may be helpful in future capillary work.

There are two main transport mechanisms that can bring heat, or energy to the capillary wall. These mechanism are convection and radiation. The process of convection is described by energy that is transported to the surface by collisions, where a particle within the plasma deposits energy to an atom on the wall. The other main form of energy transport is radiation. Photons interact with the surface atoms either by breaking molecular bonds directly, or are being absorbed into the vibrational modes of the molecules, causing heating. Conduction, the third common heat transfer mechanism, only acts as a loss mechanism in these discharges. Due to the relative long time scale in which conduction occurs, it does not effectively aid in ablation during the short time of the discharge pulse. Any conduction that does occur would be relatively small and regarded as a loss.

Ablation occurs in a number of different ways. The three main forms in which material can leave the surface are photo-ablation, macro-particles, and thermal pyrolysis, as illustrated in Figure 1.4. Photo ablation occurs when a photon has enough energy to break a molecular bond of an atom directly, potentially releasing it from the surface. In macroparticle ejection a localized hot spot within the bulk material leads to a high pressure void which explodes outward ejecting macroparticles along with the originally ablated gas. Often times these macro-particles are quickly dissociated and ionized in the plasma column, but they do affect ablation rates and efficiencies. The third form, called thermal pyrolysis, simply refers to an amount of material that leaves the surface due to the material's elevated vapor pressure at a certain elevated temperature.

Photo-ablation has been recognized as an important ablation mechanism[81] in ablation controlled arcs. For different polymers the critical wavelength,  $\lambda_c$ , lies between 250 and 350 nm[83]. Photons with wavelengths below  $\lambda_c$  have enough energy to directly break chemical bonds and are typically absorbed much closer to the surface. Photons with  $\lambda > \lambda_c$ , in general do not, and penetrate deeper into the material depositing their energy as thermal vibrational energy of the constituent atoms. This process heats both the interior of the material along with its surface which leads to thermal pyrolysis because of greatly

increased vapor pressure. Short wavelength radiation can also cause damage at significant depths within the material[71]. Any damage or heating that occurs within the material is a form of energy loss, for it does not lead to ablation. It is also important to note that the description of the mechanisms given here are strictly applicable only when each mechanism operates independently from the others. The true physical picture with all mechanisms operating at comparable levels is significantly more complicated.

Figure 1.4 is an attempt to illustrate the various ablation mechanisms and the energy transport mechanisms that typically causes them. Only the most relevant energy paths are shown for simplicity. Lower wavelength light is the only form that can cause photo-ablation as shown by the black line. Higher wavelength photons can either pass directly through the material and leave the system as radiation as shown by the green line. It can also be absorbed within the material where it is either lost through conduction or causes ablation through macro-particles and thermal pyrolysis. Note that late time ablation causes large efficiency loss in PPTs. Late time ablation is a result of the hot surface of the wall continuing to vaporize material after the electrical arc has extinguished. This material is evaporated, but efficiently accelerated. Obviously all of the mechanisms that cause ablation by thermal pyrolysis also cause late time ablation.

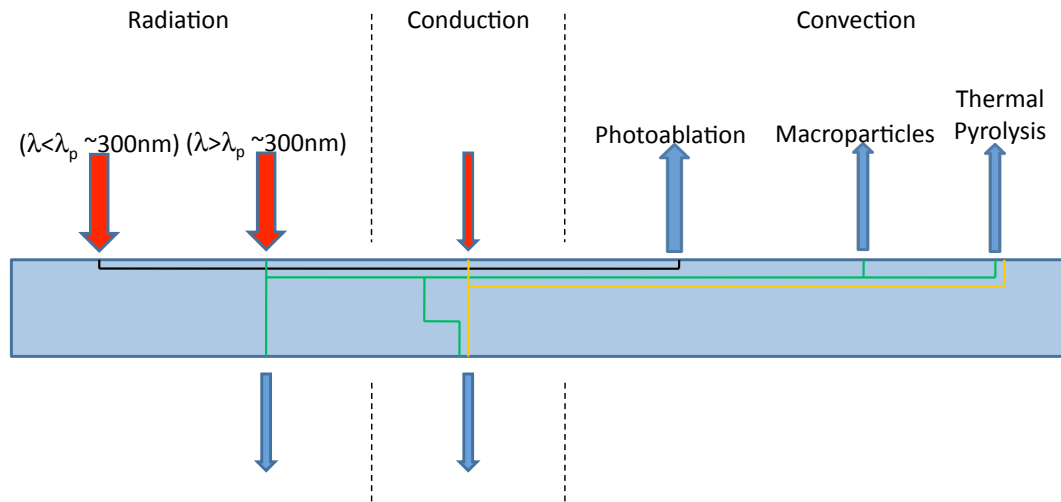


Figure 1.4: Ablation Mechanisms

An ideal electrothermal PPT is one that operates by pure photo-ablation. This is not practical in a capillary type discharge. However, research can be done to produce a discharge that contains more high energy radiation and a material can be chosen or developed that is highly susceptible to photo-ablation. Polymers, in general, have a strong sensitivity to UV light[64]. They have ablation thresholds lower than metals[49], semiconductors[86], and metal oxide semiconductors[50]. They also have much higher

ablation rates[89], which make them attractive for PPT propellants. A wide range of polymers have been tested, from white, grey, black[71], and *Cu* doped PTFE[81] to more exotic materials like Celeon® and Tefzel®[76]. White PTFE ablated less than black PTFE[81]. This is because the optical transparency of white PTFE allows soft arc radiation to penetrate deeply into the material, causing only moderate heating.

It has also been reported that doping PTFE with a small amount of *Cu* (7%) increases the ablation efficiency[81]. This is accredited to the optical penetration depth being reduced by *Cu* molecules, and by the fact that while the *Cu* in the plasma do not significantly change the thermodynamic or electrical properties of the arc, it does strongly increase the radiation emitted from the arc[91].

While understanding the absorption and ablation of materials is complicated, and not well understood, it is clear that photo-ablation is important and UV (sub-critical) radiation causes it. So, in support of what was found in literature, a spectrum simulation program called PrismSpect® was used to model the plasma that would be created by material once it has been ablated. PrismSpect® does not model the ablation process, or how well the material will ablate, but models the spectral profile of emitted radiation for a given size plasma of known composition, temperature, and density. This spectral distribution helps in the choice of a good material, at least from a radiator point of view. Several materials were simulated at a density of  $5 \times 10^{25} \text{ m}^{-3}$  and a plasma temperature of 1.5 eV. These values are typical of a capillary discharge. The PrismSpect spectra are shown in Figure 1.5. High Density Polyethylene, HDPE ( $C_4H_9$ ), 7% atomic copper doped HDPE ( $C_4H_9Cu$ ), and Teflon, PTFE ( $CF_2$ ), were all tested. In addition a black body radiator at 1.5 eV is shown as a base for comparison. Notice that for these given conditions, PTFE produces the least amount of radiation and that by adding only as small about of copper to HDPE its radiation is greatly increased. This supports the work reported by Ruchti[81]. Of even greater interest is the distribution of energy that is in above and below the  $300 \text{ nm}$  critical wavelength,  $\lambda_c$ . Figure 1.6 shows the integrated energy from 50 to 1000 nm. This figure shows the total energy as well as the energy above and below the critical wavelength which was chosen to be  $300 \text{ nm}$ . Notice that while PTFE produced the least amount of over-all radiation, it produced the largest percentage of radiation with wavelengths below the critical cut-off. This would suggest that more energy is going directly into photo-ablating and less into other less efficient processes.

Despite the results shown here, and the material testing reported in the field of ablation controlled arcs, the tests conducted in this work were done with standard polyethylene. This material was used because of its historic roll in capillary discharge and so that these results could be compared with Burton's and other electrothermal PPT research.

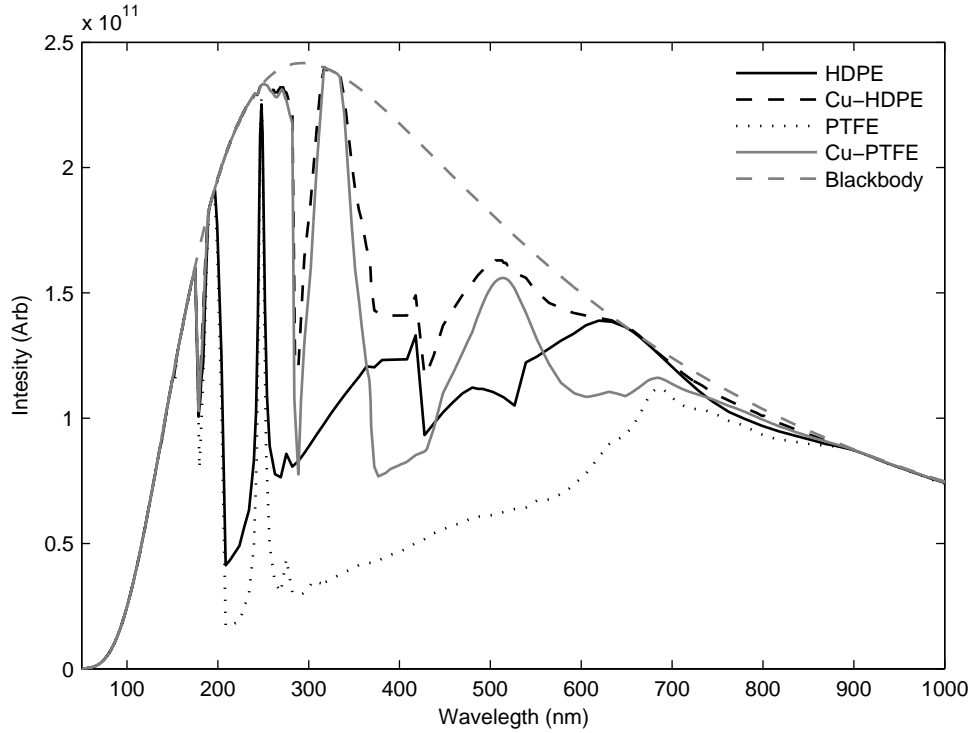


Figure 1.5: Spectrum produced by different plasma compositions at 1.5 eV and  $1.5 \times 10^{25} m^{-3}$  using PrismSpect Software

## 1.5 Capillary Physics and Assumptions

There are three primary physical assumptions that are typically used to produce simplified capillary discharge models. The first assumption (1) is that the capillary discharge is an electrothermal device so that the effect of magnetic fields can be neglected. The validity of this assumption is quantified using the plasma  $\beta$ . This parameter is defined as the ratio of thermal pressure to magnetic pressure, must be significantly greater than one for the electrothermal assumption to be valid. The second assumption (2) is that the plasma is in local thermodynamic equilibrium (LTE). Under LTE conditions charge particles are considered to be the same temperature, greatly simplifying the physical model. The third assumption (3) is that the plasma is an ideal plasma. Ideal plasmas are those in which, for the majority of the time a plasma particle is traveling, it is unaffected by other particles and only rarely experiences strong charge interactions. The validity of the ideal plasma assumption is quantified by the non-ideal parameter, which is the ratio of the mean potential felt by a particle to the mean particle kinetic energy. If the non-ideal parameter is significantly less than one, it is reasonable to neglect charge coupling between ions and electrons and model it as an ideal plasma. These simplifying assumptions are also used in this work. They must hold

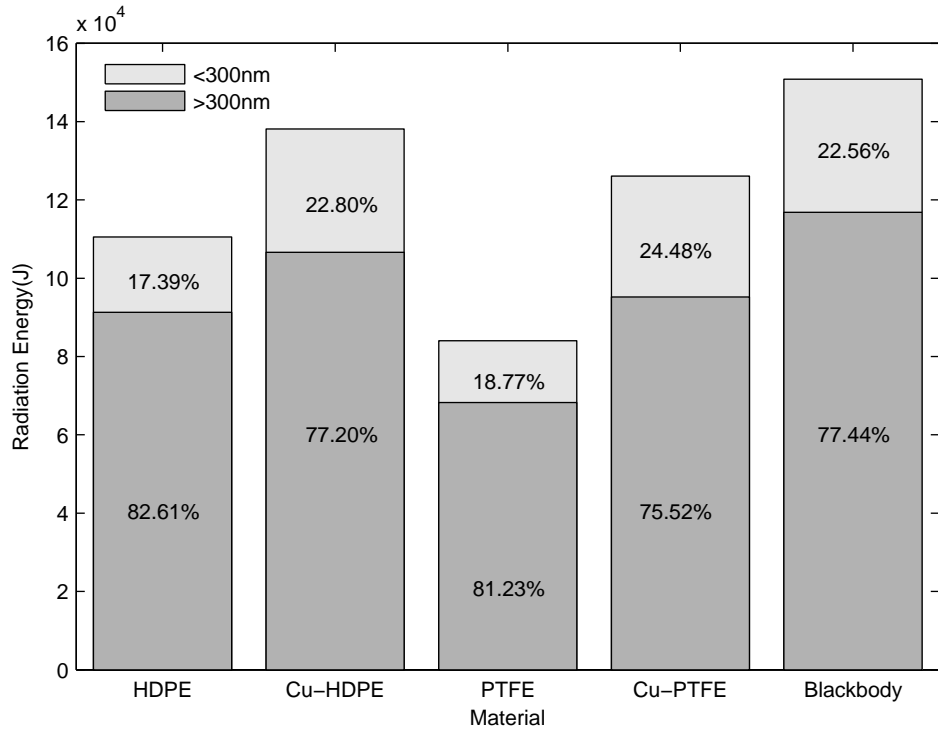


Figure 1.6: Integrated energy from 50 to 1000 nm for spectra from Figure 1.5

if meaningful comparisons between theory and experiment are to be made, and to allow interpretation of the experimentally measured results. Each simplifying assumption is described in more detail below.

### 1.5.1 Pressure Ratio

The factor  $\beta$  is the ratio of thermal pressure to magnetic pressure in the plasma. In order to model a device as purely electrothermal,  $\beta$  must be much less than one. As  $\beta$  approaches unity, the magnetic forces within the plasma are similar in magnitude to those due to thermal pressure and can not be ignored. If  $\beta$  is much larger than 1, the operating physics of the device are very different, and it operates as a z-pinch device[103]; where the magnetic force causes the plasma column to collapse upon itself, generating much greater pressures.

The parameter  $\beta$ , as mentioned earlier, is defined as the ratio of thermal pressure to magnetic pressure

$$\beta = \frac{P_T}{P_B} \quad (1.4)$$

Where  $P_T$  is the thermal pressure defined by

$$P_T = nkT \quad (1.5)$$

And  $P_B$  is the pressure caused by the magnetic field.

$$P_B = \frac{B^2}{2\mu_0} \quad (1.6)$$

The magnetic field in the capillary discharge is generated by the large current flowing though the plasma column. The relationship between the plasma current and magnetic field can be assumed from Amperes law

$$B = \frac{\mu_0 I}{2\pi r} \quad (1.7)$$

By substituting Equations 1.5 and 1.6 into Equation 1.4 an expression for  $\beta$  is obtained,

$$\beta = \frac{8nkT}{\mu_0} \left( \frac{\pi r}{I} \right)^2 \quad (1.8)$$

For a temperature ( $2 \text{ eV}$ ), density ( $1 \times 10^{25} \text{ m}^{-3}$ ), radius ( $0.002 \text{ m}$ ) and nominal current ( $6 \text{ kA}$ ) expected in the experiments conducted here, the pressure ratio  $\beta$  is about 22. Because  $\beta \gg 1$  the device is considered purely thermally driven. It is important to note that while  $\beta$  is greater than 1, if the density is an order of magnitude lower, while the other parameters are held constant,  $\beta$  can get very close to 1 and the previous assumptions may not be valid.

### 1.5.2 Local Thermodynamic Equilibrium

A system can be said to be in thermodynamic equilibrium if it is in thermal equilibrium (temperature), mechanical equilibrium (pressure), and chemical equilibrium (chemical potential). The condition of local thermodynamic equilibrium (LTE) exists when intensive properties (such as temperature) may change in the system, but are doing so slowly so there is approximate equilibrium around a point. In LTE temperatures are well defined and the electron temperature is the same as the heavy particle (molecules, atoms, and ions) temperature. To show that this is the case for typical capillary discharge plasmas produced in this work, it is necessary to look at the energy heating the particles. The average energy exchanged in an electron-ion collision is

$$\Delta\epsilon_{e\leftrightarrow i} = T \left( \frac{2m_e}{m_i} \right) \quad (1.9)$$

Where  $m_e$  is the mass of the electron and  $m_i$  is the mass of the ion. The average energy an electron gains from a surrounding electric field between collisions is

$$\Delta\varepsilon \approx eE\nu_{e,drift}\tau_{ei} \quad (1.10)$$

Where  $e$  is the unit charge,  $E$  is the electric field, and  $\nu_{e,drift}$  is the electron drift velocity which can be defined by

$$\nu_{e,drift} \approx \frac{eE\tau_{ei}}{m_e} \quad (1.11)$$

Here  $\tau_{ei}$  is the electron-ion collision frequency and can be expressed by  $\tau_{ei} = \frac{1}{\nu_{ei}}$ . Using this relation and substituting Equation 1.5.2 into Equation 1.10 a new equation for the energy gained from the electric field is obtained.

$$\Delta\varepsilon_E = \frac{e^2}{m_e} \frac{E}{\nu_{ei}} \quad (1.12)$$

The electron collision period,  $n\nu_{ei}$ , can be described by the number of particles, their effective cross-section, and the velocity in which they are moving.

$$\nu_{ei} = n\sigma v \quad (1.13)$$

where  $\sigma$  is the collision cross section area described by  $\sigma = \pi r_o^2$  in which the impact parameter is

$$r_o = \frac{e^2}{4\pi\varepsilon_0 mv^2} \quad (1.14)$$

Assuming a Maxwellian distribution the electron velocity can be estimated to an order of magnitude by  $v^2 = \frac{kT}{m_e}$ . Substituting the values into equation 1.12 an equation is obtained for the average energy gained by an electron between collisions, due to the electric field, as a function of the electric field, temperature and number density.

$$\Delta\varepsilon_E = \frac{256\pi^2\varepsilon_o^2 k^3}{e^6} \frac{T^3 E^2}{n^2} \quad (1.15)$$

The LTE parameter can now be defined[22] as a ratio of energy exchanged during electron-ion collision to the energy gained by the electron from the electric field.

$$K = \frac{\Delta\varepsilon_{e\leftrightarrow i}}{\Delta\varepsilon_E} \quad (1.16)$$

Combining equations 1.9 and 1.15 into 1.16 a value for the LTE can be obtained.

$$K = \frac{1}{128} \frac{e^6}{\pi^2 \varepsilon_o^4 k^3} \frac{m_e}{m_i} \left( \frac{n}{ET} \right)^2 \quad (1.17)$$

Therefore at a given temperature of  $4 \text{ eV}$ , a number density of  $1 \times 25 \text{ m}^{-3}$  and an electric field of  $1 \times 10^5 \text{ V/m}$  the LTE parameter of  $K \approx 1 \times 10^9$ . This indicates that the plasma is strongly dominated by collisions and can be considered in local thermodynamic equilibrium.

### 1.5.3 The Non-Ideal Parameter

The Non-Ideal plasma parameter,  $\Gamma$ , is defined by

$$\Gamma = \frac{W_{PE}}{W_{KE}} \quad (1.18)$$

Where  $W_{PE}$  is the potential energy between two charged particles and  $W_{KE}$  is the average kinetic energy for a particle.

$$W_{PE} = \frac{e^2}{4\pi\varepsilon_o r} = \frac{e^2 n^{1/3}}{4\pi\varepsilon_o} \quad (1.19)$$

Where the distance between the particles,  $r$ , can be express by  $n^{-1/3}$ . And the kinetic energy is

$$W_{KE} = kT \quad (1.20)$$

By combining these equations an expression for the non-ideal parameter is obtained.

$$\Gamma = \frac{e^2 K T n^{1/3}}{4\pi\varepsilon_o} \quad (1.21)$$

For a temperature of  $2 \text{ eV}$  and a density of  $1 \times 10^{25} \text{ m}^{-3}$ , typical for the experiments conducted in this work, the calculated  $\Gamma$  is about 0.16. Because  $\Gamma$  is less than 1 the plasma can be considered ideal and is dominated by its kinetic or thermal energy.

## 1.6 Evaluation of Thruster Performance

Understanding the device physics is important, but the key metrics for consideration of pulsed electrothermal thrusters are the performance metric. A capillary discharge is being investigated as a spacecraft

thruster, and while measurements such as current and temperature are important in understanding the discharge process, the overall concern is with developing a thruster that can be operated within the needed niche discussed in Section 1.1.

Therefore one of the most importance diagnostic tools is the thrust stand that is mentioned in section 3.4.2. This device permits a full evaluation of the thruster as a propulsion device. The thrust stand can measure the impulse,  $I$ , directly and the average mass loss is calculated from scale data. From this an average measurement of  $I_{sp}$  can be calculated by the following relationship,

$$I_{sp} = \frac{I}{\Delta m g_o} \quad (1.22)$$

Here  $I$  is the total impulse imparted to the thrust stand by the thruster,  $\Delta m$  is the average mass loss per shot, and  $g_o$  is the gravitational constant. The propulsion efficiency,  $\eta$ , can also be obtained from,

$$\eta = \frac{E_{thrust}}{E_{electrical}}, \quad (1.23)$$

where the thrust energy,  $E_{thrust}$  can be described by  $\frac{1}{2}g_o I_{sp} I$ . The  $E_{electrical}$  is simply the electrical energy used by the thruster,  $\int V j dt$ . Here  $V$  is the instantaneous voltage across the capillary, and  $j$  is the instantaneous current that passed through the device. These 3 parameters,  $I$ ,  $I_{sp}$ , and  $\eta$ , define the performance of the capillary discharge as a thruster. There are many other parameters that are important when considering a thruster for a spacecraft, but at this stage of basic research and development, these parameters are sufficient to indicate whether the capillary discharge has potential as a future propulsion system.

## 1.7 Ignition Methods

It has been shown that the ignition properties of a capillary discharge can greatly influence the plasma conditions of the main discharge plasma[82]. Work in the field of soft x-rays producing capillary discharges has shown[8]: low pre-pulse currents are insufficient for effective capillary pre-ionization and high currents prevent effective pinching due to largely preheated plasma. In addition to what can be found in the literature, initial capillary tests with wire ignition at the AFRL also showed a dependence on the ignition condition, in the form of a dual mode of operation. These findings were part of initial work associated with the study and are discussed further in Section 6.3.

It was felt that ignition was important to investigate. The presented study will examine how pre-discharge condition influence the overall capillary operation. The research that was carried out chose to explore: different ignition methods; how each method effected thruster performance; and to explain the the dual mode operation observed in early wire ignition testing. Capillary discharges have been ignited using many different techniques over the years. Some of these methods are used for their simplicity and others for creating complex plasma profiles, as is done for plasma wave guides, mentioned in Section 1.3. In this work wire, gas breakdown, and spark ignition techniques were examined and their effects on the overall discharge and thruster performance investigated.

The preliminary capillary discharge experiments were ignited using a thin, 0.004 diameter, aluminum wire, as described in Section 2.1.1. This method is certainly not applicable in a spacecraft propulsion system, but this method has frequently been reported in literature and thin wire is considered very reliable and easy to implement. Through initial application of this method it is possible to understand and develop the capillary circuit, become familiar with the techniques needed to contain high pressures, and to develop and tune diagnostic equipment. It was also in these preliminary tests that the need to further explore the effects of ignition conditions on device operation was established. It was noticed while using the wire technique that the capillary would discharge in two distinct current modes. Further initial ignition tests were not only an improvement in overall design for test purposes, but also provided a better understand of multi-mode operation, which will be discussed further in subsequent chapters.

Following the initial ignition tests and proof of concept, a Paschen ignition scheme was adopted, as is explained in Section 2.1.2. This permitted further progress towards a spacecraft thruster, and allowed the device to be mounted on a thrust stand which enabled more accurate impulse and specific impulse measurements . The discharge was also run in a reverse configuration by placing the anode at the exit of the capillary. However it was quickly discovered that this method did not work with the current design. Basically, as the discharge plume expanded into the chamber it created conductive paths between the exposed anode and the grounded chamber walls, causing secondary arcs and stray discharges.

One of the most common and simplest ignition techniques use a spark plug, such as an integrated semiconductor type spark plug[18], near the capillary exit. The 3rd design, which is described more thoroughly in Section 2.1.3, uses a coaxial spark ignitor near the exit of the capillary discharge. This technique allowed the testing of spark ignition techniques without committing to major redesign changes. Initial tests showed that the method worked quite well, and the overall design was quickly changed to incorporate this technique into a single housing, instead of continuing to investigate the external coax spark ignitor.

Once the spark ignition technique was shown to be effective, an internal three-electrode system was designed as described in Section 2.1.4. This design used the same technique at the coaxial ignitor, but placed the spark internally, between the anode and cathode, allowing a more reliable ignition.

### 1.7.1 Wire Ignition

Attempts to understand the electrically driven wire explosion process can be traced back as far as 1774 when Nairne was studying the conservation of current in series circuits.[24]. However, work on the subject did not really progress until the late 1950s and early 1960s. This work continued through the recent decades as more uses for exploding wire were discovered.

The wire ignition process, while very reliable in terms of its ability to ignite a capillary, is a chaotic and nonuniform process. Capillary discharge operation not only depends on the mode of wire vaporization, but the ablated mass and thrust energy will be strongly influenced by the initial plasma conditions following the wire explosion. One of the most interesting works on wire explosion, as it applies to capillary type devices, was reported by Taylor[93]. His work goes into great detail about the mechanism and structure of an exploding wire. Figure 1.7 shows a wire explosion, as photographed by an intensified

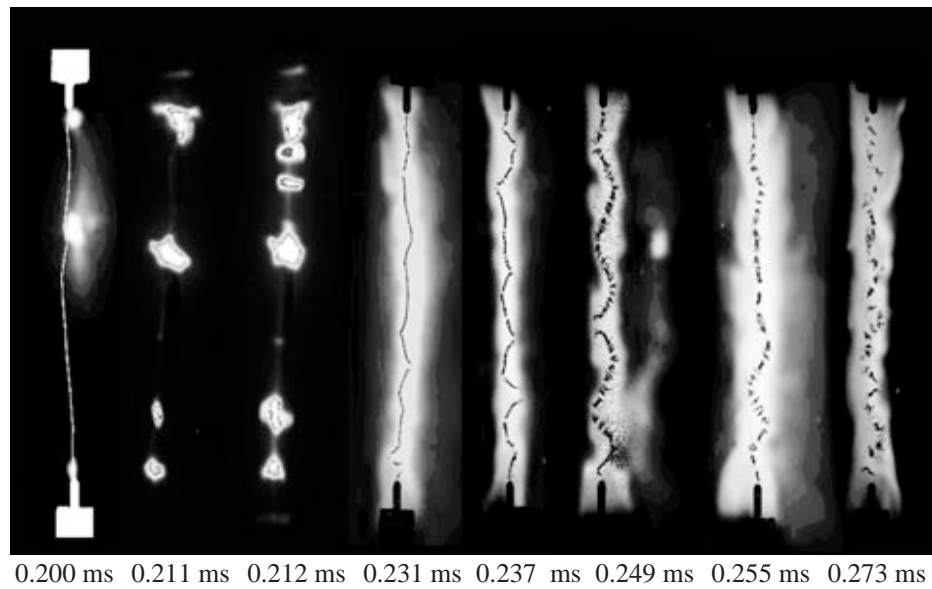


Figure 1.7: Photograph and x-radiograph montages of an exploding wire[93]

fast frame digital camera and a flash x-ray system, to obtain details of the wire structure hidden by the expanding plasma. As can be seen the wire does not vaporize evenly. Breaks occur within the wire due

to hot spot formation in the material. These hot spots may occur due to a variety of inhomogeneous factors, most noticeably kinking during thermal expansion, but also; thermal stress waves, impurities, lattice dislocation, and physical damage. As the breaks develop, the resistance increases, thus causing a voltage drop across each break. A point is reached when the voltage attains the Paschen or similar threshold for electric breakdown, and an arc discharge occurs. The discharge current, plasma temperature or resistivity, and the spot dimensions will all effect the ohmic heating that occurs. The resistance of the entire system rises as the length of the plasma section increase, and the amount of wire between the plasma spots decrease. Once the wire is completely sheathed in a conductive plasma the energy distribution along the length of the system is likely to become more uniform. This resistive equilibrium occurs 10's, if not 100's, of micro seconds into the explosion. At this point, within an ablative capillary, material from the ablation capillary wall will govern that physical operation of the discharge. Therefore, it is likely that the wire does not full explode to the late stages seen by Taylor. It is possible that initial fragmentation and plasma hot spots formed in the early stages of wire explosion ignite the capillary discharge.

Another problem with wire ignition was its effect on spectroscopic diagnostics. Line spectrum from the aluminum not only pollute the Stark broadened hydrogen Balmer lines, but would also change the plasma density which was of interest. The amount of wire used to ignite the capillary was on order of the amount of material ablated from the capillary walls. So it was possible that a large fraction of the plasma composition could be aluminum. This is unlikely that the wire full decomposes. More probable that a large number of macro particles are produced and expelled out the cathode. The degree or wire explosion, the amount of ions formed, and therefore the exact plasma composition, could not be known. The amount of aluminum material not only influenced the capillary discharge plasma composition, but also made it impossible to measure accurately any thruster performance characteristics with confidence. Wire material exiting the capillary would give sporadic impulse measurements, as well as making it impossible to account properly for mass loss in order to calculate such metrics as  $I_{sp}$  and  $\eta$ . Because the ultimate goal was to understand capillaries and their application as a spacecraft thruster, it was necessary to develop a new ignition method and allow for proper thruster performance measurements.

In Summary, wire explosion is not valuable in a spacecraft propulsion system, it is also of limited value for determining the effects of ignition conditions on overall performance because of its complexity and nonrepeatability. The technique is, however, very widely used and it is included in this study for comparison purposes.

### 1.7.2 Paschen Ignition

In order to successfully study and understand the capillary discharges and their ignition, it was strongly felt that the wire needed to be removed and another method used. This not only progressed toward the end spacecraft thruster design, but also allowed for more in-depth accurate studies. Removing the wire removed that material from the plasma. This fact allowed more accurate analysis of the plasma, knowing that it was not “polluted” with elements other than the carbon and hydrogen from the polyethylene (and the small amount of electrode material that is eroded). It also allowed for proper mass accounting and confident Impulse and  $I_{sp}$  measurements.

A Paschen breakdown ignition scheme seemed the most logical next step in the study of capillary ignition phenomenon. The idea was to eliminate the wire from the experiment and lower the background pressure to a range where the space between the anode and cathode would break down based on the principles of Paschen's Law. Paschen found that breakdown voltage could be described by the equation

$$V = \frac{a (pd)}{\ln (pd) + b} \quad (1.24)$$

Where  $V$  is the breakdown voltage in volts,  $p$  is the pressure in atmospheres and  $d$  is the gap distance in meters. The constants  $a$  and  $b$  depend upon the composition of the gas. For air at standard atmospheric pressure of 760 Torr,  $a = 43.6 \times 10^6$  and  $b = 12.8$ [3]

By this account it would take 49.5, 33.0, 24.7, and 19.8 Torr to break down our 4, 6, 8, and 10 cm capillaries, respectively at 2500 V. These values were based on Paschen's law for parallel plates and gave a good idea, but not exact value to accurately predict the breakdown for our geometry. What more, the gas composition can greatly affect the breakdown properties, as seen in Figure 1.8. Even a small change in humidity can affect these curves.

### 1.7.3 Coaxial and 3-Electrode Ignition

The coaxial igniter and 3-electrode ignition system operate under the same general principle. They provide an electric field disturbance as well as ionized material that allows the main discharge to occur. These ignition systems use a voltage difference applied across two electrodes separated by an insulating material to create a surface flash over. In the case of the coaxial igniter this flash over occurs radially as the core is charged to high voltage and the shielding or outer cathode is held at ground, with a teflon insulator separating the two. The 3-electrode igniter used the same concept but different geometry. A high voltage

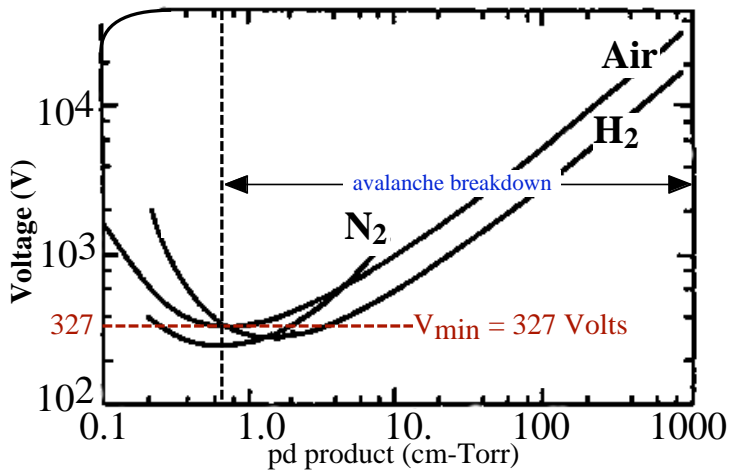


Figure 1.8: The Paschen curve for dry air, nitrogen, and hydrogen.[27]

electrode is placed a small axial distance away from the capillary's anode, separated by a polyethylene insulator. Here the flashover occurs axially instead of radially.

There are two main schools of thought behind surface flashover. One predicts a sub-surface process and the other an above-surface process; the second being the more widely accepted[70]. Above-surface flash over of insulators in a vacuum can be described mostly as a 3 phase process[72]. Phase one is a fast buildup of a saturated secondary electron avalanche. This phenomena takes place in about two nano seconds and produces currents of 10 to 100  $mA$ . This avalanche occurs when electrons are released by field emission from the cathode by means of microfractures, impurities, and field increase[11]. The field emitted electrons strike the insulator surface and release secondary electrons. If the yield is greater than 1, the struck position takes on a positive charge. This positively charged surface area re-attracts back the secondary electron that was emitted, causing further electron surface strikes and secondary electrons. As long as the secondary electron yield is greater than 1, an electron avalanche is formed. This avalanche cascades towards the anode because of the electric field formed between anode and cathode. The second phase occurs from electron induced gas desorption and current amplification via the Townsend process. This leads to 10 to several 100  $A$  in several hundred nanoseconds. The space between the electrodes becomes more positively charged due to the slower drift velocity of ions in the desorbed gas layer. The result is an enhanced internal electric field, and therefore more cathode field emission and total current. The third phase is shorter, at several nanoseconds, and creates about 1  $A$ . It is based on the nonlinearity between the field emission current and electric field, which leads to an impedance collapse.

The mechanisms involved in fully understanding surface flashover are complicated. For ignition of the main capillary discharge, it is important that the neutral and charge particle leave the surface during the second phase of the surface flash over. It is these particles that create a conductive path for the discharge to occur. It is speculated that the mechanisms that start the surface flashover in the ignitor are the same as those that starts the the main discharge. The processes can be thought of as a small capillary discharge igniting a larger one.

# Chapter 2

## Experimental Setup

In this section the experimental setup involved in operating a capillary discharge will be examined. Because this project was started from scratch there was significant required design work associated with the capillary. Design iterations will be explained along with the logic behind each development and change. It is often difficult to find good accounts of experimental setups in the literature. The information in this section presents a detailed account of how the devices were built and tested, providing information for future experimenters. This section also covers other hardware setups including; circuits, facilities, and diagnostics.

### 2.1 Capillary

While the capillary configuration remained fairly constant throughout this test program, the housings changed quite significantly. These changes were mostly motivated by; arc prevention, pressure sealing, and the ignition method. Throughout the experiments standard, off-the-shelf, 4 *mm* inner diameter, 6 *mm* outer diameter, polyethylene tubing that is common to the medical and food industries, was used. Polyethylene ( $\approx CH_2$ ) was chosen as the capillary material because it has significant heritage as a capillary discharge propellant[19, 16, 17]. All capillary designs allowed the testing of different lengths, from 40 – 100 *mm*.

#### 2.1.1 Capillary Design V1.0 for Wire Testing

The first design (V1.0) was machined polyethylene tube sized to fit into two high pressure weld-neck flanges that had been welded end-to-end. The anode in this setup was made from maraging steel which was connected to the power system by a copper rod screwed into the back of the anode. The anode and transfer rod were insulated with several Teflon<sup>®</sup> pieces. A sketch of the internal workings of this design is shown in Figure 2.1. Several problems arose with the design, the largest of which was electrical

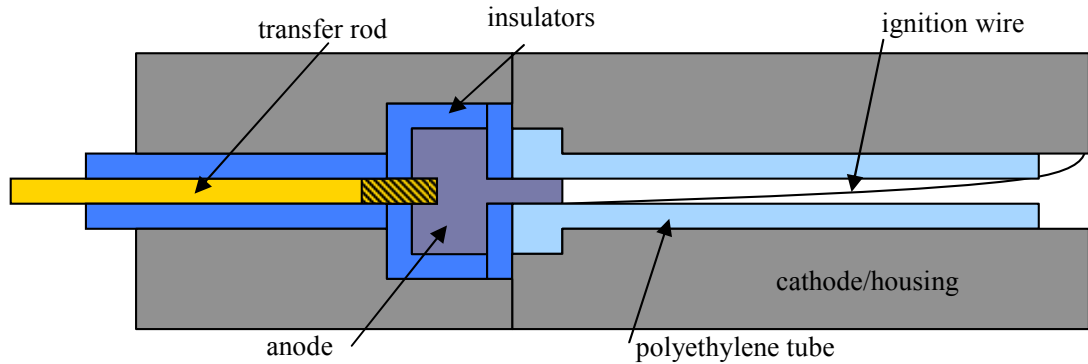


Figure 2.1: Schematic of Capillary Discharge Design V1.0

shorting that occurred around the anode. The insulation was composed of separate Teflon<sup>®</sup> pieces press-fit together to form a seal, but the inevitable small cracks between the pieces would reveal a shorter path to ground than the 100 mm from anode to cathode. This would cause the device to short before ignition took place. This initial problem was overcome by using more accurately machined parts that compressed to form tight seals. However, after ignition, the high pressure gas or plasma would push between the Teflon<sup>®</sup> pieces producing another short during the discharge. Because of the persistent electrical shorting, the relative difficulty of loading the ignition wire, as well as the machining time to produce these parts, a new simpler design was needed. Design V1.1 addressed these issue before any major testing could begin.

### Capillary Design V1.1

Several different setups were considered to deal with the issue of blow-by gases. Factors such as wire loading method, housing assembly, reload time, capillary mass loss measurements, and arc prevention all had to be carefully considered. Different methods of sealing multiple tubes and sheathing were tested. Ultimately, it was shown that a single long capillary that covered the entire anode with a single sheathing would work best. This redesign phase used stock 4 mm, ID, 6 mm OD tubing fitted in a 6 mm ID, 8 mm OD tube. This tube-within-a-tube assembly fit nicely in the Design V1.0's high pressure flanges with little modification. A resin casting compound was used in the thruster housing to fill the gaps for previous design methodology. Several different anode material were tried to reduce electrode mass loss. Welding electrode tungsten rod that was either 1.5% lanthanated or thoriated was used. Figure 2.2 shows a sketch of Design V1.1 which was implemented the first round of wire ignition tests.

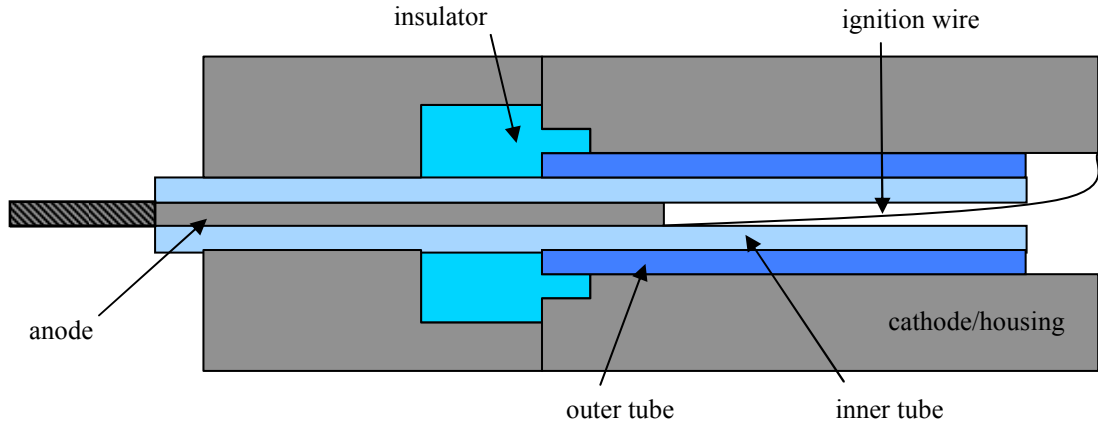


Figure 2.2: Schematic of Capillary Discharge Design V1.1

Several concerns arose from this design. Foremost, force sensors were attached to the high pressure flange assembly, which could have difficulty acquiring accurate measurements. In this design the anode is slip-fit into the inner most tube. The inner tube is then slip-fitted into the outer tube. These types of fits could be problematic if the slip fits fails resulting in a shift of the tubes. Internal movement of comments would causing inaccurate force measurements. While safety precautions were taken, the impact on force measurement may be significant. The blow-back gas problem was not completely alleviated with this design and it did cause capillary rupture and capillary separation at voltages above approximately 3250 V. Gas residue and charring occurred back up the Anode rod, however it did not appear that gas made it all the way to the other end of the capillary (near the threaded cable attachment point).

Design V1.1 proved to be reliable and safe. The majority of the experimental results presented with wire ignition were collected using this design. Although there may be differences in insulation and anode material, the design concept remained the same throughout most of the wire tests. This design and ignition technique was simple enough to allow preliminary investigation of the capillary physics. It was possible to test current and voltage probes, as well as light collection from the capillary exit, in an effort to measure temperature and pressure from emission spectroscopy that will be discussed in Section 3.5.

### 2.1.2 Capillary Design V2.0 for Paschen Breakdown Testing

For the next phase of testing a Paschen breakdown ignition system was implemented as mentioned in Section 1.7. For this method there was no wire and the opportunity was taken to simplify the whole setup and entirely redesign a new system. The large high pressure flanges were replaced with a standard

stainless steel pipe. This pipe was threaded and inserted into a simple stainless steel pipe union. The other end of this union had an NPT to compression adapter fitting attached. A diagram of how these parts are assembled is shown in Figure 2.3. The two main sealing issues were addressed in Design 2. First was at the anode rod, which was again, slipped into the back of the tube and housing assembly. The use of compression fitting allowed the tube to be squeezed around the anode rod forming a tight seal. Throughout this phase of testing no blow-back gases were witnessed past the compression fitting. This design implementation was carried throughout all future designs. The compression fitting did an excellent job of holding the anode in place and no slipping occurred. Originally stainless steel ferrules were used. There was a concern about arcing though the polyethylene due to the compression force applied at this location, however, no incidences occurred. The other sealing attempt was made at the cathode end. Charring was occasionally observed on the outside of the polyethylene tube. It was believed to be from gas exiting at the cathode end. A small stainless steel insert was welded into the end of the housing to form a seal with the tube end. This insert had two other important effects. It allowed for better spectroscopic measurements by restricting the gas expansion until it reached a region were it could be accessed by the optical system. This is discussed further in Section 3.5. The other added benefit was that it resulted in easier Paschen breakdown since it brought the electrode material closer to the centerline of the capillary. This resulted in increasing the view factor to the anode. In other words, creating a more direct line-of-sight between the two electrodes.

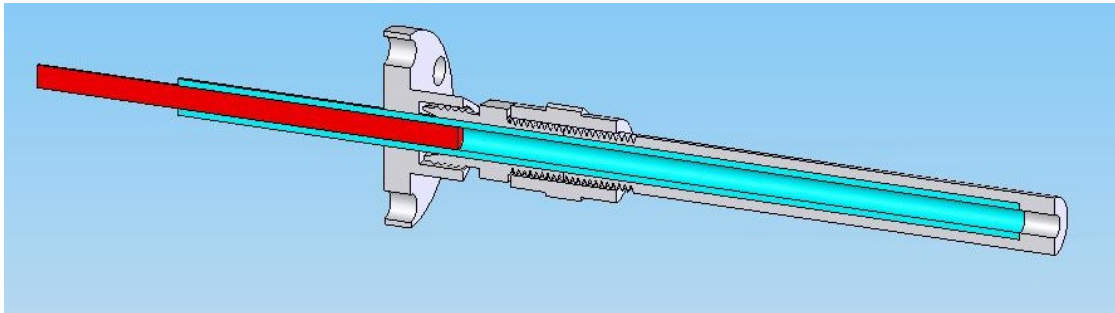


Figure 2.3: Schematic of Capillary Discharge Design V2.0

Several problems did arise with this design as well; most of which were associated with the cathode. First was the minor issue of the seal between the cathode and tube end. A significant amount of soot was witnessed between the inner housing wall and the outer capillary tube. The second and more major problem was from cathode erosion. In almost all cases the amount of mass lost from the cathode was significantly higher, on the order of several times, than that of the polyethylene tubing. These problems,

as well as the effect of erosion on thruster performance are discussed in Section 6.2. It was clear that the cathode needed to be redesigned. A Tungsten cathode would offer resistance to both conventional electrode erosions and against the exiting high temperature gas.

### Capillary Discharge V2.1

With the design concepts proven, the redesigned V2.1 housing was machined from one piece of stainless steel, instead of using standard tubing and fittings. An insertable tungsten anode was adopted and held in place by a standard AN nut. The housing now consisted of a 1/2 in stainless steel tube with a compression fitting machined on one end, and an AN fitting on the other, as shown in Figure 2.4. It was discovered that this cathode insert design provided an excellent way to seal the tube at the cathode end. The tube was loaded into the housing, allowing for a small amount of material to protrude past the edge of the housing. This extended material could then be melted, or made malleable, using a heat gun and flattened into a disc or lip. This lip was then compressed between the housing and the insert to form a tight seal. With

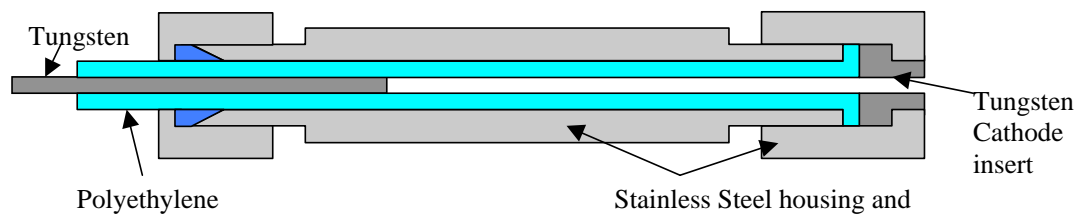


Figure 2.4: Schematic of Capillary Discharge Design V2.1

this new design, cathode erosion was more reasonable, the overall assembly was lightened so it could be mounted on the thrust stand, and new liner tubes could be easily loaded. This V2.1 design was used throughout the Paschen breakdown experiments.

The one issue that the V2.1 design did not solve was, the charring between the liner tubing and the stainless steel housing. While it was clear that the seals at both the anode and the cathode held, the soot between the capillary tube and the housing increased. Capillaries began breaking, shorting in as little as 3 or 4 shots. The reasons for this are discussed in Section 6.4.

### Capillary Discharge V2.2

One final revision was made to the second design. The original inspiration for the revisit of this design was to fix problems associated with full tube collapse. In a tube collapse, the capillary brakes open near

the middle and the arc attached to the housing wall. This caused pitting and damage that made it more difficult to load capillary tubes, or extract them, without damage. The design philosophy behind the new housing was to use standard stainless steel tube for the housing. In the event of a collapse the main body of the housing could be replaced without having to re-machine the entire housing. Also, the simplicity and versatility of this design permitted a variety of materials to be tried for housings. The materials that were tested and their effects on the discharge are discussed in Section 6.6.

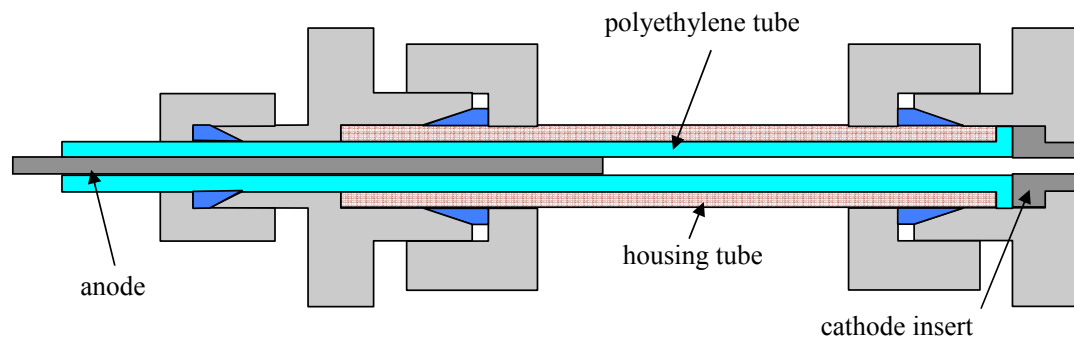


Figure 2.5: Schematic of Capillary Discharge Design V2.2

While the tungsten cathode inserts did reduce the erosion at the anode, they did not eliminate it entirely. The cathode itself still exhibited the same erosion pattern as seen previously with the stainless steel electrode, only taking much longer to develop.

### 2.1.3 Capillary Design V3.0 with Coax Ignitor

The initial proof of concept tests for the coaxial ignitor, discussed in Section 1.7, were conducted using the Design V2.2 and a 1/8 *in* copper and Teflon coaxial rod. The ignition circuit, developed by RE Beverly III and Associates for spark gaps, suited this application quite well. The circuit consisted of a trigger transformer and power supply, controlled by a pulser or trigger generator via a fiber optic cable. The pulser itself was triggered by a TTL signal from the control computer.

The coaxial rod assembly was positioned near the exit plane of the capillary, as shown in Figure 2.6. Several different ordination angles and positions were tried before the capillary would ignite under full vacuum. While the capillary was successfully ignited a few times, it was sporadic and unpredictable. It was believed that this problem was due to worn electrodes from the previous Paschen testing. Ignition in hard vacuum proved more difficult than the previous methods, and the electrode geometry played a larger

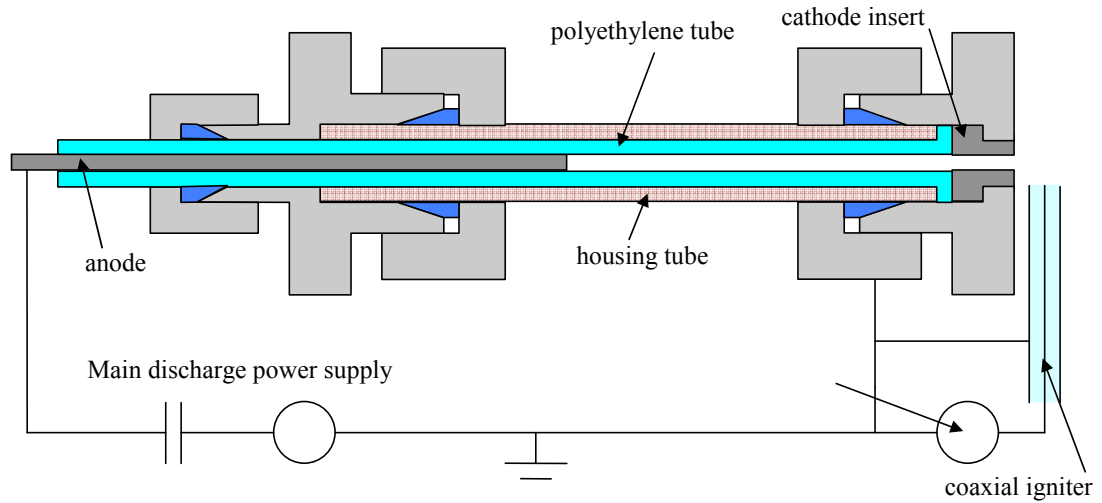


Figure 2.6: Schematic of Capillary Discharge Design V3.0

role. It is therefore not surprising that the short  $4\text{cm}$  capillaries ignited more easily under this method and the method in Section 2.1.4, than the  $10\text{cm}$  capillaries. Because the relative difficulty of machining tungsten, it was far easier to make completely new housings adapted to electrode geometry than to make new electrodes. Therefore, it wasn't until the set of electrodes for Design four were completed that the coaxial ignitor could be tested.

The coaxial ignitor was only used for a small number of geometries and power levels, to prove that the discharge could be started by either a spark or electric field disturbance. The ignition method of using a spark igniter was designed into an internal section of the housing, known as our 3-electrode ignition system or 3EIS.

#### 2.1.4 Capillary Design V4.0 with 3-Electrode Ignitor

The 3 electrode system contains a third high voltage spark electrode that creates a field disturbance to start the capillary discharge, similar to the design used by Kaganovich[56]. The high voltage electrode is placed behind the cathode (between the anode and cathode) separated by several mm of ignition material, which is made out of the same material as the capillary itself. The ignition electrode was placed at that location for several reasons. First it was anticipated that material (ions and electrons) emitted from the ignition material surface would be caught between the anode and cathode, making ignition easier. The second reason was that cathode erosion was still a problem, and a slight cone angle was machined onto the cathode. While the cathode erosion was much less with tungsten, the same pattern was seen as with the

stainless steel cathode used in Design 2. As discussed in section 6.2, figure 6.4 indicated that the erosion pattern tended to expand the exit of the cathode to a certain diameter. It was believed that by adding a conical cathode, erosion would be reduced even further. 4 different cathodes were originally machined with 0°, 5°, 10°, and 15° half angle, However only the 10° was used during these ignition tests.

Design V4.0 also employed many capillary discharge design lessons learned from all previous designs (V1.0-V3.0). The anode end was sealed with a compression fitting as before. The housing was machined from aluminum to add structural support to the polyethylene capillary, and to keep the device light so the scale could resolve the mass loss. Material was also removed from the middle section of the housing for the same reason. The old cathode end was replaced by a flange like system. This allowed for a larger internal volume in which to place the ignition electrode with proper electrical insulation. The same lip method was employed in this design. A set of 12 bolts supplied the compression needed to seal the capillary, as shown in Figure 2.7.

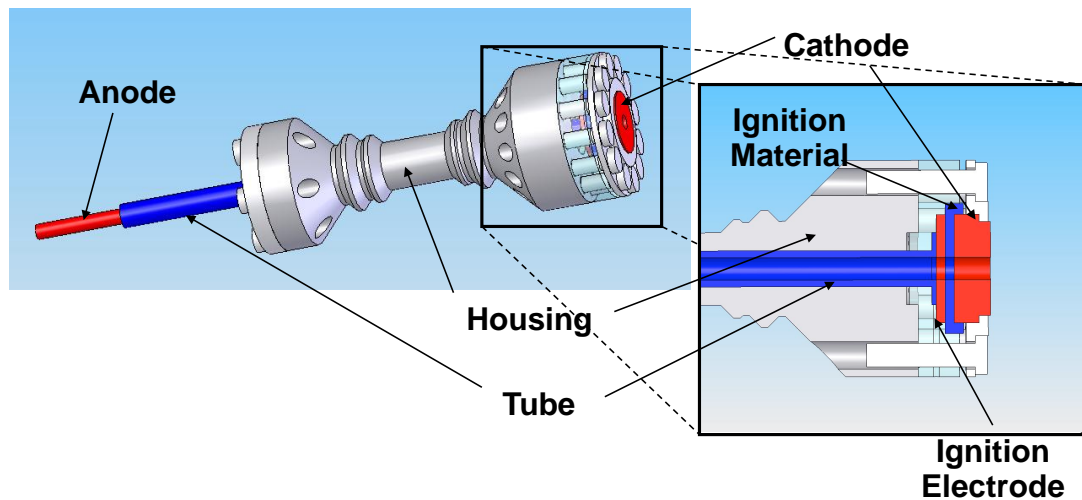


Figure 2.7: Schematic of Capillary Discharge Design V4.0

The original ignitor housing was made from acrylic. This setup fired a couple of times, but the materials dielectric strength was high enough and eventually arcing occurred through the material between the ignition electrode and the bolts. Nylon bolts were used to secure the cathode and subsequent seals. While this did stop the arcing problem it did not apply enough compression to seal the device, especially at higher powers and pressures. The ignitor housing was redesigned with a large diameter hole pattern which allowed for more material between the ignition electrode and the bolts. A different material with a higher dielectric strength was also used, PolyChloroTriFluoroEthylene (PCTFE) called Kel-F®. PCTFE offered

a unique combination of physical and mechanical properties: nonflammability, chemical resistance, near zero moisture absorption, and excellent electrical properties. It is also easy to machine and holds excellent tolerances that are needed in the ignitor housing.

In this design the ignition electrode and the cathode were made out of 1.5% lanthanated tungsten, which material has excellent electrical and thermal properties, but it is very brittle. The  $1/16$  in thick ignition electrode would crack under compression, especially if the lip that was used to seal the capillary to the electrode was uneven. Several of the tungsten ignition electrodes were ruined during the first half of the test matrix before the material was changed to stainless steel. While the mass loss of the tungsten electrode was less, it proved too brittle. Stainless steel offered much better mechanical properties and mass loss due to erosion was still only a few percent of the total mass loss.

Tests began with 4 cm capillaries and progressed to longer capillaries. For the final design the capillary was operated reliably and repeatably at shorter capillary lengths. However, at longer capillary lengths of 8 cm and 10 cm, ignition was not as reliable. The cause was most likely the same reason that caused the external coaxial ignitor faults. It is a combination of; poor view factors between the anode and cathode, which only gets worse as the cathode wears, and additionally the absence of conductive material that occurs between the anode and cathode. As the capillary gets longer, it becomes ever more difficult to generate a conductive path down the capillary, making ignition more difficult.

## 2.2 Circuit

Typical capillary discharge operate with both simple LRC circuits and more complicated pulse forming networks (PFNs). For the present studies a simple LRC circuit was chosen, which allowed the circuit parameters to be easily varied over a wide range, and resulted in simpler and more accurate comparisons with performance models. The capacitor bank assembled for this work consists of four 0.5 mF capacitors<sup>1</sup>. Each capacitor has a maximum current rating of 100 kA and a maximum voltage rating of 10 kV. The capacitors can be arranged in different configurations to achieve the required current and voltage. Arranging all four capacitors in parallel provides a total capacitance of 2 mF. The constant current capacitor charging power supply was limited to 6000V, yielding a maximum useable pulse energy of 36 kJ and a maximum peak current of 400 kA. Up to four 10 $\mu$  H (nominal) inductors from Cortec Enterprises were also added to control the responsiveness of the circuit.

---

<sup>1</sup>General Atomic capacitors, model 32259

### 2.2.1 Switches

A circuit element that is effectively neglected in capillary discharge modeling, but has proven very important in capillary discharge experiments, is the control switch. The switch can; input noise into the discharge pulse, limit the maximum current for the discharge, limit the total lifetime of the system, and affect the shape of the current pulse. Several different control switches were tested and the relative merits of each are described below.

#### **Insulated-Gate Bipolar Transistor (IGBT)**

IGBTs are solid-state semiconductor switching devices that have been designed for industrial applications such as air-conditioners and electric vehicles. They are noted for their high efficiency and can handle relatively high currents and voltages, but are presently unable to handle the high peak current and voltage ( $10's$  of  $kA$  at up to  $6\text{ kV}$ ) that can be encountered while testing capillary discharges. A Mitsubishi<sup>2</sup> IGBT was used during lower voltage capillary discharge experiments. IGBT peak current and voltage specifications are steadily increasing, indicating that they may be able to fulfill the capillary discharge switching role within the next decade. One of the benefits of IGBTs is the relative ease of operation. IGBTs are voltage controlled latching devices that are turned on by simply applying the required voltage to the gate. They stay latched open until the discharge itself is extinguished.

#### **Spark Gap**

The spark gap is a plasma switch that has been used in high-power applications for decades. While simple in design and concept they have proven to be more difficult to set up and operate. A spark gap switched circuit was tested for capillary discharges with capacitor voltages ranging from  $2\text{ kV}$  to  $4\text{ kV}$ . The particular spark gap used during the tests was from Perkin-Elmer. The spark gap required a  $20 + kV$  spike to trigger the switch. They also have a minimum switching voltage which, for the specific switch used in this study, was  $2\text{ kV}$ . Spark gaps can handle large instantaneous power loads, but are also greatly limited in the total charge per pulse. The spark gap also introduced a large voltage spike in the main capillary discharge which, caused several problems when trying to reach higher voltages.

---

<sup>2</sup>Model number CM1200HC-66H

### **Silicon-controlled Rectifier (SCR or Thyristor)**

A thyristor is a solid-state device similar to an IGBT. It has the added bonus of being unidirectional, much like a diode, and capable of handling larger peak power levels. The thyristors currently installed in the experimental setup are from West code<sup>3</sup>. It was possible to find commercially available driver boards for thyristors that are designed to produce the fastest switching time. The thyristor currently installed in the setup can switch the entire voltage range from 0 – 4500 V in and has a maximum peak current of 30 kA. This allowed the full range of discharge tests to be conducted with a single switch. Also, unlike the spark gap, there is no high-voltage trigger to cause voltage spikes at higher powers.

## **2.3 Facilities**

Two separate facilities were used during capillary discharge testing. For the wire explosion tests, which were conducted at atmospheric pressure, a cylindrical steel chamber was set up vertically to house the discharge device. The device itself was mounted to the top flange and shot downward into the cylinder. On the bottom flange a port was opened to an exhausted line that removed vapors from the chamber after firing. There were 4 rectangular view ports on the side of the cylinder for optical access. The chamber was not vacuum sealable, but did allow for a safe environment for testing. It also reduced the noise and light produced by the discharge.

The second test facility used in the capillary discharge tests was a full vacuum chamber, shown in Figure 2.8. This chamber had a vertical section similar to the atmospheric test facility. It also had a horizontal section to house the thrust stand mentioned in Section 3.4.2. The chamber was constructed out of a stainless steel ISO 400 4-way cross, and two ISO 400 Spools. An ISO 400 Tee section was later added so that a 3500 l/s diffusion pump could be added. The pump was never used because the 1000 l/s Varian 1000 turbomolecular pump provided adequate pumping. The Tee section did add more horizontal length to the chamber, therefore allowing more space to manipulate the thrust stand and align it with optical view ports.

The vacuum chamber's turbo molecular and backing pump allowed it to reach pressures of mid  $10^{-5}$  torr in several of hours. This pump down time was drastically increased as the inside of the chamber became coated with carbon soot from the discharge. The carbon itself did not ultimately affect

---

<sup>3</sup>Model number UK R3708FC45V

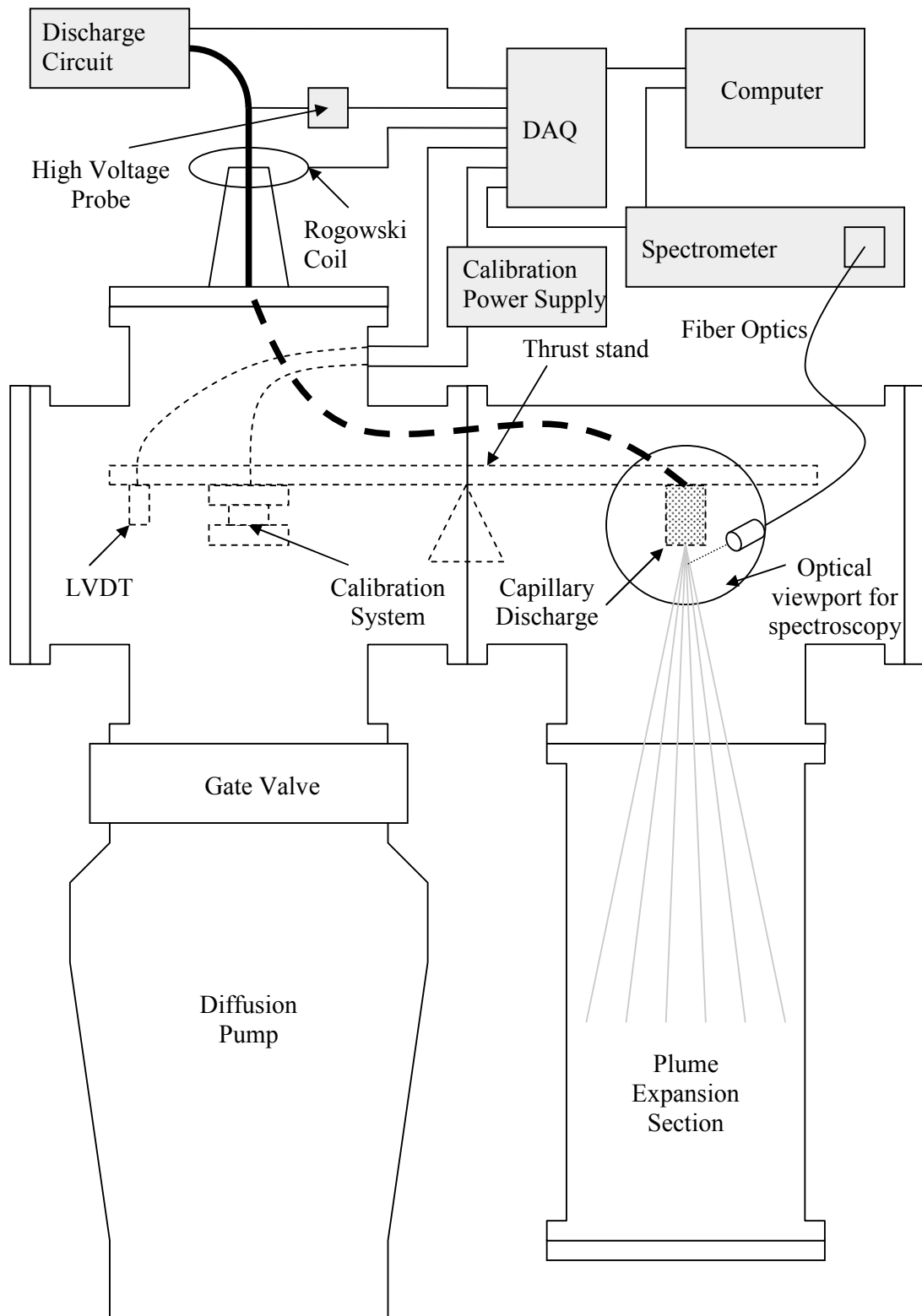


Figure 2.8: Picture of Capillary Discharge Vacuum Chamber

the chamber pressure, but would adsorb water molecules readily and continuously desorb the water during pumping. This carbon layer proved exceedingly difficult to clean, which would have to be done on a regular basis. To keep outgassing to a minimum, the chamber was always kept at a low pressure to stop water molecules from adsorbing to the carbon. By only opening the chamber briefly to swap out capillaries, pump down times were kept to a minimum.

The Chamber was equipped with three Baratron pressure transducers to measure the pressure from atmospheric pressure down to 1 *mtorr*. A hot cathode ion gauge was used to measure pressures below 1 *mtorr*. In addition to these standard pressure gauges, the chamber also contained a residual gas analyzer (RGA). This was useful for determining the partial pressures within the chamber, and whether or not pumping problems were due to leaks, outgassing, or thruster exhaust.

# Chapter 3

## Diagnostics

A complete suite of high temporal resolution diagnostics has been assembled and validated to provide a detailed understanding of the capillary discharge plasma, as well as time resolved comparisons with capillary discharge model results. Both experimental control through synchronized triggering and data acquisition functions are handled using a PXI based National Instruments data acquisition system (DAQ). The PXI system was chosen primarily because of its high speed with parallel channels, allowing 2.5 Msamples/s on each of the 16 analog input channels. The PXI system is also equipped with an 8 channel analog output card for control purposes. The fiber optic data transfer option was chosen so that the control box is isolated from the experimental operator and also to reduce the signal noise during data transfer. Since the PXI is a stand-alone system, it is able take advantage of a Labview Real-Time module if feedback control is ever desired. The data collected though this system are current, voltage, and force measurements.

### 3.1 Current

Commercial Rogowski coils<sup>1</sup> were used to measure current up to 12  $kA$  at various points in the capillary discharge circuit. The coils are connected to an integrator box that outputs the instantaneous current passing through the coil. The response time of the coils and integrator is shorter than that of the data acquisition system. The output sensitivity is  $0.5mV/A$ , it is calibrated to within  $\pm 0.2\%$  and can typically vary with conductor position by  $\pm 1.0\%$ . These current probes are placed throughout the electrical circuit and are noninvasive. The inductor loop simply needs to be placed around the wire in which the current is to be read. Typically a coil was placed on the capacitor bus bar to measure the total current discharged and a second was placed directly before the capillary. Probes were also used within the circuit to test switch properties and the effects of parallel and series resistors.

---

<sup>1</sup>Powertek model CWT60B

## 3.2 Voltage

A high-voltage probe<sup>2</sup> was used to measure the voltage relative to ground at various points in the circuit. The probe could read a maximum of 12  $kV$  with an accuracy of 0.1% for DC applications. The standard divider ratio of 1000 : 1 allowed the probe output to be directly connected to the National Instruments DAQ. Currently two probes are employed, one reading the voltage on the capacitor bank at all times and the other reading the voltage at the anode. Because of the large current, even with small resistances in grounding lines, there can still be a measurable voltage drop between the cathode and earth ground. Future experiments could also measure the cathode voltage relative to ground to obtain a more accurate measurement of the voltage difference across the capillary discharge. These measurements were not carried out in this work.

## 3.3 Mass Loss

The mass loss from the capillary wall is measured using a digital scale<sup>3</sup> with a readability of 0.1  $mg$ . The individual masses of the tubes, anode, cathode, and ignition components (when present) are all weighed separately and then weighed again after assembly. This technique, because of its redundant measurements, also gives an indication of the measurement accuracy. After a set of 5 fires, all the components are weighed again (both together and separately). By weighing the components together and separately it is possible to determine the mass loss of the electrode as well as the material ablated from the capillary wall. For calculating of specific impulse and efficiency the total mass loss of the device is used. Mass loss measurements for the wire ignited capillaries, Design V1.0 and V1.1, is also take. No useful information is determined from these measurements and they are not presented in this work

## 3.4 Force Measurements

Measuring the thruster performance characteristics of a capillary discharge presents many unique challenges. Because of its short pulse length, force is only output for several hundreds of microseconds. In addition, during the discharge time there are high electric and magnetic fields that can affect and disturb sensitive instrumentation, as will be shown in Section 3.4.1. PPTs use a solid propellant, making

---

<sup>2</sup>North Star High Voltage model PVM-10

<sup>3</sup>Sartorius CP224S

it impossible to use mass flow meters to measure propellant use and, therefore, obtain specific impulse. Conventionally, PPT's are weighed before and after testing to obtain mass loss. Usually PPT mass loss is averaged over many discharges, 100's or 1000's of discharges. This method of weighing the solid propellant before and after operation can also raises issues of handling, contamination, oxidation and absorption which may complicate mass measurements. In this work two methods for obtaining impulse, and subsequent performance parameters, were attempted; a piezoelectric method, and at thrust stand method. The problems and limitation of each method are discussed in the following sections.

### 3.4.1 Piezoelectric Force Sensors

Force measurements were originally planned to be made with 3 PCB Dynamic Force Sensors<sup>4</sup> connected to a Sensor Signal Conditioner<sup>5</sup>. The backing plate of the thruster housing is attached to force transfer rods as shown in Figure 3.1. These transfer rods allow the sensor to be preloaded with the required  $100 \text{ ft-lb}$ . Plastic or rubber washers are used on both sides of the ring style sensor to protect them from the large voltages and currents used in the experiment. Because the devices are piezoelectric devices, there was some concern that the electromagnetic field that passed from the main power lead could affect the device, especially since they are not strongly tied to ground. Tests were conducted with a straight copper feed through and a high power resistor. This simulated the power for the discharge without creating any force allowing noise levels and feed back to be observed in the sensor. These original test did not show any problem with sensor interference. However, upon firing of the actual thruster, a large level of noise was observed in the piezoelectric sensor data. Figure 3.2 shows a series of 10 different force measurements using the setup shown in Figure 3.1. Throughout the 10 shots, the damping of the thruster assembly was modified by using different insulating washers. The only change that made a significant difference was the use of rubber washer adjacent to the force sensors. This was employed for the second half of the firings (5-10) and it is clear that at the tail end of the Force graph the vibration is significantly less.

Despite the original optimistic outcome of these measurements the system proved to be problematic. The noise during the wire explosion created a large negative force that has been cut off in Figure 3.2. In addition the noise or vibrations after the discharge were much larger than the force from the discharge itself. This was lessened by the rubber washers, but was still very significant. During testing, a number

---

<sup>4</sup>Model 201B03 ICP®

<sup>5</sup>Model 484B06 Line-Powered ICP®

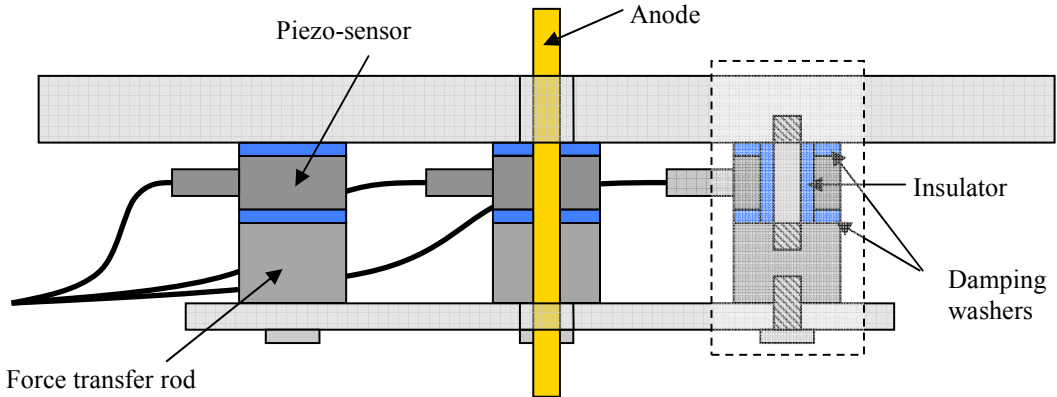


Figure 3.1: Schematic of original Piezoelectric Force Sensor Setup

of sensors were damaged and stopped working. They were replaced and during that time the thruster design was updated. When the system was put back together for testing again, it did not seem to read properly. When the sensors were tested individually, and as a system, using a hammer they seemed to be operating properly. However, the sensors did not seem to pick up any usable force data from the capillary. Eventually, after much trouble shooting, the desired piezoelectric system to measure time resolved force was abandoned for a simpler, more proven, diagnostic technique.

### 3.4.2 Thrust Stand

To avoid many of the issues associated with a piezoelectric force measurement system, a more conventional thrust stand was adopted. A number of thrust stands for electric propulsion devices, and more particularly PPTs, have been designed[107, 37, 28, 42]. In previous work done by Burton [16], a linear thrust stand was used to measure his PET thruster performance. By measuring the recoil velocity and knowing the recoil mass, he could calculate the impulse bit. The thruster was “freely suspended” by using a linear bearing on a horizontal steel shaft, making sure the center of mass was on axis and directly over the bearing to prevent off axis forces or binding. Current was feed through flexible strips of copper mesh. The thruster was sealed to the vacuum environment using a flexible rubber diaphragm to separate the electric connections and position sensors outside at atmospheric pressures. A coil spring was used to counter balance the load from the pressure difference across the sealing diaphragm. The recoil velocity was measured using a non-contatct inductive RF transducer. Calibration was carried out using a swinging pendulum and laser system to measure striking and rebounding velocities. While Burton obtained results

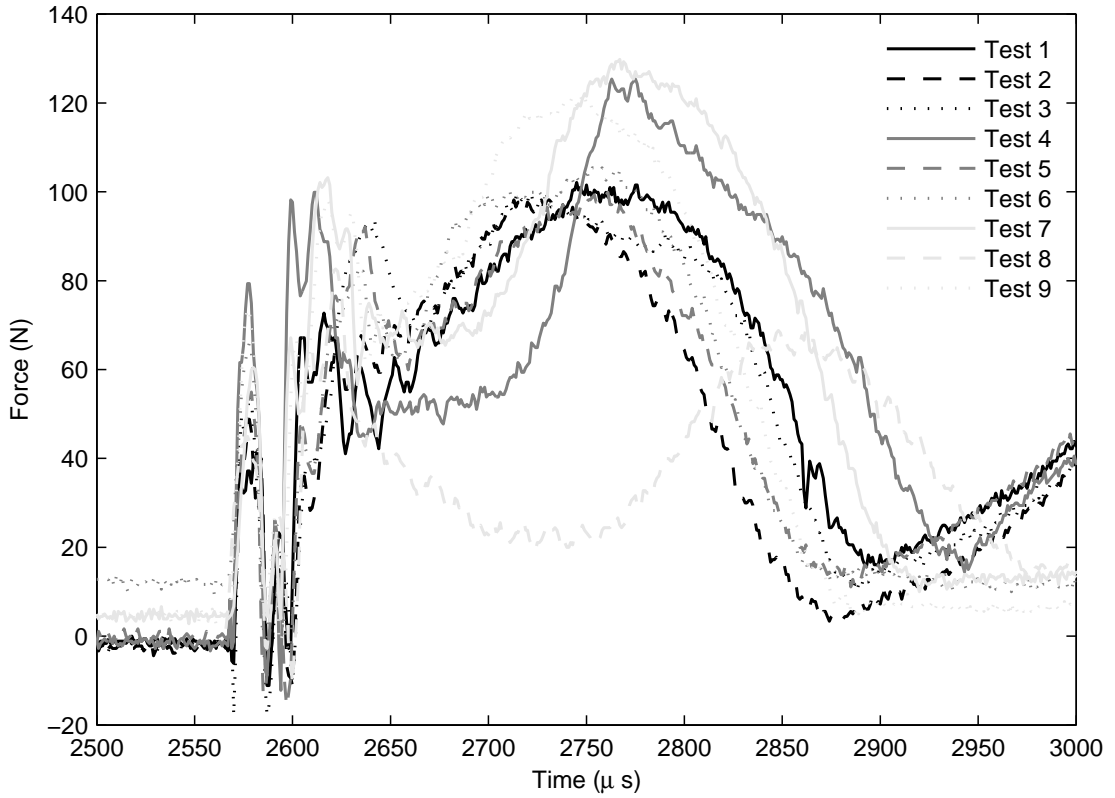


Figure 3.2: Data from Piezoelectric Force Sensors

from his stand, it was felt that improvements could be made. Burtons design had many contacts with the surrounding environment, and was not “freely suspended”, which could influence impulse measurements.

Instead of using a linear stand, it was decided to use a torsion type system to measure the total impulse of the discharge similar to the design described in [58], which is the result of a half-decade of development at USC. While this system can not resolve time dependent thrust levels, as with a piezoelectric system, it did offer many advantages. Because of the relatively high impulse levels, several new design challenges were addressed, such as higher moments of inertia and stiffer spring constants.

The thrust stand used for measuring capillary discharge impulses is simply a damped torsional force balance. The stand rotation motion can be described by an under-damped second order equation[58]

$$I\ddot{\Theta}(t) + C\dot{\Theta}(t) + K\Theta(t) = M(t) \quad (3.1)$$

where  $I$  is the moment of inertia,  $C$  is the damping coefficient, and  $K$  is the spring constant.  $M(t)$  is the forcing moment acting upon the stand. Using a small angle approximation,  $\sin \Theta = \Theta$  and the geometric relation  $\sin \Theta = \frac{X}{R}$ , it is possible to rewrite 3.1 as a linear equation.

$$I \frac{\ddot{X}(t)}{R_s} + C \frac{\dot{X}(t)}{R_s} + K \frac{X(t)}{R_s} = F_c(t) R_c \quad (3.2)$$

where  $X(t)$  is the linear displacement as a function of time,  $R_s$  is the distance from the sensor to the pivot point,  $F_c(t)$  is the calibration force acting on a distance  $R_c$  from the pivot. These dimensions are more clearly illustrated in Figure 3.3, which shows a simplified schematic of the thrust stand.

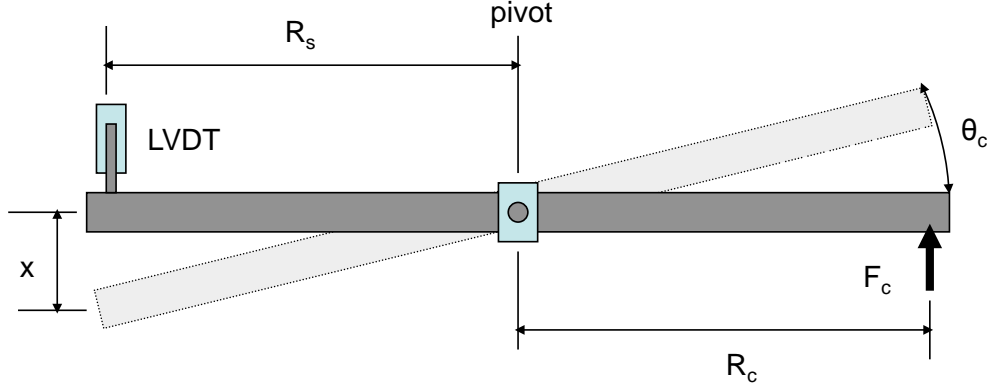


Figure 3.3: Schematic of Capillary Discharge Thrust Stand

Because the stand operated on the principles of low frequency oscillations the important information of the stand occurs on a large time scale compared to that of the discharge. Any disturbance from the discharge itself can most likely be disregarded. In addition, by mounting the thrust stand so that it deflects in the horizontal plane, it is possible to simultaneously measure both total impulse and mass loss, as done in Ref. [58]. This is done by examining both the dynamic and static characteristics of the stand. Impulse measurements can be inferred from the range of the dynamic motion of the stand as shown in Figure 3.4. The range is the maximum distance the stand deflects in the thrust plane. By precisely measuring the displacement caused by an impulse event, the total impulse can be determined based on the calibration techniques discussed later in this section. It is worthwhile to note that the typical range is measured as

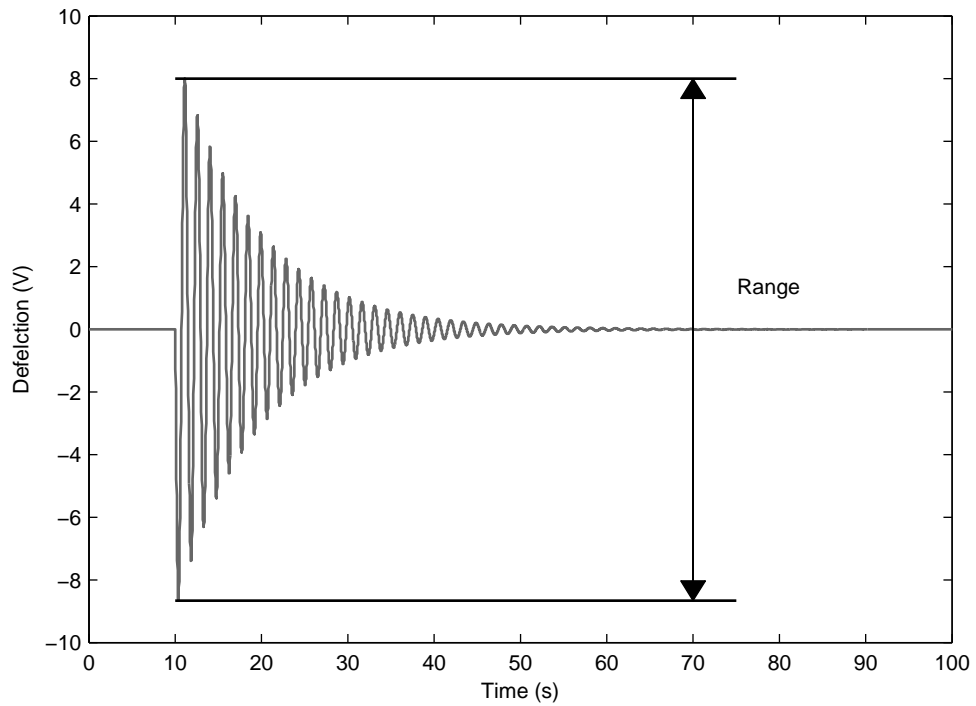


Figure 3.4: Simulated LVDT reading for expected impulse from an operational capillary discharge

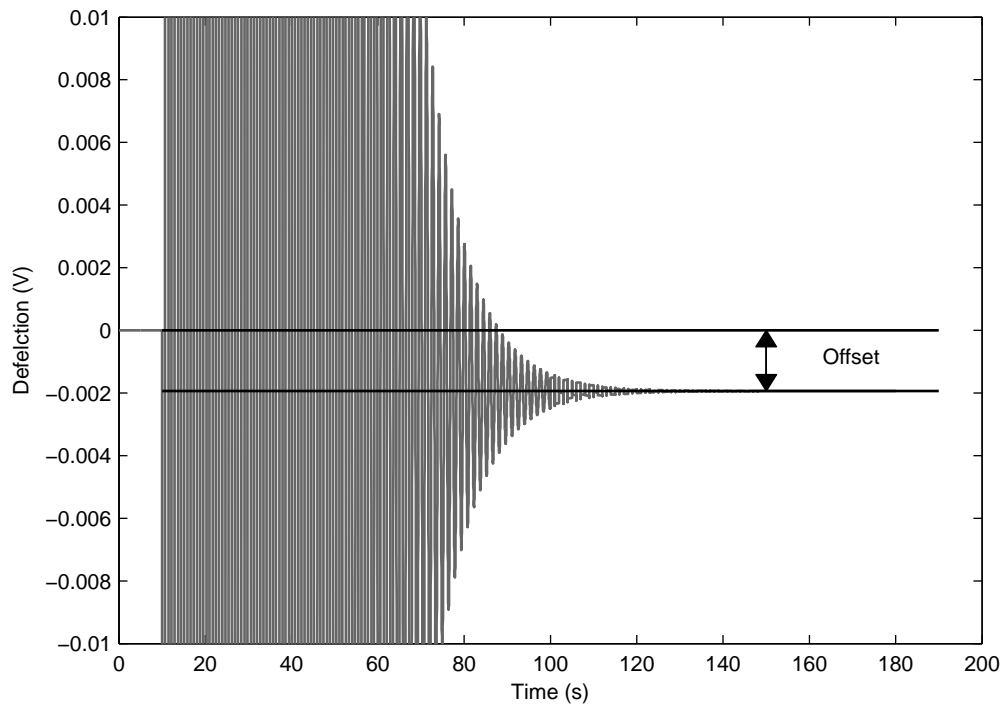


Figure 3.5: Simulated LVDT reading for expected mass loss from an operational capillary discharge

the distance between the maximum and minimum of the first oscillation. However, it is possible to use subsequent peaks and values, if also done in the calibration. The static or steady state deflection stand can reveal the mass loss of the device. Because the thrust stand is mounted in the horizontal plane, like a balance scale, when mass is lost on one side, the stand should be offset to a different position. Figure 3.5 shows the same data as Figure 3.4, only zoomed in on a smaller Y-scale. The stand clearly has different zero positions before and after the thruster fires. It is important to keep in mind that the mass loss is quick and occurring at the same time as the impulse. However, the capillary discharge, as well as most thruster systems with high  $I_{sp}$ 's, the force due to mass loss is very small compared to the motion caused by the thrust, therefore, the error caused to the impulse measurement should be very small (much less than 1% in our case).

The thrust stand itself consists of 3 main components. The arm, whose mass created the majority of the moment of inertia,  $I$ , the flexures which provide the restoring force or spring constant,  $K$ , and the electromagnetic damping system, which uses eddy current effects to create a damping force,  $C$ . These components are shown in Figure 3.6. In addition to the main components of the stand itself, there are

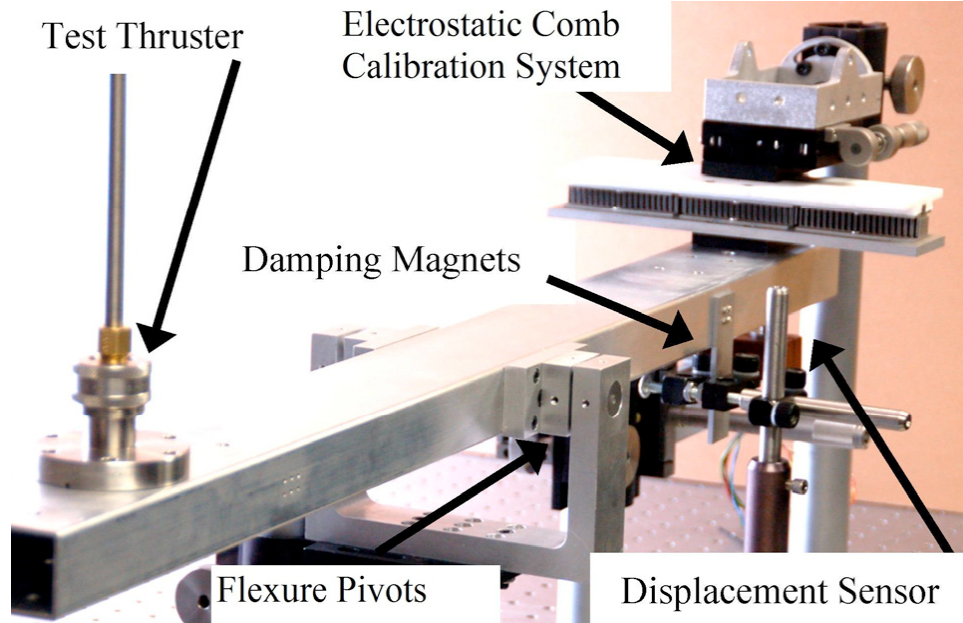


Figure 3.6: Picture of the Capillary Discharge Thrust Stand

several other components that are required in order to make thrust measurements. The thruster itself,

which is described in section 2.1, is usually placed at the end of one of the arms. However, it can be placed anywhere along the arm so long as it is oriented in the vertical direction, in order to oscillate the stand. The other two components need to make thrust measurements and the displacement sensor and the calibration system.

### Displacement Measurements

Distance measurements for this kind of thrust stand are typically made with a linear variable differential transformer, LVDT. A model of the device is shown in Figure 3.7. The primary coil (A) is the main

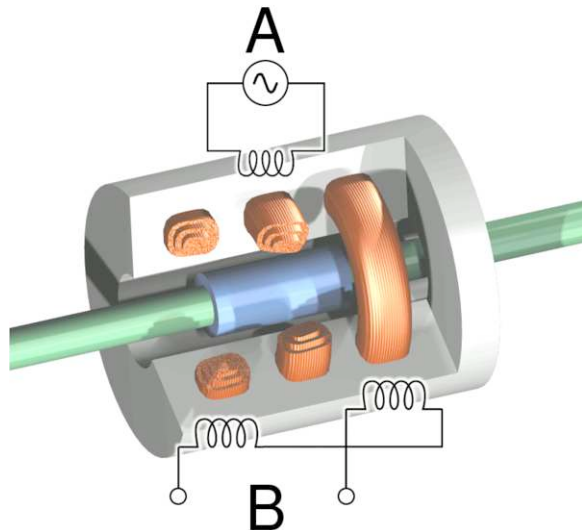


Figure 3.7: Cut away drawing of an LVDT [2]

driving coil and the secondary outer coils (B) are the sensing coils. A ferromagnetic core slides through the coils along the center axes. The device operates by applying an alternating current through the primary coil, usually between 1 to 10 kHz. This causes a voltage to be induced in the secondary coils. As the ferromagnetic core moves it changes the mutual inductance of the system and the induced voltage changes in the secondary coil. This change in voltage can be correlated to the position.

Interferometers offer another good option for determining the displacement of the thrust stand. A commercial off-the-shelf Michelson interferometer<sup>6</sup> was also tested with the thrust stand. This type of interferometer, shown in Figure 3.8 uses the principle of superposition of light to determine distance. The

---

<sup>6</sup> SIOS, SP-Series Plane-Mirror miniature interferometer, Model SP 120

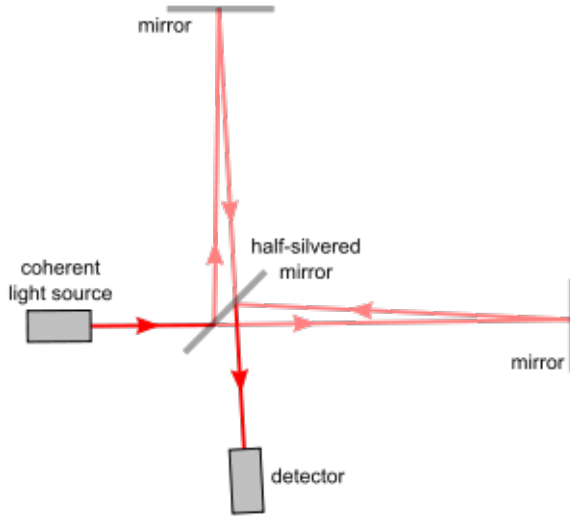


Figure 3.8: Schematic of the light path through a Michelson interferometer [1]

device operates by splitting a coherent light source into two separate paths. One path takes the light to a stationary mirror and back to a collector. The other part of the light travels to a mirror that is moving. when the light is recombined there is a phase difference between them. Waves that are in phase will undergo constructive interference while waves that are out of phase will undergo destructive interference. When one mirror is moving, the light moves through these patterns of interference, which creates a fringe pattern of bright spots. The detector can be used to determine the change in this pattern and count the fringes as they pass. Each fringe can account for a known distance of movement corresponding to the wavelength of light, and a change in distance can be determined.

These devices are very accurate and their speed is only limited by the rate at which the detector can read. Also, because the interferometer is an optical device, it is free from electro magnetic interference that might be caused by a plasma environment.

A comparison of an LVDT and interferometer were conducted using the calibration technique discussed in Section 3.4.2. A comparison plot of the two measurement sensors are plotted in Figure 3.9 While there is a discrepancy between these two techniques it is small. The reason for the discrepancy is still unknown. When both device where used to measure the displacement on a linear displacement stage, they both measured identical values. It was only on the torsional thrust stand that this discrepancy was seem. However, both devices are very linear and would work well with the thrust stand. The actual displacement is irrelevant. The only requirement is that the relative displacement is linear and repeatable.

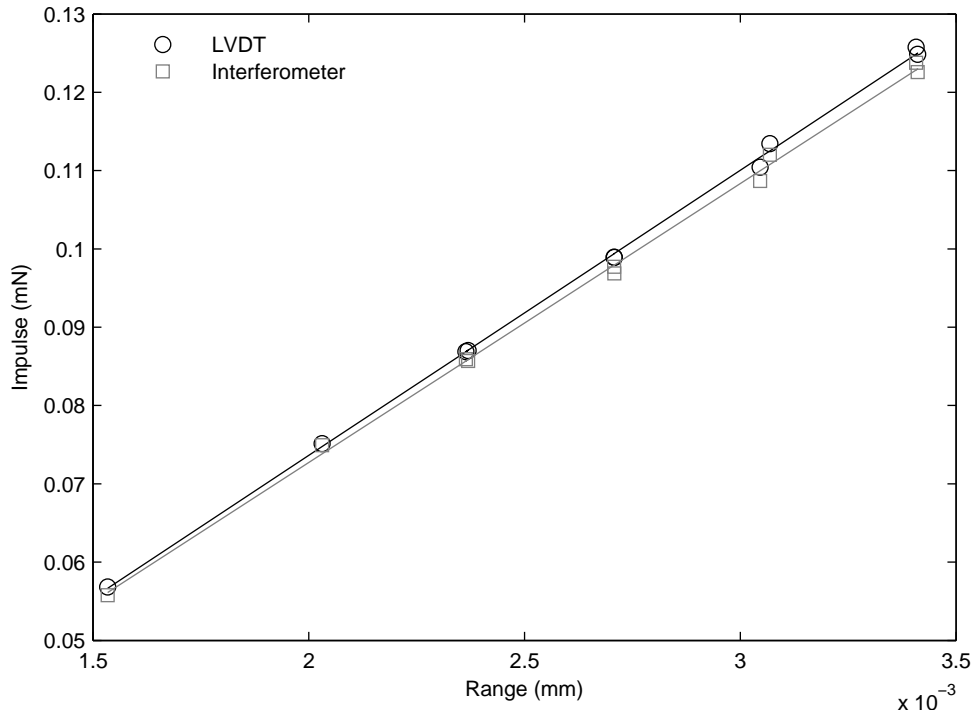


Figure 3.9: LVDT and Interferometer data for as standard impulse calibration with electrostatic fins

This is because of the calibration technic discussed in Section 3.4.2. The LVDT was used with the capillary discharge thrust stand because of its long history with this system. The interferometer does offer many advantages it was not used until it could be better understood and fully characterized.

### Calibration

Small thrust stands have used a wide variety of calibration schemes. Conventionally, calibration of similar stands have used hanging weights from a string-pulley system[105, 62]. These system can be clumsy and show errors in the milli-Newton range. A method developed by Jamison [53] used a gas dynamic calibration method which used results from direct simulation Monty Carlo (DSMC) numerical models and analytical solutions for free molecular orifice flow. This method, while reliable and accurate, involve messy oil baths and sophisticated flow and pressure controls. The oil baths are not only used as viscous dampeners on these stands, but also act as a seal for feeding the pressurized gas to the that calibration device. Because the capillary discharges have a large impulse and need to be calibrated for larger impulses there may have been problems with these kinds of oil bath seals.

The calibration system chosen for the capillary discharge thrust stand was an electrostatic calibration system based on techniques from Gamero-Castaña[34]. In this work an electrostatic calibration technique is described that utilizes two parallel plate electrodes separated by a gap to create force. This force is given by

$$F_{ESP} = \frac{1}{2} \varepsilon_o \left( \frac{V}{L} \right)^2 A_p \quad (3.3)$$

where  $\varepsilon_o$  is the permittivity of free space of the gap medium,  $V$  is the voltage difference applied between the electrodes,  $L$  is the gap distance between electrodes, and  $A_p$  is the area of the electrode. Equation 3.3 shows that the force is a function of  $1/L^2$ . This is problematic for a torsional thrust stands where one electrode would be attached to the stand, and therefore moving. Because the force is inversely proportional to the square of the gap distances even a small change in distance can greatly affect the calibration force. For this reason an electrostatic comb system was used based on work by Johnson and Warne[55]. This system is based on interlocking charged combs. When the gap distance is equal to the width of the comb the applied force can be described by

$$F_{ESC} = 2N\varepsilon_o V^2 \left( 1.0245 - \frac{g}{\pi x_o} \right) \quad (3.4)$$

where  $N$  is the number of comb pairs,  $g$  is half the gap distance and  $x_o$  is the engagement of the combs. Notice that as the engagement became larger then the gap distance the force asymptotes near  $2N\varepsilon_o V^2$ . A more detailed account of these electrostatic comb calibration systems and their accuracies are discussed by Selden[84].

Electrostatic combs can be used to produce very small forces. The system used by Selden[84] was capable of only applying forces on the order of hundreds of micro-Newtons with reasonable voltages. The capillary discharge can create large forces that only last for a brief period of time, hundreds of microseconds. The total impulse has been estimated to be on the order of tens of milli-Newtons.

When creating large impulse electrostatically there are limits in both voltage and pulse length. The voltage limit can be determined by what can be applied in vacuum without arcing. This was safely estimated to be about 3000 V. The pulse time is limited to 1/10 the natural period of the stand[29]. Pulse times greater than this effect the stand oscillation degrading the measurements. It has also been shown that when measuring total impulse bits the force and pulse time do not matter so long as the 1/10 limit is obeyed. In other words, we do not need to create a 100 N force for 100  $\mu$ s in order to create the 10 mNs

need to calibrate in the range of our thruster. Instead it was possible to create a  $100\text{ mN}$  force for  $100\text{ ms}$ , provided the natural frequency of the stand was greater than  $1\text{ s}$ .

In order to achieve the impulses needed multiple sets of larger combs were designed and fabricated. The number of comb pairs,  $N$ , was increased from 5 to 10 and the typical comb cross section of  $1\text{ mm}$  by  $1\text{ mm}$  was increased to  $1\text{ mm}$  by  $20\text{ mm}$ , which created more of a fin design. Finally, 3 sets were made to attach on a single mount. By making these geometric changes it was possible to output a greater force without violating the linear attraction force as discovered by Johnson and Warne[55]. Each individual set of fins was precisely calibrated on a micro balance. The data for one set of scale data is shown in Figure 3.10. It shows that the attractive force is very linear as a function of voltage squared. It is also

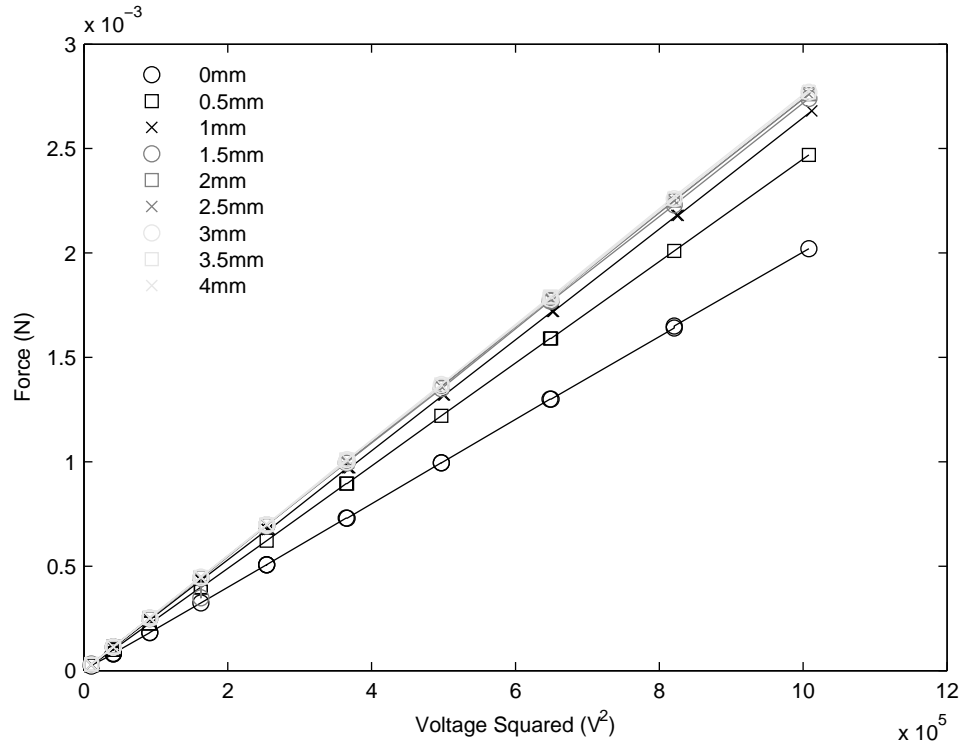


Figure 3.10: Electrostatic Fin Validation Data

worth while to notice how the force changes with a function of engagement distance. As the engagement becomes larger then the gap distance the engagement factor does not affect the force produced as predicted. All calibrations are done with  $4\text{ mm}$  engagement which allow for  $2\text{ mm}$  oscillations while still remaining in the constant force range.

A Piezo-electric hammer was also tested as a calibration system, but it was not implemented in our test conducted in Chapters 5.2 - 5.5. The electrostatic fin system could create impulse up to about  $10 \text{ mNs}$ . While this is within the range of impulses created by the capillary discharge, it did not span the entire range of operation. To fully calibrate the thrust stand the upper impulse range a piezo-electric hammer could have been used<sup>7</sup>, which would allow calibration in the  $10^{-4}$  to  $10^1 \text{ Ns}$  range. Figure 3.11 shows a comparison of the 2 calibration techniques. In this comparison plot it can be seen that the piezoelectric

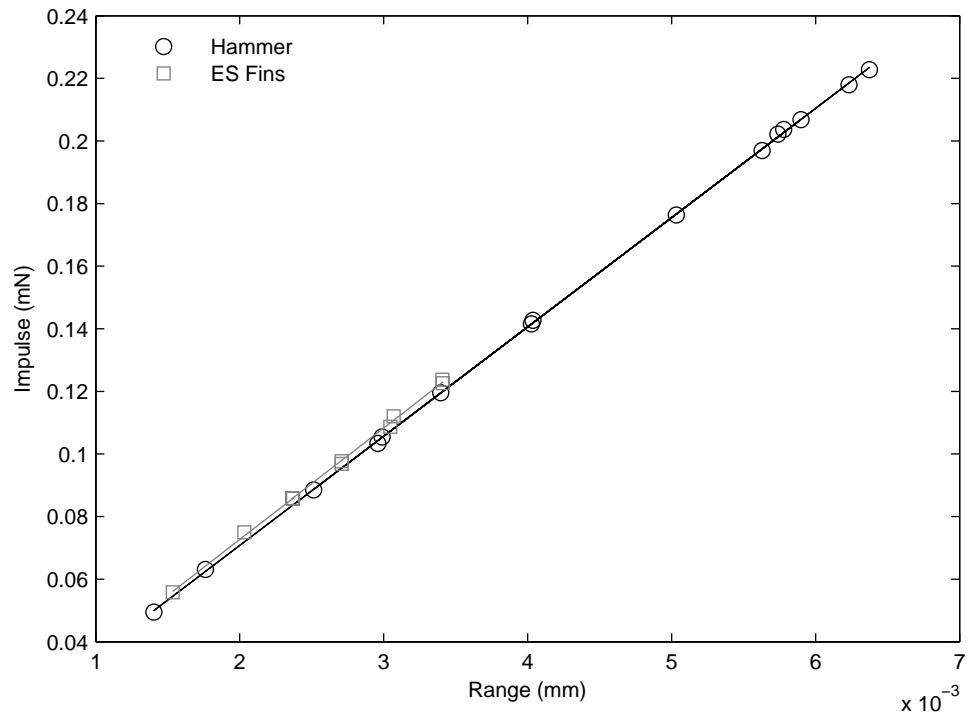


Figure 3.11: Hammer and ES Fin data collected utilizing the LVDT

hammer and electro-static fins are in close agreement. The hammer was able to impart impulse in both in the same range and well above the range of the ES Fins. Even so, when the ES fin calibration line is extended up to the higher ranges there is still good agreement.

The PE Hammer was not used for calibration in the test data presented here. While initial results looked promising, the time to develop and implement a full calibration system to work in vacuum was not trivial. The ES fin system did an excellent job calibrating in the low impulse ranges, and could be extrapolated to higher impulses without introducing significant error.

---

<sup>7</sup>PCB Peizotronics Impact Hammer, Model 086C01

## Thrust Stand Optimization

The linear range and accuracy of the detector directly sets the maximum impulse and minimum mass loss that can be resolved by the thrust stand[66]. The static or steady state condition that occurs both before and after the capillary discharge is only a function of the mass lost during the discharge and the spring constant,  $K$ , of the stand. The stiffer the flexures the less the stand will deflect. This deflection must be enough to be resolved by the LVDT and ancillary data acquisition system. The linear range determines how far the stand can deflect and still remain within the usable range of the LVDT. The dynamic distance the stand moves from the impulse applied by the discharge is a function of both  $K$  and the moment of inertia,  $I$ . It is a balance of these two constants that allows for the specific impulse to be made.

A simple Matlab code<sup>8</sup> was used to model the thrust stand motion. A first iteration of the thrust stand was designed and built in order to validate this code. Once the code was verified the stand parameter could be varied to see how the stand fundamental characteristic would change. Figure 3.12 shows how much the stand would deflect for an expected mass loss of  $12\ mg$ [77]. The plot shows that for better resolution

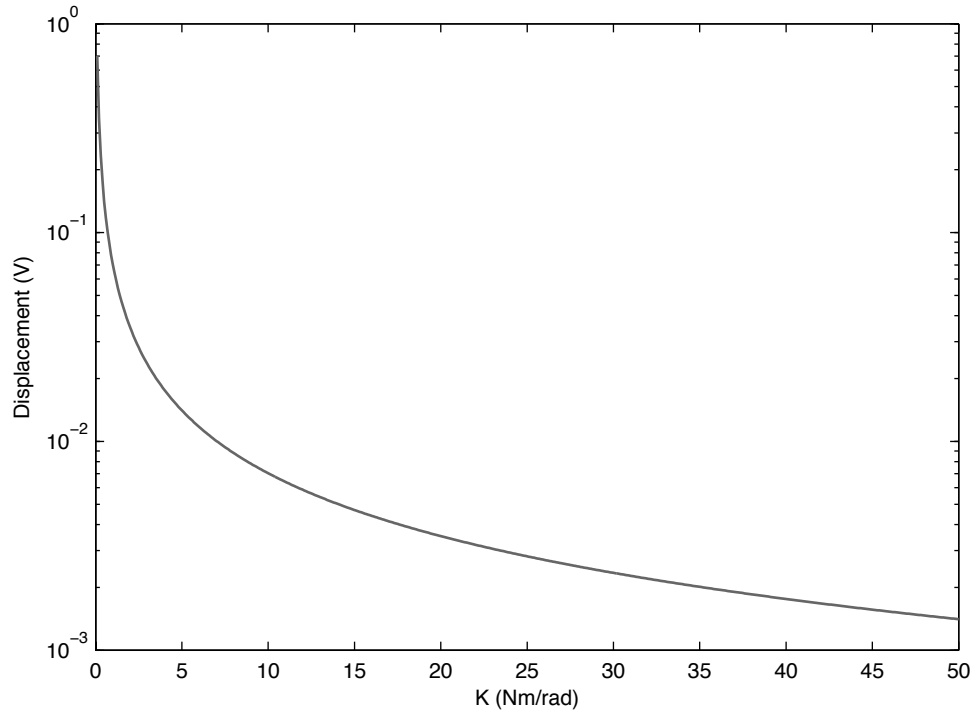


Figure 3.12: Thrust Stand Deflection vs.  $K$

---

<sup>8</sup>Code written by T.C. Lilly

measurements, larger displacements can be obtained using smaller values of spring constant. With a 16-bit DAQ, it is possible to measure less than a  $mV$  on a  $-5$  to  $+5$   $V$  scale as seen by the following analog to digital conversion calculation.

$$\frac{10\text{ }V}{2^{16}} = 0.00015\text{ }V \quad (3.5)$$

Therefore it is possible to resolve the mass loss using any of these spring constant flexures shown in Figure 3.12.

As mentioned earlier, the stand's range is a function of both the  $I$  and  $K$ . Figure 3.13 shows the stand's deflection as a function of moment of inertia for various  $K$  value flexures that are available from the manufacturer<sup>9</sup>. The deflection shown here is based on the impulse predicted from Pekker[77]. The range decreases with increasing spring constant and moment of inertia. Because the moment of inertia scales logarithmically, it is desirable to use higher spring constants. This however could affect the limit of mass loss measurements. This ultimately leads to choosing a  $K$  value that balances the steady state sensitivity needed to resolve mass loss and the dynamic restoring force needed to limit the range from the discharge's impulse. In the end the stand was modified to handle the entire range of impulse and mass loss. The stiffest flexures were used and the moment of inertia greatly increased to keep the stand from deflecting out of range. This was done by attaching  $5\text{kg}$  to the end of each arm. The damping plate was also changed to a copper plate which provided a large eddy current dampening force needed to settle the high inertial stand. The modifications made to the thrust stand are reflected in the coefficients shown in Table 3.1. With this modifications the stand would oscillate about  $\pm 8\text{ }V$  at maximum impulse, which is

Thrust Stand	1 <sup>st</sup> Iteration	Optimized
$K\text{ [Nm/rad]}$	41.75	36.22
$C\text{ [Nm s/rad]}$	0.191	0.428
$I\text{ [Nm s}^2\text{/rad]}$	0.245	1.988

Table 3.1: Coeffecients for 1st interation & optimized CD thrust stand

within the LVDT's  $\pm 10\text{ }V$  range. It would also cause the stand to have a steady state deflection of  $2\text{ }mV$ , which would be well resolved with the 16-bit DAQ.

---

<sup>9</sup>Riverhawk Company's Flexural Pivot Bearings

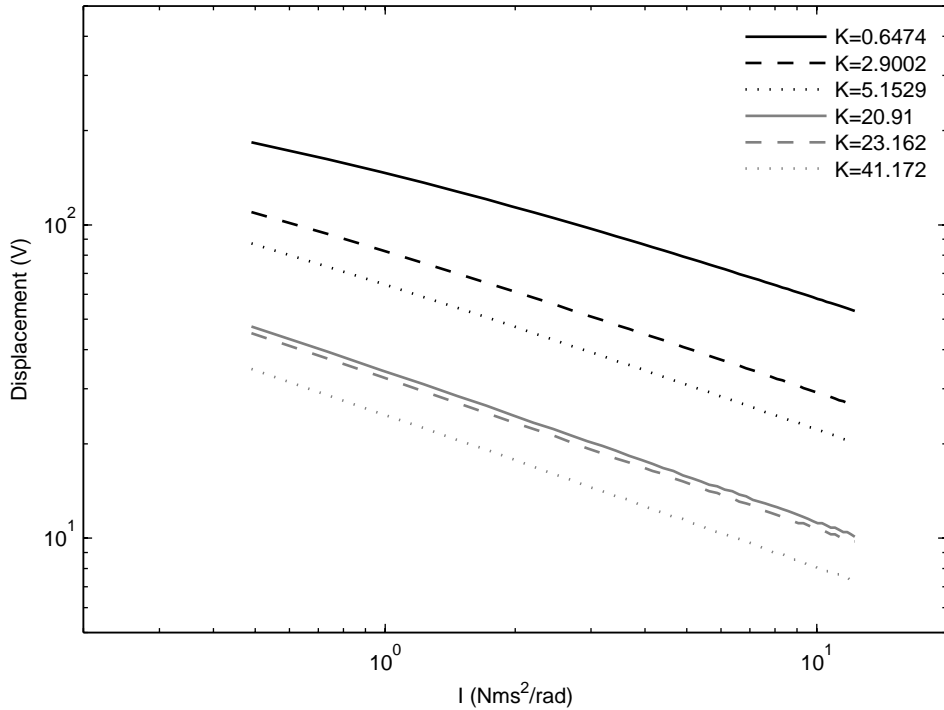


Figure 3.13: Thrust stand range vs.  $I$  for multiple  $K$  values

### Thrust Stand Offset Problem

The thrust stand was set up in the horizontal position in order to take both impulse and mass loss measurements. However, the thrust stand failed to take accurate mass measurements despite the prediction of the model discussed in Section 3.4.2. While the deflection of the stand should have been readable by the LVDT and DAQ, much larger and more sporadic mass loss measurements were observed. The deflection the stand was experiencing would equate to 100's of  $mg$ , much higher than predicted, measured on the scales, or is even reasonably possible. In fact the stand even showed a gain in mass indicating that the problem was a measurement error. A trend was quickly noticed in this error that is shown in Figure 3.14. This figure shows the mass loss of 10 consecutive capillary discharges, or rather 2 sets of 5. The first set of firings was conducted in the afternoon, one right after the other, approximately 10 minutes apart. The experimental setup was left intact and pumped down over night. In the morning, under the same condition, on the same capillary, the second set was taken. The plot shows a trend towards the real mass loss of about  $10mg$ .

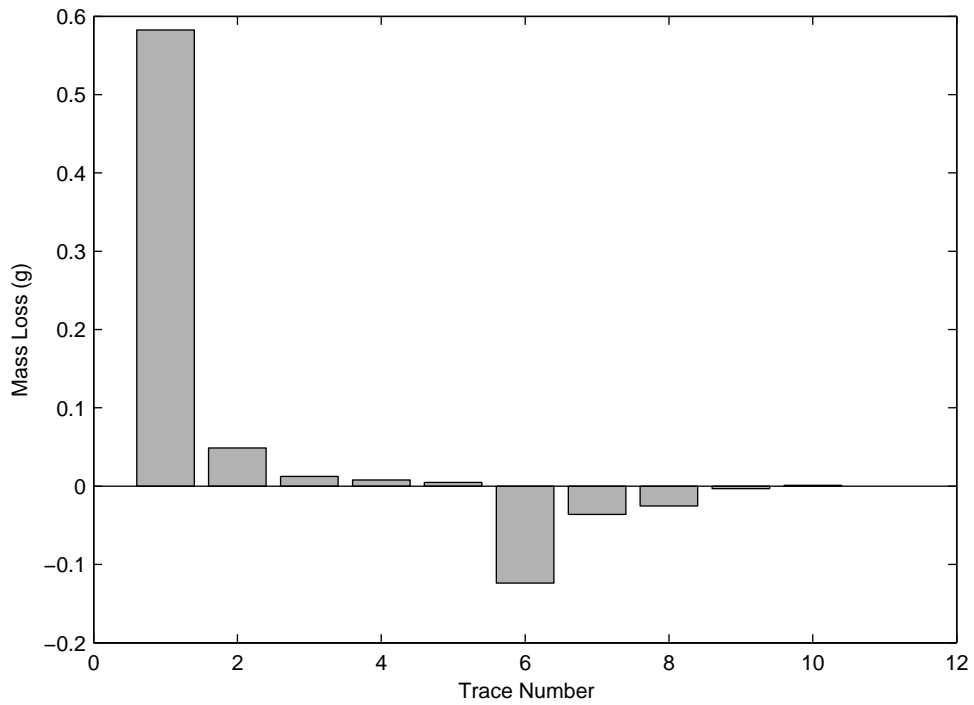


Figure 3.14: Mass loss as measured by thrust stand displacement for 10 consecutive shots

There is speculation into what might be causing this effect; everything from thermal drift of the sensor to loose flexures. The two most likely culprits are the high power wiring and an electronic jolt to the LVDT. The cable that runs power to the stand carries a very large current for a very short period of time. This high  $\frac{di}{dt}$  can cause magnetic fields that might affect the wire position or stiffness; just like in the case of an inductor constrict around the center. It is possible that the wire at sharp corners might create fields and forces that could move the wire location. A number of different wires, both stranded and unstranded, were tested, as well as the wire location. Different mounting brackets were used to either hold the wire more tightly or looser, as it weaved its way form the voltage feedthrough to thruster. While these did seem to affect the measurement, it was not conclusive, and didn't eliminate the problem.

The other possible cause for this phenomenon is with the LVDT Sensor itself. There has always been an unexplained drift with this sensor. The effect is small, fairly linear, and can be calibrated out for long displacement traces. It was thought that the plume from the discharge might be effecting the sensor, causing some type of instantaneous drift. Tests were run using the sensor grounded and ungrounded, and even with a Faraday type cage surrounding it to eliminate any effects from charged particles or electromagnetic fields. Non of these modification effected the signal or zero offset problem. It was also

thought that the large power spike might effect the devices electronics. This can sometimes be seen in the current traces when the rogowski coils will read zero current before the discharge switch is opened and then after the current pulse, when the probe should be reading zero current, it is offset by a couple of amps. The effect is very small and introduces very little error into measuring the large currents. But a similar effect on the LVDT that attempts to resolve  $mV$ , this may be a problem.

The stand was never able to read in-situ mass loss and the measurement was taken using a scale before and after fired to obtain an average mass loss for the firings. There is an ongoing effort to make individual in-situ  $I_{sp}$  measurement per shot. A modified thrust stand adapted for supplying power directly through the flexures eliminating the need for wires is being constructed. There has also been work to use an interferometric displacement sensor instead of the LVDT. Since is an optical measurement technique it should be free from electrical noise created by the discharge. This results will hopefully be shown in future publication.

### 3.5 Optical Diagnostics

The plasma densities and temperatures routinely encountered in capillary discharges make them difficult to investigate experimentally. Commonly used plasma probes such as Langmuir probes are not suited to make plasma measurements for typical capillary discharge temperatures, pressures, and time scales. Instead it was chosen to use Optical Emission Spectroscopy (OES), in which the light that is emitted from the plasma is observed through a spectrometer and analyzed. The captured spectrum can either be analyzed by spectral intensity or spectral shape. Accurate intensity measurements have been used on these types of discharges[?], however this method involves very elaborate calibration schemes. For this experimental work spectral line shape were examined to reveal information about plasma.

The capillary discharge is a pulsed device necessitating time resolved measurements. Within the lifetime of the plasma there is an ignition process, a rapid heating process, a near quasi-steady state discharge and finally an extinguishing period. It is necessary to take spectral measurements with sufficient temporal resolution to resolve the critical features of the discharge. A minimum temporal resolution of roughly  $10 - 20\mu s$  would be required to take more than ten spectral measurements in a nominally  $200 - 400\mu s$  discharge pulse. There is also a wide range of radiant intensities encountered during the different phases of the discharge pulse. In order to achieve the required temporal resolution a Princeton Instruments Pixis CCD camera (400B) was used to collect the separated light from a half meter Acton spectrometer (SP500i). The CCD camera has the capability to run in kinetics mode. Kinetics mode is

method of binning and shifting the pixels of the CCD to allow rapid consecutive exposures. To do this the collected light was transported in a  $10\mu m$  fiber optic cable illuminated only the uppermost portion of the chip, while the rest of the chip sits in darkness. The illuminated section of the chip collects charge for a specified amount of time before the charge is then shifted down into the dark part of the chip where it is stored. When the chip is full, it is read off all at once. The chosen CCD chip has 400 vertical pixels. The original setup was capable of illuminating a minimum of 10 pixels with a  $100\mu m$  fiber. This allowed a maximum of 40 spectral measurements (39 usable, because the last could be over exposed) to be stored on the CCD before it must be read. The time resolution is primarily a function of the shift speed or charge transfer rate from pixel to pixel. If it takes  $3\mu s$  to transfer one pixel and each spectral measurement consists of 10 pixels from light to dark, then the time resolution is  $30\mu s$ . The overall data collection time for 40 spectra is  $1.2\ ms$ . Figure 3.15 shows how kinetics works. The boxes represent super pixels,

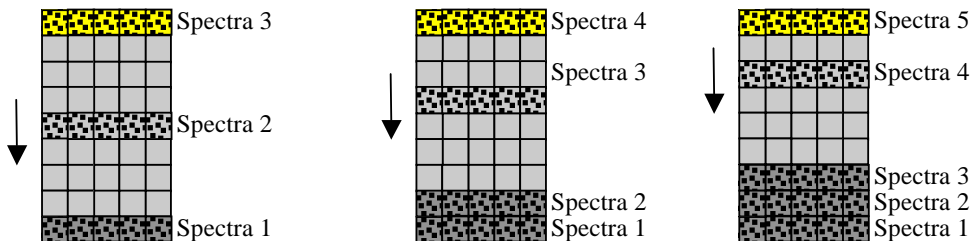


Figure 3.15: Diagram of Kinetics Mode Operation

which in our case would be 10 pixels in height and 1 pixel in width (wavelength). The yellow area is the region exposed to light. Charge builds up over the exposure time and is then shifted down the chip, quickly filling it up.

The maximum shift speed of the Pixis CCD camera was advertised to be  $3.2\ \mu s$ . However, at that speed the charge exchange efficiency (CEE) is very low and the data is completely lost and unreadable off the chip. At  $6.2\ \mu s$  the data gets slightly corrupted as it is transferred down the chip. Charge bleeds over to surrounding pixels and spectral peaks are broadened and distorted. The magnitude of the distortion can be determined by taking spectral measurements of a light emitting diode (LED). Early spectra undergo much more distortion than later ones because they travel farther on the chip, undergoing more charge exchanges. The fastest transfer speed with acceptable distortion for the factory calibrated setup is  $9.2\ \mu s$ . By keeping the charge per pixel low by using heavy filtering of incoming light, the kinetics mode can be run with little degradation in signal. Collaborative work with Princeton Instruments carried out to optimize the

camera operational voltages that would allow quicker charge transfer with better CEE without sacrificing well depth (the total amount of charge each pixel can hold). After several modification  $3.2 \mu s$  were successfully achieved

It is also important to make the illuminated spot as small as possible on the CCD chip. A custom fiber optic system was setup in order to accomplish this. A custom system was created by Oz Optics. Light is captured through a collimator assembly which is designed to collect a  $100 \mu m$  spot  $25 cm$  away. This allows good spectral resolution from outside the chamber. The collimator focuses the light into a  $10 \mu m$  silicon fiber that carries the light throughout our optical system. The light travels though a filter housing assembly in which various  $0.5 in$  neutral density filters can be used to reduce the light intensity. Light is then carried to a 3-way beam splitter that divides the light up equally into 3rds. One of those 3 leads takes the light into our spectrometer and CCD. The other 2 leads are available for future diagnostic equipment. Another nice feature of the optical setup is an additional beam splitter after the collimator. The splitter has a ratio 95% and 5% so that most of the light travels to the spectrometer. The other lead from the splitter is connected to a visible LED laser also supplied by Oz Optics. This feature allows for easy alignment and focusing of the optical system. However, all these fiber optic components added a significant about of noise to the spectral data. In the final setup only a short fiber was used between the lens and the spectrometer.

With a  $100 \mu m$  fiber the spot size was 20 pixels. The  $10 \mu m$  fiber does not allow a spot size of 2 pixels due to optical properties of the mirrors and gratings of the spectrometer. A spot size of only 5 pixels was achieved. By positioning the spot half off the edge of the chip so that it illuminates only 5 pixels and achieving the  $3.2 \mu s$  shift speeds, a time resolution of  $16 \mu s$  was achieved.

### 3.5.1 Temperature from Resistivity

Because the magnetic field is relatively small it is possible to calculate temperature based on the Spitzer resistivity[7, 87] which is defined as the ratio of the rate at which electrons in the unit volume gain momentum by impact with positive ions, to the current density.

$$\eta = \frac{P_{ei}}{j} \quad (3.6)$$

The momentum gained by an electron in a collision is  $m_e(v_i - v_e)$ , where  $v_i$  and  $v_e$  are the electron and ion velocities, respectively. The number of collisions per unit time can be expressed simple by  $\nu n_e$ , where

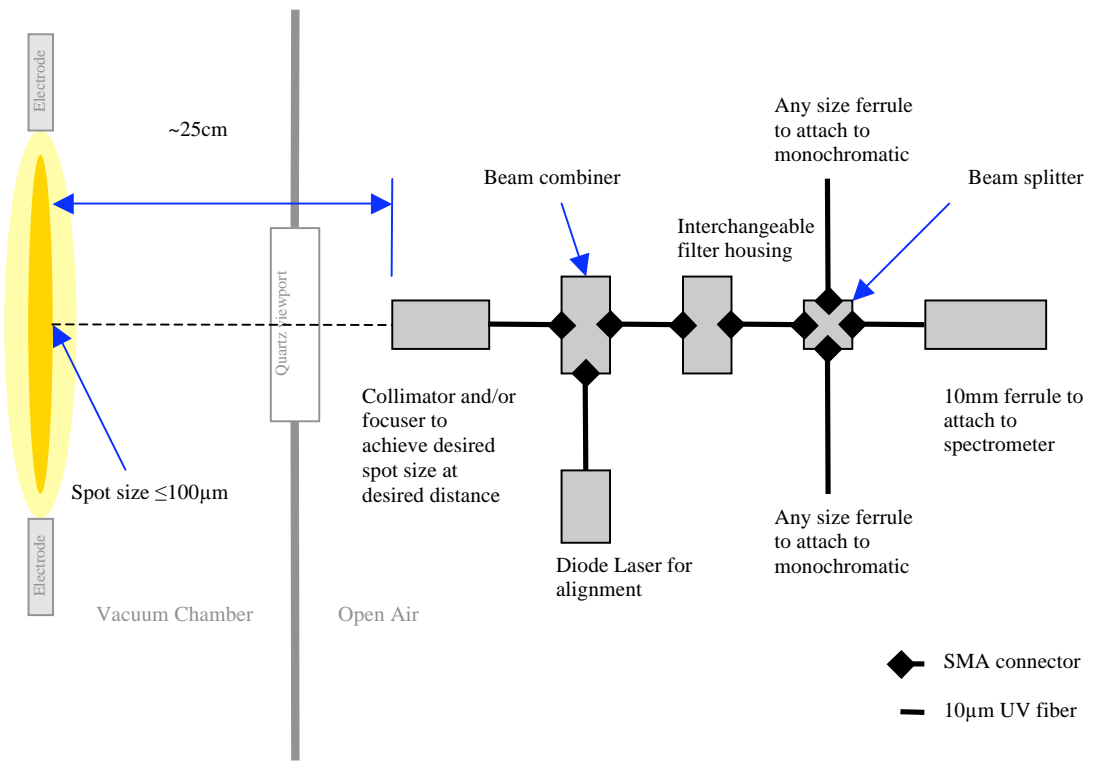


Figure 3.16:  $10\mu\text{m}$  Optical System

$\nu$  is the collision frequency. The current density can be expressed  $n_e e(v_i - v_e)/c$ . Using these simplified definitions Equation 3.6 becomes,

$$\eta = \frac{m_e c^2 \nu}{n_e e^2} \quad (3.7)$$

This however is an order of magnitude approximation and it has been shown that for a fully ionized gas there is large uncertainty in collision frequency. A more rigorous calculation can be made to achieve a more precise value. A Lorentz gas assumption was used, which states that the electrons are not interacting with each other and the ions are not moving. With these assumptions the resistivity can be written as

$$\eta_L = \frac{\pi^{3/2} Z m_e^2 c^2 \nu \ln \Lambda}{2(2kT)^{3/2}} \quad (3.8)$$

In order to make this expression more accurate electron-electron interactions must be taken into account. This is done by adding a ratio of conductivities for a Lorentz gas

$$\eta = \frac{\eta_L}{\gamma_E} \quad (3.9)$$

The values for  $\gamma_E$  have been determined by Spitzer and Härm[88] and are shown in the Table 3.2.

Ionic Charge Z	1	2	4	16	$\infty$
$\gamma_E$	0.582	0.683	0.785	0.923	1.000

Table 3.2: Ratio of conductivity in a Lorentz gas

The Spitzer resistivity is valid for a fully ionized plasma. For a partially ionized plasma it is important to consider both collision frequencies of the ion and the neutrals. Classically the conductivity of a plasma, which is simply the inverse of the resistivity, and can be expressed as

$$\sigma = \frac{n_e e^2}{m_e(\nu_{ei} + \nu_{en})} \quad (3.10)$$

Where  $n_e$  is the electron number density,  $e$  is the electron charge,  $m_e$  is the mass of the electron,  $\nu_{ei}$  is the collision frequencies of electrons with ions and  $\nu_{en}$  is the collision frequencies of electrons with neutrals. The electron-neutral frequency can be written as

$$\nu_{en} = V_e(n_{C0}\sigma_{eC0} + n_{H0} + \sigma_{eH0}) \quad (3.11)$$

Where,  $n_{C0}$  is the neutral carbon atom concentration in the plasma,  $n_{H0}$  is the neutral hydrogen atom concentration in the plasma,  $\sigma_{eC0}$  is the electron transport cross-section with neutral carbon atoms, and  $\sigma_{eH0}$  is the electron transport cross-section with neutral hydrogen atoms, and  $V_e$  is the mean electron velocity that is defined as

$$V_e = \left( \frac{8kT}{\pi m_e} \right)^{1/2} \quad (3.12)$$

The ion-neutral cross-sections are assumed to be constant and were obtained from Powel and Zielinski[78, 79].

$$\sigma_{eC0} = 30\pi a_0^2 \quad (3.13)$$

$$\sigma_{eH0} = 17\pi a_0^2 \quad (3.14)$$

The expression for  $\nu_{ei}$  is more complete, and can be expressed as,

$$\nu_{ei} = \frac{38Zn_e e^2 \log(1 + 1.4\Lambda_0^2 4\pi\varepsilon_0)^{1/2}}{\gamma_e m_e T^{3/2}} \quad (3.15)$$

Where,  $n_e$  is the electron concentration,  $Z$  is the average ion charge, and  $\gamma_e$  is a function of  $Z$  as expressed in Table 3.2. The  $\Lambda_m$  term is an expression derived by Zollweg and Liebermann[111] and is given by

$$\Lambda_m = \frac{12\pi\epsilon_0 kT}{Ze^2} \left( \frac{\epsilon_0 kT}{n_e e^2} + \left[ \frac{3}{4\pi n_i} \right]^{2/3} \right)^{1/2} \quad (3.16)$$

The equation above can be rewritten so as to show a clear distinction between kinetic energy and the coulomb potential energy. For an ideal plasma, where the high temperatures cause the kinetic energies to be much greater than the potential energy, as determined in Section 1.5.3, it is possible to simplify this equation into the usual Spitzer result for conductivity. However, for the calculations done here, the full set of equations is used and the resistivity can be calculated for given temperature and pressure. These resistivities for the plasma's conditions are plotted as shown in Figure 3.17. By using this plot it is possible to estimate the temperature.

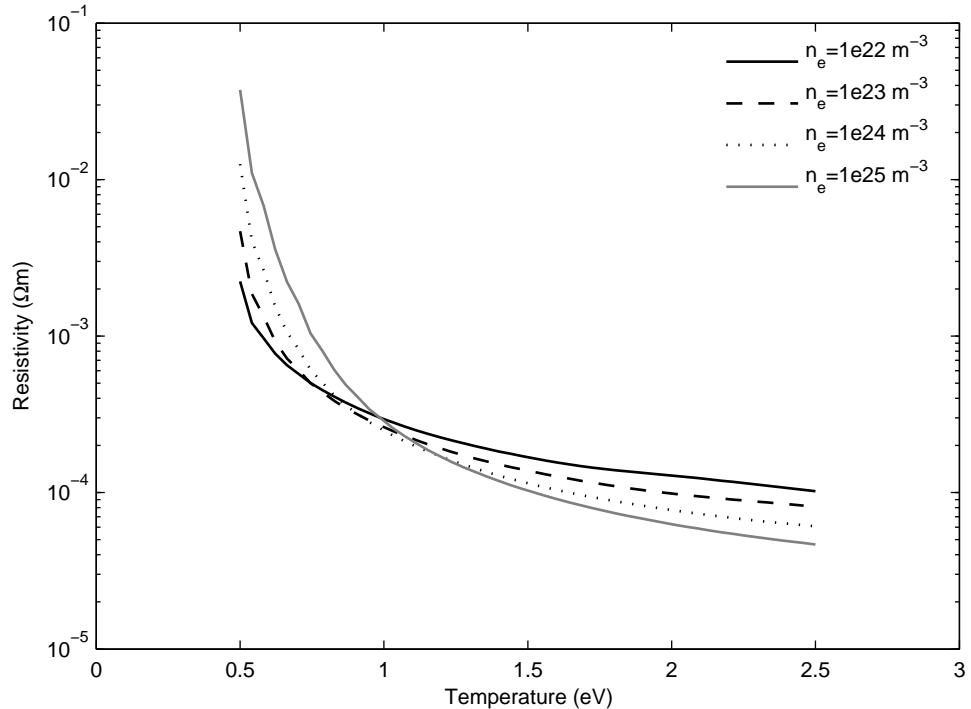


Figure 3.17: Polyethylene plasma resistivity as a function of temperature for various number densities

### 3.5.2 Electron Number Density

There are numerous ways to measure the electron number density,  $n_e$ , of a plasma. Two of the most common methods, for high density plasmas, are based on the phenomena of Thomson scattering and Stark broadening. Thomson scattering, or the scattering of light by free electrons, is an active technique of measuring both  $n_e$  and the electron temperature,  $T_e$ . This method uses a laser beam that is passed through the plasma and measured by a spectrometer on the other side. The  $T_e$  can be determined from the FWHM of the broadened laser light from the relation  $\Delta\lambda^{Thomson} = 7.1 \times 10^{-7} \lambda_o (T_e/m_e)^{1/2}$ . The  $n_e$  can be determined from the integration of the intensity of the full spectral profile, after proper calibration. The Thomson scattering technique can be difficult, expensive, and impose numerous experimental difficulties[94]. The other option is Stark broadening which is a passive method that is based on the broadening of spectral lines spontaneously emitted from the plasma itself to determine  $n_e$ , provided  $T_e$  is known. Also, techniques have been developed to acquire both  $n_e$  and  $T_e$  simultaneously using multiple Balmer lines[96]. Stark broadening is well characterized, especially for hydrogen lines, it is considerably faster, easier, and less expensive.

#### Hydrogen Line Broadening

There are several mechanisms that contribute to the broadening of a spectral line. These mechanisms can cause shifting as well, which can complicate the analysis even further. Because of all the different broadening mechanism, it is important to understand which is the dominant one and which ones can be neglected.

Natural Broadening is caused by the uncertainty in energy states of an excited particle as dictated by the uncertainty principle. Typically this broadening effect is valued to be

$$\Delta_{1/2}^N \approx 1 \times 10^{-4} [\text{\AA}] \quad (3.17)$$

It is typically neglected and will be neglected here as well.

Doppler broadening is an effect of the motion of the radiating particles themselves. This is similar to the Doppler effect observed with sound waves. A siren traveling towards an observer will exhibit a higher pitch to the observer than the same siren moving away from the observer. Similarly, a photon emitted from a particle moving towards the observer will undergo a shortening or red-shift, and a photon emitted from a particle moving away from the observer will undergo a lengthening or blue-shift. This

broadening effect has a Gaussian distribution. The full width half max, FWHM, for this gaussian-type Doppler distribution is

$$\Delta_{1/2}^D = 7.16 \times 10^{-7} \lambda_o \sqrt{\frac{T}{M}} [\text{\AA}] \quad (3.18)$$

Where  $\lambda_o$  is the natural wavelength in Angstroms,  $T$  is the plasma temperature in  $K$ , and  $M$  is the emitter mass in atomic mass units. In the plasma considered here, which has relatively low temperatures, the Doppler effect on  $H_\alpha$  and  $H_\beta$  is less than 1 Å. It is also possible to neglect this effect as well for the capillary discharge conditions. If the plasma was hotter the effect would be increased and if the plasma was less dense the pressure broadening would be much smaller and the effect could not be ignored.

Resonance broadening or self broadening is broadening caused by the neutral perturbation of the atom itself. This effect takes place when atoms of the same species transition from a higher energy state to ground state of the same type. The full width half maximum can be expressed by

$$\Delta_{1/2}^R = 8.6 \times 10^{-30} \sqrt{\frac{g_i}{g_k}} \lambda_o^2 \lambda_r f_r N_i [\text{\AA}] \quad (3.19)$$

Here,  $g_i$  is the statistical weight of the upper energy level,  $g_k$  in the statistical weight of the lower energy level,  $\lambda_o$  is the natural wavelength in angstroms,  $\lambda_r$  is the wavelength of the resonant line in angstroms,  $f_r$  is the oscillator strength of the resonant line, and  $N_i$  is the ground state number density in  $cm^{-3}$ . Because this broadening effect is due to neutral-neutral collisions, it can usually be neglected if the ionization fraction is greater than a few percent. In the presented work a fairly hot plasma that is highly ionized is being studied, as a result the neutral-neutral broadening can be neglected.

Van der Waals broadening is similar to that of resonant broadening. It is caused by dipole transitions of excited atoms with atoms in ground state of different types. An estimation of the effect can be written

$$\Delta_{1/2}^W \cong 3 \times 10^{-30} \lambda_o^2 C_6^{2/5} \left( \frac{T}{\mu} \right)^{3/10} N [\text{\AA}] \quad (3.20)$$

Where  $\lambda_o$  is the natural wavelength in angstroms,  $C_6$  is the interaction constant,  $T$  is the plasma temperature in  $K$ ,  $\mu$  is the atom-perturber reduced mass, and  $N$  is the perturber density in  $cm^{-3}$ . Again, and for the same reason as resonance broadening, Van der Waals broadening can be neglected as well.

Another type of broadening worth mentioning is the broadening effect from the instruments and optical equipment. This broadening effect can vary for different equipment and setups. It can also vary as a function of position on the CCD chip. Luckily this broadening effect is constant and can be calibrated out using a simple mercury pen lamp. The spectrometer used in this experiment show mercury line on the

order of a couple of angstrom. Considering the line broadened of interest here is on the order of 10's of nm this spectrometer broadening could be ignored.

Stark broadening is the final type of line broadening. Stark broadening is due to the interaction between charged particles. This interaction between emitted electromagnetic radiation and the sounding electric field was first described by Johannes Stark in 1913. The first statical approach to explain the phenomenon was developed by Holtsmark[47]. His model was based on a *quasi-static* theory that took into account static ions which played a much larger roll than electrons. Later models included the influence of both ions and electron collisions, such as models done by Hill[43, 44].

While line broadening can be fit with relatively simple Lorentzian profiles, their actual shape is much more complicated. Original theoretical profiles[98, 57] based on the *quasi-static* approximations show much more structure around the centerline line the experimentally observed[104, 45]. Unified theory or VCS[98] usually over predicts these structures. In  $H_\alpha$  the centerline is greatly extended, displaying much high peak intensities. Unlike  $H_\alpha$  and  $H_\gamma$ ,  $H_\beta$  has no central unshifted stark component and therefore exhibits a dip or central miniumn[104].  $H_\gamma$  has less structure around the centerline but shows exaggerated shoulders or wings to its profile.

Although highly exaggerated by early models these structures are very physically sound. Structure, like the central dip in  $H_\beta$ , increases with the electron density. And for a given  $n_e$  the dip becomes less pronounced when  $T_e$  is increases[96]. This observation stressing the importance of ion dynamics on the line shape. These structures are also effected by the mass of a perturbing ion. A reduced mass,  $\mu$ , is often used which can range from 0.5 for protons to nearly unity of heavier ions like  $Ar^+$ [75]. In the case of  $H_\beta$ , heavier ions create deeper dips[5]. By increasing  $\mu$  to inf it was found that the profile become more like Unified theory[104]. By including the effects of ion dynamic and reduced mass model has lessened these large structural exaggerations and have come much closer to matching experimental data.

Microfield model methods (*MMM*) take into account ion (and electron) dynamics and reduced mass. The charge particles move during the interaction time, changing the electric field as it interacts with the emitted light. Further developments were made to use computer simulation (*CS*) theory which include more full and relevant process. The *Gig-Card*[36, 35] theory has been used extensively to study  $H_\alpha$ ,  $H_\beta$ , and  $H_\gamma$ . The *Gig-Card* is computation numeric simulation that based on all the all the particle in the plasma. The plasma is considered neutral, homogeneous, and an isotopic system in thermal equilibrium. Atoms, ions, and electrons are moving quasi-randomly on the plasma. Gigosos *et al* model constitutes one of the most accurate approximations at the moment[96].

## $H_\alpha$ Line Structure

In the plasma studied here,  $H_\alpha$  was examined because of was the only line in the Balmer series that was not disperse completely into the background spectra. One of the major problems with high density plasma is the approach of near-threshold[30] conditions were spectral lines overlap and merge to give an apparent shift of the continuum spectrum[51]. As a plasma becomes higher in opacity, these effects add to the photorecombination continuum, causing large and uneven background radiation[100].

At the temperature and pressure witnessed in the AFRL capillary discharge, lines from the Paschen series were also visible. This lines have also been studies[106], but were not choose because they are in the infra red region and little data is available.

Of the Balmer series line,  $H_\alpha$  is the most intense. However, it has not been popular for diagnostic purposes. In many cases this spectral zone in known to have with a great number of line the can blur the spectrum[36]. However this is clearly not the case with the polyethylene capillary discharge where the only 2 constituent of the plasma are hydrogen and carbon. It has also been claimed that  $H_\alpha$  is without good theoretical description of it's stark broadening and the theoretical predicted line shape does not often agree with experimental results[40, 97]. This poor agreement however has been addressed by Oks' theory[73] and others who have incorporated more and more effects perturbing electric fields and ion dynamics. These effect are show to be more pronounced in cooler plasma as they approach a non-ideal state[33]. These models, and their progression, are discusses further in Section 3.5.2.  $H_\alpha$  can also be problematic because of known self absorption issues[94]. A central dip was seen in the  $H_\alpha$  line of the capillary discharge at higher currents, which would mean higher  $n_e$ . The structure of hydrogen lines can often show dips within their central region as purely a function of the broadening mechanism. However this is not a phenomenon observes in  $\alpha$  lines as discussed in Section 3.5.2.

To calculate strak broadening of  $H_\alpha$  exactly would be very difficult. Fortunately the pattern is well approximated by a Lorentzian fit with a full width half max as described by

$$\Delta_{1/2}^{S,H} \cong 2.5 \times 10^{-9} \alpha_{1/2} N_e^{2/3} [\text{\AA}] \quad (3.21)$$

Where  $\alpha_{1/2}$  is the fractional intensity width in angstroms and  $N$  is the electron density in  $\text{cm}^{-3}$ . The fractional intensity widths are referenced from Huddlestone[48] and tabulated in Table 3.3.

While hydrogen broadening has been heavily studied there are few devices that can create a hydrogen plasma with  $n_e \geq 10^{24}$ . This is one of the reason it is hard to find data and models suited for CD plasmas.

Table 3.3: Fractional Intensity Widths[48]

T (K)	T (eV)	N (#/m <sup>3</sup> )	$\alpha_{1/2}$
5000	0.431	$1 \times 10^{21}$	$9.69 \times 10^{-3}$
5000	0.431	$1 \times 10^{22}$	$14.9 \times 10^{-3}$
5000	0.431	$1 \times 10^{23}$	$18.9 \times 10^{-3}$
5000	0.431	$1 \times 10^{24}$	N/A
5000	0.431	$1 \times 10^{25}$	N/A
10000	0.862	$1 \times 10^{21}$	$7.77 \times 10^{-3}$
10000	0.862	$1 \times 10^{22}$	$13.4 \times 10^{-3}$
10000	0.862	$1 \times 10^{23}$	$18.6 \times 10^{-3}$
10000	0.862	$1 \times 10^{24}$	$21.5 \times 10^{-3}$
10000	0.862	$1 \times 10^{25}$	N/A
20000	1.723	$1 \times 10^{21}$	$6.01 \times 10^{-3}$
20000	1.723	$1 \times 10^{22}$	$11.4 \times 10^{-3}$
20000	1.723	$1 \times 10^{23}$	$17.5 \times 10^{-3}$
20000	1.723	$1 \times 10^{24}$	$22.6 \times 10^{-3}$
20000	1.723	$1 \times 10^{25}$	$23.5 \times 10^{-3}$
30000	2.585	$1 \times 10^{21}$	$4.98 \times 10^{-3}$
30000	2.585	$1 \times 10^{22}$	$10.0 \times 10^{-3}$
30000	2.585	$1 \times 10^{23}$	$16.6 \times 10^{-3}$
30000	2.585	$1 \times 10^{24}$	$22.5 \times 10^{-3}$
30000	2.585	$1 \times 10^{25}$	$25.7 \times 10^{-3}$
40000	3.447	$1 \times 10^{21}$	$4.50 \times 10^{-3}$
40000	3.447	$1 \times 10^{22}$	$9.22 \times 10^{-3}$
40000	3.447	$1 \times 10^{23}$	$15.8 \times 10^{-3}$
40000	3.447	$1 \times 10^{24}$	$22.3 \times 10^{-3}$
40000	3.447	$1 \times 10^{25}$	$26.9 \times 10^{-3}$

Three devices often used to validate theory at high densities are gas-liner pinches[10, 20], laser-produced underwater plasmas[32, 31], and flash tubes[99]. A gas-liner pinch by Böddeker produces the highest  $n_e (\approx 10^{25} \text{ m}^{-3})$  but at much higher  $T_e (6 - 10 \text{ eV})$ . Models have been fit to this work[74] with some degree of success. The capillary discharge may be unique in being able to produce cooler higher density plasmas.

Stark broadening has been used to measure electron number densities in ablative discharges. Carbon has been used to measure lower densities,  $n_e = 3 \times 10^{22} \text{ m}^{-3}$ , in PPTs[67]. In teflon ( $CF_2$ ) plasmas, where fluorine is present, number densities can be determined using Stark Broadening up until  $n_e = 3 \times 10^{23} \text{ m}^{-3}$ , where strong broadening and rising background spectrum wash out the line[61]. Hydrogen has been in much higher density plasma.

One of the more relevant works on Hydrogen broadening in capillary discharges was done by Ashkenazy *et al*[7]. In their work they examined  $n_e$  of a capillary discharge in the range of  $10^{22} - 10^{25} \text{ m}^{-3}$  using both  $H_\alpha$  and  $H_\beta$  line broadening. Both lines showed good agreement with each other up to

$3 \times 10^{23} \text{ m}^{-3}$ , as was predicted by literature[39].  $H_\alpha$  was used to measure densities up to  $1 \times 10^{25} \text{ m}^{-3}$ , however results shown as shift and discrepancy above  $5 \times 10^{24} \text{ m}^{-3}$ . This was attributed to self-absorption of the line causing the FWHM to be larger due to poor Lorentzian fits. One of the major problems with Ashkenzy *et al* work was that the optical emission spectroscopy (OES) measurements were made by time integrated over the whole discharge. Others[92] have taken similar measurements using an OMA with a fast gate to take one quick spectra during their discharge. However, with current technology and state of the art CCD cameras it is possible to make full time resolved measurements of the a capillary discharge, which was done here.

The reasons behind asymmetry are not well studied. To date most MMM, whether based on theory or computer simulation, have only taken into account terms of first order in the perturbing electric field, and therefore can only produce symmetric profiles[95]. In order to model these shifts and asymmetric higher order terms must be included. Some of the mechanisms that might be responsible for these effects are: the quadrupolar effect, electron impacts, the quadratic Stark effect, and fine structure of ions. However all these effects are not of the same importance and their relative importance can vary depending on the  $T_e$  and  $n_e$  of the plasma.

While the exact reasons for the shifts and asymmetries are still debated, there has been reasonable success in modeling and predicting them, specially in regards to line shift. Flih[33] shows an excellent fit to  $H_\alpha$ 's FWHM and a near linear trend is shown for  $n_e$  in the  $1 - 5 \times 10^{24} \text{ m}^{-3}$  at  $\approx 1 \text{ eV}$ . It is probable that this trend would hold for our higher densities. However, as we have seen experimentally,  $H_\alpha$  gets harder to profile with simple lorentzians at higher densities because of self-absorption. While this greatly affects Lorentzian fit and their FWHM values it might not affect the shift of the center line of these fits. Flih's work also shows a very linear trend of this shift with  $n_e$ . One problem is that the FWHM can range from  $6 - 15 \text{ nm}$  while the shift is only  $0.6 - 1.8 \text{ nm}$ . It may be hard to resolve such small shifts over such a largely broadened and distorted profile.

### 3.5.3 Mach Disc diagnostics

It may be worthwhile to note that based on work done by Kohel[59], it may be possible to use the geometry of the under expanded plasma jet to determine plasma properties. Based on preliminary high speed video it is possible to see a clear shock structure in the capillary plume, as shown in Figure 3.18. The most

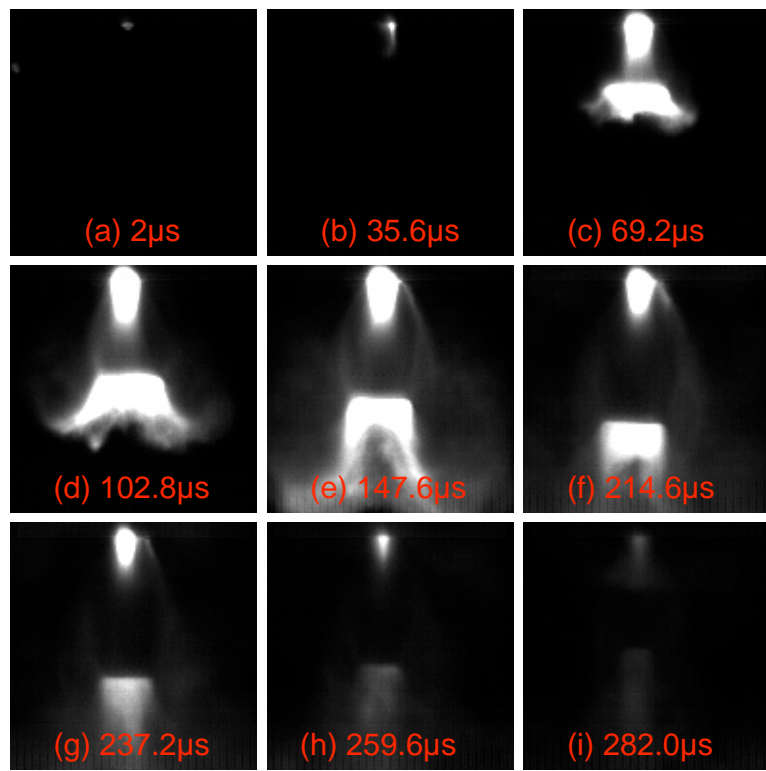


Figure 3.18: Still frames from high speed video of a capillary discharge

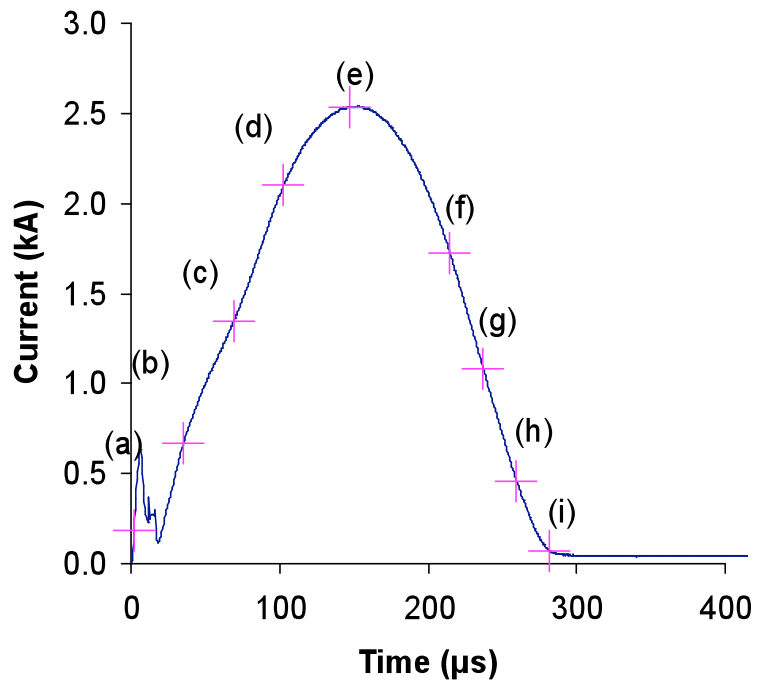


Figure 3.19: Current trace showing when images from Figure 3.18 occur

noticeable feature is the Mach disk that is pushed out of the capillary opening some distance from the exit plane. This type of diagnostic was not attempted but may be of interest in future work.

# Chapter 4

## Modeling

A parallel effort was conducted in developing a computational model for the capillary discharge. This work was conducted by others, but there was close collaboration between the experimental and computational work. The zero-dimesional model was used in designing the capillary discharge device and in interrupting the experimental data so the work will be described here. Certain short coming that are inherent of a zero-dimensional model were observed and a one-dimensional model was created in an effort to better match experimental results.

### 4.1 Zero-Dimensional Model

Work done by Leonid Pekker[77] has followed the progression of capillary modeling starting with the work done by Loeb and Kaplan[68], which used a many assumptions to simplify a capillary discharge model. Later work done by Powell and Zielinski[78] added the Saha equation to more actually calculate plasma composition and enthalpy. From these previous works Pekker developed a model based on the conservation laws for mass and energy. Mass is conserved though the balance of mass addition do to ablation of the walls and mass loss due to flow out the exit, per unit volume.

$$\frac{d\rho}{dt} = \frac{d\rho_a}{dt} + \frac{d\rho_e}{dt} \quad (4.1)$$

The conservation of energy can be expressed by

$$\frac{d}{dt}\rho\bar{\varepsilon} = \eta j^2 + \frac{d\rho_e}{dt}h_e - \frac{2}{R}q_r|_{R_c} + \frac{d\rho_a}{dt}h_a \quad (4.2)$$

Where the total energy and enthalpy includes kinetic and internal energies. The enthalpy contribution due to the mass addition is accounted for in the second term and the contribution due to mass loss though the exit is accounted for in the fourth term of the right hand side of Equation 4.2. The first term on the right hand side of the Equation 4.2 is the Ohmic heating and is determined by the plasma conditions,  $\eta$ , the plasma resistivity and  $j$ , and current density. The third term is the radiation flux to the capillary wall.

Modeling the radiation flux is one of the more challenging parts of capillary discharge modeling. Before any experiments were done two different radiation models were used in the model. These two different types of radiation models helped us bound the capillary discharge operational regime. This is discussed further in the next section. Because experimentally the capillary operates in between the 2 extremes a radiation software package called PrismSPECT® was used to calculate the total radiation flux. This software can accurately model the radiating spectrum for a given composition, temperature, and density. A database was formulated from these 3 input parameter and was used in Pekkers capillary discharge code when comparing to experimental data shown in Chapters 5.2 - 5.5

## 4.2 One-Dimensional Model

A one-dimensional model was created by Sergey & Natasha Gimelshein in order to incorporate some of the flow field physics that were missing from the zero dimensional model. This axial 1D model was based on the work down by Edamitsu and Tahara[?]. Their computational and experimental work was on a smaller, lower energy, electrothermal PPT with energies of 5 to 15 J. While considerably different from the capillary discharge presented in this work, the same basic concepts and physics applied. Their unsteady numerical model simulated the electrical circuit, plasma flow, heat transfer to the wall, heat conduction inside the wall, and ablation. The results of which matched their experiment very well[?].

The assumptions used in the 1D model are similar to the 0D. The plasma flow was considered in ionization equilibrium, single ionized, one-fluid plasma flow, and in LTE. The Effects of the magnetic field are not considered and the total pressure and electron number density were assumed to be radial constant. The conservation of mass, momentum and energy are conserved axial and expressed by:

$$\frac{\partial(A\rho)}{\partial t} + \frac{\partial(A\rho u)}{\partial x} = L_{cir}\Gamma \quad (4.3)$$

$$\frac{\partial(A\rho u)}{\partial t} + \frac{\partial}{\partial x} [A(\rho u^2 + p)] = p \frac{\partial A}{\partial x} - f L_{cir} \quad (4.4)$$

$$\frac{\partial(Ae)}{\partial t} + \frac{\partial}{\partial x} [Au(e + p)] = A(Q_j - Q_{rad} - Q_{conv} + Q_{ab} - \Phi) \quad (4.5)$$

where  $A$  is the cross-sectional area,  $\rho$  is mass density,  $\Gamma$  is ablation mass flux,  $u$  is the average velocity in the cross-section,  $p$  is the pressure,  $f$  is the frictional stress on the surface,  $\Phi$  is the energy dissipation due to viscosity, and  $e$  in the total energy.

In the energy equation 4.5, for typical experimental voltage and capillary length the convection energy loss term term,  $Q_{conv}$ , and viscous energy losses,  $\Phi$ , are more than two orders of magnitude less than the joule heating,  $Q_j$ , and radiation energy loss,  $Q_{rad}$ . The energy fluxes as a function of time are shown in Figure 4.1. The curves for  $Q_{ab}$  and  $\Phi$  are omitted as they are indistinguishable from zero. The convection

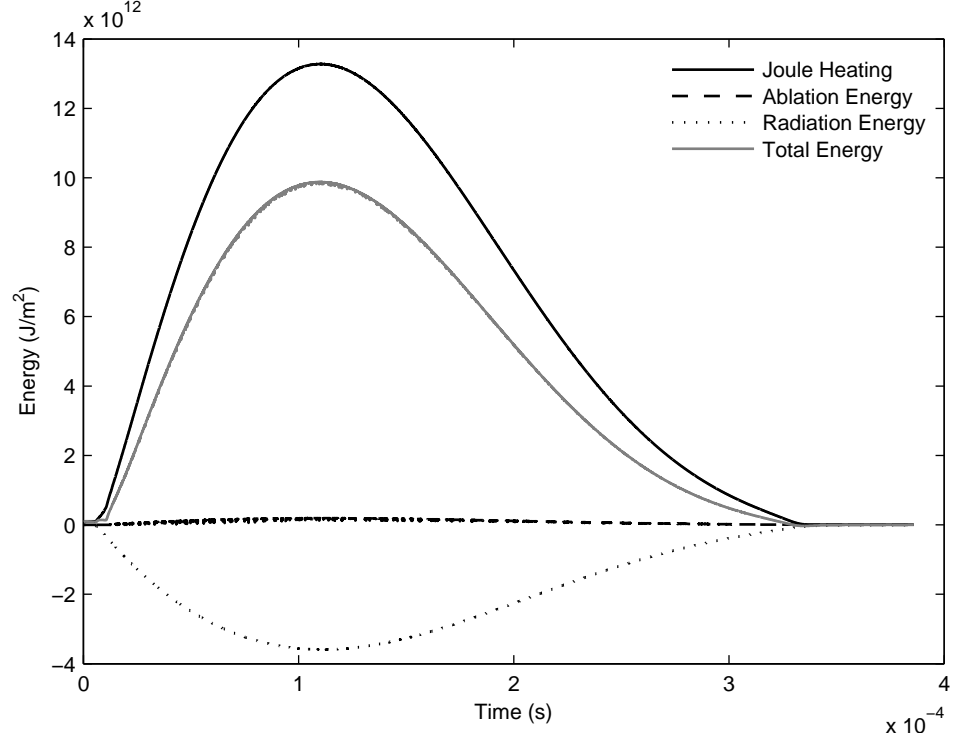


Figure 4.1: Energy Fluxes for a 5cm 2500V Capillary Discharge

flux and viscous losses did not affect the results of the 1D model as they were much smaller than other energy fluxes, and were omitted in increase computational time. It was also observed that the results very weakly depended on the polyethylene saturated vapor pressure as a function of temperature so that the surface temperature adjusted itself in such a way that the mass flux of polyethylene remained the same. Therefore, there was no need to solve the heat transfer equations for the capillary wall. The polyethylene flux from surface was determined by the energy flux coming to the surface divided by polyethylene "unzipping" energy. This simplification produced similar results obtained by the full simulation with heat transfer equation for capillary wall, but ran much quicker.

# Chapter 5

## Results

In this chapter the data collected from the capillary discharge experiments will be summarized. The data follows the progression of the capillary discharge similar to the design progression in section 2.1. The first section will cover the basic circuit setup and subsequent sections will examining the ignition data. Just as the experiment became more elaborate in design so did the diagnostics. While the data for wire ignition was interesting and yielded a good understanding of capillary physics and modeling, it wasn't until the Paschen and 3-electrode ignition experiments that interesting thruster performance data was produced.

### 5.1 Circuit

The basic circuit is a simple one, as described in Section 2.2. In order to fully understand the discharge it is important to understand the circuit controlling it. The LRC circuit was assembled as it was to be used in the experiment. All the same components, bus bars, cabling and connectors were used. Originally, tests used an extended anode that would run completely through the thruster housing, grounding to the cathode. This setup was compared a simpler setup in which the power cable was connected directly to ground. There was no noticeable effect on the circuit parameters between these 2 setup, and that later was used. The only other difference between the experimental setup and the test circuit was a  $0.5 \Omega$  resistor<sup>1</sup> that approximated the resistance that would normally be due to the discharge plasma. This resistor had a known resistance to within  $\pm 5\%$  and therefore the circuit parameters could be known to  $\pm 5\%$ .

The circuit was discharged and the current profiles recorded. This data was then fed into a least squares fit model<sup>2</sup> that could vary the  $L$ ,  $R$ , and  $C$  parameters until the profiles matched. This was done for a variety of different inductances that would be tested in Section 5.2. The results of this analysis are shown in Figure 5.1. Plot (a) shows that the inductance of the circuit increases linearly as four inductors are added in series. It also shows that the circuit itself has an inductance of  $7 \pm 0.4 \mu H$  and that each

---

<sup>1</sup>Gerneral Atomics, High Energy Resistor, Model 93849

<sup>2</sup>Model written my Dr Marcus Young, AFRL

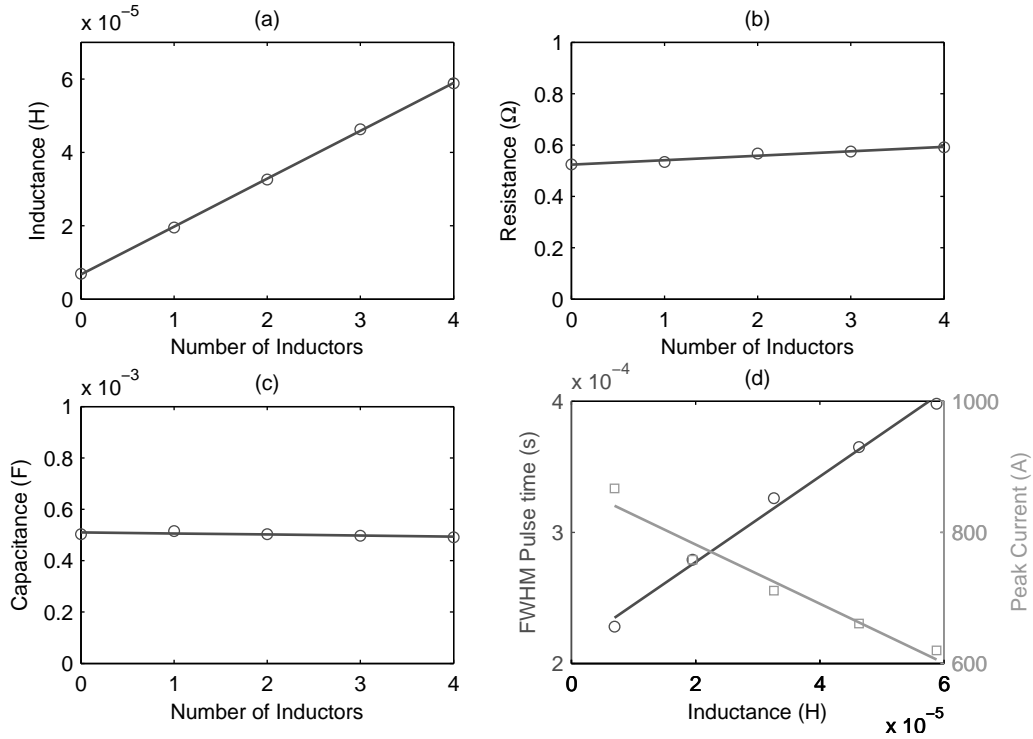


Figure 5.1: (a) Inductance, (b) resistance, and (c) capacitance as a function of number 10  $\mu$ H inductors. (d) Pulse length and peak current as a function of Inductance

inductor had an average inductance of  $13 \pm 0.7 \mu$ H, not the 10 advertised by the vendor. Plot (b) shows that each inductor adds slightly more resistance. By subtracting 0.5  $\Omega$  from these resistance values it is possible to estimate the parasitic resistance of the circuit, ranging from  $24 \pm 1 \mu\Omega$  to  $91 \pm 5 \mu\Omega$ . Plot (c) indicated the the capacitance is not affected and is within the specification of the manufacturer. Plot (d) shows how that inductance affects the pulse shape. As the the inductance increases the pulse time increases and the peak current decreases, as is expected from LRC circuit theory. The circuit parameters obtained in this analysis are also used in both computer models.

## 5.2 Wire Ignition

Wire ignition was carried out first because of its historical importance in capillary discharge research. While this method can not be seriously considered for any space applications, it has been proven in many laboratory capillary discharges. The techniques of exploding wire ignition are discussed in Section 1.7 and the associated test apparatus is described in great detail in Section 2.1.1.

### 5.2.1 Test Procedures

As mentioned in Section 2.1.1 the original design went through many iteration before properly operating and sealing. The system used in these ignition tests consisted of a tube within a tube configuration. The outer tube was reused, but a new inner tube was replaced between each firing. The inner tubes were held rigid using a 4 mm metal rod while the outer tube was pressed on. The two tubes fit very tightly within each other. Subsequent to assembly the support rod was removed and the aluminum wire was feed down the length of the tube assembly. The wire was usually cut long to make it easier to feed in the tubes and trimmed later. The anode was then slid into the back end of the tubes, holding the wire in place. The insertion depth was varied in order to create the correct length capillary for the desired test. This whole assembly was then introduced into the housing through the exit orifice until the outer tube butted against the internal insulator, which can be seen in Figure 2.2. The fit of the tubes inside the house was such that it could be introduced without requiring much force, yet would hold in position. Once in place, the power cable could be connected to the anode and the wire attached to the cathode flange. The wire was attached by looping it out with plenty of slack, or pulled tight to the attachment point, it did not seem to affect the discharge.

### 5.2.2 Data

Once the discharge was operating reliably and repeatably a number of parameters were varied in order to observe the corresponding effects on the discharge. The first and easiest of these parameters was the voltage potential of the capacitor bank. By changing the capacitor to different voltages, the voltage driving the capillary discharge was varied. Figure 5.2 shows the discharge current as affected by these voltage changes. As the driving voltage or potential across the discharge increases so does the current and total power input into the device. While the current increases the pulse width does not. Discharges typically last 250 to 300  $\mu s$ . The discharges can also vary more significantly at lower voltages, about 8% variation, compared to at higher voltages, where there is a variation of 2%. The initial current pulse seen in Figure 5.3 around 100  $\mu s$  are due to wire explosion. This clearly demonstrates the chaotic nature of this ignition system as discussed in Section 1.7.1.

To change the pulse length one needs to modify the circuit parameters. By increasing the inductance the current pulse flattens out with lower peak currents and longer pulse lengths, as exhibited in Figure 5.3. Four separate 10  $\mu H$  inductor coils were used to change the overall inductance of the circuit. The parasitic

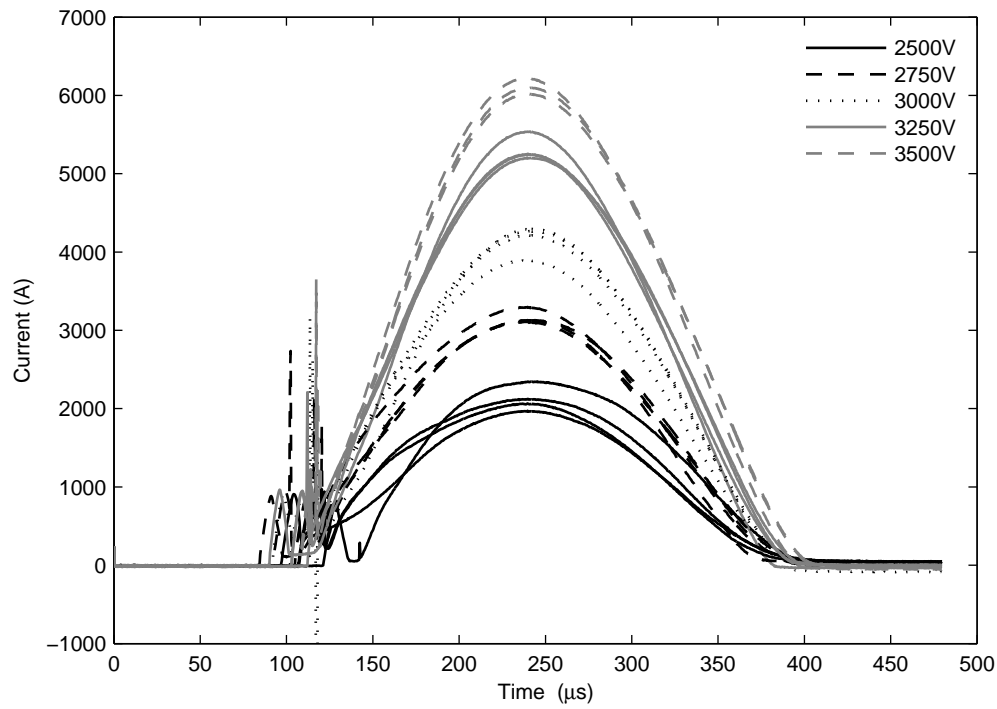


Figure 5.2: 10 cm, 10  $\mu$ H capillary discharge currents for varying capacitor voltage

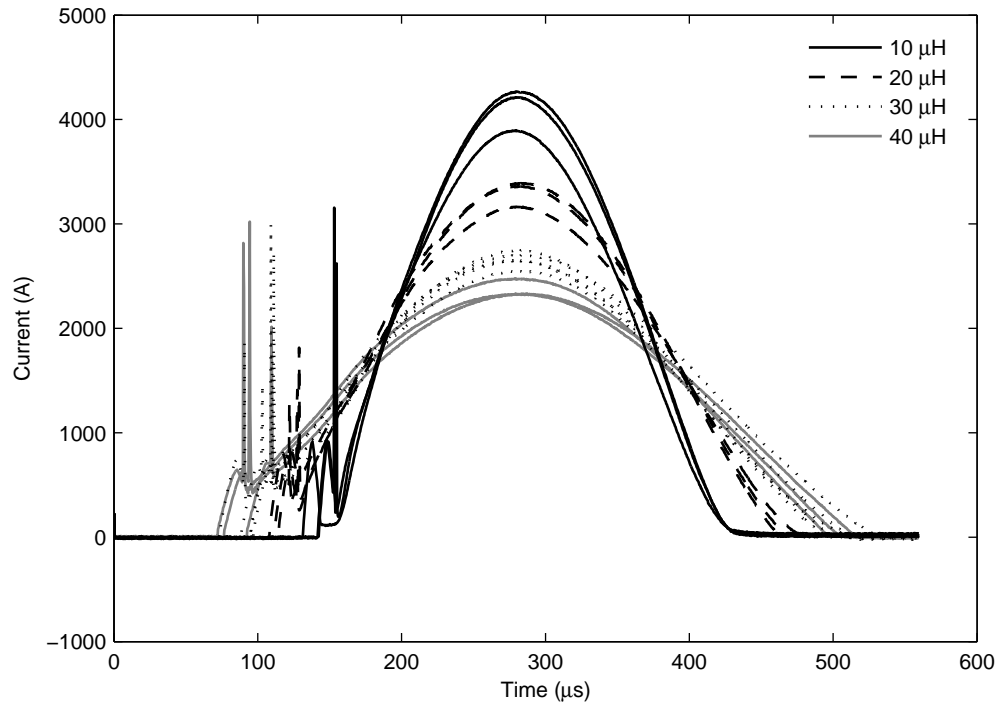


Figure 5.3: 10 cm, 3000 V capillary discharge currents for varying inductances

inductance of the wiring, capacitors, and circuit components was not small compared to the coils, as shown in Section 5.1. From the Table 5.1 notice that while the change in current peak and pulse length were not proportional, they are in fact such and the total power input into the system changes very little, with a percent deviation of less the 2%.

Table 5.1: Inductive Effects on Discharge Circuit Parameters

Num. Inductors	Inductance	change in $t_{discharge}$	change in $J_{max}$	
1	$10 \mu H$	0%	0%	$1149 J$
2	$20 \mu H$	37%	-20%	$1159 J$
3	$30 \mu H$	53%	-35%	$1188 J$
4	$40 \mu H$	89%	-42%	$1182 J$

The other major parameter changed in these initial tests was length. By sliding the anode deeper into the capillary ,the capillary length was shortened. The effect of this geometry change is shown in Figure 5.4. Plot (a) indicated that by shortening the capillary, the peak discharge current increases. This

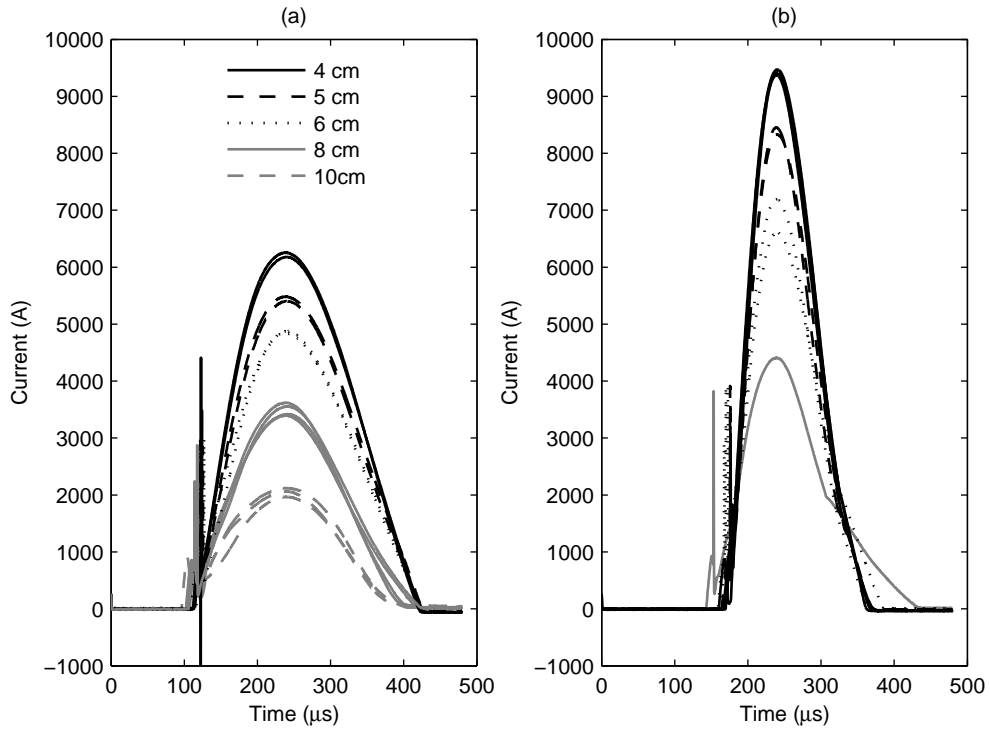


Figure 5.4: (a)Low Current and (b)high current modes of a 2500 V capillary discharge currents for varying lengths

makes sense in that the capillary plasma column has a resistivity or resistance per length. So if the column is shortened, the overall resistance will decrease, causing larger currents. Another way to think of this is, if the capillary length is shortened for a given  $\Delta V$  between the anode and cathode, the voltage gradient increases, which leads to larger currents.

One of the most interesting effects seen in the capillary discharge experiments preformed in this study are the random occurrences shown in the Plot (b) of Figure 5.4. These current plots were taken at test conditions identical to the data shown in Plot (a). This high current (HC) mode of operation, shown in Plot (b), produced significantly higher current pulses and slightly smaller pulse widths. Despite the difference between these 2 modes, the power of the high current mode is only about 12% less that of the lower current or normal mode. The two modes occur at random, but the discharge always operates at one of the two forms and never in-between. The HC mode also occurred more frequently as the length of the capillary was decreased. Most of the previous tests were at 10 *cm* and no HC mode was ever observed. It wasn't until testing started for an 8 *cm* capillary that the phenomenon was observed. Of the five 8 *cm* shots fired in Figure 5.4, the HC mode discharge occurred only once. It occurred 2/5 times at 5 and 6 *cm*, and 3/5 times for the 4 *cm* test. Section 6.3 contains discusses this phenomenon.

## 5.3 Paschen Breakdown Ignition

Paschen breakdown proved the next logical step in the ignition tests. The reasons and techniques for which are discussed in Section 1.7.2. Details of the apparatus are described in Section 2.1.2

### 5.3.1 Test Procedures

For these ignition tests dry nitrogen was used to create the required background pressure. The capillary was mounted on the thrust stand, as described in Section 3.4.2 within the vacuum chamber. The chamber was pumped down to its lowest limit using just the backing pump; usually around 20 *mTorr*. The chamber was then refilled back up to the operating pressure necessary for breakdown, usually around 20 *Torr*, depending on the length and voltage being tested. This was done in order to keep a more stable and repeatable ignition environment for testing.

The exact breakdown pressure was determined experimentally for each new capillary setup. This was done quickly by over filling the chamber with nitrogen, around 50 *Torr*. The capacitors were charged to the voltage desired and the control switch was left open. The valve to the pump was opened slightly and the chamber pressure would start to decrease. Eventually the pressure become enough for a Paschen

breakdown to occur. The breakdown pressure was noted for future tests with that particular length capillary and voltage.

Tests were set up and run for a variety of lengths and voltages. For each length and voltage combination a capillary tube, cathode, and anode were all weighed. The entire thruster assembly was put together compressing both the anode and cathode seals, as described in Section 2.1.2. The device was then mounted to the thrust stand. The thrust stand LVDT core was aligned and tested to make sure that there was no contact or rubbing that could disturb the measurement. The combs were also checked to make sure that they were aligned and engaged as prescribed in Section 3.4.2 Once the chamber was sealed and pumped down to the appropriate pressure for ignition, the capillary was fired five times. After five consecutive shots the chamber was pumped down further so that calibration could be completed at lower pressures, where the 3000V placed on the combs would not arc. After the calibration was successfully completed, the chamber was vented and the the device disassembled. The capillary, housing assembly, anode, and cathode were all weighed separately. The mass before and after were compared and an average mass loss per the five shots was calculated.

One of the important characteristics to note when working in this regime is the occurrence of secondary discharges or restrikes. This originally happened because the SCR switch was opened with a trigger pulse that was 1 s long. This presented no problem at atmospheric pressures because the conditions required for restrikes never occurred. However at lower pressures, after the first discharge occurred, a secondary restrike would occur some  $\mu s$  later, sometimes as much as a  $ms$  later. This was caused by the remaining voltage on the capacitors. This left over charge resulted in potentials which were usually in the range of 700 to 1500 V depending on the original charging voltage and the capillary geometry. As the pressure dropped within the capillary after the current shut off and the main discharge was over, a pressure was reached that allowed this secondary restrike to occur. While it was an interesting phenomenon, it did affect impulse and mass loss measurements. The restrike problem was eliminated by only allowing the SCR switch to open for a short period of time, no longer than the discharge itself. Even though a GTO (gate shut off) switch was not used, the current dropped to zero before the restrike, which allowed the switch to latch shut preventing any further discharges from occurring. It may be worth while keeping this phenomena in mind for future multi-shot operations.

### 5.3.2 Data

As with the wire ignition tests, several parameters were varied to observe their influence on the thruster. A complete data matrix was taken for this ignition method, so that five separate voltages were tested for each of the four lengths. As with the case with previous tests, five consecutive shots were taken to build a statical average for total impulse and to increase total mass loss. Figure 5.5 shows the two parameter changes and their effect on the discharge current. Plot (a) exhibits, for a 6 cm capillary, the change

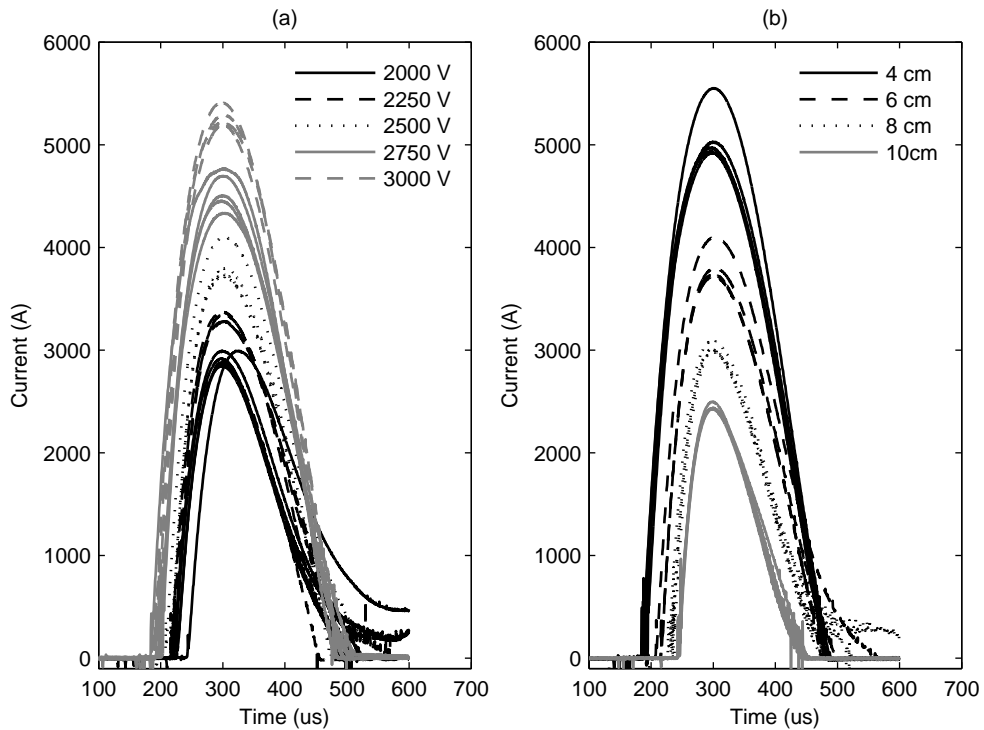


Figure 5.5: (a) 6 cm discharge currents at various capacitor voltage and (b) 2500 V discharge currents for varying lengths capillaries using Paschen ignition

in current with various driving potentials. These results showed the same trend as the wire ignition, increasing peak current with increasing voltage. Plot (b) shows the current for a 2500 V discharge for different length capillaries. The results here were as expected and the current, pulse width, and total power all increase for shorter capillaries. The results are compared more thoroughly in Section 6. It is also apparent from Figure 5.5 that there are different tails or extinctions for the discharge. This anomalous extinction led to current tails that could last 100's of  $\mu s$  to 1 ms. These tails, and possible mechanisms for them, are discussed in Section 6.6.

As mentioned in Section 1.7.2 the use of Paschen breakdown ignition allowed the determination of thruster performance characteristics, described in Section 1.6, such as  $I$ ,  $I_{sp}$  and  $\eta$ . These 3 parameters allow, for the first time, a view of how the device was operating as a space craft propulsion device. They are plotted as a function of the energy in Figure 5.6. This energy is total energy input into the device and is calculated by

$$E = \int j(t)V(t)dt \quad (5.1)$$

where the current  $j$  is measured by Rogowski coils, and  $V$  is measured by a voltage probe. Plot (a) shows an increase in total impulse with increasing input energy. This input energy is determined from the voltage on the capacitor used to drive the discharge. For a given capacitor potential, shorter capillaries are driven to higher total input energies. At a potential of 2500 V, a 4 cm discharge consumes about 1400 J, while a 10 cm consumes only 650 J. Impulses ranged from 20 to 100 mNs for various lengths and voltages. It is also worthwhile to note that the impulse is relatively independent of capillary length, and that within the length variation available, different length capillaries can create approximately the same impulse; provided that proper energy levels can be reached.

Plot (b) shows measurements of  $I_{sp}$ . This data exhibits a significant amount of scatter. Within the range of conditions, 4 cm capillaries show some of the best performance, and also the worst. The  $I_{sp}$  for 4 cm capillaries range from 350 s to 650 s, and have a standard deviation of about 105 s. 10 cm on the other hand are fairly constant at about 600 s, and a standard deviation of 33 s. This scatter is mostly accredited to erroneous mass loss. The mass loss used in the  $I_{sp}$  calculations are based on total mass loss of the entire system, including the anode and cathode which were still experiencing large mass losses, in some cases about 50% of the total. The sporadic nature of the  $I_{sp}$  measurements can be traced directly to the sporadic mass loss due to electrode erosion as will be discussed in Section 6.2. The efficiency measurements are also corrupted by electrode mass loss as shown in plot (c). Because of this, the efficiency ranges from about 8% to 18%.

While much of this Paschen Ignition data was not as clean and concise as desired, it did provide a good first look at how the discharge was operating. The capillary discharge as a thruster could linearly create impulses of 28 to 100 mNs, independent of capillary length. And, over the complete range of lengths and voltages, the capillary discharge exhibited an average  $I_{sp}$  of about 550 s and an average efficiency of about 12%.

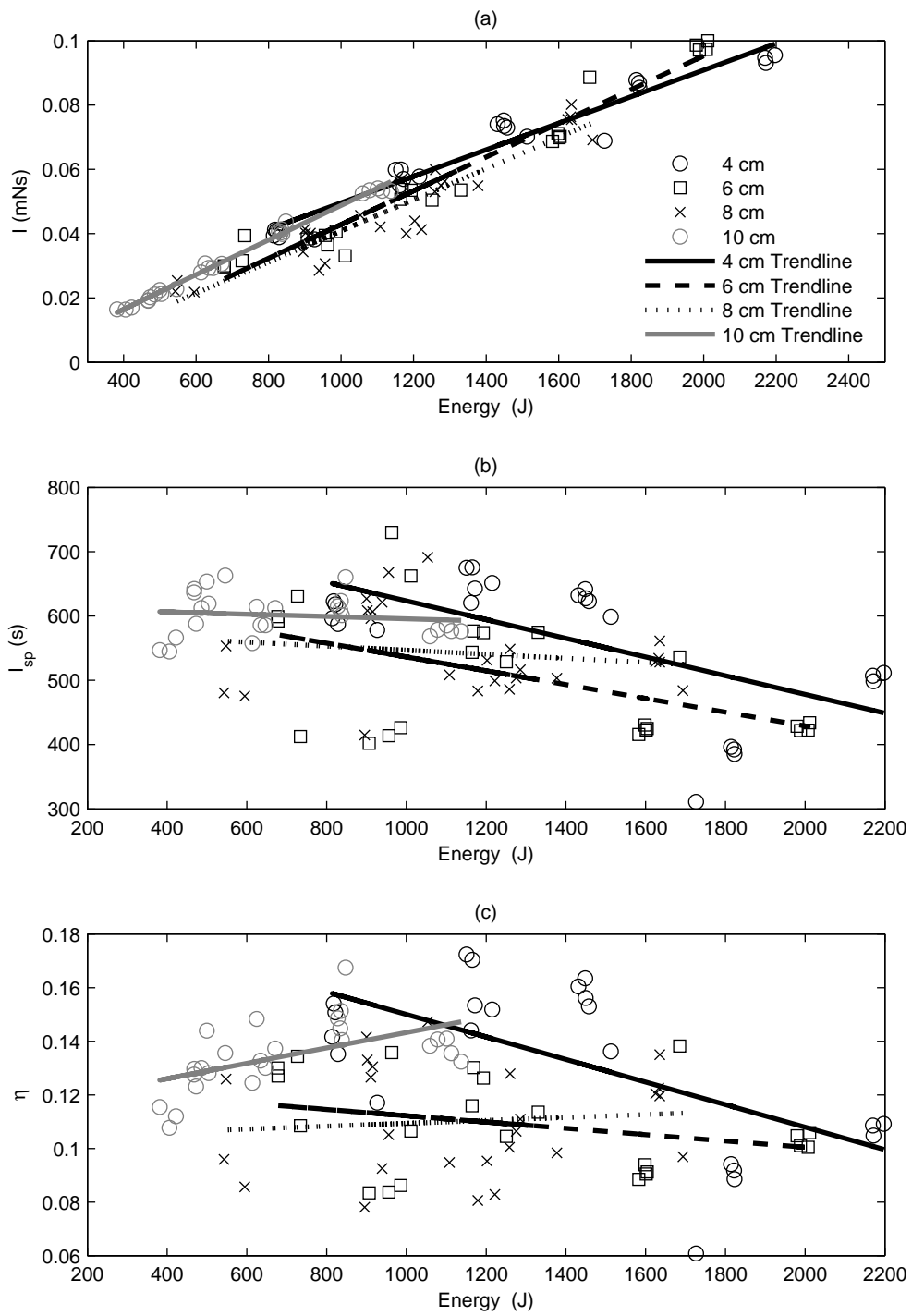


Figure 5.6: (a) Impulse, (b) Specific Impulse, and (c) Propulsion Efficiency as a function of input energy for 4, 6, 8 cm Capillaries using Paschen ignition

## 5.4 External Coaxial Ignition

A coaxial igniter described in Section 2.1.3 allowed the gap between the Paschen ignition and a full internal three electrode ignition system to be bridged. By using this method the ignition principles outlined in Section 1.7.3 could be tested without committing to a major design change.

### 5.4.1 Test Procedure

For these tests it was conceived that a coaxial cable would be held near the exit plane of the capillary. The housing that was used could be the same as the previous Paschen breakdown tests. The only difference was that the SCR switch that normally triggered the discharge was opened earlier and a high voltage ignition spark was used to initiate the discharge. This required some basic circuit, control wiring, and data acquisition modifications.

The first attempts to ignite a capillary discharge with the coaxial ignitor did not work. This ignitor itself appeared to be working fine and emitted a spark or glowing discharge. However it failed to ignite the capillary. Many different angles and orientations were tried before the capillary discharge was successfully ignited. The only way to cause ignition was by placing the ignitor directly at the edge of the exit orifice. By doing so it caused ignition, but in turn was heavily eroded by the exit plume. It was believed that easy ignition would not occur because of a worn electrode geometry that interfered with the formation of proper electric fields for the formation of a conductive path. A new set of tungsten electrodes were being machined for a three electrode design, and it wasn't until they were finished that coaxial ignition could be tested. The assembly for these test was therefore the same housing as the three electrode setup minus the ignition electrode and ignition material shown in Figure 2.7.

As already expressed, the coaxial ignitor was only tested for a short number of cases before an internal three electrode system was implemented. Only a 6 cm tube was tested for a variety of voltages. A voltage up to 3500 V was tested, in order to check and qualify the sealing configuration of the design. This was a higher voltage than previously used and the seal held quite well.

### 5.4.2 Data

The current plot for the coaxial ignition looks very similar to previous current plots as shown in Figure 5.7. The current increases with increasing voltage. The current traces were clean from start to finish, not plagued by the noise of the wire ignition or the random tails from the material used in the Paschen

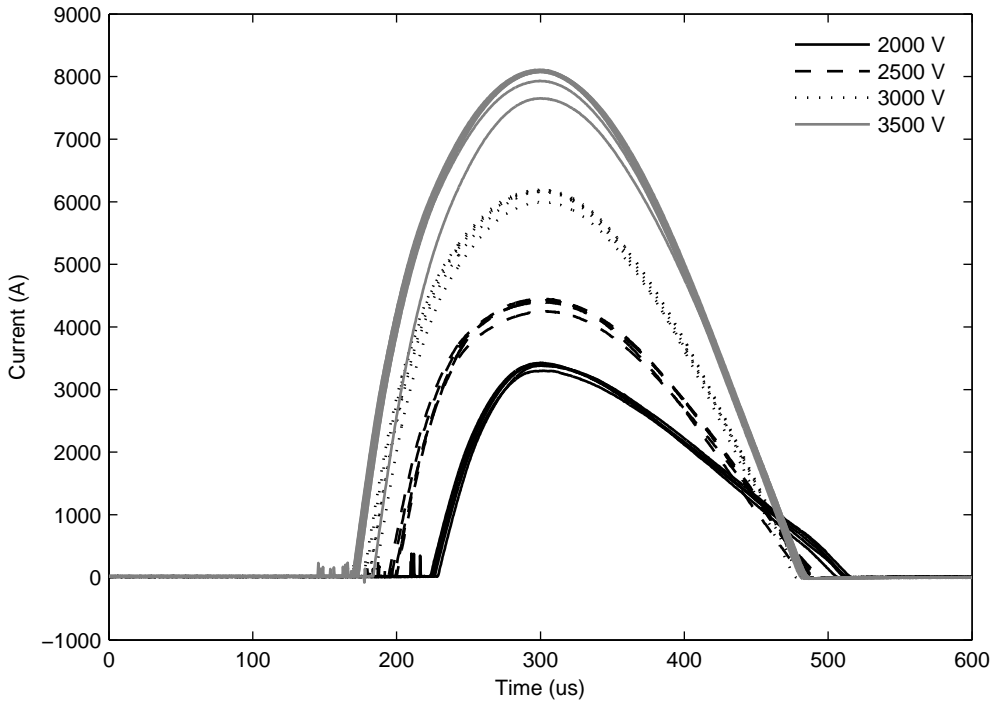


Figure 5.7: Current as a function of time for various capacitor voltages using Coax Ignitor

ignition. These current traces show very similar initial profiles, however their extinction profile change significantly with voltage. This form has been seen in previous ignition tests, but is not as pronounced as shown in this case. As the driving voltage increased the  $\frac{di}{dt}$  became larger and the pulses become more symmetric.

The thruster performance plots for the coaxial ignition exhibited much cleaner results. As presented in Figure 5.8 plot (a), the impulse has a linear relationship with the electrical energy used in the discharge with very little deviation. The  $I_{sp}$  and  $\eta$  in plots (b) and (c), respectively, show downward trends as a function of energy, as was expected for a 6 cm case. The data for these tests still showed significant mass loss of the electrode, however this mass loss was more consistent than with the Paschen ignition test. This can be seen in the  $I_{sp}$  and  $\eta$  plots, results show a much reduced scatter compared to Figure 5.6. The issue of electrode mass loss is discussed further in Section 6.2

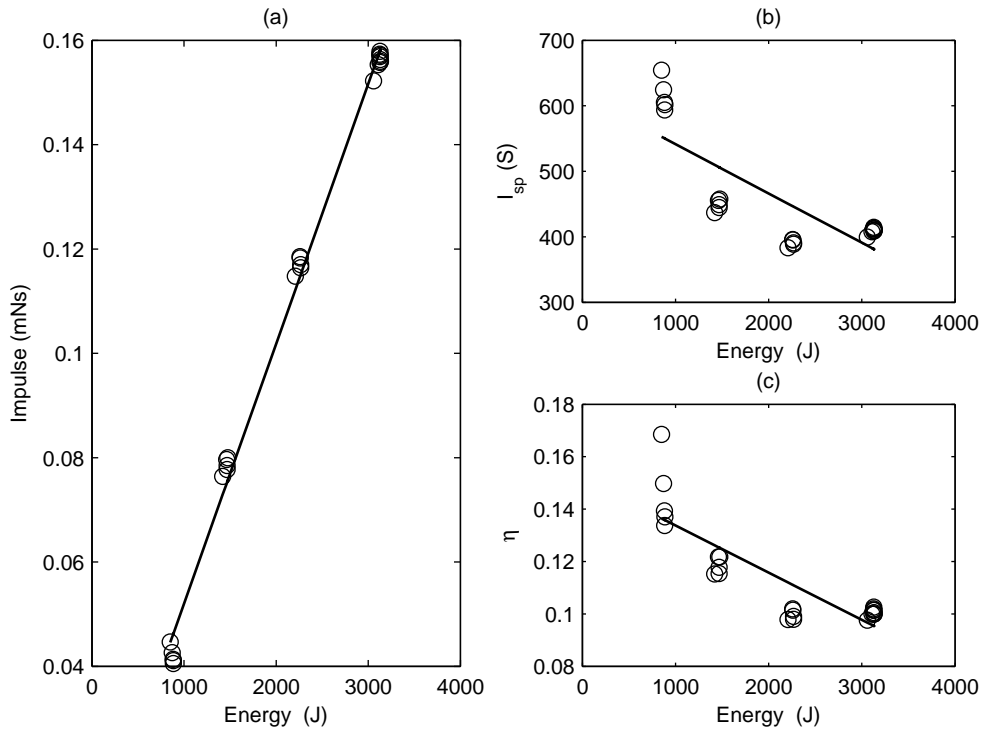


Figure 5.8: (a) Impulse, (b) Specific Impulse, and (c) Propulsion Efficiency as a function of input energy for a 6 cm Capillaries using Coaxial Ignitor

## 5.5 Internal Three Electrode Ignition

After the coaxial ignitor test proved effective, the spark ignition concept was incorporated into the thruster housing as described in Section 2.1.4. This was the final ignition method and incorporated all the design improvements that had been progressively introduced in the previous tests.

### 5.5.1 Test Procedures

To test the system the same preliminary data was taken as for the coaxial case. A 6 cm capillary was tested at 2000 V, 2500 V, 3000 V and 3500 V. These results can be compared to show that indeed these two methods preform in very much that same way.

After the preliminary testing of the three electrode ignition system(3-EIS) a full set of data was taking for several lengths and voltages, similar to that of the Paschen and wire ignition methods. 6 cm capillaries were tested first, followed by 4 cm and 8 cm. 10 cm data was attempted last and was unsuccessful. The capillary discharge had trouble igniting at these lengths. While ignition was possible it was erratic,

occurring off time, or igniting once out of every ten tries. This made it very difficult to acquire a full data set of more than few attempts. The reason for the failure of the 10 *cm* case is most likely due to the same reason as the initial coaxial tests. By this stage of testing the electrodes were worn and geometry did not lend itself towards good electric fields and conductive paths. At longer capillary lengths it became harder to ignite simply because it is harder to form conductive path along a greater length. This, in combination with a shrinking view factor between anode and cathode, made it very difficult to ignite the 10 *cm* cases.

All testing in this section was done using pre-discharged capillaries. It has been observed that the first firing of a new tube can be quite different from the following discharges, as explained in Section 6.5. Because of this, the capillary was preconditioned by pumping down and firing several times through the capillary. It is then removed from vacuum and disassembled so mass measurements can be taken before the actual tests. There was only a small observed change in diameter from this preconditioning, no effect due to this change was seen in the discharge itself.

One of the major difficulties with this design was sealing the cathode and ignition electrodes. Quite a large force had to be applied in order to do so. This however would cause the ignition electrode to crack. The ignition electrode was a wire EDM (Electric Discharged Machined) 1/16 *in* thin tungsten disc. It was made thin so as to fit within the ignitor housing and not create a large surface area for the discharge to ablate. Tungsten is a hard but brittle metal and at this thickness it can be broken by hand. Several ignition electrodes were broken, before the material had to be changed. Stainless steel held up much better structurally and was used for the second half of the testing. Little effect from this electrode switch was seen in the data.

### 5.5.2 Data

The effects of length and voltage on the current profile are shown in Figure 5.9. From these plots it is easy to see the, by now, classic response of increasing current for both increasing voltage and decreasing length. It is worthwhile noting the low deviation in the current profiles. The 3-EIS discharges were highly repeatable and consistent.

The performance measurements also show much less scatter. The trends have become much more apparent. If one looks at the performance plots in section 5.3, these same trends are also present, but much less believable, due to the data's sporadic nature (caused by random electrode mass loss). The impulse measurements in Figure 5.10 plot (a) shown that the total impulse is very consistent for all lengths, with

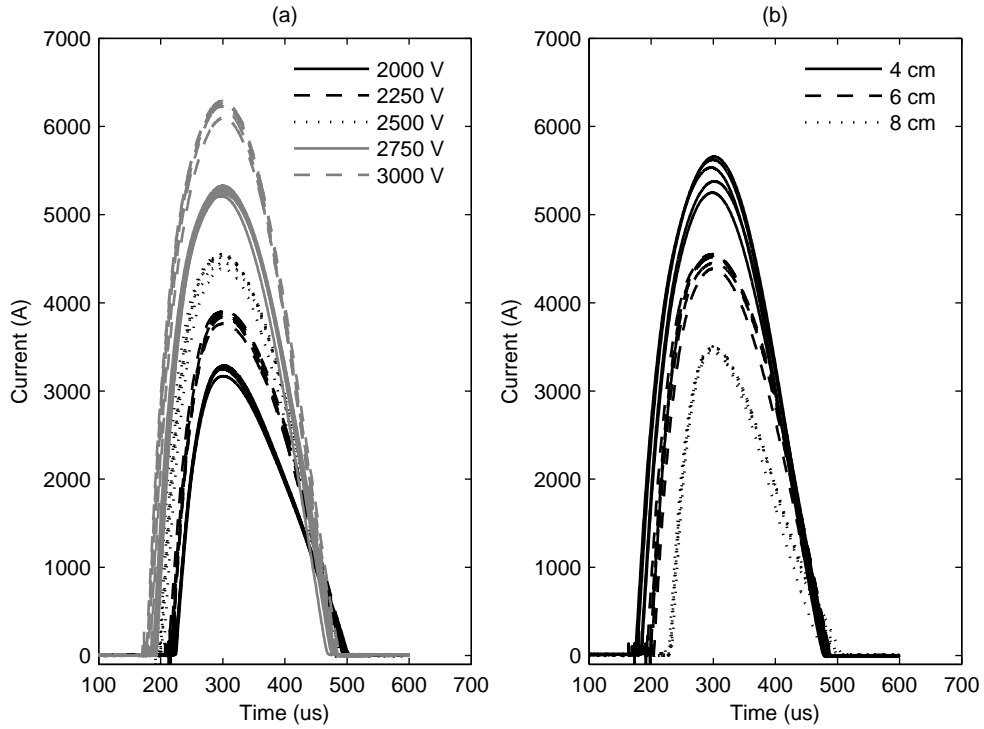


Figure 5.9: (a) 6 cm discharge currents at various capacitor voltage and (b) 2500 V discharge currents for varying lengths capillaries using 3EIS

slightly higher values for longer capillaries. The specific impulses shown in Plot (b) clearly exhibit a negative trend for all lengths as a function of voltage, with 8 cm having the highest  $I_{sp}$  in the 600's and 4 cm having the lowest, ranging from 550 s down to 350 s. It is interesting to note that the negative slope of these approximately linear lines decreases as the length increases. It is even possible that a 10 cm capillary would have positive returns for increasing discharge energy. This same trend appears in the efficiency as well. A 4 cm capillary decreases in efficiency with more power however an 8 cm capillary increases. It seems that both of the trends are most likely due to electrode erosion. And while less sporadic, electrode erosion is still a major issue and discussed in detail in Section 6.2.

## 5.6 Electron Number Density

Hydrogen Balmer alpha lines were used to determine  $n_e$  as discussed in Section 3.5.2. The optical setup used to capture these spectral lines is described in Section 3.5. The experimental data of emission intensity versus wavelength was compared to a least squares fit of a Lorentzian, as shown in Figure 5.11.

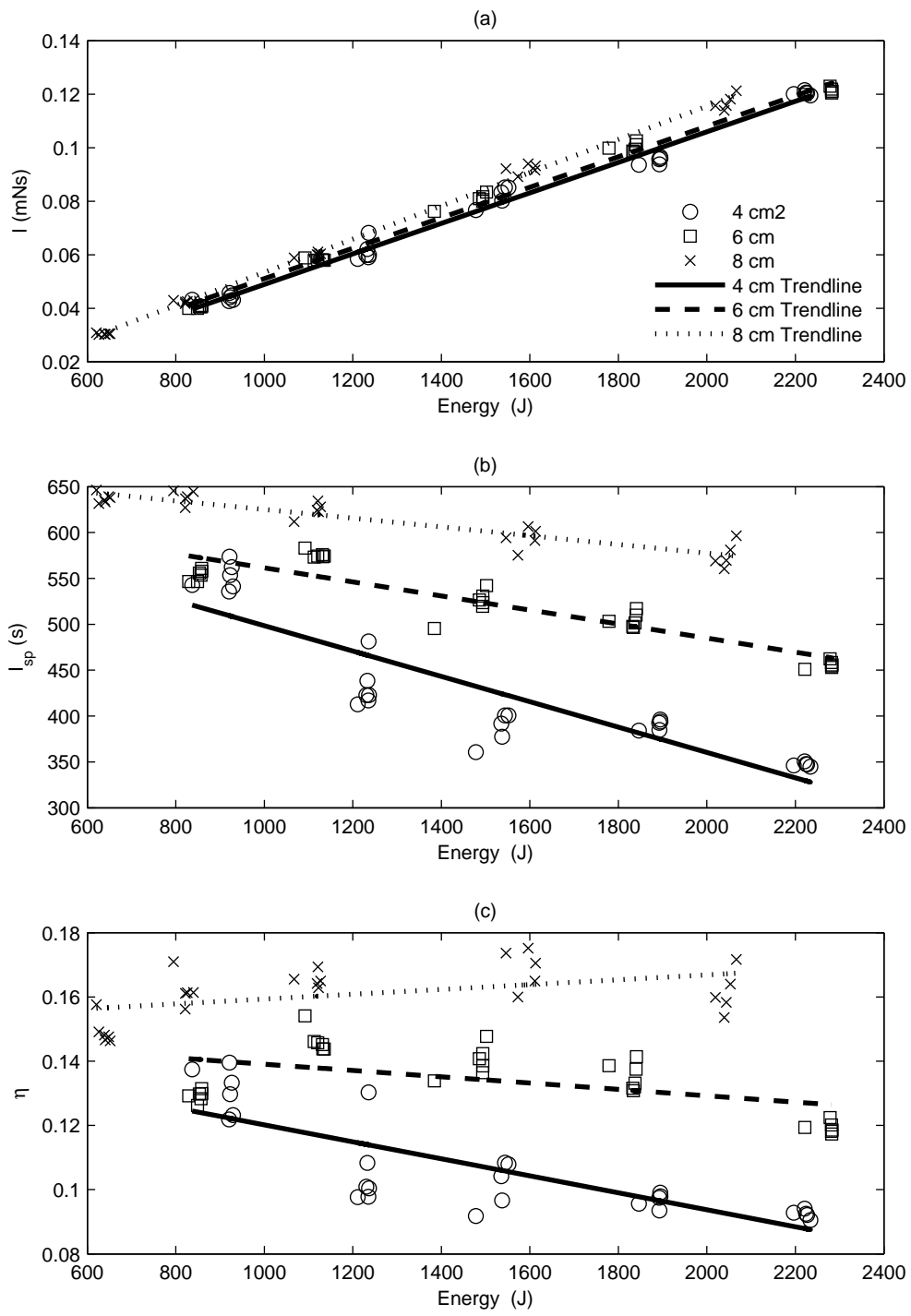


Figure 5.10: (a) Impulse, (b) Specific Impulse, and (c) Propulsion Efficiency as a function of input energy for 4, 6, 8 cm Capillaries using Coax Ignitor

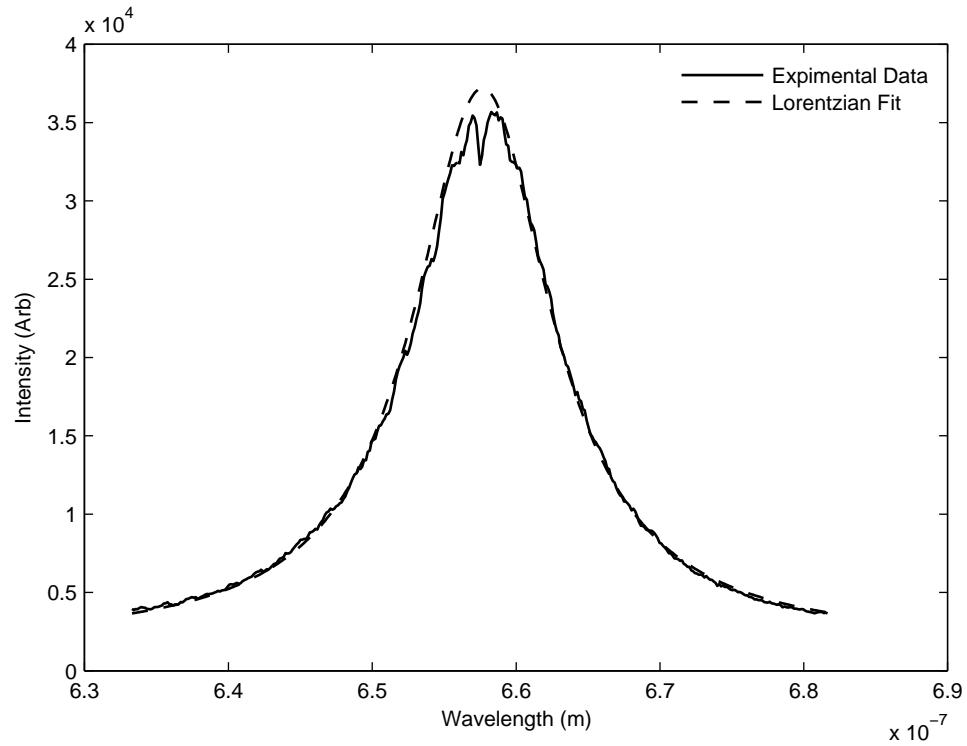


Figure 5.11: Lorentzian fit of experimental data using least squares fitting

The fit shows the spectrum from a 6 *cm* capillary operated at 2500 *V*. Both the experimental results and the fitted profile are in very close agreement except at the line center. Here, a central dip is observed experimentally. While there are many causes of central dips in spectral lines, this one was most likely due to self-absorption. The rest of the profile agrees very well, it can be assumed that the fitted Lorentzian is representative of the spectral shape with no self-absorption. Based on this Lorentzian profile, the FWHM can be found and correlated to  $n_e$ , as discussed in section 3.5.2.

The number density is highly independent of temperature for the range of temperatures typical of a capillary discharge. It is only slightly affected by the coefficient  $\alpha_{1/2}$  shown in equation 3.21. Figure 5.12 plots the number density as a function of spectral number. Each spectrum is only 16  $\mu$ s apart using the kinetics mode operation. The plot shows  $n_e$  for a number of different temperature ranging from 1 to 2 eV. Over this range the  $n_e$  has a percent deviation of less than 1%.

Figure 5.12 also compares the experimental results with the 1D computational model. The model outputs the electron number density at several locations along the capillary. The Capillary middle is half way between the anode and cathode. The Capillary end is the end of the capillary material, where it

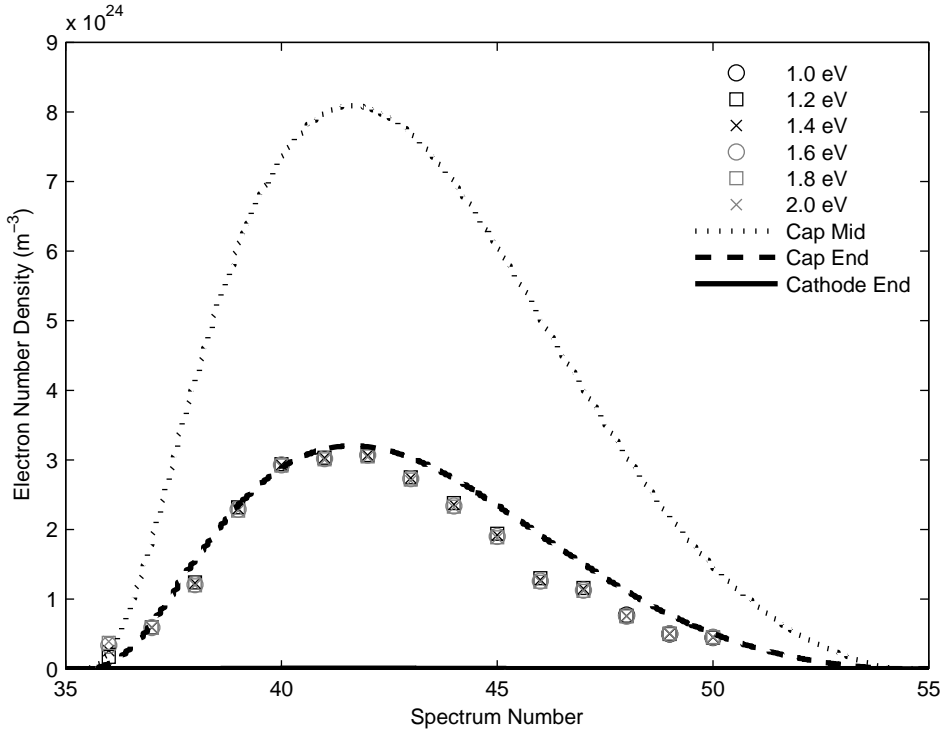


Figure 5.12: Comparison of  $N_e$  between experimental results and 1D model

meets the cathode. The cathode end is the exit plane of the device and the location where the optical measurements are taken. The Cathode, as discussed in section 2.1.4, is 1/4 *in* long and has a half angle of 10°. It is because of this geometry that the model predicts an expansion of the exit plume and a cooling of the plasma. A slightly cooler plasma has significantly lower electron number densities as represented by the black line. In the 6 *cm* case shown in the figure, these values are 2 orders of magnitude lower at the end of the capillary.

Even though the electron number densities are measured at the end of the cathode, they match the number density predicted at the end of the capillary by the 1D code, within 15%. A likely explanation for this is that at the plume is not expanding uniformly as predicted by the code. The code is based on a 1D model and does not take into account the axial profile of the discharge. Therefore, the number densities are an average across the cross section. It is very possible that the core of the discharge is significantly hotter and the edges much cooler. To complicate matters farther, when the the plasma is expanded through the cathode, the edges may cool rapidly, while the core remain generally unaffected. Because the core remains hot it still radiate brightly while the surrounding cooler plasma radiates little. CFD calculation for a hot gas at the temperatures and pressure predicted in the capillary show that this expansions should

be fairly uniform. However the discharge is a plasma and has many other processes occurring. The most relevant of which is the de-excitation and recombination. Though 3-body collision the ionization causes, can be recovered. While the thermal energy is 1 to 2 eV the ionization energy is 12 eV. If this energy is recovered it would be converted into thermal energy and could greatly effect the temperature of the expanding plasma.

The electron number density was also be examined over a range of voltages and length. Voltage tests were conducted with a 6 cm capillary. As shown in Figure 5.13 the electron number density increases as a voltage increase. This corresponds well with the thrust data measured in Section 5.5. The length tests were conducted by varying the capillary length for a 2500 V discharge. The electron number density decreases with longer capillaries as shown in Figure 5.14. This occurred because of two reasons. As seen with the thruster performance data, for a given voltage potential, longer capillaries have larger resistances and less power is dissipated into the discharge. So even though the voltage is constant, less energy is used, therefore the temperature is lower and the ionization is less. It is generally understood that longer capillaries have higher densities, but lower temperature.

In Figure 1.20 discharges at 2750 and 3000 V showed significantly higher number densities than would be expected. This large jump is also seem for the 4 cm capillaries shown in Figure 1.20. This measurements correspond to  $n_e$  values larger than  $5 \times 10^{24} \text{ m}^{-3}$ . This discrepancy was also observed by Ashkenazy *et al*[7] in there studies of capillary discharges at densities above  $5 \times 10^{24} \text{ m}^{-3}$ . The reason for this can be see in figure 5.15 which shown the Lorentzian fit for a 6 cm 2750 V test. Here the central dip do to self absorption is much larger and starts to affect the fit. While this dip can be seen in main of the spectrum, if it is small, it introduced little error into the fit and the FWHM can be determined with confidence. Here however it is easy to image a fit that has a higher peak. A high peak with a similar base would be less broadening curve with a smaller FWHM and therefore a lower electron number density. Several attempts were made to modify the least squares fitting routine to fit the curve better. Trying to fit a Lortenzian using just the wings required high fidelity data. A secondary absorption loretnzian was superimposed to account for the central dip. This however did not yield a single solution.

A final attempt was made to resolve  $n_e$  measurements above  $5 \times 10^{24} \text{ m}^{-3}$  using the shift of the hydrogen Balmer  $\alpha$  line. As mentioned in Section 1.20, Flih *et al*[33] looked at the correlation between  $H_\alpha$  broadening and shifts. He showed there exists a fairly large, and linear, shift in hydrogen broadened line. His work predicted that for a number density of  $5 \times 10^{24} \text{ m}^{-3}$  there is a FWHM on the order of 10 to 15 nm and a shift of 2 to 3 nm. The FWHM data collided for this capillary discharge agrees very well

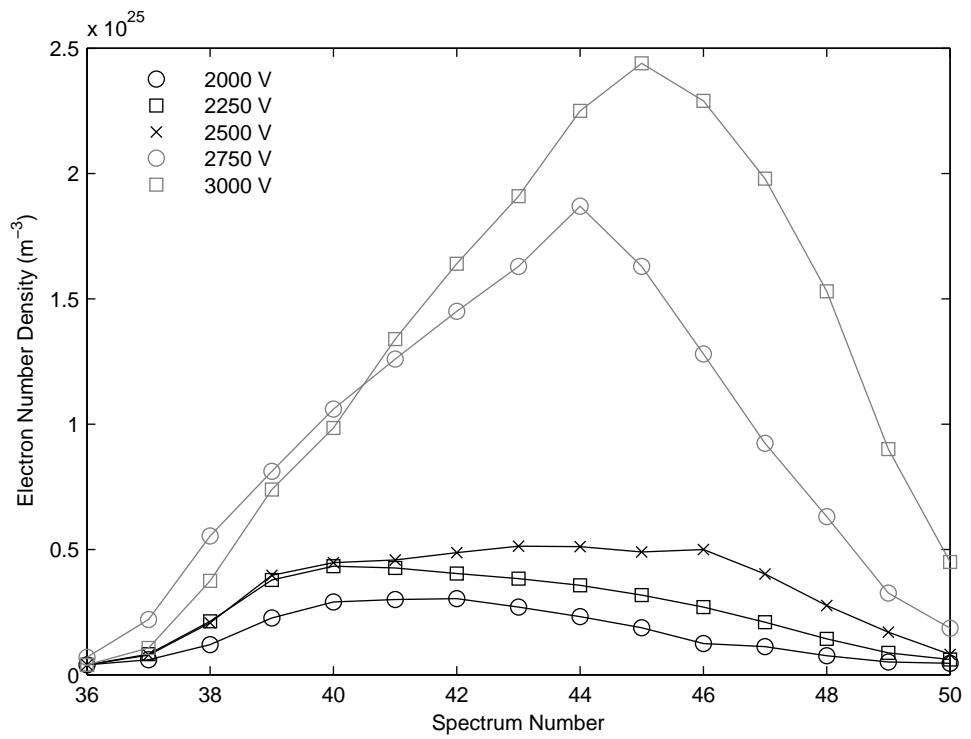


Figure 5.13:  $N_e$  for a 6 cm capillary at 2000, 2250, 2500, 2750, and 3000 V

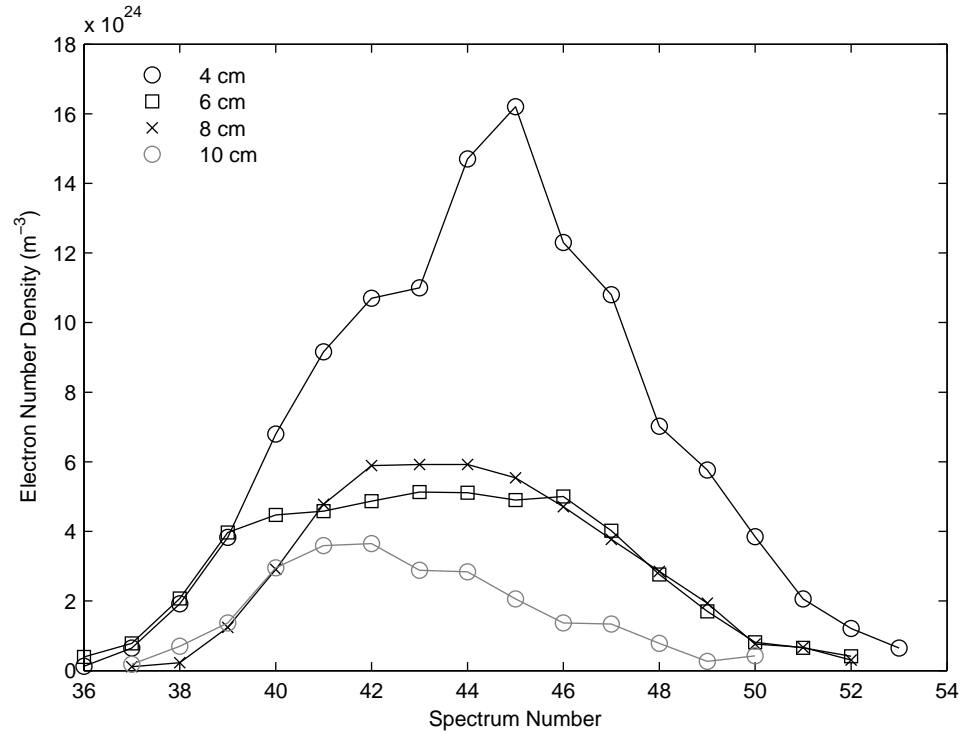


Figure 5.14:  $N_e$  for a 2500 V capillary at 4, 6, 8, and 10 cm lengths

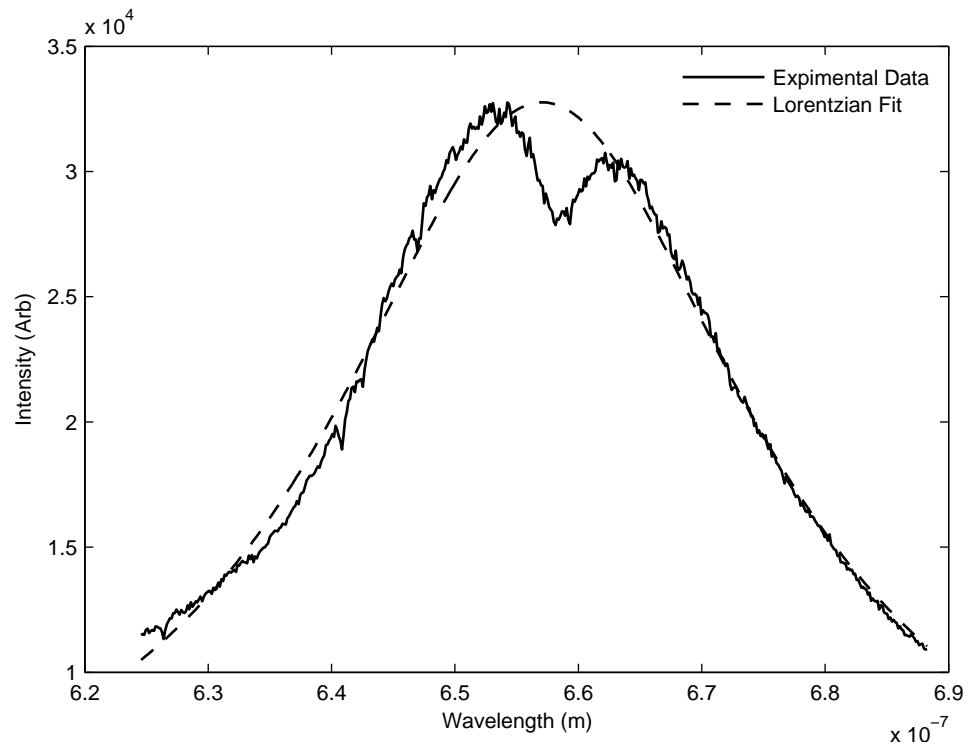


Figure 5.15:  $H_{\alpha}$  line with high self-absorption

as shown in Figure 5.16. However the results for the shifting of the centerline did not agree. Figure 5.16 (b) shows a plot of the centerline as found from the least squares fit Lorentzian profile. Shifts of 0.4 to 0.6 nm were observed. In addition it was seen the shorter capillaries had a blue shift while longer ones shifted red. The mechanism that caused this could not be identified and a shift method could not be used to measure the number density greater than  $5 \times 10^{24} m^{-3}$ .

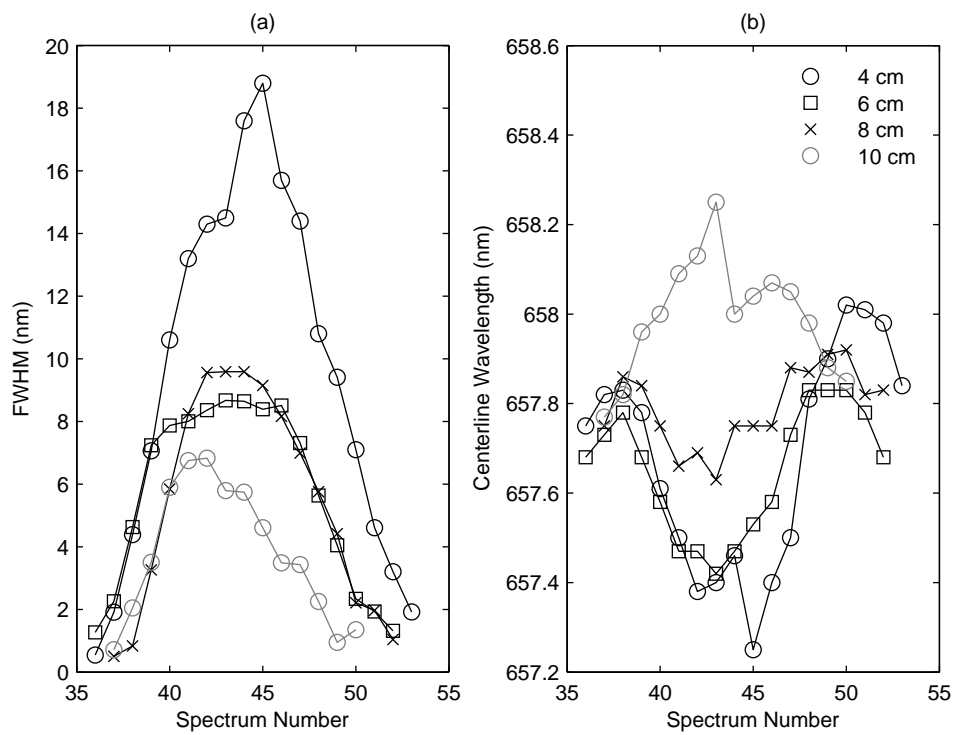


Figure 5.16: (a) FWHM and (b) centerline shifts as a function of time

# Chapter 6

## Discussion

Wire, Paschen, and three electrode ignition test for the capillary discharge have all be conducted. Through this process diagnostics have been refined and the capillary device improved. In this section these ignition methods will be compared. The work presented here discusses much more than just the ignition and will hopefully provide some greater understanding of capillary discharge and provide valuable information for future researchers in this field. Electrode erosion, material effects, external ablation, and background pressure effects will also be discussed.

### 6.1 Ignition Comparison

When comparing the different ignition techniques, the first parameter evaluated at was the current profiles shown in Figure 6.1. In most cases the profiles looked very similar except for some minor details. Surprisingly the wire ignition was not that much different than the other methods, despite the wire material added to the plasma. Capillaries ignited by wire explosions have slightly higher currents at all length and it was initially supposed that this was due to the additional material from the exploding wire. At 10 cm the wire ignition exhibited a much slower start and had a much more symmetric profile. This slower start is a trend for both the wire and Paschen breakdown ignition as a function of length, though much more pronounced with the wire. This has been estimated to be an affect of the background pressure rather than the ignition method itself. This is discussed further in Section 6.7.

The 3 electrode ignition system had higher peak currents than Paschen ignited capillaries, but lower than the wire ignition. It is reasonable to assume that this has something to due with the density of the igniting plasma. With the Paschen breakdown the column of low pressure gas within the capillary breaks down, ionizing the internal capillary volume. This might create a plasma that is initially higher in density and lower in temperature, and therefore would have a higher resistance. In the case of the 3EIS there is not much material and the plasma starts a very low density allowing it to get hotter and less resistive. The fact that the wire ignition had the highest peak current could suggest that the exploding wire created a

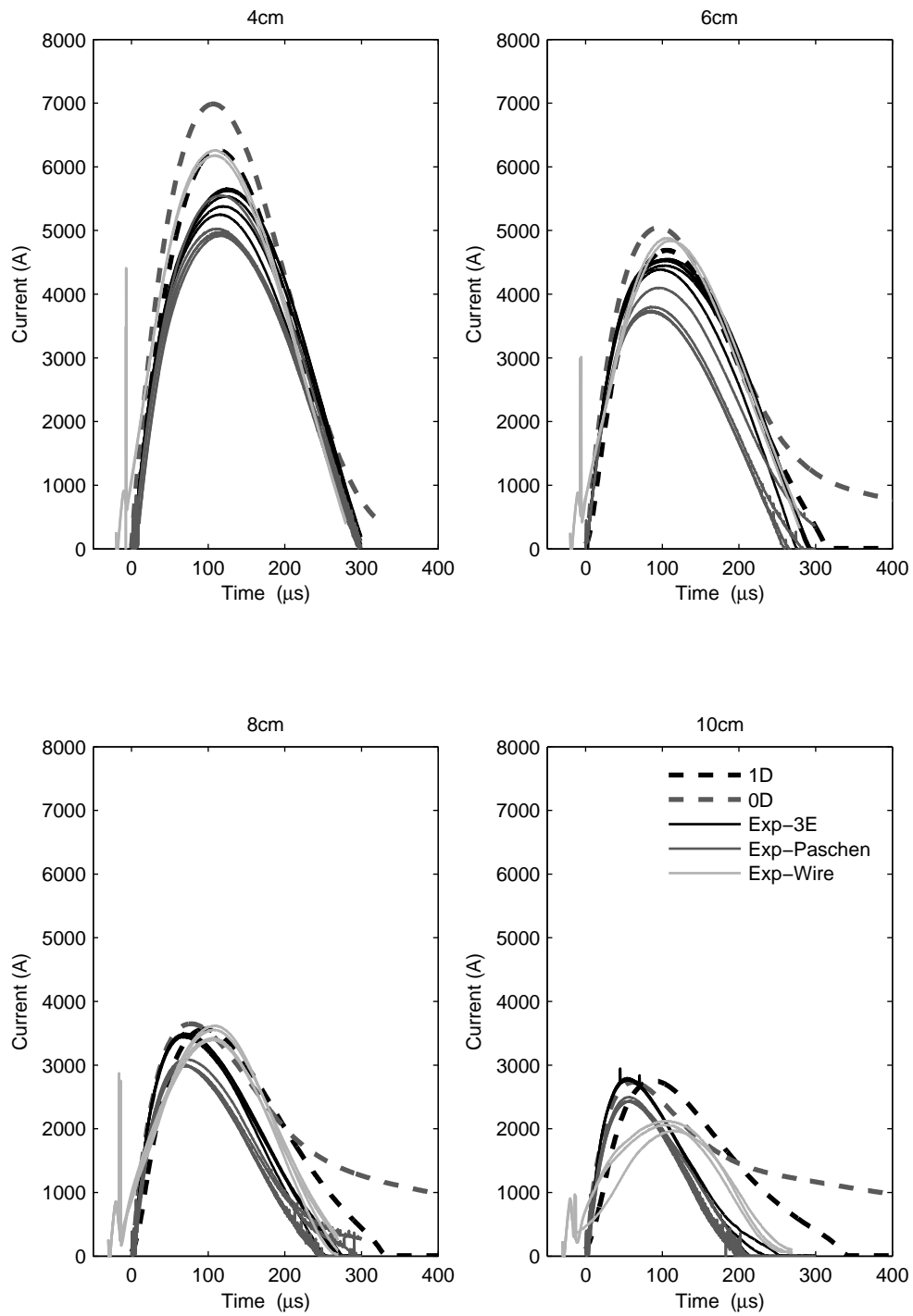


Figure 6.1: Comparison of discharge currents for 0D, 1D, and 3 ignition methods for 4, 6, 8, and 10 cm capillaries at 2500 V

hot but not necessarily dense plasma. This also supports the fact that all discharges had the same basic profile as stated earlier. If the wire was adding its own mass, equal to that of the capillary ablation mass, then it would be expected that the discharge would be very different. In section 1.7.1, wire explosion was discussed in greater detail and the chaotic nature of this process was examined. It is very possible that when the wire explodes it creates only small pocket of hot plasma and the majority of the material is ejected from the capillary without fully melting, vaporizing, and dissociating. This could also support why a dual mode of operation was never seen in other ignition tests. If the high current mode has a very high temperature, low resistance, plasma as an initially conductive path, this could only happen for wire explosion and more likely for shorter capillary lengths.

Both models compared very well to experiments for shorter capillary lengths. The 0D model exhibited a long tail extinction. The reason for the tail was never determined and could not be eliminated from the results. The 1D model describes the experiment a little more accurately. It showed very good agreement with shorter capillaries. Experimentally current pulse width got shorter as the capillary got longer, going from about  $300 \mu s$  for  $4 \text{ cm}$  to  $200 \mu s$  for  $10 \text{ cm}$ . The model however predicted the opposite trend, with discharge times going from  $300$  to  $340 \mu s$  for  $4$  and  $10 \text{ cm}$ , respectively.

The model was then compared with thruster performance. The plots from the model shown in Figure 6.2 only take into account the mass loss of the capillary and does not take into account any mass loss of the electrodes. The difference between including and not including the mass loss of the electrodes can give very different results in  $I_{sp}$  and efficiency. While ignoring electrode mass loss does give an accurate presentation of the performance of the device, it does allow for more consistent comparison with the model. From figure 5.6 and 5.10 we can see how  $I_{sp}$  and  $\eta$  decrease with energy. However if one neglects the mass loss from the electrode, these parameters trend upwards very similar to the model prediction.

The large discrepancy between the model and experiment for  $I_{sp}$  and  $\eta$  is most likely attributed to late time ablation which is not accounted for in the model. It has been shown that late time ablation can account for a large percentage of the total mass loss, on the order of  $1/3$  of the total mass loss[17]. This seems particularly true based on the information discussed in Section 1.4.1 about the ablation process. If a large about of the energy is not going to photo-ablation, it goes into heating the surface. Because heat conduction is so poor within the polyethylene capillary the surface remains hot well after the discharge has stop, causing mass to evaporated off.

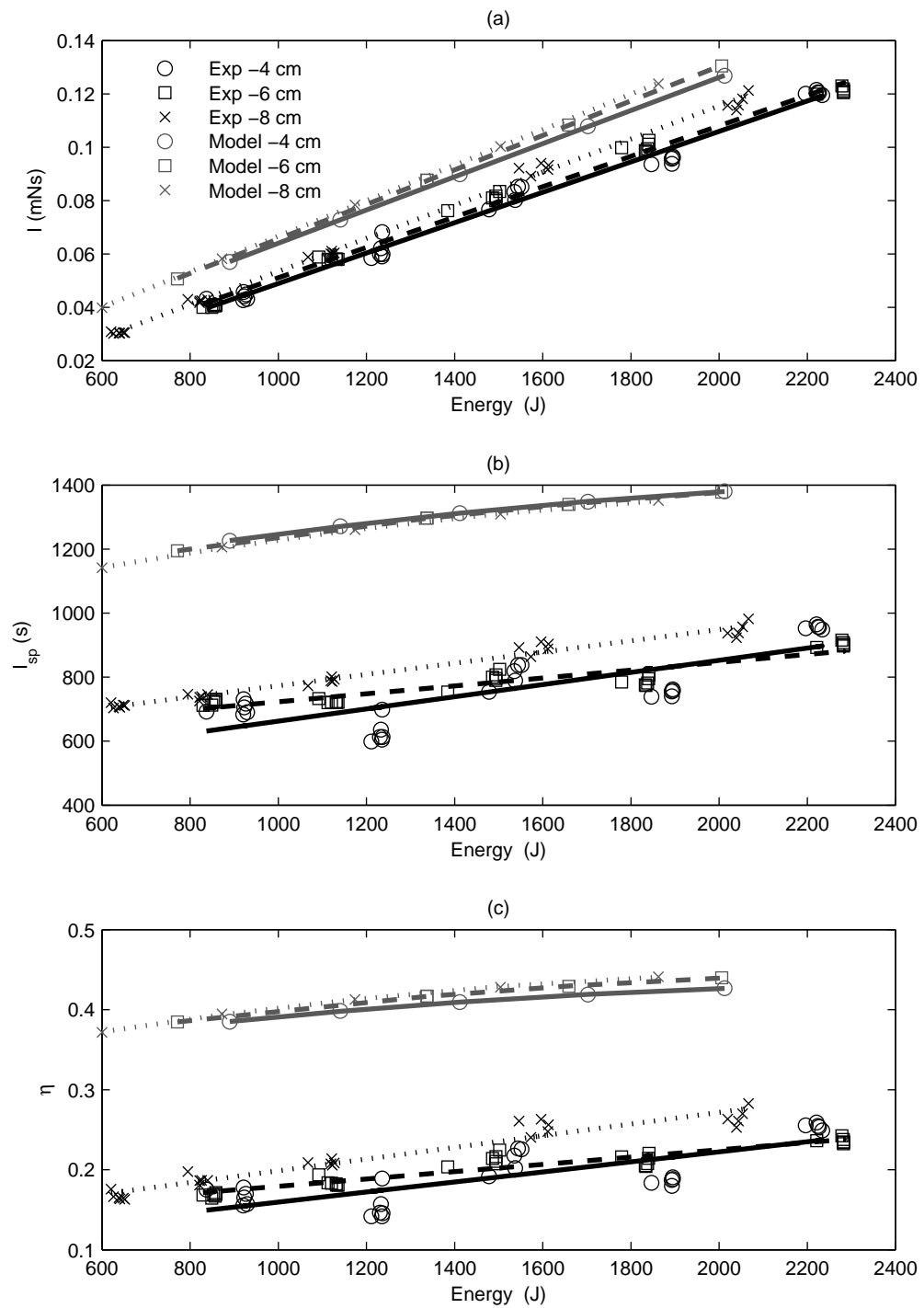


Figure 6.2: Comparison of (a) Impulse, (b)  $I_{sp}$ , and (c) efficiency for experimental and 1D model results

## 6.2 Electrode Erosion

Electrode erosion has been a large factor in this work. While the major goal was to investigate ignition, this could not be done without first looking at erosion pattern and trying to mitigate them. Major erosion problems were first noticed the minute mass measurements were taken to calculate  $I_{sp}$ 's and efficiencies. As mentioned in section 5.3, early tests showed that mass loss due to electrode erosion was significant; on order of, or significantly higher than, the mass loss of the tube itself.

To study these patterns early on, testing was done with stainless steel electrodes. While these were poor electrodes because they eroded so quickly, they did allow the observation of patterns in a relatively small amount of shots. It was noticed that the mass loss from electrodes became decreased as the device was fired more. It was also noticed that the exit orifice was expanding and eventually compromised the weld integrity causing the insert to come loose. A new housing and insert were created and this time the erosion pattern and rates were more closely monitored. Figure 6.3 shows the life of that cathode over a series of tests at 6cm of length at a capacitor voltage of 2500V. From these photos it can be seen how

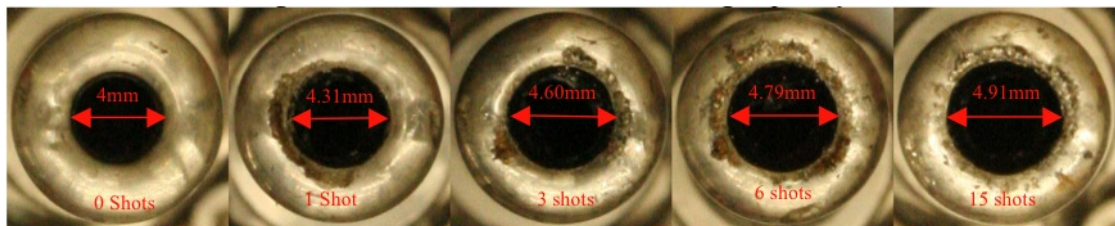


Figure 6.3: Photos of Anode Erosion

quickly the stainless steel erodes. This is consistent with what was seen in the mass loss test, in that the more consecutive firings that were performed the less mass loss occurred during each shot. Within 15 shots the exit diameter increased by 23%. Electrode erosion is common when dealing with high powered arcs. Usually, however, it is the anode that erodes more than the cathode, which was not observed in our case. Through setting up and testing the stainless steel anode again, it was possible to study this pattern with fewer shots because of the high erosion rate. Normally arc attachment, localized heating(anode or cathode spots), and sputtering cause the majority of erosion to electrodes, however, in this capillary setup there are other factors involved. Looking at the inner edge of the cathode at the exit plane, a curled jagged edge was observed, similar to a crested wave traveling outward from the center. It was also observed that the diameter at the exit plane was larger than that at the base of the insert, forming a conic shape. From

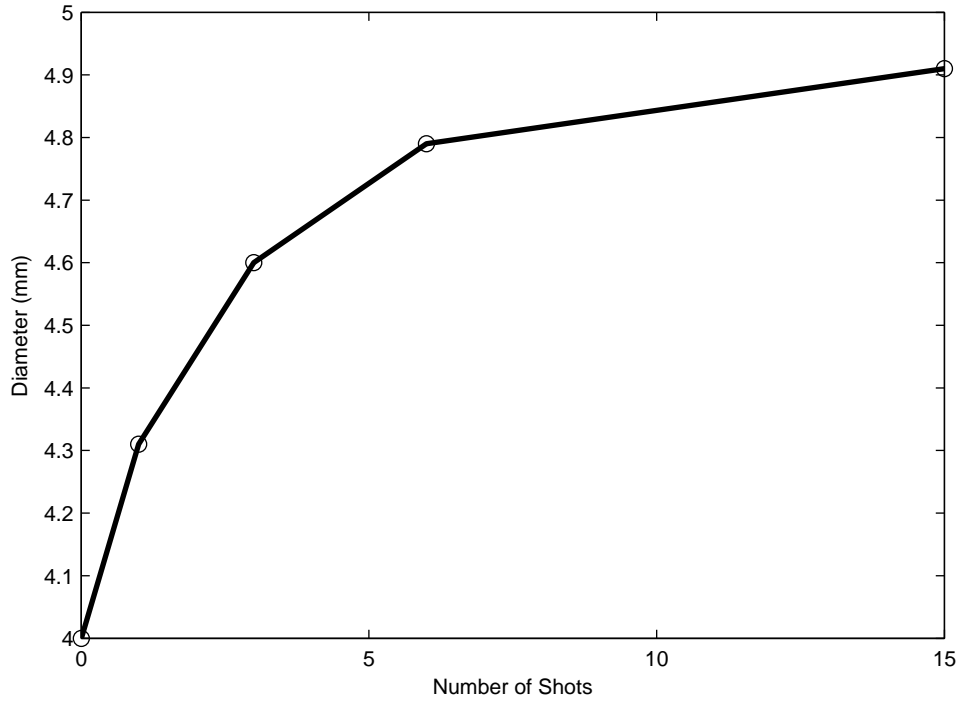


Figure 6.4: Plot of the anode erosion over 15 Firings

these two observations it was concluded that high cathode erosion was due to the high temperature, high pressure, gas exiting the device. This gas melted the stainless steel at the surface and forced it out ward. If one looks at the plot of diameter as a function time, as in Figure 6.4, one can notice that the expansion rate decrease with time. Given our aforementioned conclusion, this makes sense in that the erosion pattern naturally develops into a nozzle causing the gas to expand and cool through it. From Figure 6.4 it can be estimated that diameter change could asymptote somewhere around 5mm. This could be were the flow is cooled enough by expansion so as to not to erode the cathode tip.

As described in Section 2.1.2, tungsten electrodes were used in subsequent tests after this initial pattern was recognized. This material held up better and did not erode as quickly but the same pattern was still observed. As can be seen from the Paschen ignition data not only was the mass loss high but it was also sporadic. Figure 6.5 the percent mass loss of both the electrodes and the capillary tube for all the Paschen ignition tests. As seen in plot (a) the shorter capillaries seem to suffer much greater electrode erosion than the longer capillaries at a given energy. This was expected because of a higher ratio of capillary surface area to electrode surface area for longer capillaries. While this must be a factor it is mostly likely not the dominate cause of such high erosion rates in shorter capillaries. By plotting

mass loss as a function of peak current, as shown in Plot (b), it is possible to see a dependence free of capillary length. It becomes clear that electrode erosion is heavily dependent on peak current. Therefore, the major reason 10 cm capillaries show less electrode mass loss is because they experience much lower currents. And as it turns out the mass loss of the capillary stays fairly independent of length as shown in

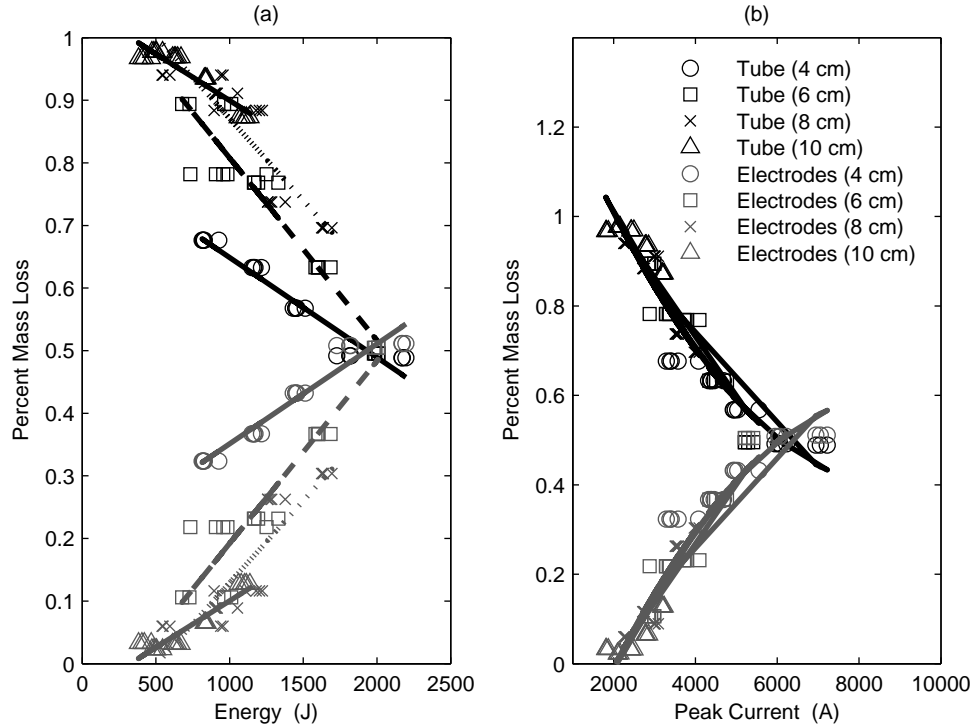


Figure 6.5: Plots of the percent mass loss for Paschen tests as a function of (a) energy and (b) current

Figure 6.6, plot (a). This plot also shown how greatly the electrodes erode compared to the ablation of the capillary for the three electrode ignitions system. Investigating the mass loss further indicated that while both anode and cathode increase in erosion as a function of energy it is the anode erosion that increases at a much faster rate, as shown in plot (b) of Figure 6.6.

### 6.3 Dual Mode Operation

The results show in Figure 5.4 in Section 5.2 show a clear dual mode of operation, the root cause of which was never discovered. The high current operation mode was only seen under the test conditions described

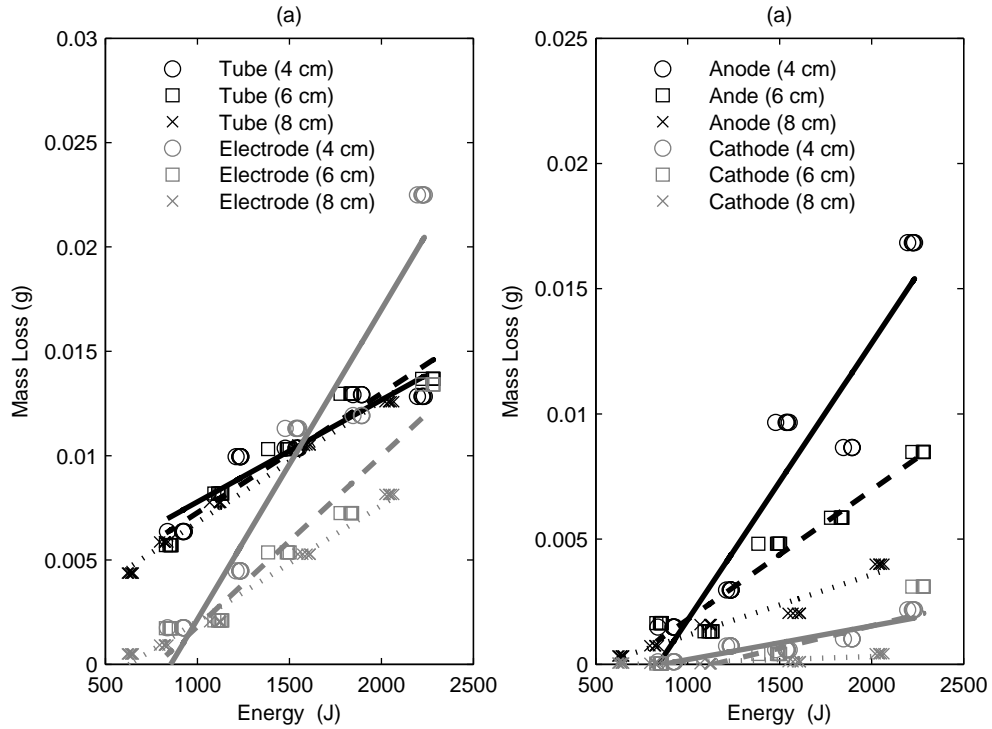


Figure 6.6: (a)Percent mass losses and (b) mass loss in

for atmospheric wire ignition. During all of the Paschen, PPT, and 3-electrode ignition no second current mode was ever witnessed.

One of the theories to why this occurs is based on the initial plasma conditions. It is proposed that due to the chaotic nature of an exploding wire it is possible that the initial condition of the capillary are different. As shown in Figure 1.7, the wire does not instantly form a plasma inside the capillary. The wire heats and breaks apart in segments before fully vaporizing. If the wire was to break a one end first, as opposed to the other it may cause the capillary to start differently. Or perhaps, In the case of the high current mode the wire did break down much more evenly, filling the capillary with an already highly ionized medium so start conducting through. This would allow for a higher  $\frac{di}{dt}$  because a strong conduction path in the capillary is already established. As opposed to the instance were the wire breaks down in one location first and the discharge therefore need to build a strong conductive path using ablated material from the wall. This argument could also explain the frequency at which the high current mode occurs. For a long capillary it would be hard to create this instant conductive plasma column uniformly over such a large distance. However in short capillary it become more likely as the segment of wire that needs to evenly explode becomes shorter.

## 6.4 Ablation Effects

As mentioned in section 1.4.1 the ablation process is very complicated. Radiation can be absorbed at the surface for penetrate into the depth of the capillary wall. These processes become even more complicated when electrode erosion is considered. Cathode and anode spots are caused by the glow-to-arc transition that occurs there[12]. The electric field near the anode and cathode can be 100 to 1000 times higher than the rest of the plasma column, causing small defects in the electrode surface to explode and metallic particle so leave the surface at very high velocities. These hot fast moving particles travel axially and imbed themselves into the capillary wall. This effect is well documented by Kukhlevsky et al[60]. In their capillary discharge experiment, similar to the one presented in this work, they showed that this particle could penetrate up to  $2.4\text{ mm}$  into the walls. The penetration path would close and the hot particle would vaporize the surrounding material causing a bubble to form. These bubbles were estimated to reach a few tens of atmosphere before bursting. Kukhlevsky et al measures about  $40\text{ bubbles/mm}^3$  and showed that they added significant mass to the Palmas column. This phenomenon was also seen in the tests conducted here. Simple examination of the white polyethylene tubes showed spots in the capillary wall. Some of these spots were dark, some were light, and other were metallic in appearance. These spots were much higher in concentration near the anode. While it is not clear whether these spots formed bubble that exploded into the capillary, it seems clear that the electrode erosion can effect the ablation process.

While collecting data sets using the tungsten cathode design, tubes would be critically damaged after only a couple of firings. This seemed odd as the amount of material ablated from each shot is not sufficient to wear though the tube nor is 5 or 10 shots. However, tube failures have occurred in just 4 shots. When the tube fails, it seems to collapse inward. Because the smoothness of this bending of the tube wall it was originally believed that this was caused by heating of the cathode and housing causing the plastic material to melt or soft and be deformed. There was also a considerable amount of soot on the out side of the tube as there has been seen throughout the history of our capillary testing. It was always assumed that this soot was gas that slipped between the cathode and the housing upon exiting the capillary. Because the new design incorporated a “lip” type seal on the cathode and a swage seal the anode, it became evident that the soot from the outside of the tube was not merely blow by gas from the main discharge. Instead this soot came from the ablation of the outside of the tube. This outside ablation causes a pressure build-up between the housing and the tube and because of the new sealed design, it would eventually cause the tube to fail inward, collapsing in upon itself.

In Figure 6.7 are pictures of highly outside ablated tubes. Both these tubes were fired at 2500V, 5 times. The lip seal has been cut off as shown by the rough surface on the right side. This unfortunately is necessary to extract the tube from the housing after the swage seal has been placed on the anode (left) end. In the case of the first picture the tube failed under a full collapse. The lip seal at the cathode ripped and caused more damage, and mass loss, to the cathode. In addition a hole was made close to the anode and the arc attached to the inner housing instead of the cathode. The second picture shows a tube that collapses but did not fail completely and split open.



Figure 6.7: Photo of Capillary Failure due to External Ablation

Evidence of a large amount of energy leaving the capillary is also corroborated by the heating of the stainless steel housing. On average test firing the stainless steel housing increased in temperature an average of  $10^{\circ}\text{C}$ . This temperature change is measured by placing a small  $T/C$  on the cathode cap. The temperature spikes high during (immediately following) the discharge but fell just as rapidly back to near the original temperature. It is unclear whether this is due to electrical noise or an actual thermal phenomena. However after the original temperature spike, the temperature would slowly increase to a maximum value and then decrease very slowly. This was primarily the housing coming to a uniform temperature as the thermal load diffused through the housing. For stainless steel the heat capacity is  $0.5 \text{ J/g}^{\circ}\text{C}$ , therefore it would take  $400 \text{ J}$  to raise the  $80 \text{ g}$  housing  $10^{\circ}\text{C}$ . Considering that the discharges used  $400$  to  $1600 \text{ J}$  of energy, this is a large fraction of the total energy that is deposited into the thruster that is not being used to ablate or heat the plasma but instead is being wasted.

## 6.5 Initial Discharge

One phenomenon that was observed during the Paschen ignition tests, when more than one firing was taken on a tube, was that the first discharge was always different than subsequent ones. A good example of this is shown in Figure 6.8, in which the current profile is plotted for a set of Paschen breakdown test. Here 5 shots were taken on the same tube. The first discharge had noticeably higher currents and longer

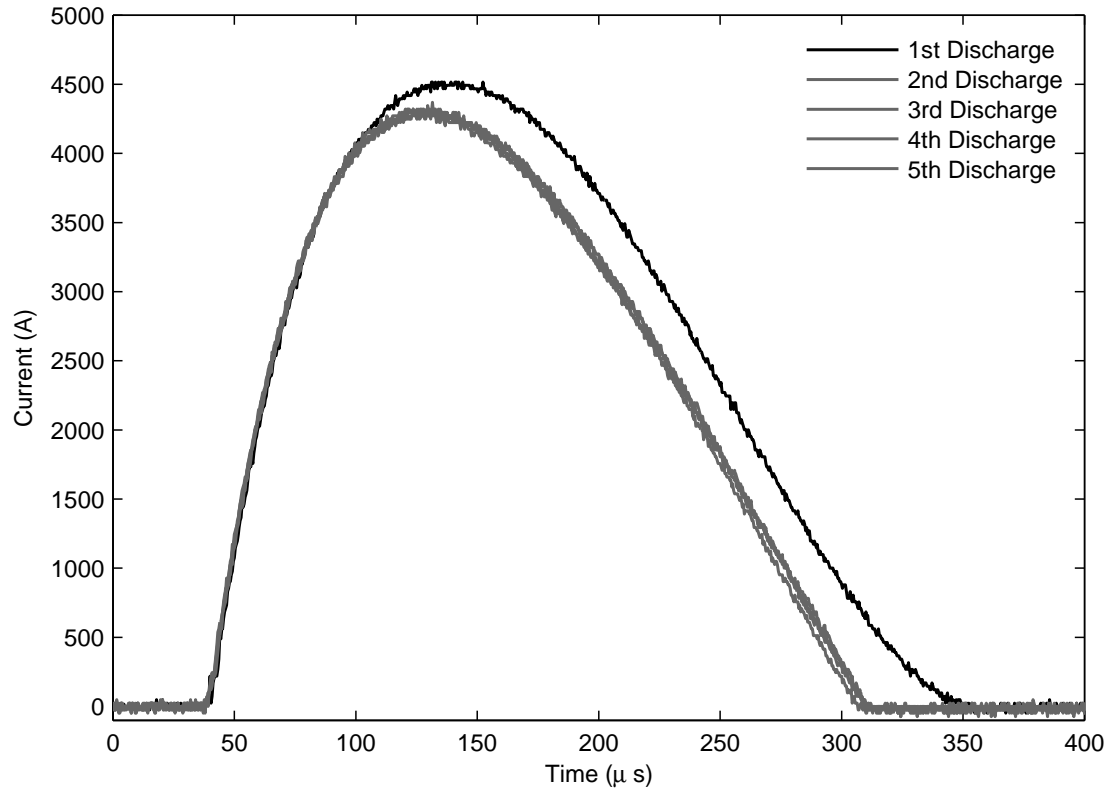


Figure 6.8: Five consecutive fires on a 6 cm capillary at 2500 V

discharge times. This effect is most likely due to the optical properties changing after the discharge. After the first discharge occurs the material surface is significantly different. It is not as smooth, roughened from the boiling and evaporation that occurs during the ablation process. There is also soot that coats the surface from previous discharges. While this effect was also seen using black capillaries, it was not nearly as pronounced. This initial discharge effect can help explain some of the sporadic data from the Paschen tests; especially in the cases when one data point is slightly off from the rest of the group. This

problem was remedied in the 3EIS tests by not only using black polyethylene, but by preconditioning the capillaries as discussed in Section 5.5

## 6.6 Material factors

Material factors played a larger roll than originally thought in capillary discharges. Not only in the capillary material but also the material of the housing that surrounds it. As discussed in Section 6.4 external capillary ablation became a large problem. The capillary design was changed in order to deal with this problem. The original inspiration to change the design to standard tubing was simply to allow for the ease of replacement. A full collapse and arcing to the housing wall causes pitting and damage that makes it exceedingly more difficult to load and extract capillary tubes without damaging them. The idea for the new housing was to use standard stainless steel pipe that could be replaced without having to re-machine the housing. When it was realized that the outside of the capillary was abating as well, this design allowed the use of different housing material to try and minimize or eliminate the secondary ablation.

A series of tests were conducted using either clear or black polyethylene tubes in stainless steel, clear polycarbonate, or alumina housings. The effect of these materials on the current profile are shown in figure 6.9. Notice that a clear polyethylene in stainless steel had a long tail while the same tube in alumina had the shortest tail. The black tubing showed small tails and were also effected slightly by the housing material. This suggests that radiation not only penetrates deep into the capillary wall but also passes through the capillary material interacting with the housing wall. The energy that reaches that far is either absorbed at the surface causing the exterior ablation, is absorbed within the housing, causing the temperature raise discussed in section 6.4, or as suggest here, reflects back into the plasma effect the discharge itself. It is interesting to note that neither material of the tube nor the housing affected current raise or peak power, but mostly effected the extinction of the device. Except for the case of the polycarbonate and clear polyethylene test which showed a slightly higher peak current.

## 6.7 Background Pressure Effects

As seen in Figure 6.1 and mentioned in Section 6.1 wire ignition test showed a much different initial current profile than the other ignition methods. This was particularly true for longer capillaries. It was

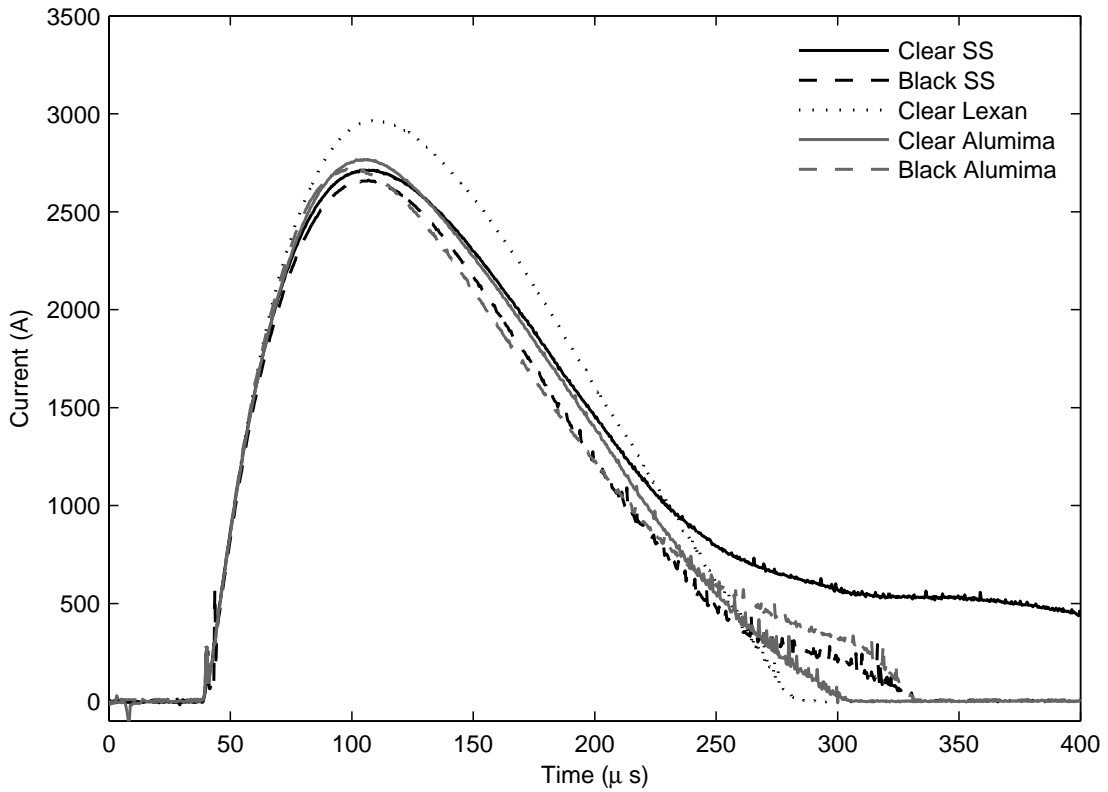


Figure 6.9: Current Traces for Various Capillary Materials

believed that part of this effect was due to the background pressure of the capillary. A small series of tests were conducted using the wire ignition method at a variety of different background pressures. The same housing and setup that was used in the Paschen ignition was also used for these tests. The thin ignition wire was simply attached between the cathode and anode. A 6 cm capillary at 2500 V was fired over 5 orders of magnitude of pressure. The pressure showed a clear effect on the discharge current as shown in Figure 6.10. The current profiles in this graph have all be normalized to the same peak value to more clearly illustrate the shifting profiles. The peak current was not effected outside the normal deviations seen between shots. The extinction, or second half of the current profile, was not effected either. What was effected was the  $\frac{di}{dt}$  after the wire explosion. For the atmospheric test, there is a clear change in curvature and the presents of an initial current pulse from the exploding wire. This transitions away with lower pressures until 0.4 mtorr, where the initial hump is no longer present and there is a consistent  $\frac{di}{dt}$  through the entire ignition process. It is difficult to determine weather the effect see is purely an affect of the pressure within or outside the capillary. It is very possible that within a certain pressure regime the

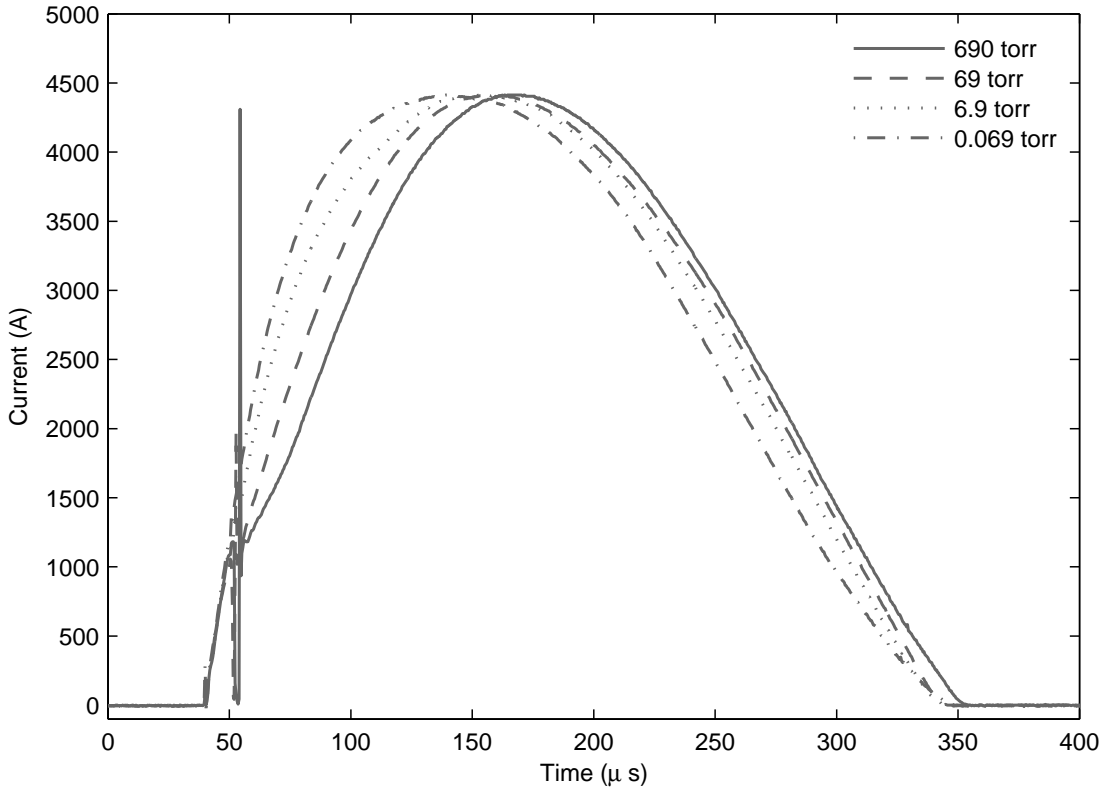


Figure 6.10: Current Traces for Various Background Pressures

wire acts like the dominate mechanism for that regime. For example it is possible at very low pressure the wire breaks creating a spark similar to the 3EIS and causing it to ignite by those mechanisms.

Because of the small but noticeable effect of pressure on the current profile, it would have been nice to investigate the effect of the pressure on thruster performance. However none of the other ignition techniques can be used over a wide range of pressures. The Paschen ignition only worked for a very specific pressure, around a couple of *torr*, and the 3EIS needs deep vacuum to ignition. The wire ignited capillary was put on the thrust stand to look at the impulse. No  $I_{sp}$  of  $\eta$  could be measured because of the inability to accurately account for the mass. The results of the stand deflection as a function of background pressure are shown in Figure ?? The results from this test show a surprising trend, however the reasons are inconclusive. It is believed that the performance differences of two or three times is based on a combination of plume expansion and amount of wire that is vaporized. At atmospheric pressures were there is a slower current raise it is possible that the wire material more fully breaks down and adds to the plasma composition. In the low temperature range, near the Paschen regime, the first little break

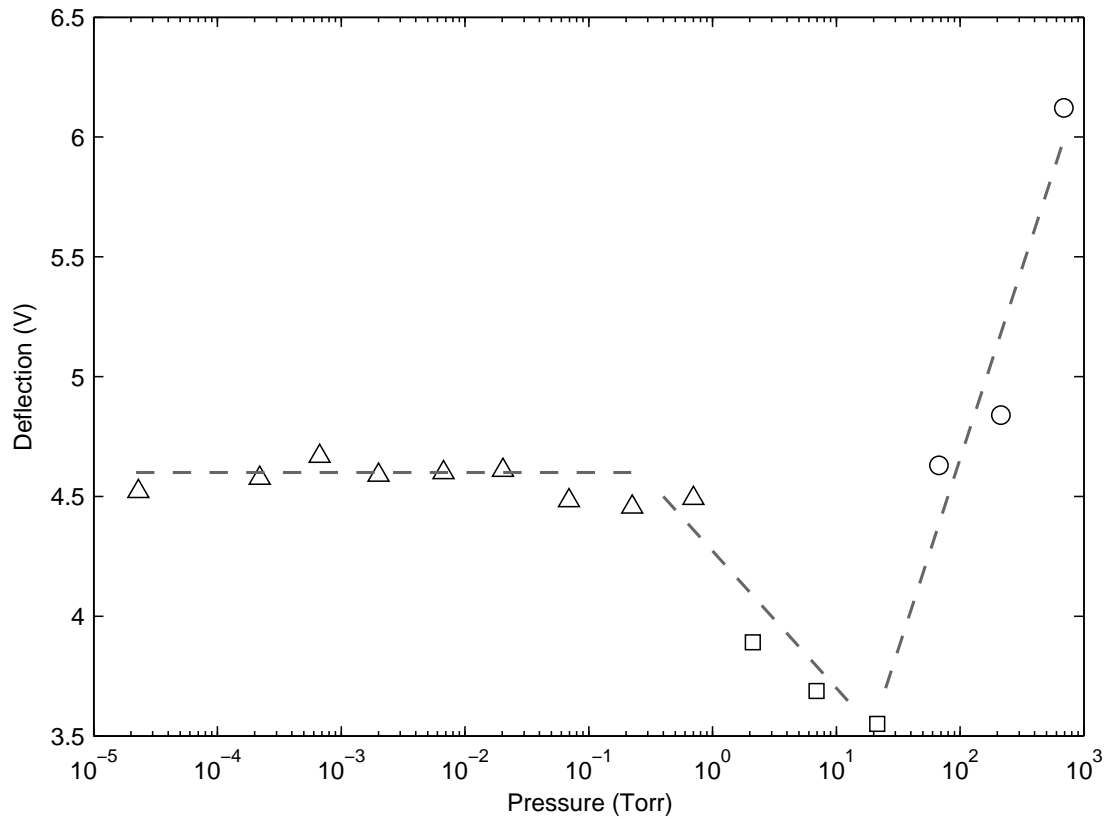


Figure 6.11: Thrust Stand Deflection vs. Background Pressure

in the wire could cause a paschen breakdown the therefore large sections of wire might be blown out the the capillary without fully vaporizing; adding little material to the discharge that would be heated and expelled, creating more thrust. This does not however explain way the impulse increases again at full vacuum conditions. If it became the case that the wire now more fully explodes, because the capillary became harder to ignite again, one would assume that this would show up in the current profile. However as shown earlier vacuum wire ignition appear to happen very quickly.

# Chapter 7

## Conclusions

Capillary discharge ignition methods were studied in depth. Their effect on the discharge properties and thruster performance were observed. Wire ignition method proved to be the most reliable over all lengths of capillaries. However, this method produced a dual mode of operation. This dual mode was caused by the chaotic nature of the wire exposing within the capillary, which caused the initial conditions to vary. Dual mode operation was not seen using other ignition methods.

Despite initial beliefs the type of ignition method did not play a large role in the discharge process. The methods tested here did not largely effect the overall discharge. While wire method did produce slightly higher currents, it is easily accredited to the additional mass of the wire and not a fundamental difference of operation. Even the larger  $\frac{dI}{dt}$  seen in longer capillaries ignited with wire are explained by the difference in background pressure. Once the main capillary discharge is started the arc is quickly controlled by the ablated material process, and the method that was used to achieve those conditions had little effects.

The Paschen ignition method also worked well over a full range of capillary lengths. Paschen ignition allowed for the first look at AFRL capillary thruster performance. The Paschen setup also allowed for a number of capillary issues to be addressed; from electrode erosion, to pressure sealing, to diagnostic development. In the end Paschen ignition did not lead to a space craft system, but it did have valuable merits. One of the more interesting phenomenon seen with Paschen testing were capillary re-strikes. The re-strike occurred after the capillary extinguished itself. As the remaining gas exhausted out of the capillary, the pressure would drop to a range where the capillary could discharge again based on the remaining charge on the capacitors. These were eliminated by only allowing the SCR switch to open for a short period of time. This was not advantageous for thrust measurements conducted here, but may be used in the future for repeat operation using a pulsed forming network. It could be conceived that the capillary would only need to be ignited once for a series of consecutive discharges.

Of the three ignition methods tested the three-electrode ignition system worked the most reliably and is the most suitable for space applications. This method showed no major performance differences over the other methods, but it did allow for ignition in full vacuum and for thruster measurements to be made.

The 3EI system did have trouble igniting the longer capillary lengths. However it is believed that with less wear on the cathode and more accurate machining of ignition electrodes and material that longer capillaries can be ignited.

The AFRL capillary used in this ignition study has not been fully optimized and is therefore not operating near its full potential. As mentioned earlier in this work similar capillary discharges have shown experimental efficiencies as high as 56% and a theoretical efficiency as high as 80%. The two major factors needed to increase the efficiency of the ARFL CD are a nozzle and better ablative materials. In order to study ignition a nozzle was not necessary. However to convert the high thermal energy of the capillary plasma into directed kinetic energy a nozzle is needed. It is also important to consider the length of the nozzle. The nozzle needs to allow for the plasma to de-ionized. This allows for a large amount of the energy used to ionize to be put back into the flow as thermal energy which is then expanded by the nozzle into directed energy ultimately producing higher thrust and efficiencies.

Another important contributor to the efficiency is the material. As was learned throughout these ignition tests the material plays a large role in the extension of the discharge. It was also observed that a significant amount of the radiation energy does not ablate the material but passes into or through the capillary material. This was evident by both the outside ablation and the heating of the housing. However, even when black polyethylene was used and outside ablation was eliminated, thrust efficiency did not improve. This suggests that radiation is still being absorbed through the capillary. While the radiation energy does not pass through the capillary it is not being absorbed near the surface. The energy is dissipated through the capillary volume which does not lead to efficient ablation. There is a large resource of material ablation paper that could add in the selection and testing of different material. Paper on PPTs and ablation controlled arc have already looked at different materials in their ablation process. While the devices are slight

Electrode erosion was also identified as a key contributor to performance differences between ignition methods. Because of the design differences between the various housings and the improvements made to electrode material and shape throughout the testing, the electrode wear changed throughout these. While in an ideal experimental setup only one variable is changing, it was difficult to do so for these tests. For future work it would be important to recall the improvements made to electrode in this study and interesting to test other materials like a carbon anode and a longer cathode with more surface area.

# Reference List

- [1] <http://en.wikipedia.org/wiki/interferometry>.
- [2] <http://en.wikipedia.org/wiki/lvdt>.
- [3] [http://en.wikipedia.org/wiki/paschen's\\_law](http://en.wikipedia.org/wiki/paschen's_law).
- [4] *NRL Plasma Formulary*. Naval Research Laboratory, Washington, DC, 1980.
- [5] B. W. Acon, C. Stehlé, H. Zhang, and A. Montaer. Stark-broadened hydrogen line profiles predicted by the model microfield method for calculating electron number density. *Spect. Acta B*, 56:527–539, 2001.
- [6] V. Akimov, I. Nagel, I. Ogleblina, N. Antropov, A. Pokryshkin, G. Popov, and A. Rudikov. Analysis of ppt potentialities in solving the satellite orbit control tasks. In *25th International Electric Propulsion Conference*, number 97, page 146, 1997.
- [7] J. Ashkenazy, R. Kipper, and M. Caner. Spectroscopic measurements of electron density of capillary plasma based on stark broadening of hydrogen lines. *Physics Review A*, 43(10):5568, 1991.
- [8] A. Ben-Kish, M. Shuker, R. A. Nemirovsky, A. Fisher, A. Ron, and J. L. Schwob. Plasma diagnostic in capillary discharge soft x-ray lasers. *Physics Review Letters*, 87(1), 2001.
- [9] J. J. Blandino, R. J. Cassady, and T. T. Peterson. Pulsed plasma thrusters for the new millennium interferometer (ds-3) mission. In *25th International Electric Propulsion Conference*, number 97-192, 1997.
- [10] St. Böddeker, S. Günter, A. Könies, L. Hitzschke, and H-J Kunze. *Physics Review E*, 47(2785), 1993.
- [11] H. C. Boersch, H. Hamisch, and W. Ehrlich. Surface discharge through an insulator in a vacuum. *Z. Angew. Phys.*, 15:518, 1963.
- [12] S. P. Bugaev, E. A. Litvinov, G. A. Mesjac, and D. I. Proskurovskij. *Usp. Fiz. Nauk.*, 115(101), 1975.
- [13] R. L. Burton. Performance of an sp-100/pulsed electrothermal thruster orbit transfer vehicle. In *Joint Propulsion Conference*, 87-2017. AIAA, 1987.
- [14] R. L. Burton. Design and predicted performance of a liquid hydrogen pet thruster. In AIAA, editor, *Joint Propulsion Conference*, 88-3107, 1988.
- [15] R. L. Burton, D. Fleischer, S. A. Goldstetn, D. A. Tidman, and N. K. Winsor. Investigation of a repetitive pulsed electrothermal thruster. *NASA*, (CR-179464), 1984.

- [16] R. L. Burton, S. A. Goldstetn, B. K. Hilko, D. A. Tidman, and N. K. Winsor. Investigation of a pulsed electrothermal thruster. *AIAA Paper*, (TD83-10), 1983.
- [17] R. L. Burton, S. A. Goldstetn, B. K. Hilko, D. A. Tidman, and N. K. Winsor. Experimental investigation of a pulsed electrothermal (pet) thruster. In *20th Joint Propulsion Conference*, 1984.
- [18] R. L. Burton, F. Rysanek, E. A. Antonsen, M. J. Wilson, and S.S. Bushman. Pulsed plasma thruster performance for microspacecraft propulsion. In M. Micci, editor, *Chap 13 AIAA Progress Series, Micropulsion for Small Spacecraft*. AIAA, 2000.
- [19] R.L. Burton, S.A. Goldstein, D.A. Tidman, and N.K. Winsor. Theory of the pulsed electrothermal thruster". *AIAA Paper*, 82(1952), 1982.
- [20] S. Büscher, Th. Wrubel, S. Ferri, and H-J Kunze. *J. Phys. B: At. Mol. Opt. Phys.*, 35(2889), 2002.
- [21] S.S. Bushman, R.L. Burton, and E.L. Antonsen. Arc measurements and performance characteristics of a coaxial pulsed plasma thruster. In *Joint Propulsion Conference*, 1998-3660. AIAA, 1998.
- [22] J.-L. Cambier and L. Pekker. 0-d model of a capillary discharge considering partially ionized plasma. Internal report, Air Force Research Lab, December 2005.
- [23] R. J. Cassady, N. J. Meckel, W. A. Hoskins, R. M. Myers, S. R. Oleson, and M. McGuire. Pulsed plasma thruster systems for spacecraft attitude control. In *10th AIAA/Utah State University Conference on Small Satellites*, September 1996.
- [24] W. G. Chace. *A Survey of Exploding Wire Progress, Explodding Wires Vol. 3*. Plenum, New York, 1964.
- [25] E.Y. Choueiri. A critical history of electric propulsion: The first 50 years (1906-1956). *Journal of Propulsion and Power*, 20(2):193, 2004.
- [26] J. Christensen, K. Freick, S. Hart, K. Norenberg, T. Haag, M. Patterson, V. Rawlin, J. Sovey, J. Anderson, R. Becker, and J. Polk. Design and fabrication of a 2.3 kw ion thruster for the deep space 1 mission. *AIAA Paper*, pages 87–3327, July 1998.
- [27] J. D. Cobine. *Gaseous Conductors*. Dover Publications Inc., 1941.
- [28] E. A. Cubbin, J. K. Ziemer, E.Y. Choueiri, and R.G. Jahn. *Review of Scientific Instruments*, 68, 1997.
- [29] B. D'Souza and A. Ketsdever. Investigation of time-dependent force on a nano-newton-second impulse balance. *Review of Scientific Instruments*, 76, 2005.
- [30] L. G. D'yachkov, G. A. Kobzev, and P. M. Pankrav. The hydrogen balmer spectrum in the near-threshold region: unified semiclassical calculations of line and continuum contributions. *J. Phys. B: At. Mol. Opt. Phys.*, 21, 1988.
- [31] A. Escarguel, B. Ferhat, A. Lesage, and J. Richou. *J. Quan. Spec. Rad. Trans*, 64(353), 2000.
- [32] A. Escarguel, E. Oks, J. Richou, and D. Volodko. *Physics Review E*, 62(2667), 2000.
- [33] S. A. Flih, E. Oks, and Y. Vitel. Comparison of the stark widths and shifts of the h-alpha line measured in a flash tube with theoretical results. *J. Phys. B: At. Mol. Opt. Phys.*, 36:283–296, 2003.
- [34] M. Gamero-Castana, V. Hruby, and M. Martinez-Sanchez. In *International Electric Propulsion Conference*, 2001.

[35] M. A. Gigosos, M. Á. González, and V. Carde noso. Computer simulated balmer-alpha, -beta, -gamma stark lines profiles for non-equalilibrium plasmas diagnostics. *Spect. Acta B*, 58:1489–1504, 2003.

[36] M. A. Gigosos and V. Carde noso. New plasma diagnostic tables of hydrogen stark broadening including ion dynamics. *J. Phys. B: At. Mol. Opt. Phys.*, 29:4795–4838, 1996.

[37] J. H. Gilland, M. L. R. Walker, and E. J. Pencil. In *Electrical Propulsion Conference*, number 2005-215, 2005.

[38] J. Gilligan and R. Mohanti. Time-dependent numerical simulation of ablation-controlled arcs. *Plasma Science*, 18(2):190–197, 1990.

[39] H. R. Griem. *Spectral Line Broadening by Plasma*. Academic, New York, 1974.

[40] H. R. Griem. *Principles of Plasma Spectroscopy*. Cambridge University Press, 1997.

[41] W. J. Guman and D. M. Nathanson. Pulsed plasma microthruster propulsion system for synchronous orbit satellite. *Journal of Spacecraft and Rockets*, 7(4):409, 1970.

[42] T. W. Haag. *Review of Scientific Instruments*, 68, 1997.

[43] R. A. Hill. Tables of electron density as a function of the half-width of stark-broadened hydrogen lines. *J. Quan. Spec. Rad. Trans*, 4:857–861, 1964.

[44] R. A. Hill. Fractional-intensity widths and stark-broadened formulas for the hydrogen balmer lines. *J. Quan. Spec. Rad. Trans*, 7:401–410, 1967.

[45] R. A. Hill, J. B. Gerardo, and P. C. Kepple. *Physics Review A*, 3(855), 1971.

[46] R. R. Hofer. Development and characterization of high-effeciency, high-specific impulse xenon hall thrusters. Cr-2004-213099, NASA, 2004.

[47] J. Holtsmark. Über die verbreiterung von spertrallinien. *Ann. der Physik*, 58, 1919.

[48] R.H. Huddlestone and S.I. Leonard. *Plasma Diagnostic Techniques*. Academic Press, 1965.

[49] I. Hussla and R. Viswanathan. *Surface Science Letters*, 145:488, 1984.

[50] A. Inam, X. D. Wu, T. Venkatesan, S. B. Ogale, C. C. Chang, and D. Dijkkamp. *Applied Physics Letters*, 51:1112, 1987.

[51] D. R. Inglis and E. Teller. Ionic depression of series limits in one elecrtron spectra. *Astrophys. J.*, 90:439–448, 1939.

[52] R.G. Jahn. *Physics of Electric Propulsion*. Dover Publications Inc., Mineola, NY.

[53] A. J. Jamison, A. Ketsdever, and E.P. Muntz. Gas dynamic calibration of a nano-newton thrust stand. *Review of Scientific Instruments*, 73(10), 2002.

[54] S. W. Janson. The on-orbit role of electric propulsion. *AIAA Paper*, (92-2220), 1993.

[55] W. A. Johnson and L. K. Warne. Electrophysics of micromechanical comb actuators. In *Micro-electromechanical Systems, Journal of*, volume 4, pages 49–59, 1995.

[56] D. Kaganovich, P.V. Sasorov, Y.Ehrlich, C. Cohen, and A. Zigler. Investigation of double capillary discharge scheme for production of wave guide in plasma. *Applied Physics Letters*, 71:2925, 1997.

- [57] P. Kepple and H. R. Griem. *Physics Review*, 173(317), 1968.
- [58] A. Ketsdever, R. Lee, and B. D'Souza. Thrust stand micro-mass balance for the direct measurement of specific impulse. *Journal of Propulsion and Power*, 24(6):1376–1381, 2007.
- [59] James M. Kohel, Lester K. Su, Noel T. Clemens, and Philip L. Varghese. Emission spectroscopic measurements and analysis of a pulsed plasma jet. *Transactions on Magnatism*, 35(1):201, 1999.
- [60] S. V. Kukhlevsky, J. Kaiser, L. Palladino, A. Reale, G. Tomassetti, F. Flora, G. Giordano, L. Konma, M. Liška, and O. Samek. Physical process in high-density ablation-controllld capillary plasmas. *Physics Letters A*, (335-341), 1999.
- [61] S. V. Kukhlevsky, J. Kaiser, O. Samek, M. Liška, and J. Erostýák. Stark spectroscopy measurements of electron density of ablative discharges in teflon- $(cf_2)_n$  capillaries. *J. Phys. D: Appl. Phys.*, 33:1090–1092, 2000.
- [62] J. Lake, G. Cavallaro, G. Spanjers, P. Adkison, and M. Dulligan. In *Joint Propulsion Conference*, number 2002-3821, 2002.
- [63] A. V. LaRocca. Pulsed plasma thruster system for attitude and station control of spacecraft. *First Western Space Congress*, pages 688–702, 1970.
- [64] S. Lazare and V. Granier. Ultraviolet laser photoablation of polymers: A review and recent results. *Laswe Chem*, 10:25–40, 1989.
- [65] R. W. Lee and A. Zigler. Multiple pulse laser excitation of capillary discharge. *Applied Physics Letters*, 53(21):2028–2029, 1998.
- [66] T. C. Lilly, A. P. Pancotti, A. D. Ketsdever, M. Young, and J. A. Duncan. Developement of a specific impulse for a pulsed capillary discharge. In *Joint Propulsion Conference*, 2008.
- [67] F. Liu, Z. Nie, X. Xu, Q. Zhou, L. Li, and R. Liang. Measurement of electron density by stark braodening in an ablative pulsed plasma thruster. *Applied Physics Letters*, 93(111502), 2008.
- [68] A. Loeb and Z. Kaplan. *Transactions on Magnatism*, 25:342, 1989.
- [69] N. J. Meckel, R. J. Cassady, R. D. Osborne, W. A. Hoskins, , and R. M. Myers. Investigation of pulsed plasma thrusters for spacecraft attitude contro. In *25th International Electric Propulsion Conference*, number 97-128, August 1997.
- [70] H. C. Miller. Surface flashover of insulators. *IEEE Transactions on Electrical Insulation*, 1989.
- [71] L. Muller. Modelling of an ablation controlled arc. *Journal of Physics D: Applied Physics*, 26:1253–1259, 1993.
- [72] A. Neuber, M. Butcher, L. L. Hartfield, and H. Krompholz. Electric current in dc surface flashover in vacuum. *Journal of Applied Physics*, 1999.
- [73] E. Oks. Reduction of spectral line shifts due to the acceleration of electrons by the ion field in plasmas. *J. Phys. B: At. Mol. Opt. Phys.*, 35:2252–2260, 2002.
- [74] W. Olchawa. Computer simulation of hydrogen spectral line shapes in dense plasmas. *J. Quan. Spec. Rad. Trans*, 74:417–429, 2001.
- [75] D. H. Oza, R. L. Greene, and D. E. Keller. Dependence of the half width of plasma-broadened hydrogen lines on reduced mass, temperature, and denisty. *Physics Review A*, 38:2544–2551, 1988.

[76] D. J. Palumbo and W. J. Guman. Effects of propellant and electrode geometry on pulsed ablative plamsa thruster preformance. In *Electrical Propulsion Conference*, 1975.

[77] L. Pekker and J.-L. Cambier. A model of ablative capillary discharge. In *IHTC-13*, August 2006.

[78] J. D. Powel and A. E. Zielinski. Theory and experiment for an ablating-capillary discharge and application to electrothermal-chemical guns. Technical Report Tech. Rep. BRL-TR-3355, US Army Ballistic Res. Lab., Aberdeen Proving Ground, June 1992.

[79] J. D. Powel and A. E. Zielinski. Capillary discharge in the electrothema gun. *Transactions on Magnatism*, 29:591–569, 1993.

[80] J. Powell and A.E. Zielinski. Theory and experiment for an ablating capillary discharge and application to electrothermal-chemical guns. Technical Report Report BRL-TR-3355, Army Ballistic Research Laboratory, June 1992.

[81] C. B. Ruchti and L. Niemeyer. Abaltion controlled arcs. *Transactions on Plasma Science*, 14:423, August 1986.

[82] J. Schmidt, K. Kolacek, V. Prukner, V. Bohacek, M. Ripa, P. Sunka, and O. Frolov. Influence of initial conditions on capillary discharge device capex 2. In *Pulsed Power Conference*, volume 2, pages 729–732, 2003.

[83] W. Schnabel. *Polymer Degradation*. Hanser, 1981.

[84] N.P. Selden and A. Ketsdever. Comparison of force balance calibration techniques for the nano-newton range. *Review of Scientific Instruments*, 74(12), 2003.

[85] N. Shafir, D. Zoler, S. Wald, and M. Shapira. Reliable, highly reproducible plasma injectors for electrothermal and electrothermal-chemical launchers. *Transactions on Magnatism*, 41(1):355–359, 2005.

[86] G. B. Shinn, F. Steigerwald, H. Stiegler, R. Sauerbrey, F. K. Tittel, and W. L. Wilson. *Journal of Vacuum Science Technology*, B4:1273, 1986.

[87] L. Spitzer. *Physics of Fully Ionized Gases*. Intersciecne Publishers, 1962.

[88] L. Spitzer and R. Harm. *Physics Review*, 89:997, 1953.

[89] R. Srinivasan. *Journal of Vacuum Science Technology*, B1:923, 1983.

[90] F. Stefani, I. R. McNab, J. V. Parker, M. Alonso, and T. Klatt. A plasma railgun experiment addressing launch-to-space issues. *IEEE Trans Mag*, 43(1):194–197, 2007.

[91] D. C. Strachan, D. Lidgate, and G. R. Jones. Radiative energy losses from a high current air blast arc. *Journal of Applied Physics*, 48(6):2324–2330, 1977.

[92] T. Sueda, S. Katsuki, and H. Akiyama. Behavoir of capillary plasmas with different diameters. *Jpn. J. Appl. Phys.*, 36(4A):2346–2350, 1997.

[93] Michael J Taylor. Formation of plasma around wire fragments created by electrically exploded copper wire. *Journal of Physics D: Applied Physics*, 35:700–709, 2002.

[94] J. Torres, J. Jonker, M. J. van de Sande, J. J. A. M. van de Mullen, A Gamero, and A Sola. An easy way ti determine simultaneously the electron density and temperature in high-pressure plasmas by using stark broadening. *J. Phys. D: Appl. Phys.*, 36, 2003.

[95] J. Torres, J. M. Palomares, M. A. Gigosos, A. Gamero, A. Sola, and J. J. A. M. van de Mullen. An experimental study on the asymmetry and the dip of the  $h_{\beta}$  line profiles in microwave produced plasmas at atmospheric pressure. *Spect. Acta B*, 63:939–947, 2008.

[96] J. Torres, J. M. Palomares, A. Sola, J. J. A. M. van de Mullen, and A. Gamero. A stark broadening method to determine simultaneously the electron temperature and density in high-pressure microwave plasmas. *J. Phys. D: Appl. Phys.*, 40:5929–5936, 2007.

[97] M. J. van de Sande and J. J. A. M. van de Mullen. Thomson scattering on a low-pressure, inductively-coupled gas discharge lamp. *J. Phys. D: Appl. Phys.*, 35(1381), 2002.

[98] C. R. Vidal, J. Cooper, and E. W. Smith. *Astrophys. J. Suppl.*, 25(37), 1973.

[99] Y. Vitel. *J. Phys. B: At. Mol. Opt. Phys.*, 20(2327), 1987.

[100] Y. Vitel, T. V. Gavrilova, L. G. D'yachkov, and Yu. K. Kurilenkov. Spectra of dense pure hydrogen plasma in balmer aera. *J. Quan. Spec. Rad. Trans.*, 83:387–405, 2002.

[101] R. J. Vondra. The mit lincoln laboratory pulsed plasma thruster—a final report on the les-8/9 pulsed plasma thruster. *AIAA Paper*, pages 76–998, November 1976.

[102] R. J. Vondra and K. I. Thomassen. Flight qualified pulsed electric thruster for satellite control. *Journal of Spacecraft and Rockets*, 11(9):613, 1974.

[103] P. Vrba and M. Vrbova. Z-pinch evolution in capillary discharge,. *Contrib. Plasma Phys.*, 40(5-6):581–595, 2000.

[104] W. L. Wiese, D. E. Kelleher, and D. R. Paquette. *Physics Review A*, 6(1132), 1972.

[105] M. Wilson, S. Bushman, and R. Burton. In *International Electric Propulsion Conference*, number 97-122, August 1997.

[106] T. Wujec, W. Olchawa, J. Halenka, and J. Musielok. Experimental and theoretical stark broadening studies of the hydrogen paschen  $\beta$  line. *Physics Review E*, 66, 2002.

[107] J. K. Ziemer, E. A. Cubbin, E. Y. Choueiri, and D. Birx. *AIAA Paper*, (97-2925), NA.

[108] A. Zigler, Y. Ehrlich, C. Cohen, J. Krall, and P. Sprangle. Optical guiding of high-intensity laser pulsed in a long plasma channel formed by a slow capillary discharge. *J. Opt. Soc. Am. B*, 13:68–71, 1996.

[109] D. Zoler and R. Alimi. A proof of the need for consistent treatment in modeling of capillary ablative discharges a proof of the need for consistent treatment in modeling of capillary ablative discharges. *Journal of Physics D: Applied Physics*, 28:1141–1152, 1995.

[110] D. Zoler, D. Saphier, and R. Alimi. A numerical study of the evolution of plasma parameters in an ablative capillary discharge for a two-pulse form of energy input. *Journal of Physics D: Applied Physics*, 27:1423–1432, 1994.

[111] R. J. Zollweg and R. W. Liebermann. Electrical conductivity of nonideal plasmas. *Journal of Applied Physics*, 62:3621, 1987.



# **A Study of Ignition effects on Thruster Performance of a Multi- Electrode Capillary Discharge using Visible Emission Spectroscopy**

Anthony Pancotti



# Purpose

## **Viability of a capillary discharge electrothermal pulsed plasma thruster**

- Efficient ( $\eta_t > 65\%$ ) operation over the specific impulse range of 750s to 3000s.
- Fill a desired niche which has historically shown rather poor efficiencies

## **Understand the operating physics through experiments and computational modeling**

- Through experimental methods
  - compare with previous work in capillary discharges
  - testing newly developed diagnostics tools
  - validate capillary discharge models

## **Study of ignition on thruster performance of a capillary discharge**

- exploding wire
- Paschen breakdown
- spark ignition

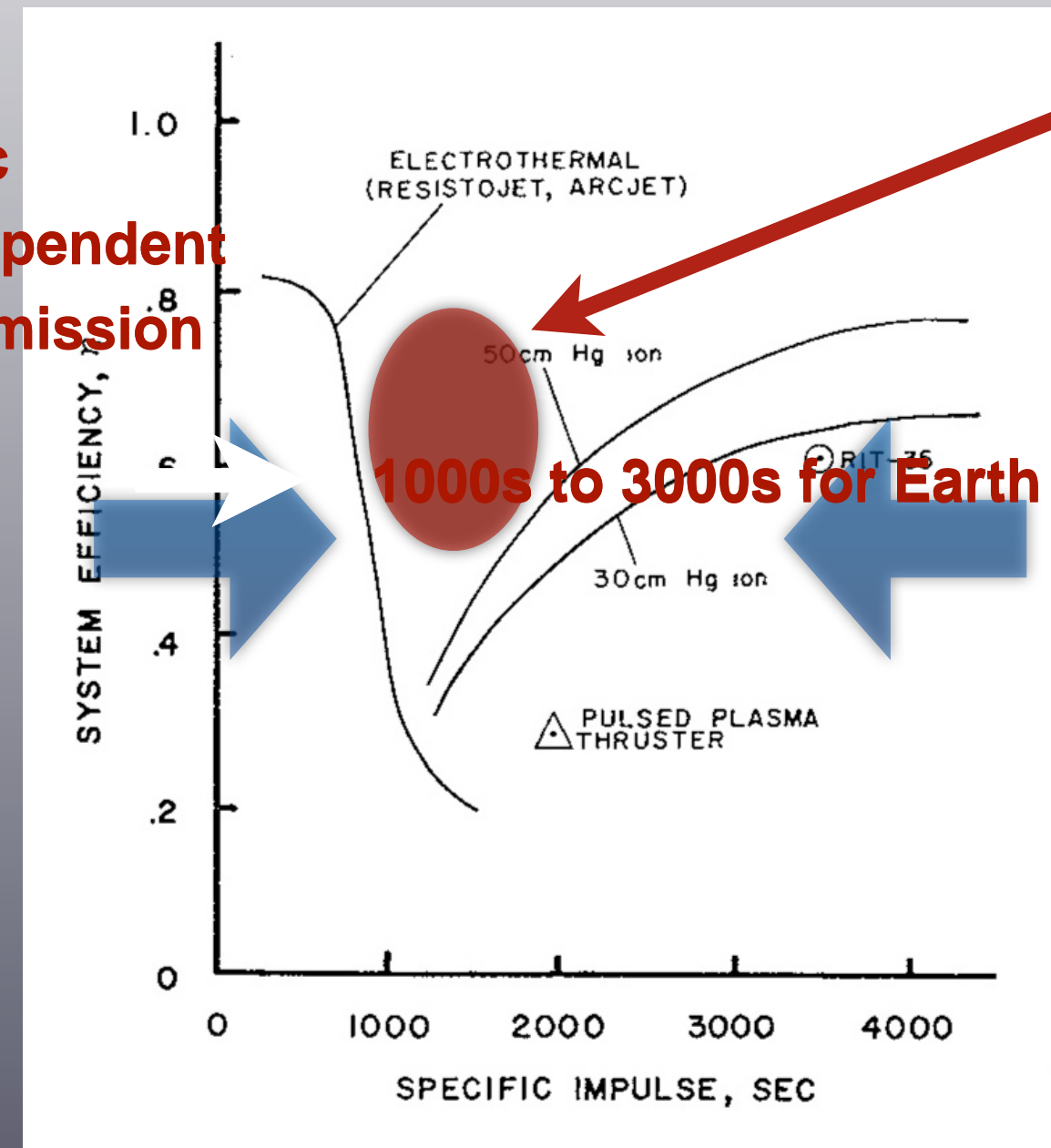


# Need for CDT

Optimal specific impulses are dependent on the specific mission

## Electrothermal Thrusters

- Station Keeping
- Efficient  $I_{sp} < 1000s$
- Orbit insertion
- materials limitations
- Frozen  $I_{sp}$  / lossless
- Drag compensation
- Formation flying
- Attitude control



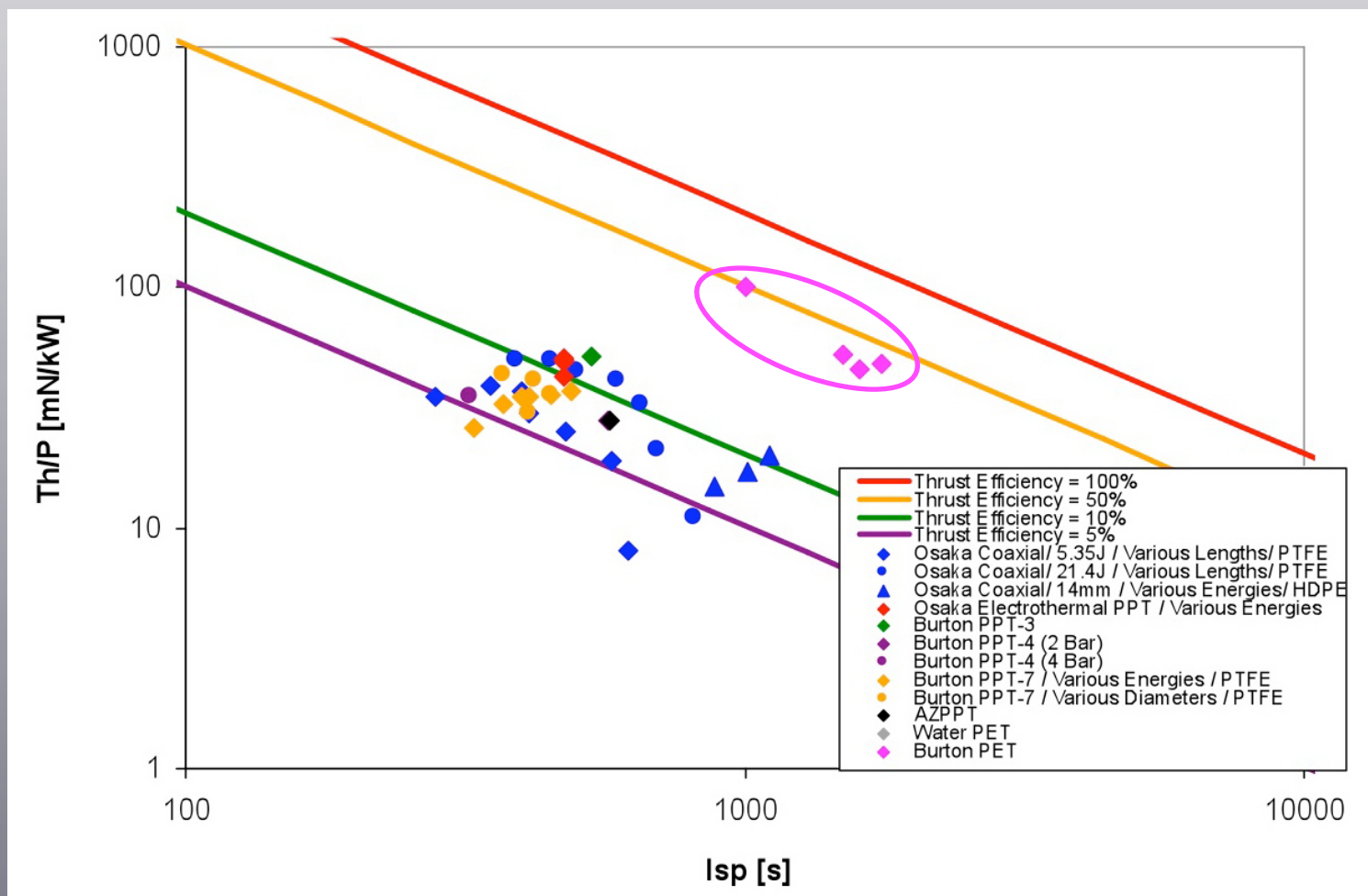
This work investigated the possibility of filling this niche

Electrostatic and Electromagnetic thrusters for Earth orbiting spacecraft

- efficient at  $I_{sp} > 1000s$
- Relative high ionization cost



# Other CDT's



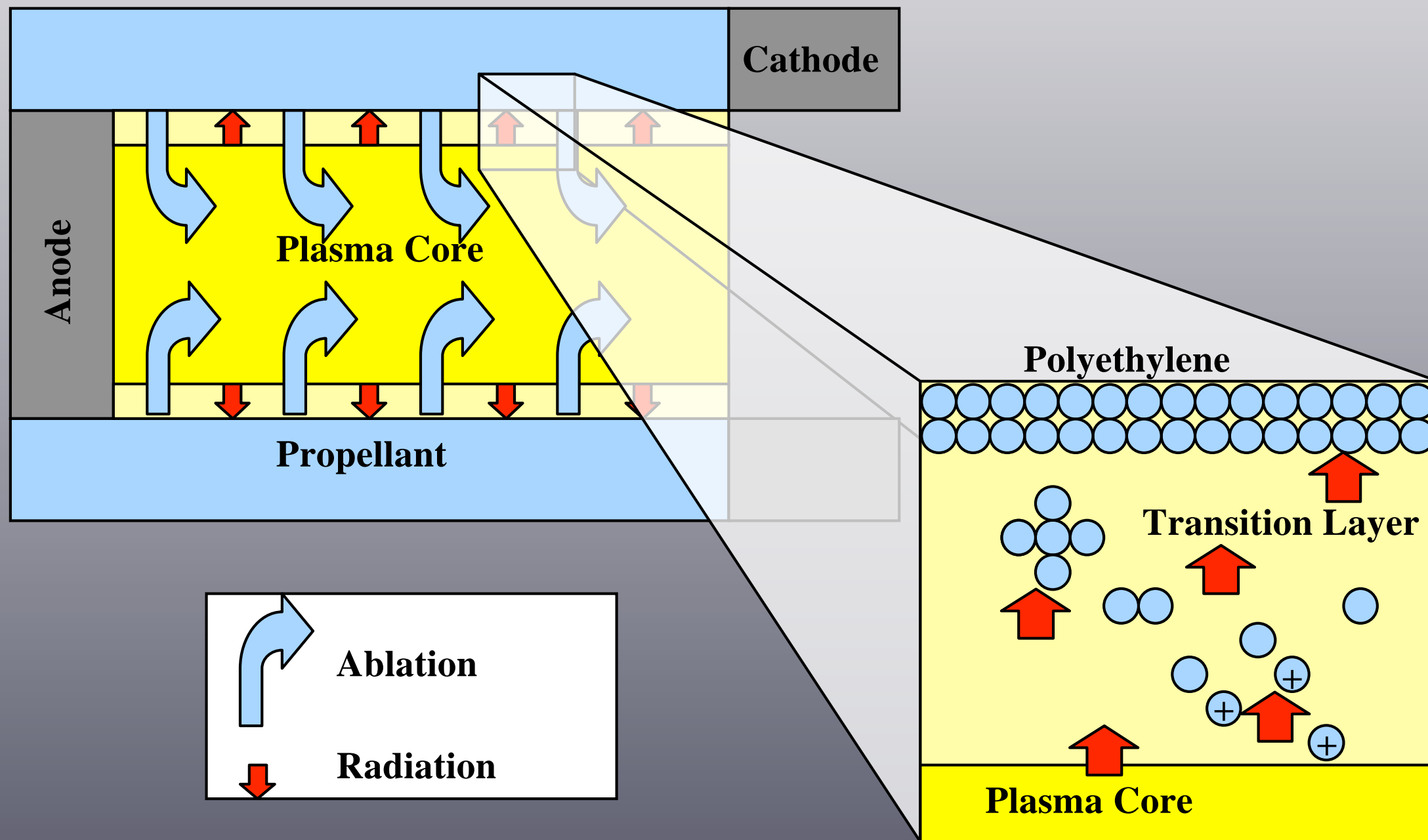
## Burton's PET

- Polyethylene
- 4 mm diameter
- several cm in length
- Low impulse (0.086 Ns @ 1600s I<sub>sp</sub>)
  - 15  $\mu$ s
  - 23 kA
  - 56%
- High impulse (0.2 Ns @ 1000s I<sub>sp</sub>)
  - 48  $\mu$ s
  - 15 kA
  - 37%

Burton predicted efficiencies as high as 80%



# Capillary Process





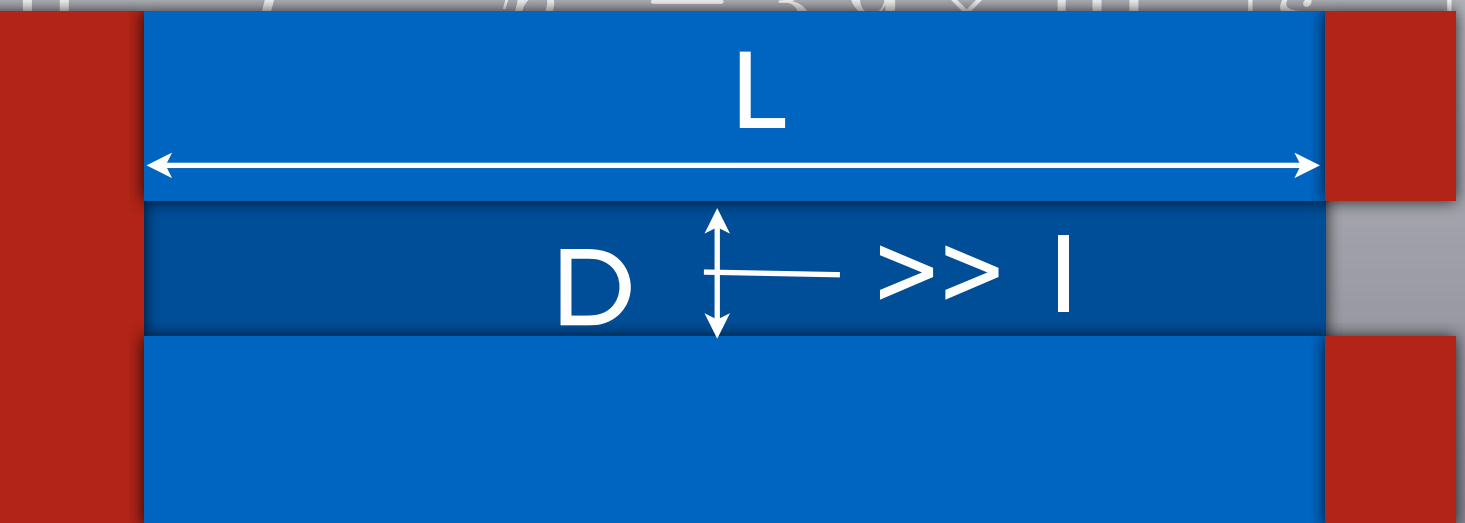
# High Efficiency

1. High recombination at the Exit
2. Large dimensional ratio (L/D)

$$\nu_e = \alpha_3 n^2 = 8.75 \times 10^{-27} T^{-4.5} n^2 = 3.0 \times 10^{10} [s^{-1}]$$

Therefore, ionization costs can be recaptured

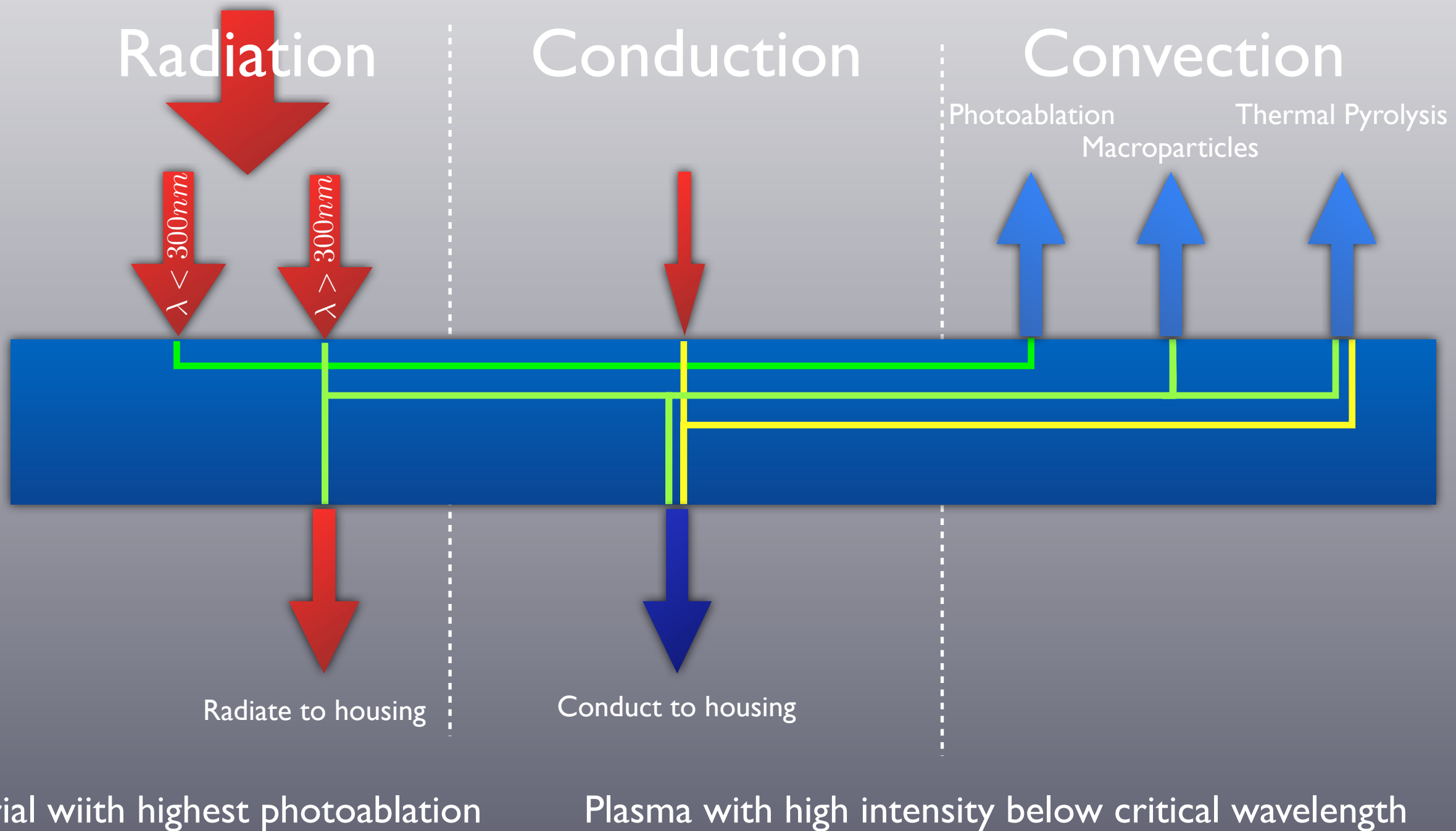
$$\begin{aligned} \text{Evaporate } C_2H_4 \text{ from wall } & U = 0.5 \text{ eV} \sqrt{\frac{8kT}{\pi N}} \\ \text{break C-C bond} & 4.5 \text{ eV} \\ \text{break 4 C-H bonds} & 14.0 \text{ eV} \\ \text{Total 6 atoms: } & 19.0 \text{ eV} \\ \text{energy/atom} & \lambda = \frac{U}{\nu_e} = 2.5 \times 10^{-5} [cm] \\ \text{mean ionization energy/atom} & 12.8 \text{ eV} \\ \hline \text{Total/ion: } & 16.0 \text{ eV} \end{aligned}$$



Large surface area  
Small exit area

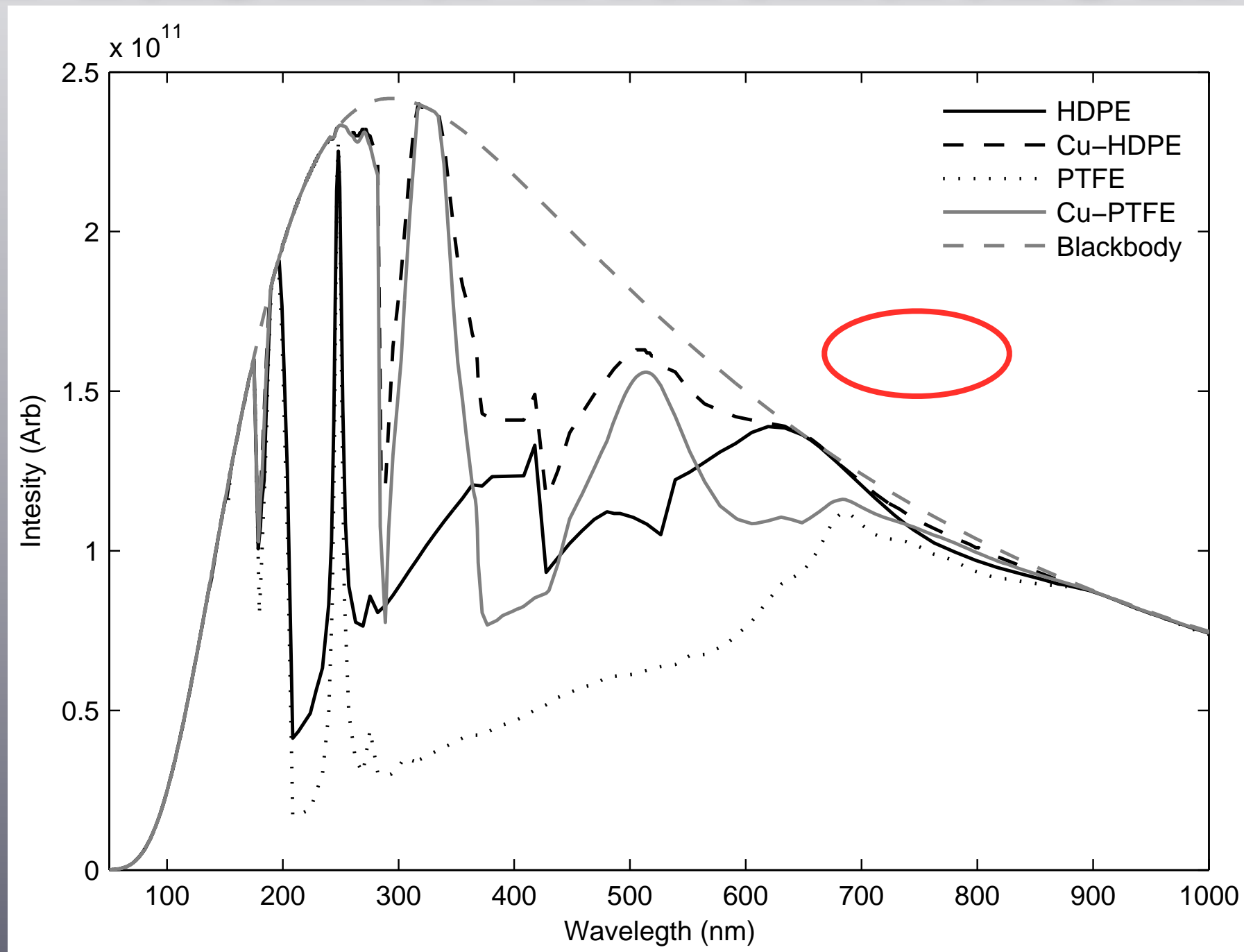


# Ablation Process





# Plasma Radiation



Support by ablation controlled literature



# Physical Assumptions

$$\beta = \frac{P_T}{P_B} \gg 1$$

Pressure Ratio

Thermal pressure

Magnetic pressure

## Local Thermodynamic Equilibrium

$$\text{Non-Ideal Parameter 1} = \frac{\Delta \varepsilon_{e \leftrightarrow i}}{\Delta \varepsilon_E}$$

$\Delta \varepsilon_{e \leftrightarrow i}$  Energy exchange during a collision

$\Delta \varepsilon_E$  Energy gained from the electric field

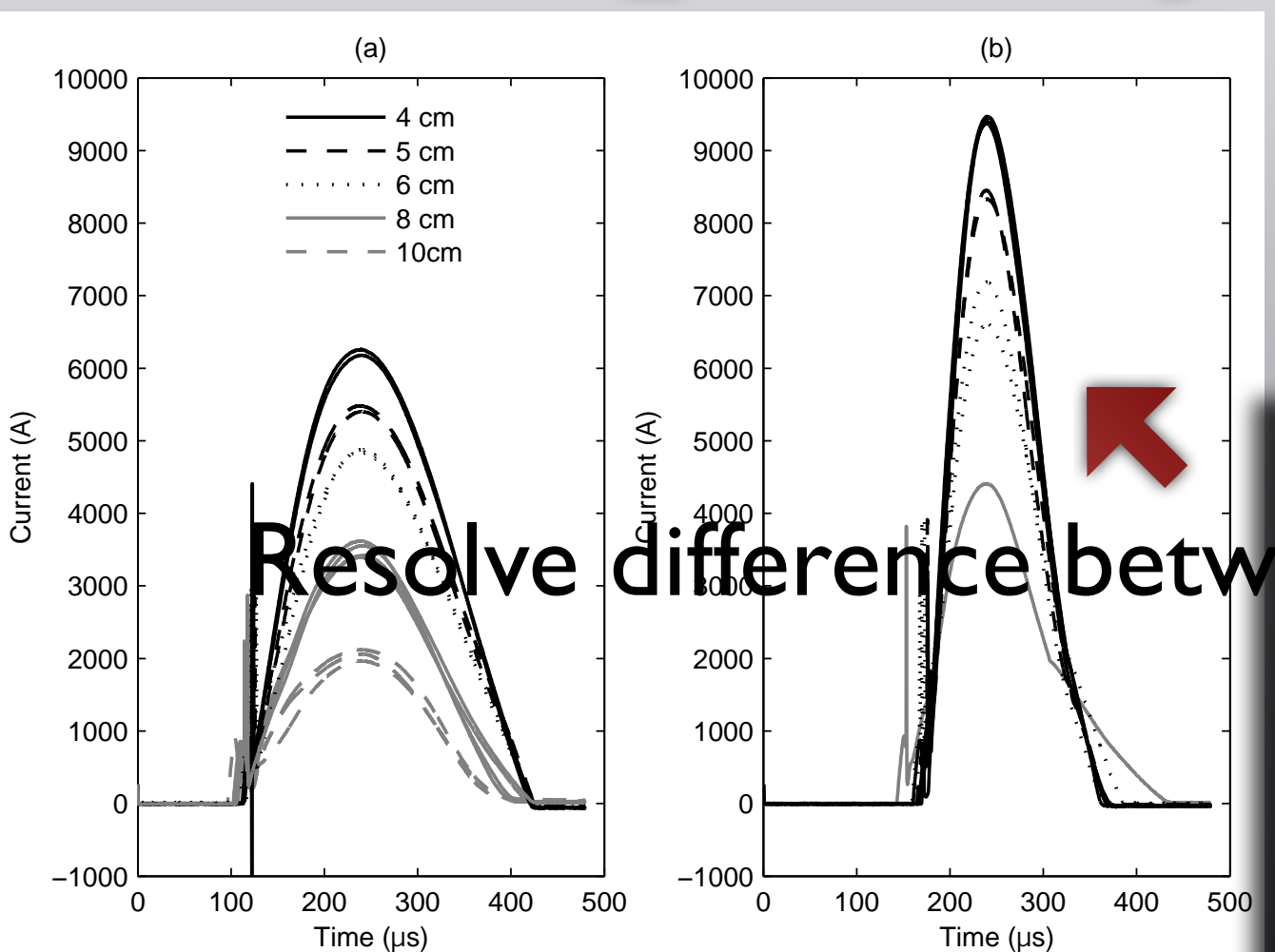
$$\Gamma = \frac{W_{PE}}{W_{KE}} \ll 1$$

$W_{PE}$  Potential energy between charge particles

$W_{KE}$  Average kinetic energy



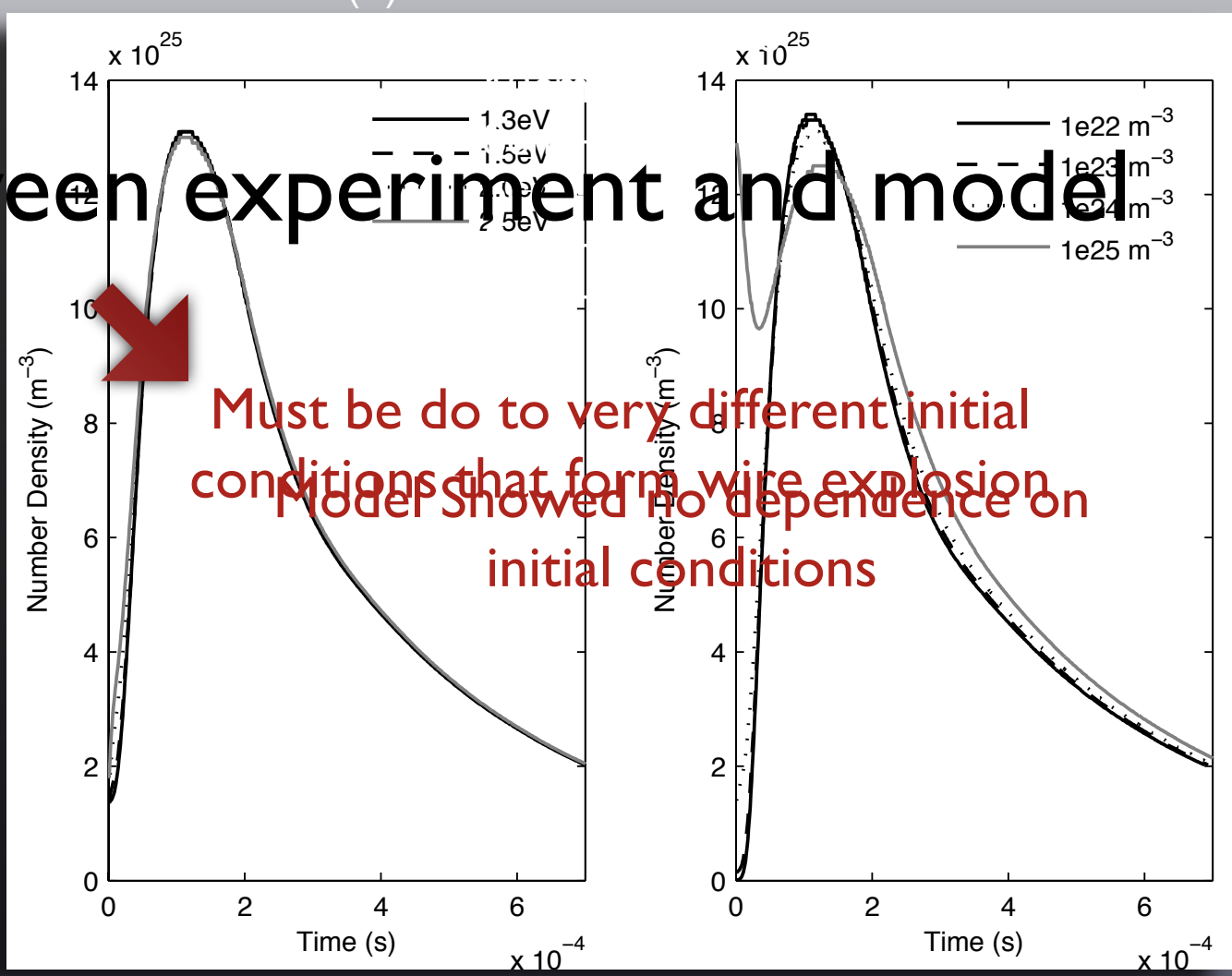
# Capillary Ignition



0D Model results for varying initial conditions

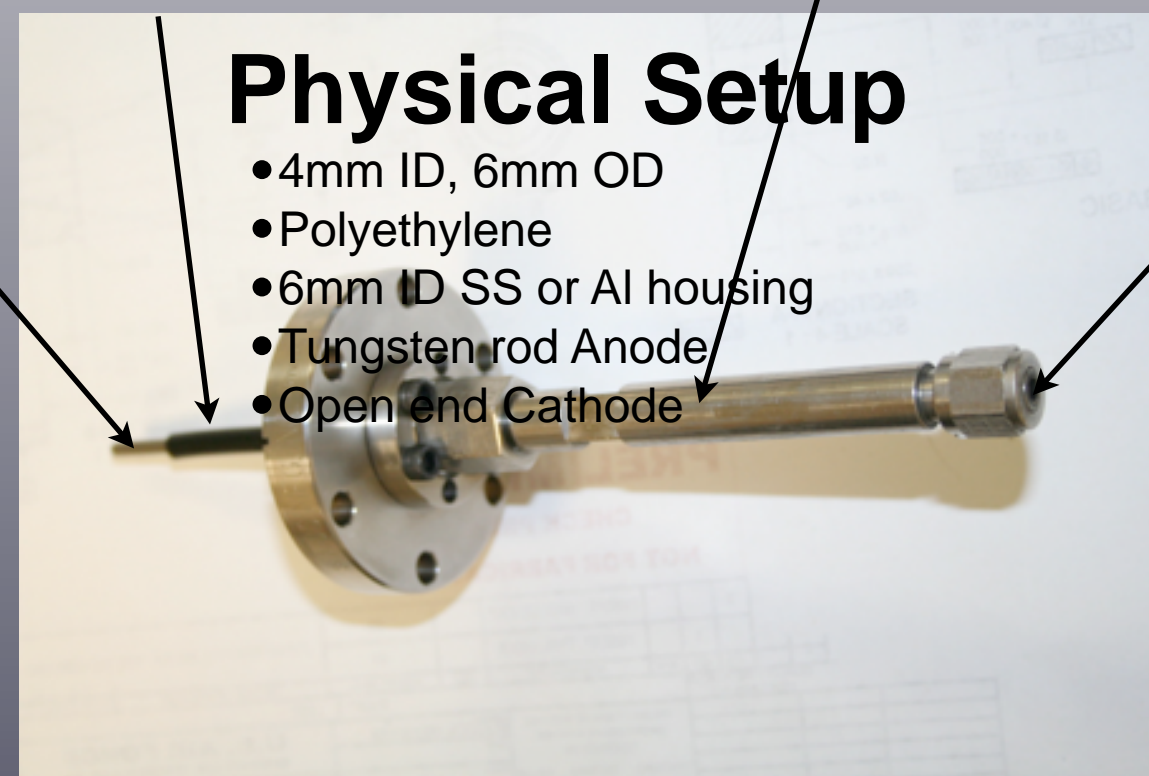
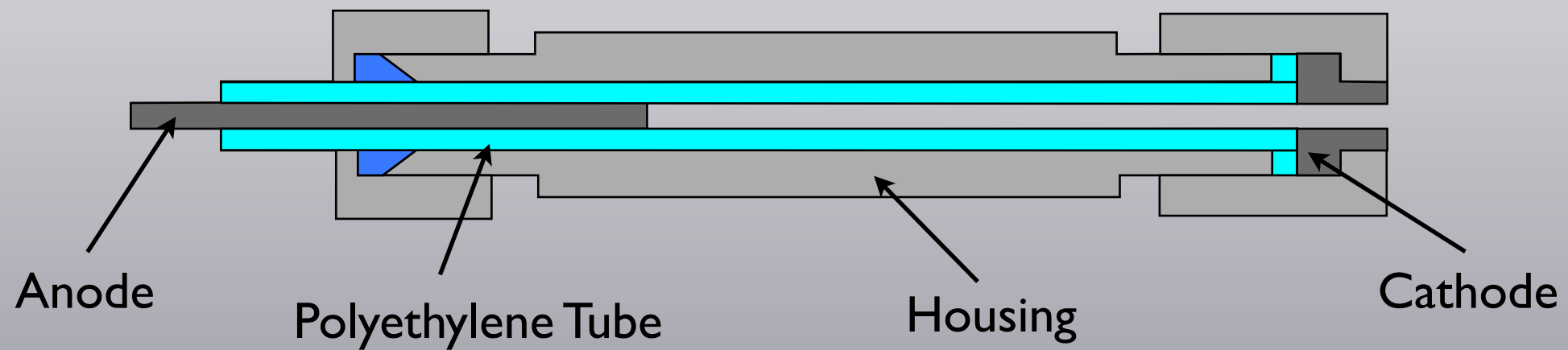
Early wire ignition test

(a) Low Current mode





# Capillary Design

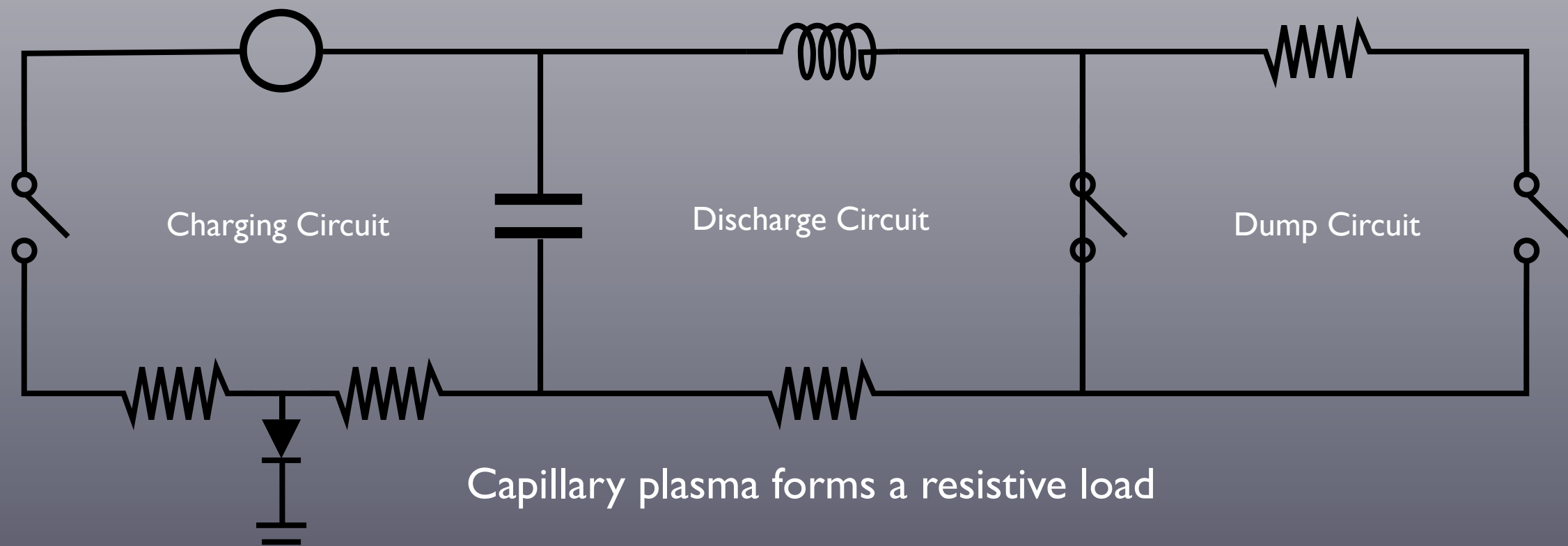




# LRC Drive Circuit

## Circuit Parameters

- 0.5 mF capacitor
- $13 \pm 0.7 \mu\text{H}$  from inductor
- $7 \pm 0.4 \mu\text{H}$  parasitic
- $24 \pm 1 \mu\Omega$  parasitic
- SCR switch

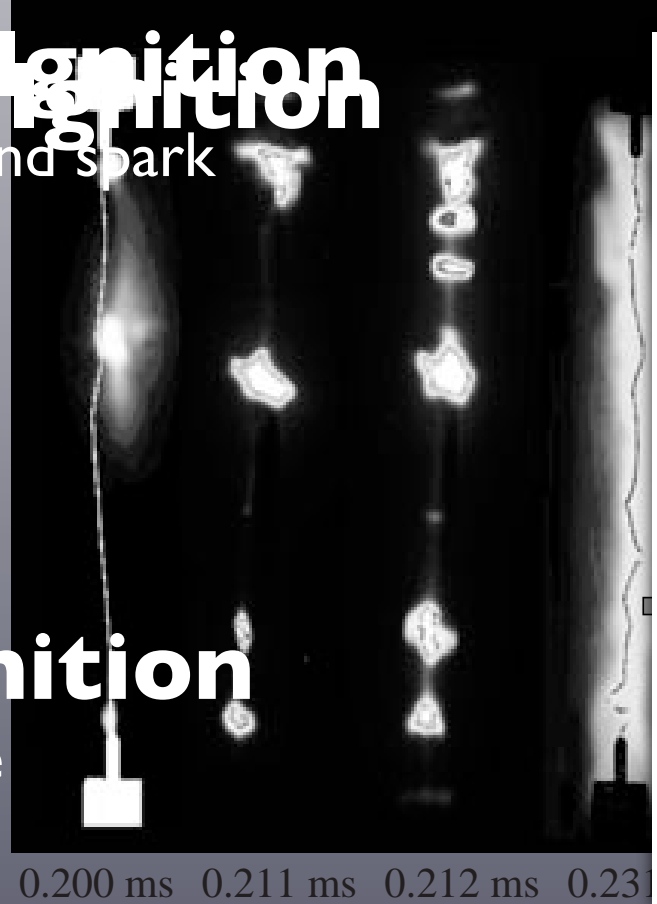




# Ignition Design

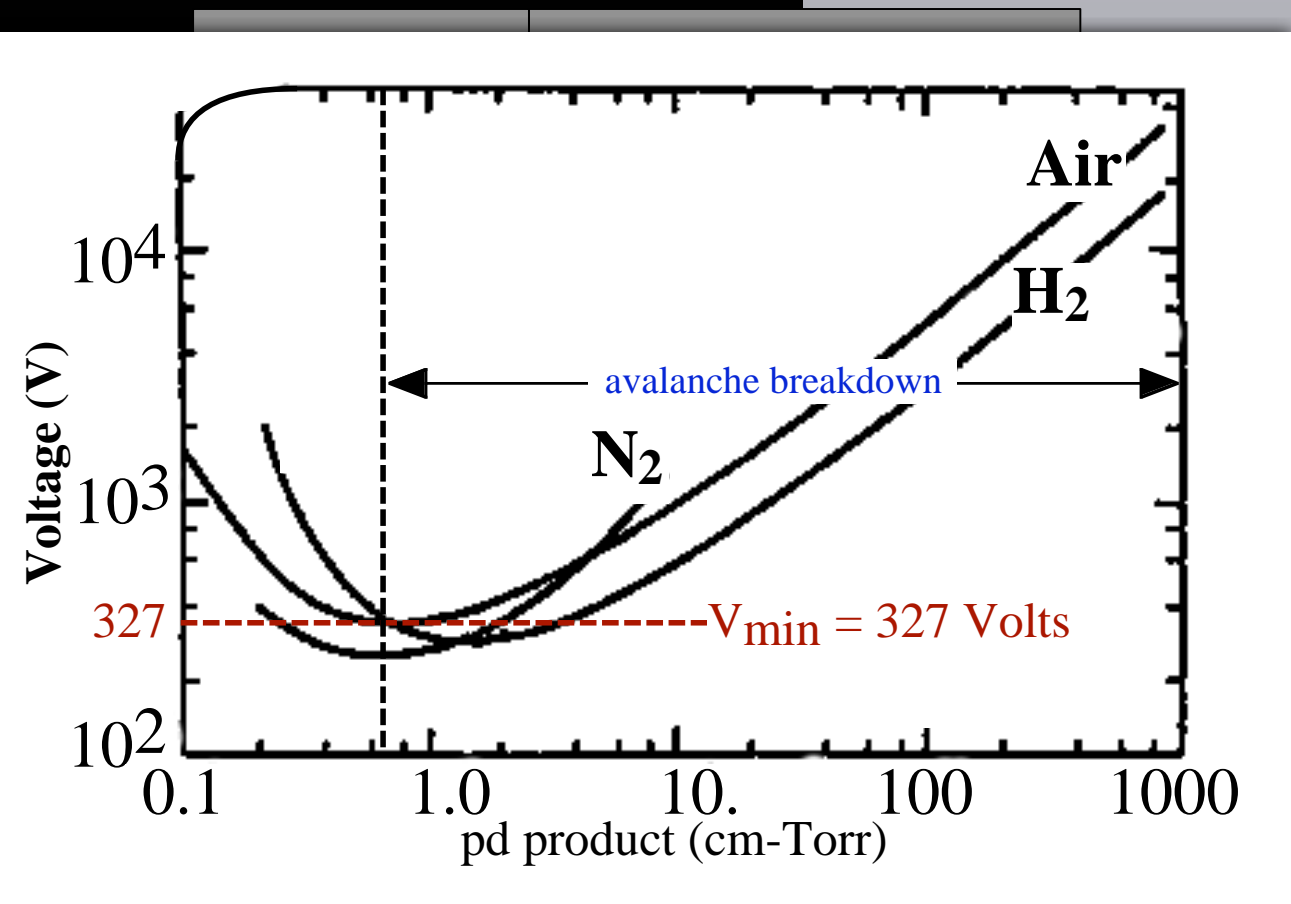
## Paschen Ignition

- between wire and spark
- historic
- basic physics
- relatable



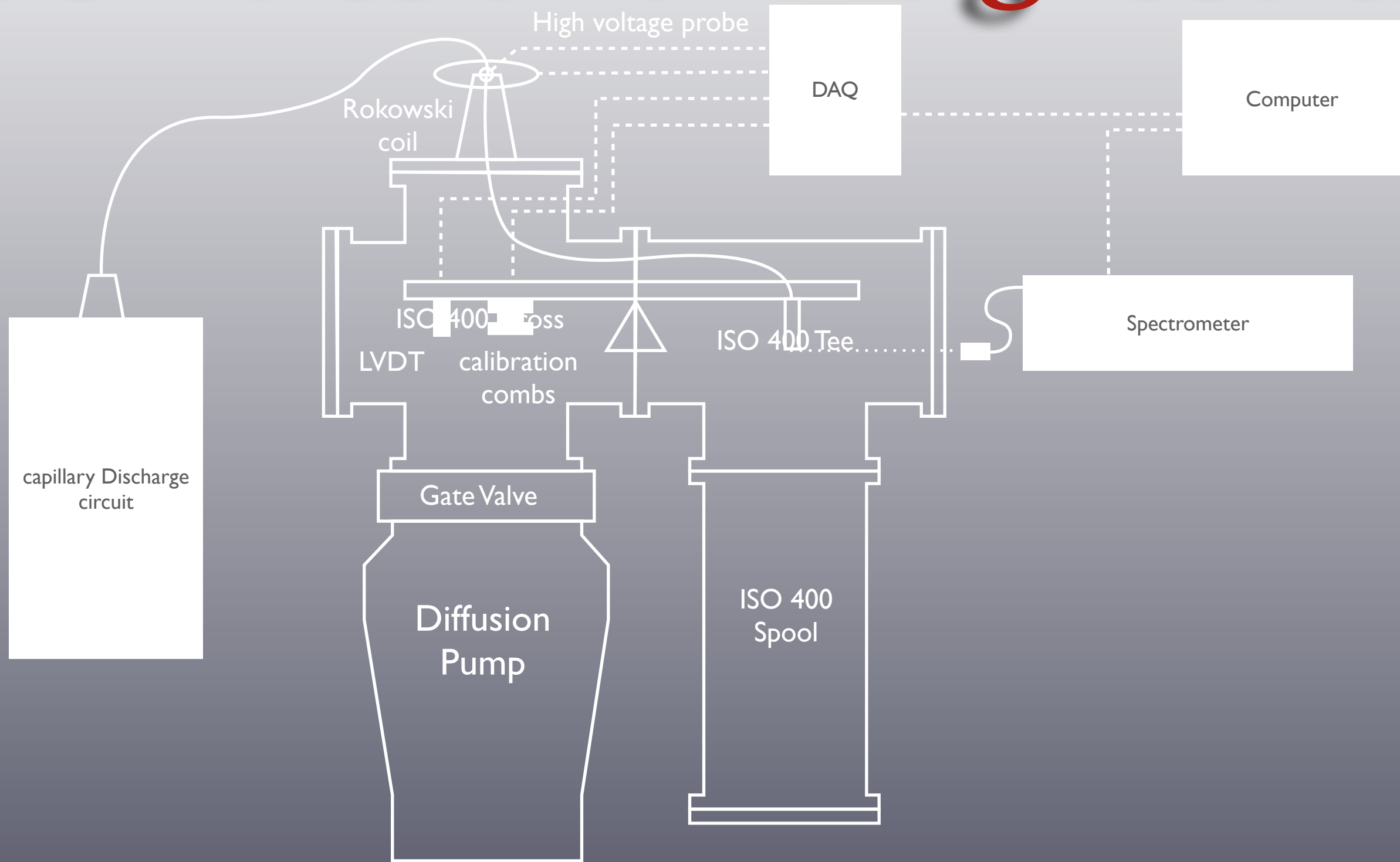
## Spark Ignition

- space applicable





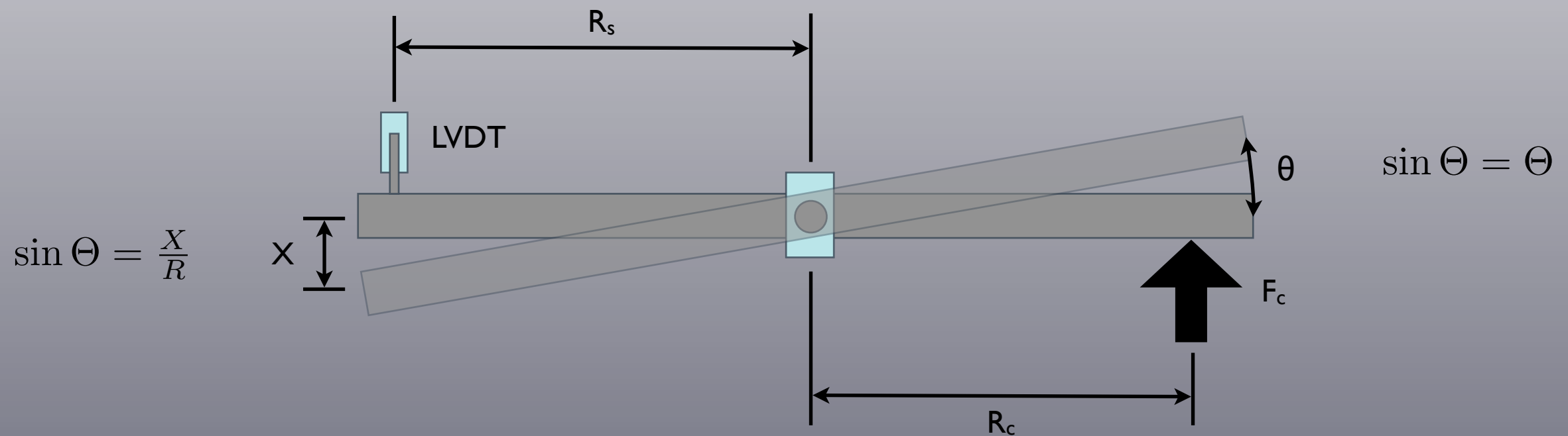
# Facilities and Diagnostics





# Thrust Stand

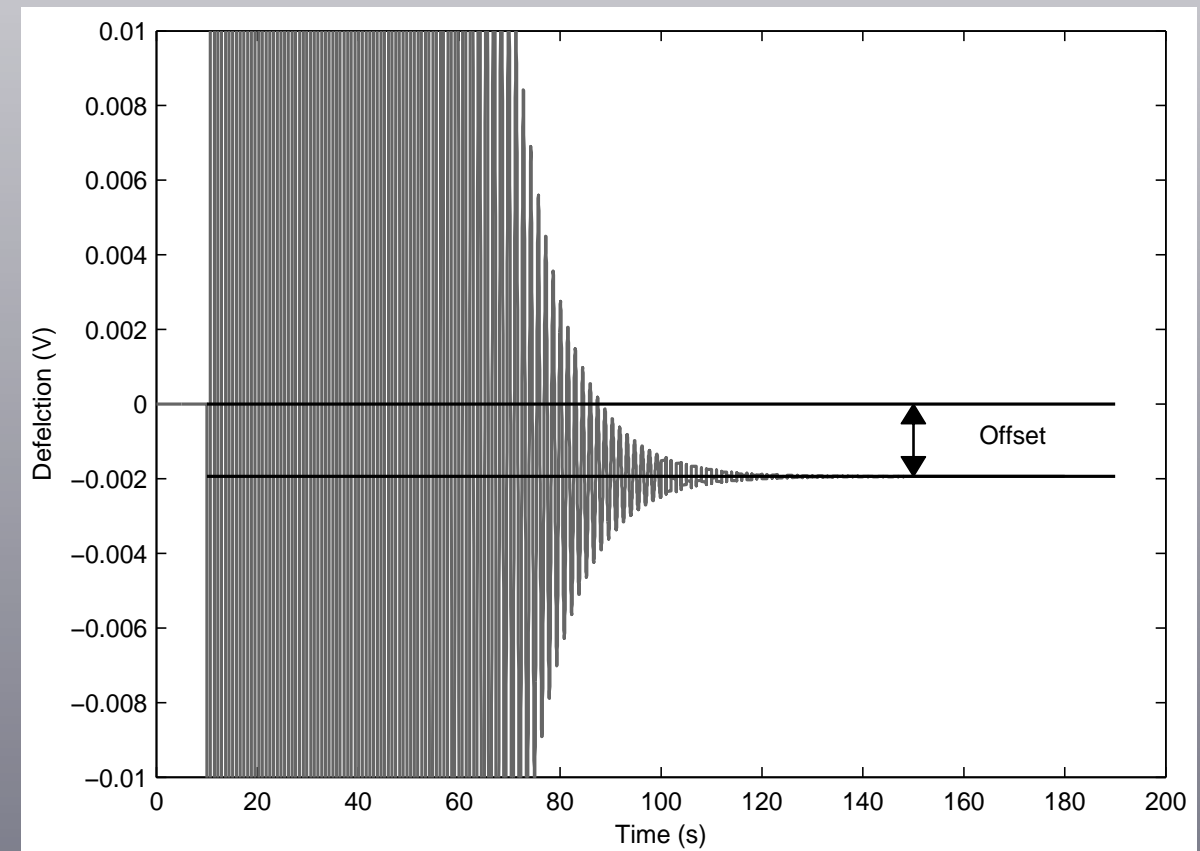
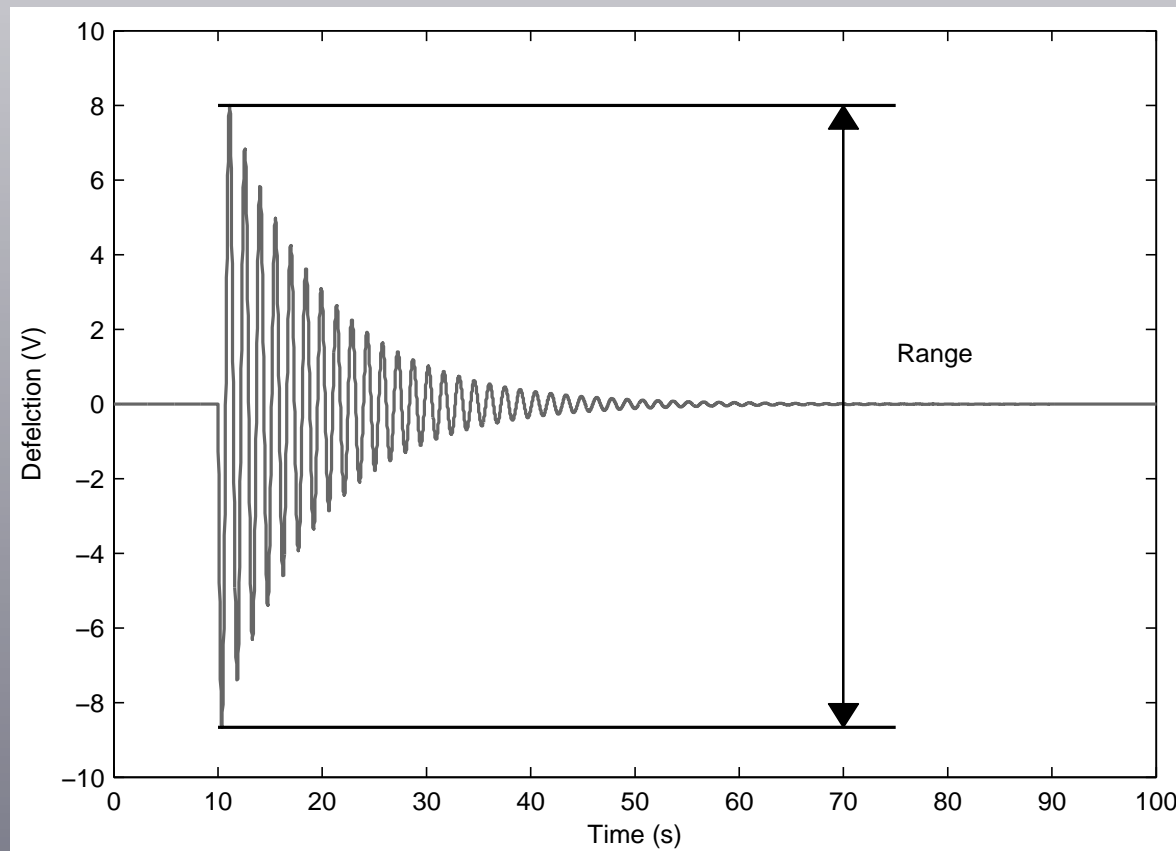
$$I\ddot{\Theta}(t) + C\dot{\Theta}(t) + K\Theta(t) = M(t)$$



$$I\frac{\ddot{X}(t)}{R_s} + C\frac{\dot{X}(t)}{R_s} + K\frac{X(t)}{R_s} = F_c(t) R_c$$



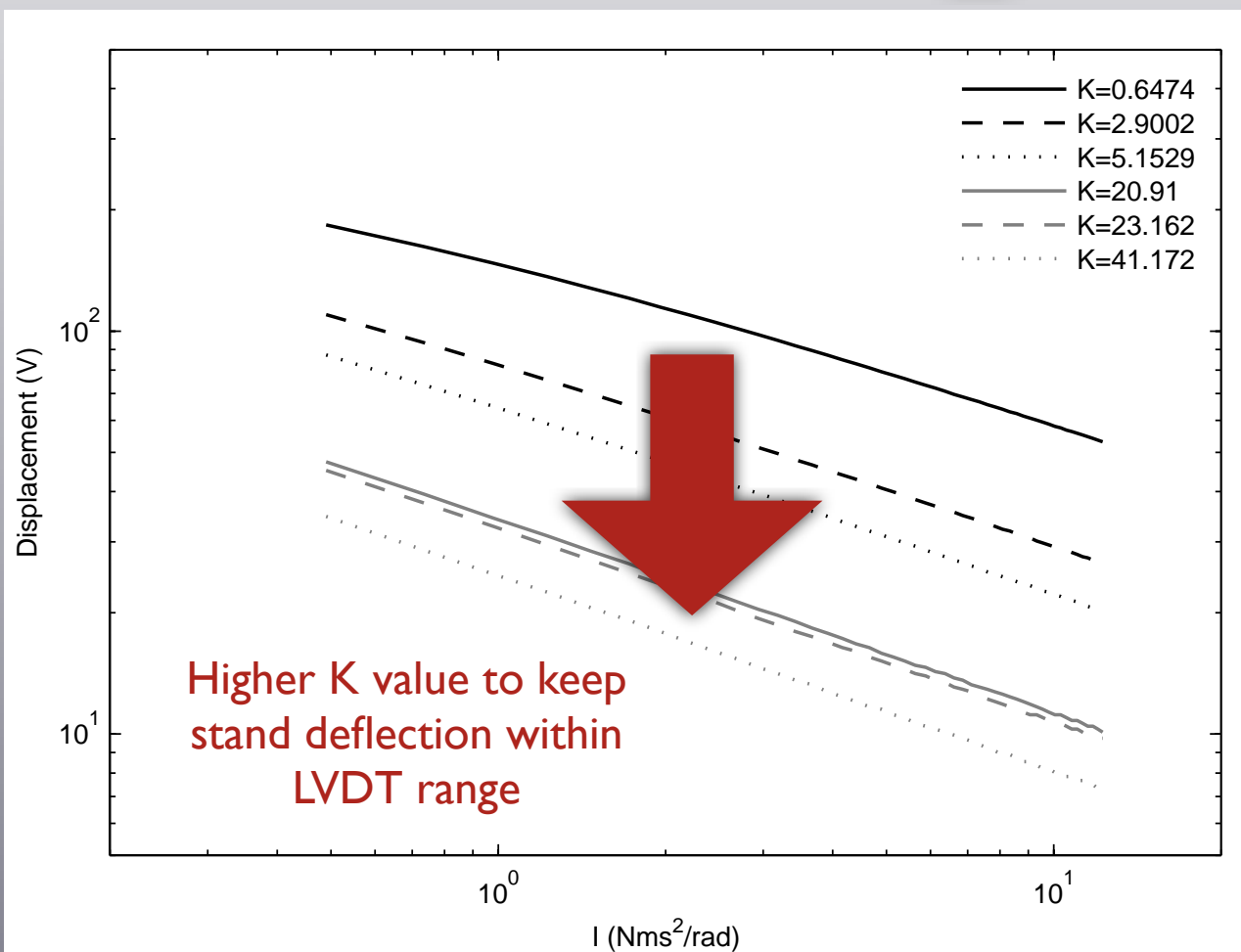
# In-situ Isp



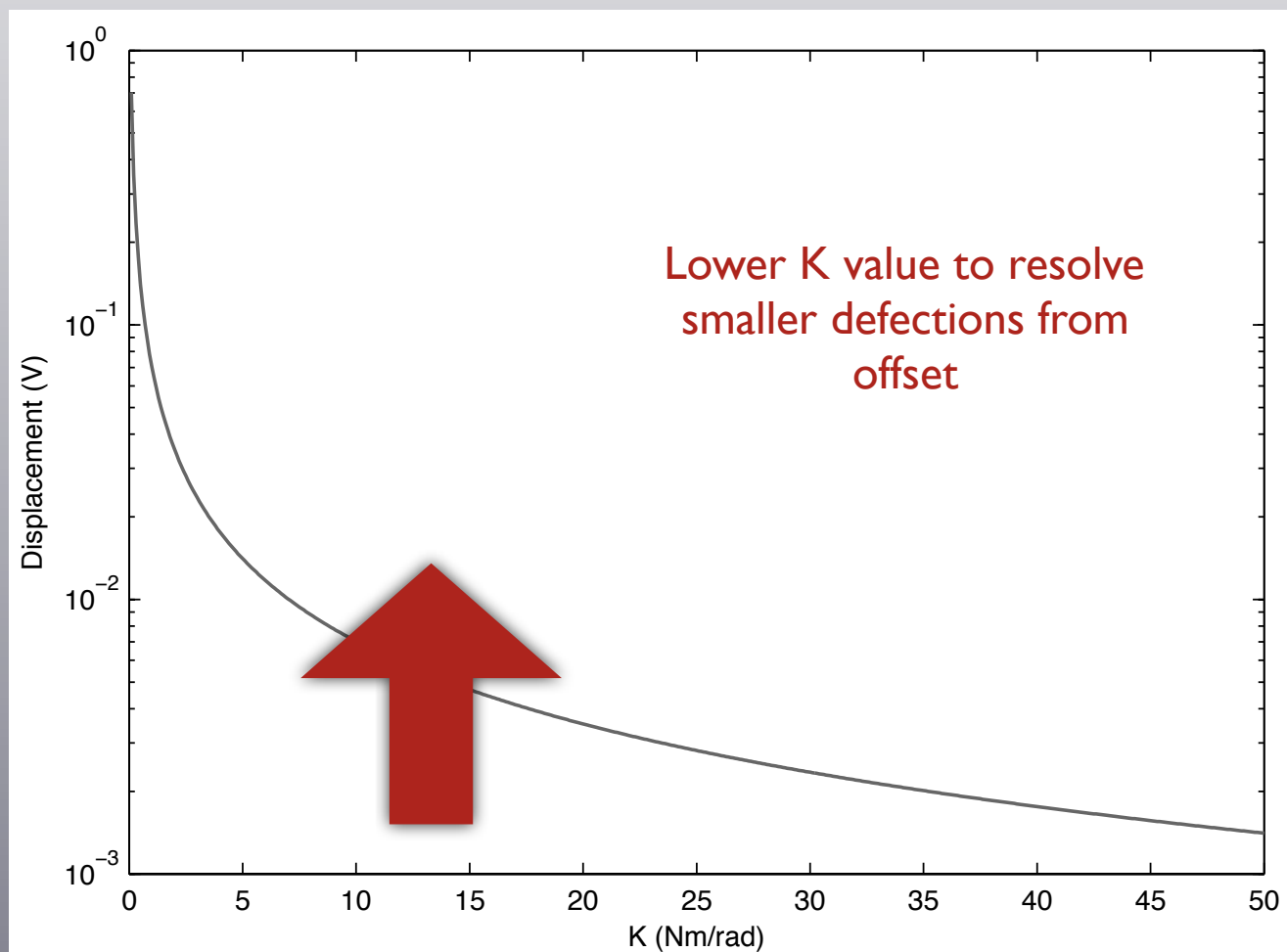
Specific Impulse and efficiency can be determined  
from impulse and efficiency measurements



# TS Optimization



Higher  $K$  value to keep stand deflection within LVDT range



Lower  $K$  value to resolve smaller deflections from offset

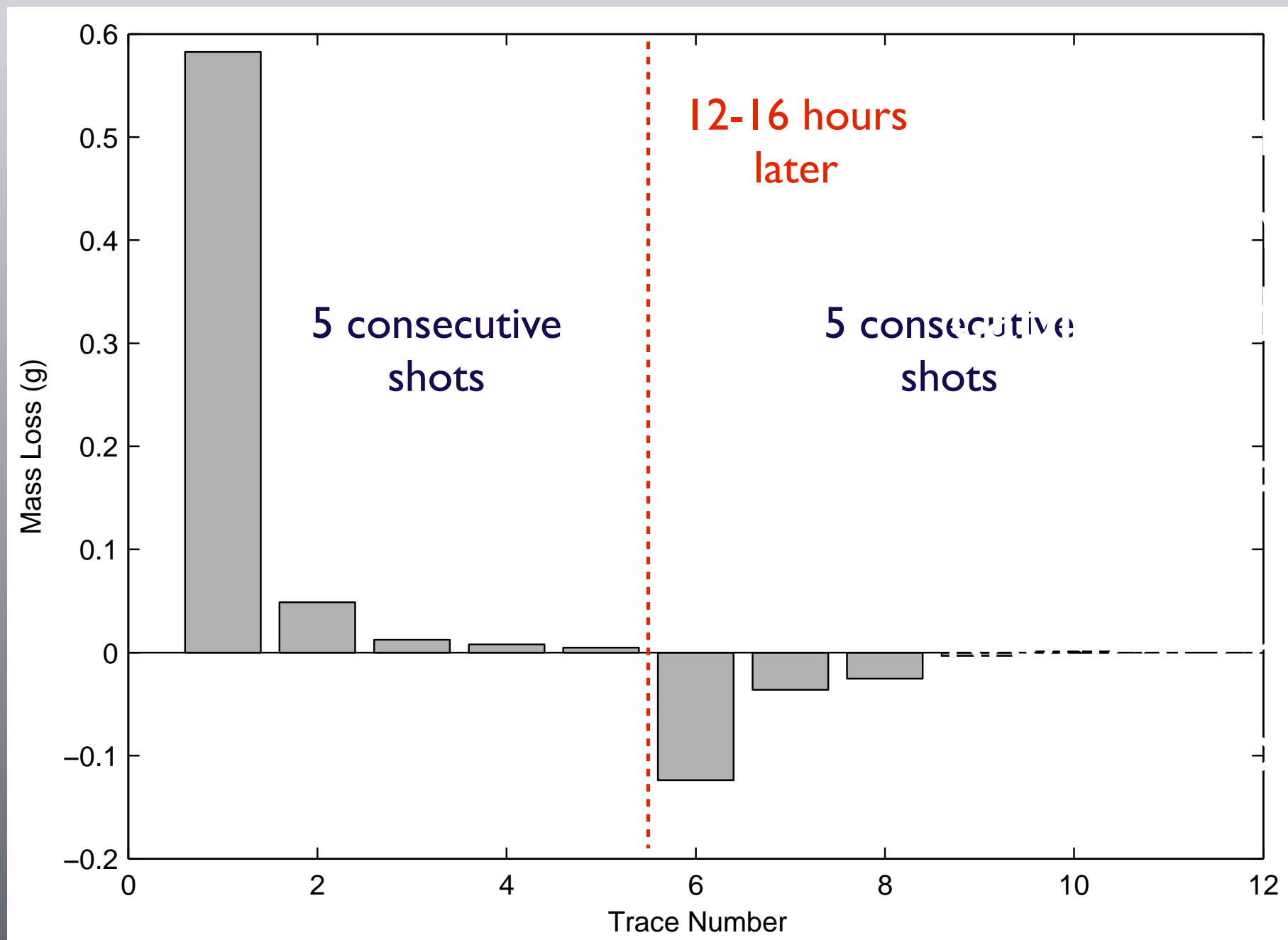
$$I \frac{\ddot{X}(t)}{R_s} + C \frac{\dot{X}(t)}{R_s} + K \frac{X(t)}{R_s}$$

	Thrust Stand	1 <sup>st</sup> Iteration	Optimized
$K$ [Nm/rad]	41.75	36.22	
$E_{\text{FWL}}(t)$ [rad]	0.101	0.028	
$I$ [Nms <sup>2</sup> /rad]	0.245	1.988	

8V oscillation  
2mV steady state deflection



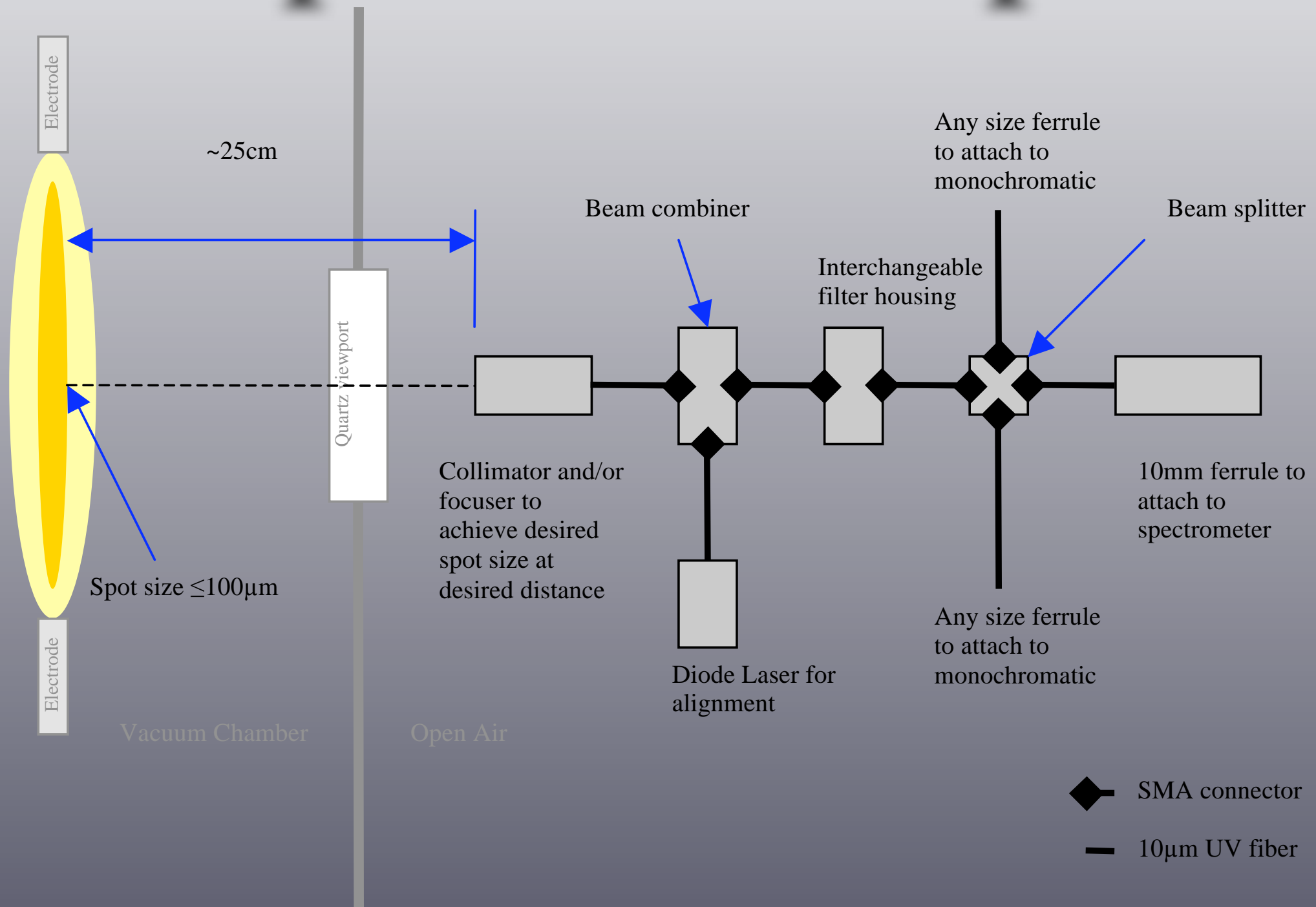
# In-situ Specific Impulse



magnetic  
ace from  
scharge  
ange in  
stant



# Optical Setup

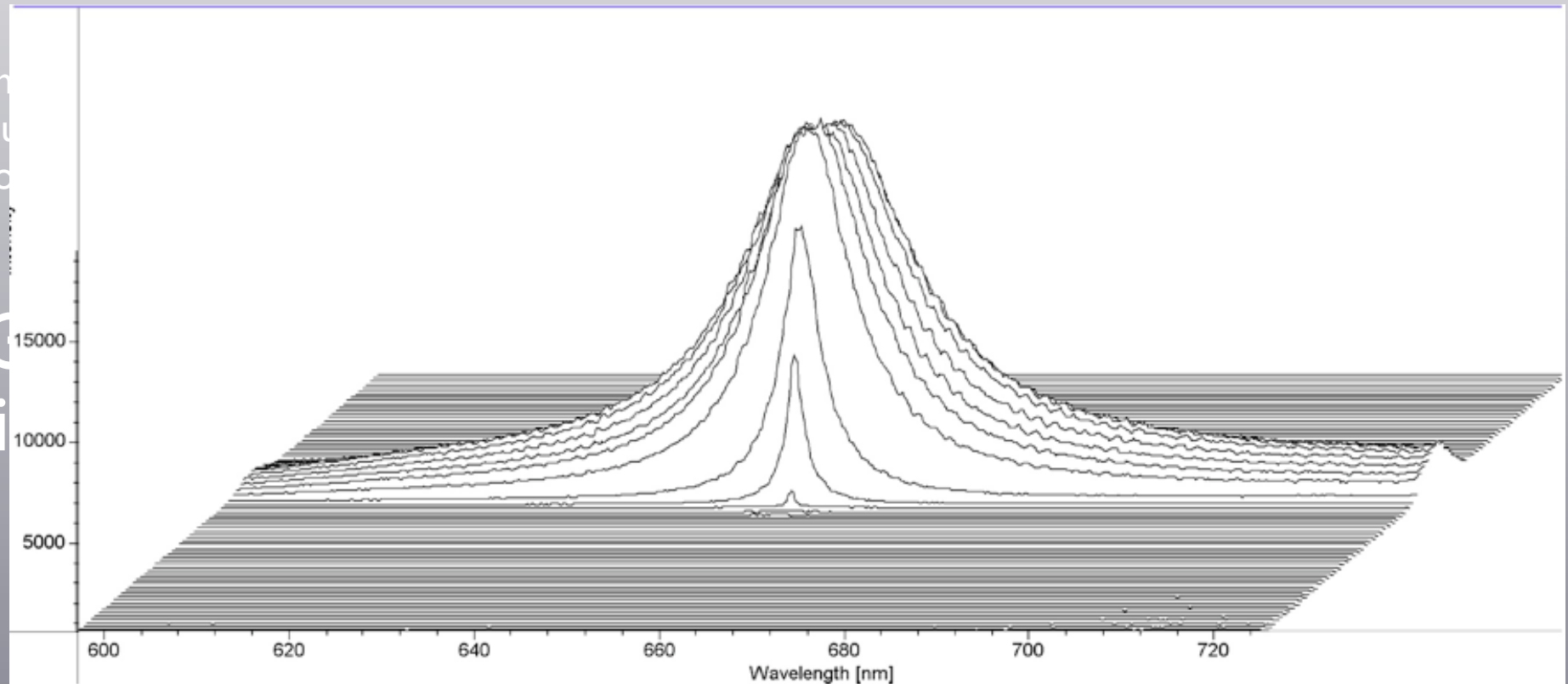




# Kinetics Mode

only small area  
the chip is illuminated  
by fiber optics

Shi



1340

Resolution = 16  $\mu$ s  
/ 512 pixels = 79 spectra



# H Line Broadening

Neutral Broadening

Doppler Broadening

Resonance Broadening

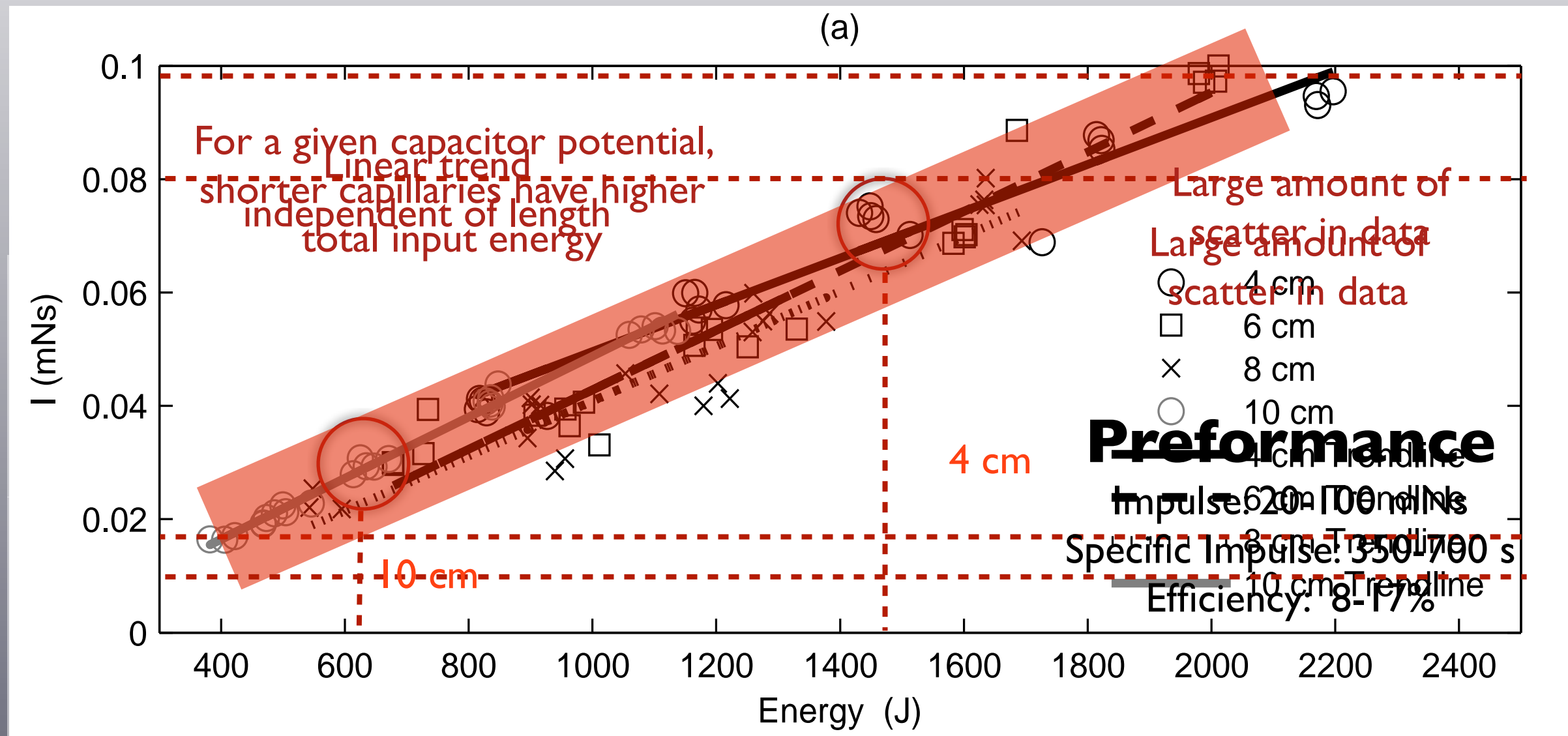
Van der Waals Broadening

Stark Broadening

Table 3.3: Fractional Intensity Widths [48]			
$\Delta_{1/2}^N$	$1 \times 10^{-4} \frac{A}{T(K)} \frac{1}{T(eV)}$	$N (\#/m^3)$	$\alpha_{1/2}$
$\Delta_{1/2}^N \approx 1 \times 10^{-4} \frac{A}{T(K)} \frac{1}{T(eV)}$		$1 \times 10^{21}$	$9.69 \times 10^{-3}$
$\Delta_{1/2}^D = 7.16 \times 10^{-7} \lambda \sqrt{\frac{g_i}{M}}$	$\lambda \sqrt{\frac{g_i}{M}}$	$1 \times 10^{22}$	$14.9 \times 10^{-3}$
		$1 \times 10^{23}$	$18.9 \times 10^{-3}$
		$1 \times 10^{24}$	N/A
		$1 \times 10^{25}$	N/A
$\Delta_{1/2}^R = 8.6 \times 10^{0.862} \sqrt{\frac{g_i}{g_k}} \lambda^2 \alpha_{1/2}^{21} f_r N_i^{77} \frac{1}{\lambda} \frac{1}{T} \frac{1}{10^{-3}}$	$\sqrt{\frac{g_i}{g_k}} \lambda^2 \alpha_{1/2}^{21} f_r N_i^{77} \frac{1}{\lambda} \frac{1}{T} \frac{1}{10^{-3}}$		
	$10000$	$0.862 \sqrt{\frac{g_i}{g_k}} \times 10^{22}$	$13.4 \times 10^{-3}$
	$10000$	$0.862 \times 10^{23}$	$18.6 \times 10^{-3}$
	$10000$	$0.862 \times 10^{24}$	$21.5 \times 10^{-3}$
$\Delta_{1/2}^W \approx 3.862 \times 10^{-30} \lambda^2 C_6^{2/5} \frac{1}{T} \frac{1}{10^{-3}}$	$\lambda^2 C_6^{2/5} \frac{1}{T} \frac{1}{10^{-3}}$	$N [\text{\AA}]$	
	$20000$	$1.723 \times 10^{21}$	$6.01 \times 10^{-3}$
	$20000$	$1.723 \times 10^{22}$	$11.4 \times 10^{-3}$
	$20000$	$1.723 \times 10^{23}$	$17.5 \times 10^{-3}$
	$20000$	$1.723 \times 10^{24}$	$22.6 \times 10^{-3}$
	$20000$	$1.723 \times 10^{25}$	$23.5 \times 10^{-3}$
	$30000$	$2.585 \times 10^{21}$	$4.98 \times 10^{-3}$
	$30000$	$2.585 \times 10^{22}$	$10.0 \times 10^{-3}$
	$30000$	$2.585 \times 10^{23}$	$16.6 \times 10^{-3}$
	$30000$	$2.585 \times 10^{24}$	$22.5 \times 10^{-3}$
	$30000$	$2.585 \times 10^{25}$	$25.7 \times 10^{-3}$
	$40000$	$3.447 \times 10^{21}$	$4.50 \times 10^{-3}$
	$40000$	$3.447 \times 10^{22}$	$9.22 \times 10^{-3}$
	$40000$	$3.447 \times 10^{23}$	$15.8 \times 10^{-3}$
	$40000$	$3.447 \times 10^{24}$	$22.3 \times 10^{-3}$
	$40000$	$3.447 \times 10^{25}$	$26.9 \times 10^{-3}$



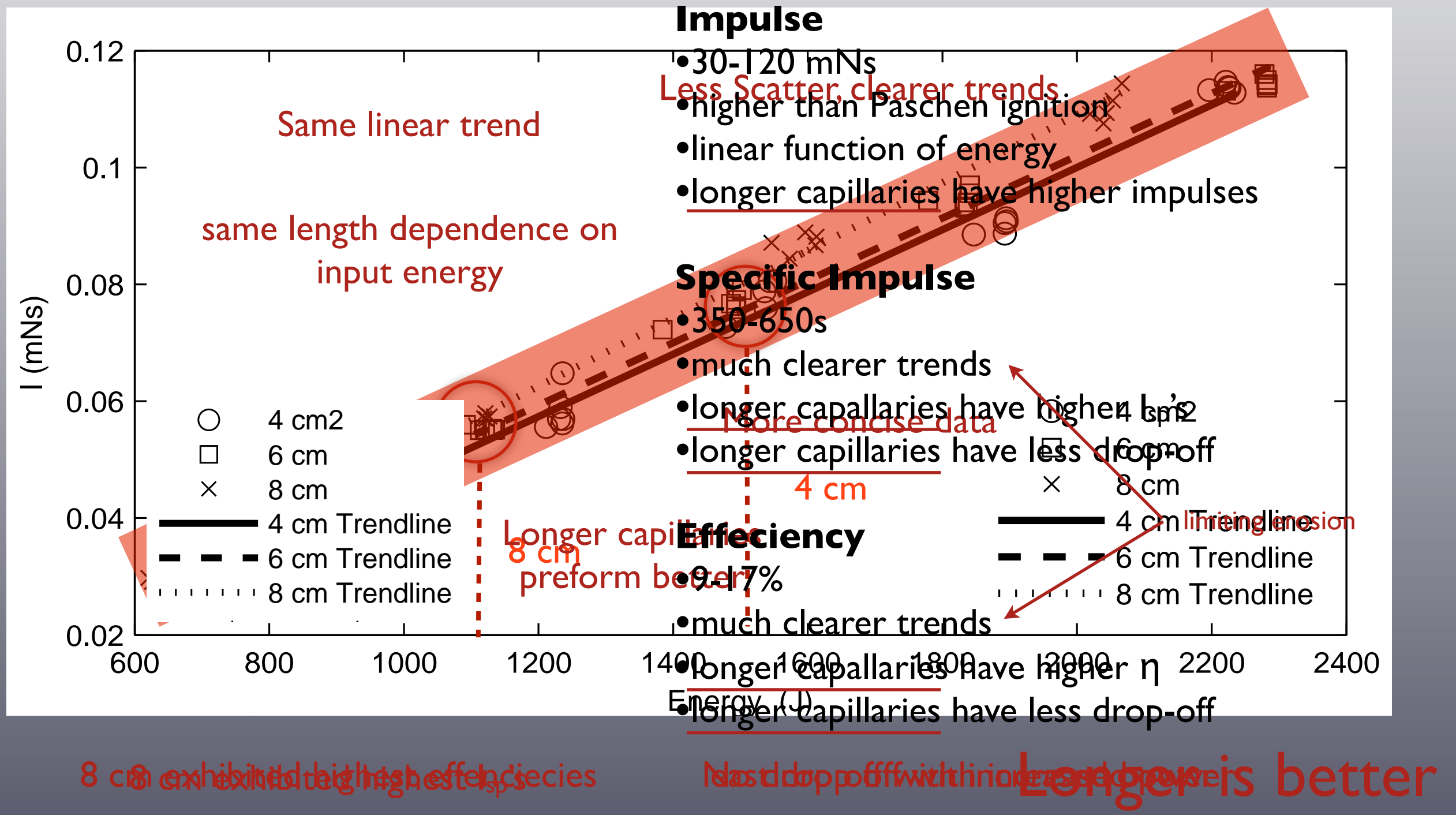
# Paschen Performance



Address by limiting electrode erosion

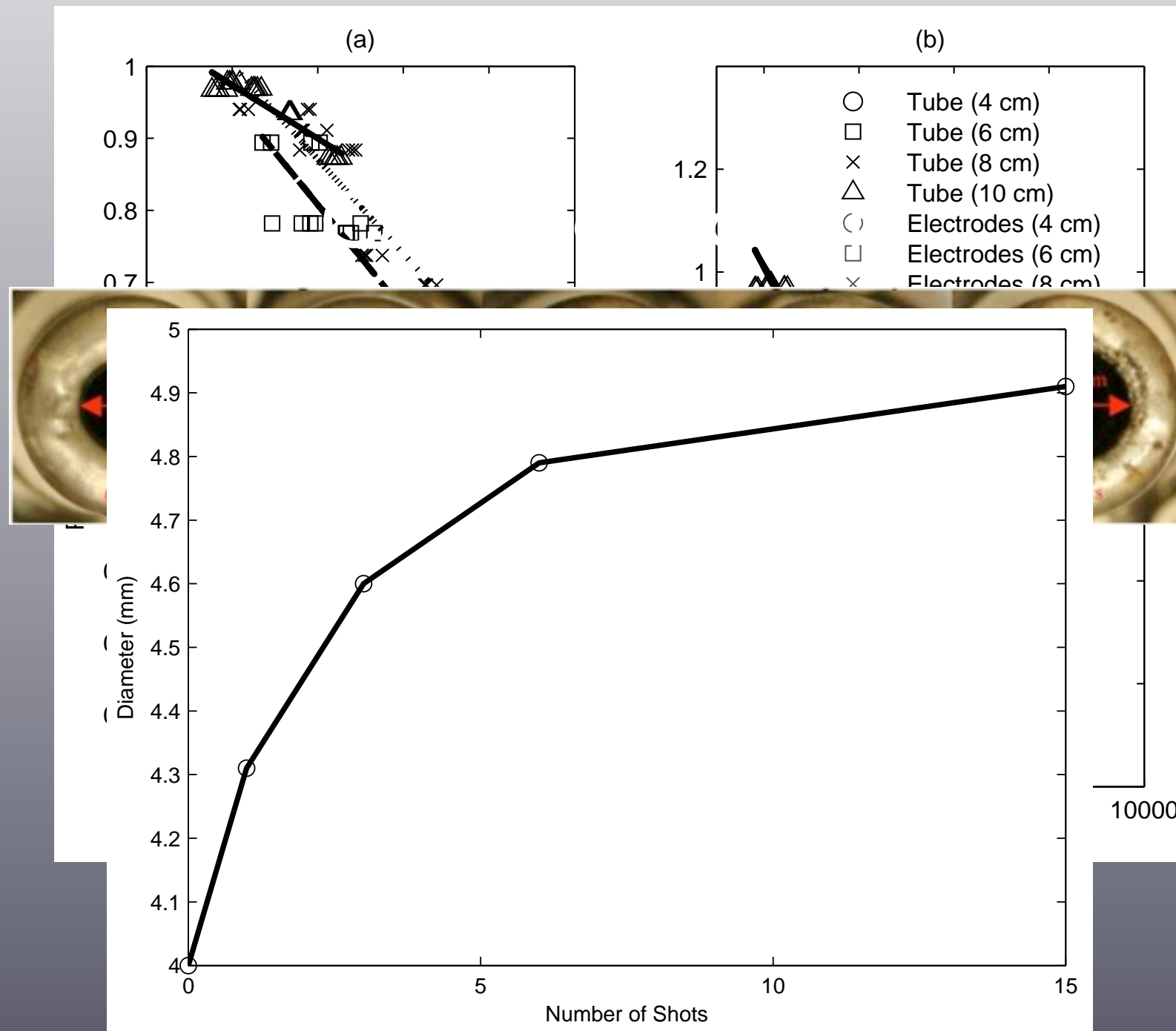


# 3E Performance





# Mass Loss



Shows a dependent on  
on length and energy

Really a function of  
peak current

Tube mass stays linear  
with length

Anode has higher  
erosion rates than  
cathode



# Models

0 Dimensional  
1 Dimensional

$$\frac{d\rho}{dt} = \frac{d\rho_a}{dt} + \frac{d\rho_e}{dt}$$

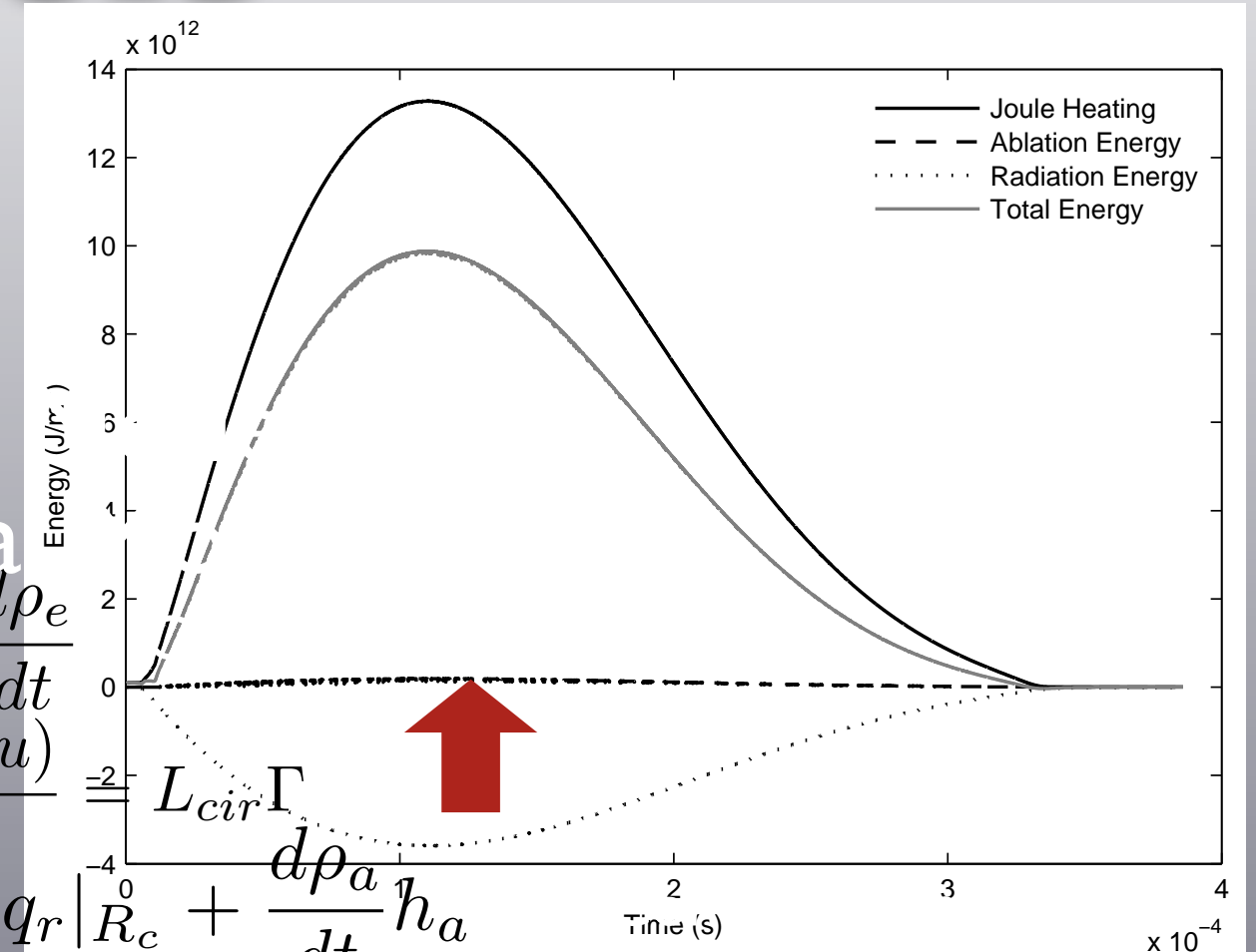
$$\frac{\partial(A\rho)}{\partial t} + \frac{\partial(A\rho u)}{\partial x}$$

$$\frac{d}{dt}\rho\bar{\varepsilon} = \eta j^2 + \frac{\partial t}{dt}\rho_e h_e - \frac{\partial x}{R}q_r \Big|_{R_c} + \frac{d\rho_a}{dt}h_a$$

$$\frac{\partial(A\rho u)}{\partial t} + \frac{\partial}{\partial x} [A(\rho u^2 + p)] = p \frac{\partial A}{\partial x} - f L_{cir}$$

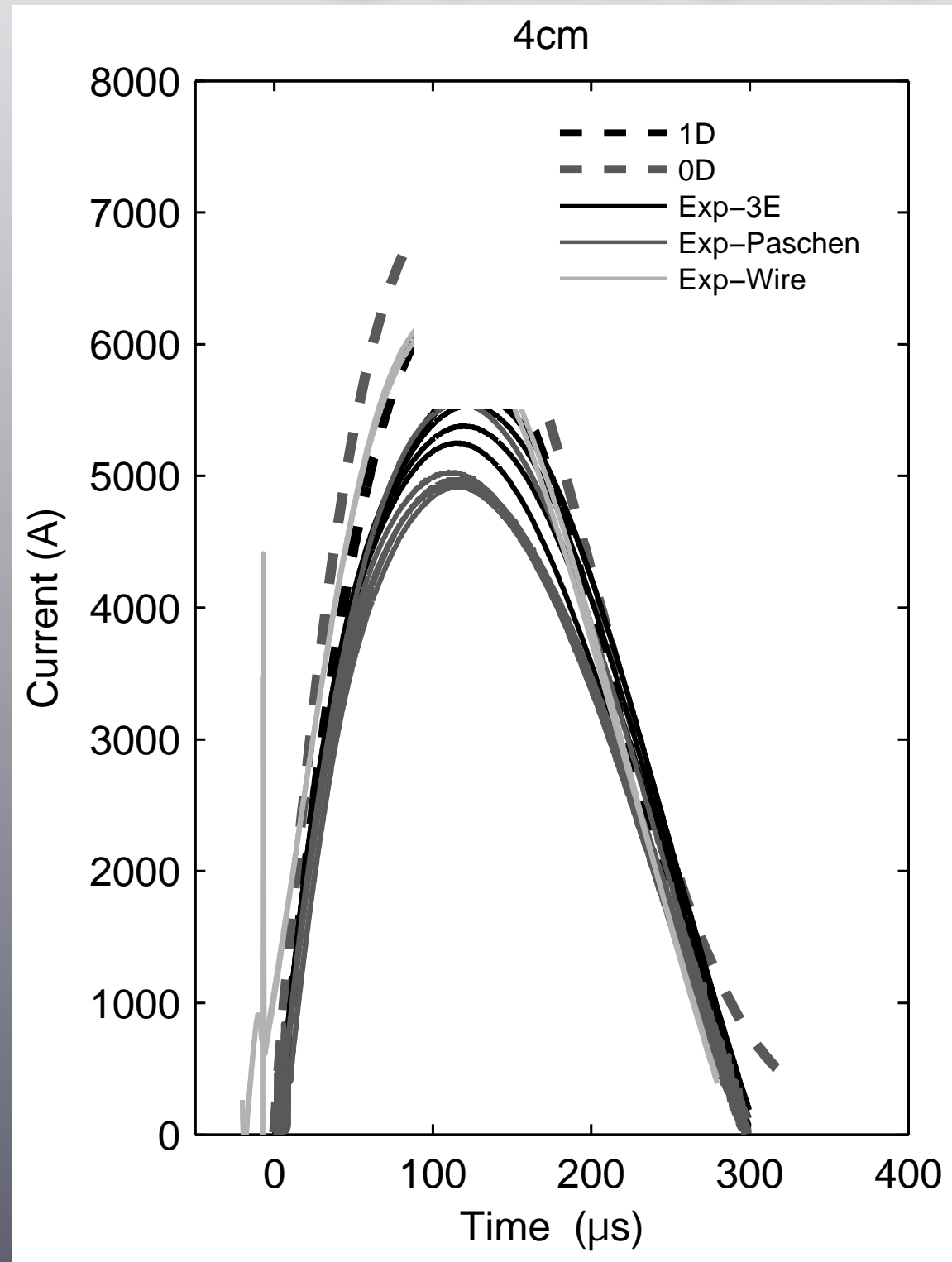
$\frac{\partial(Ae)}{\partial t} + \frac{\partial}{\partial x} [Au(e + p)] = A(Q_j - Q_{rad} - Q_{conv} + Q_{ab} - \Phi)$

Only Joule heating and  
radiation loss were  
considered





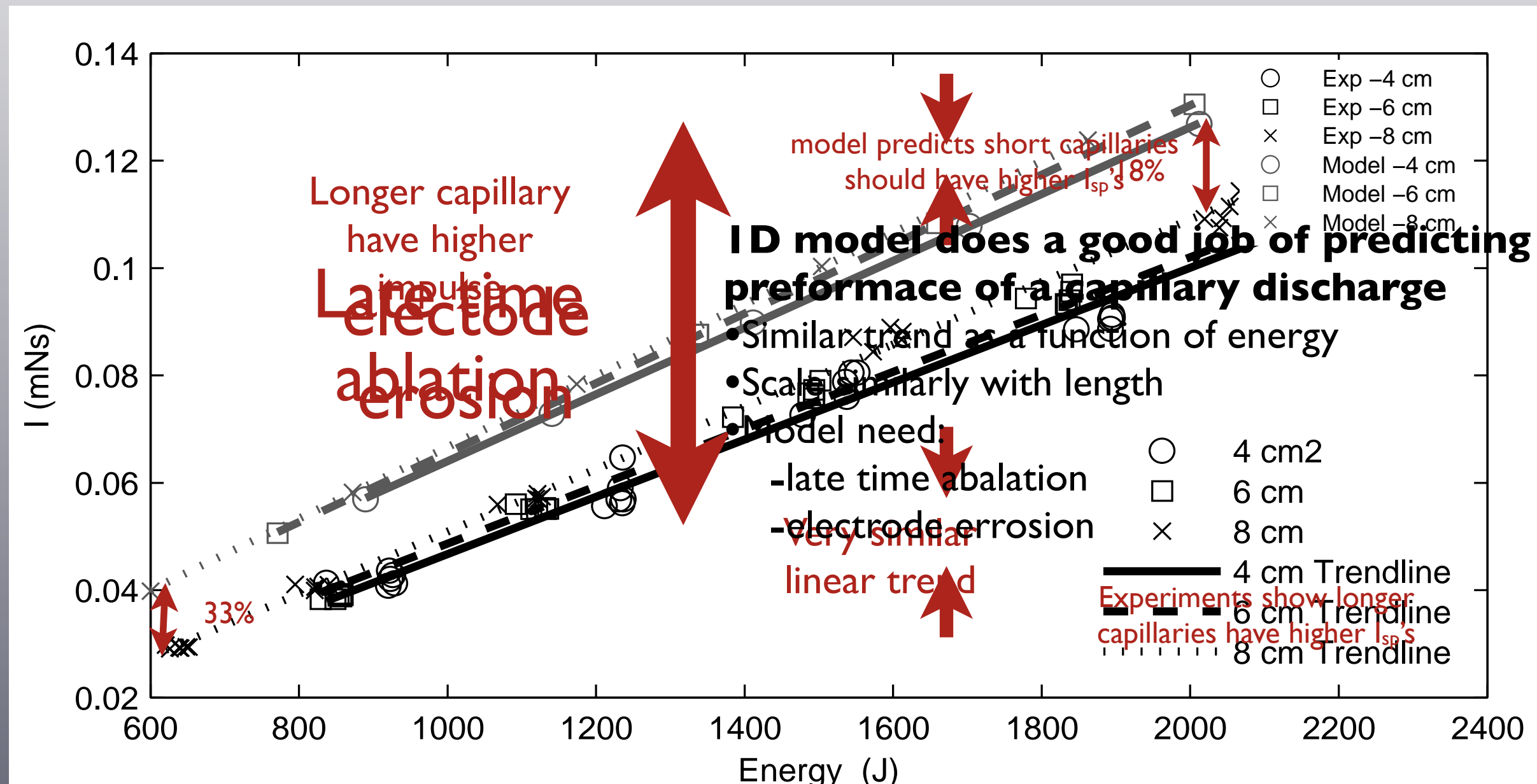
# Current Compare



- Similar profiles
  - exploding wire mass?
- Exploding wire highest current
  - Paschen has lowest
- Model over-predicts tail
  - 0D large over-prediction
- Divergence of initial  $di/dt$ 
  - only for longer capillaries
  - 10cm wire ignited has very different profile



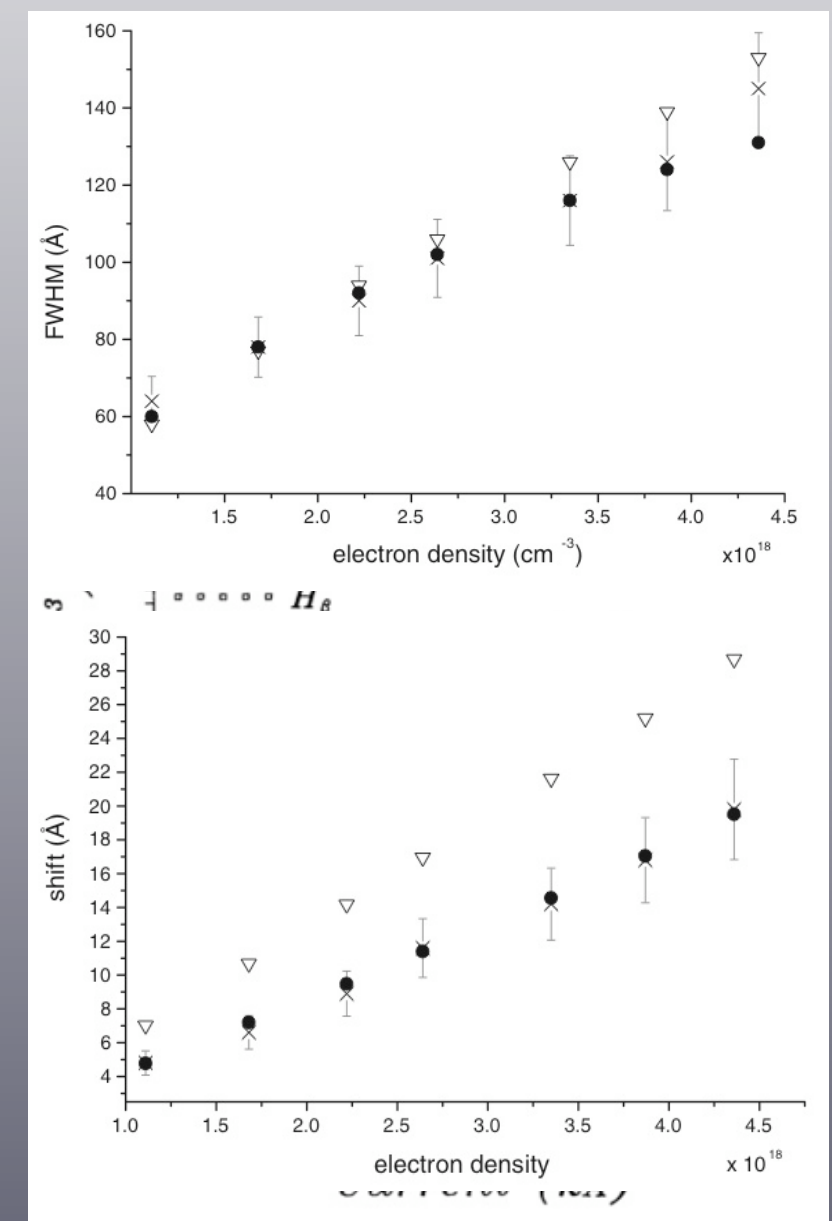
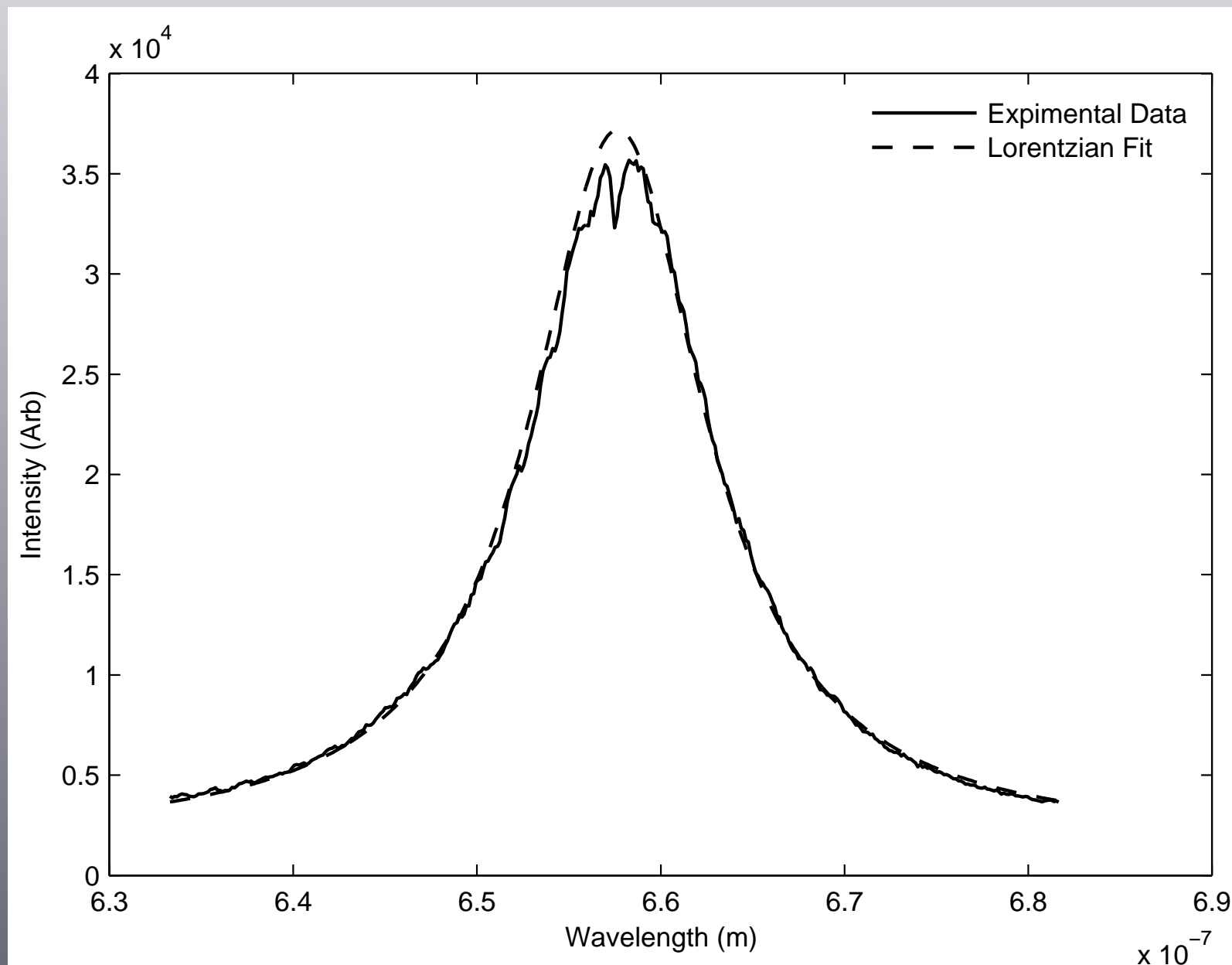
# Performance Compare



Experimental results contain only tube mass loss



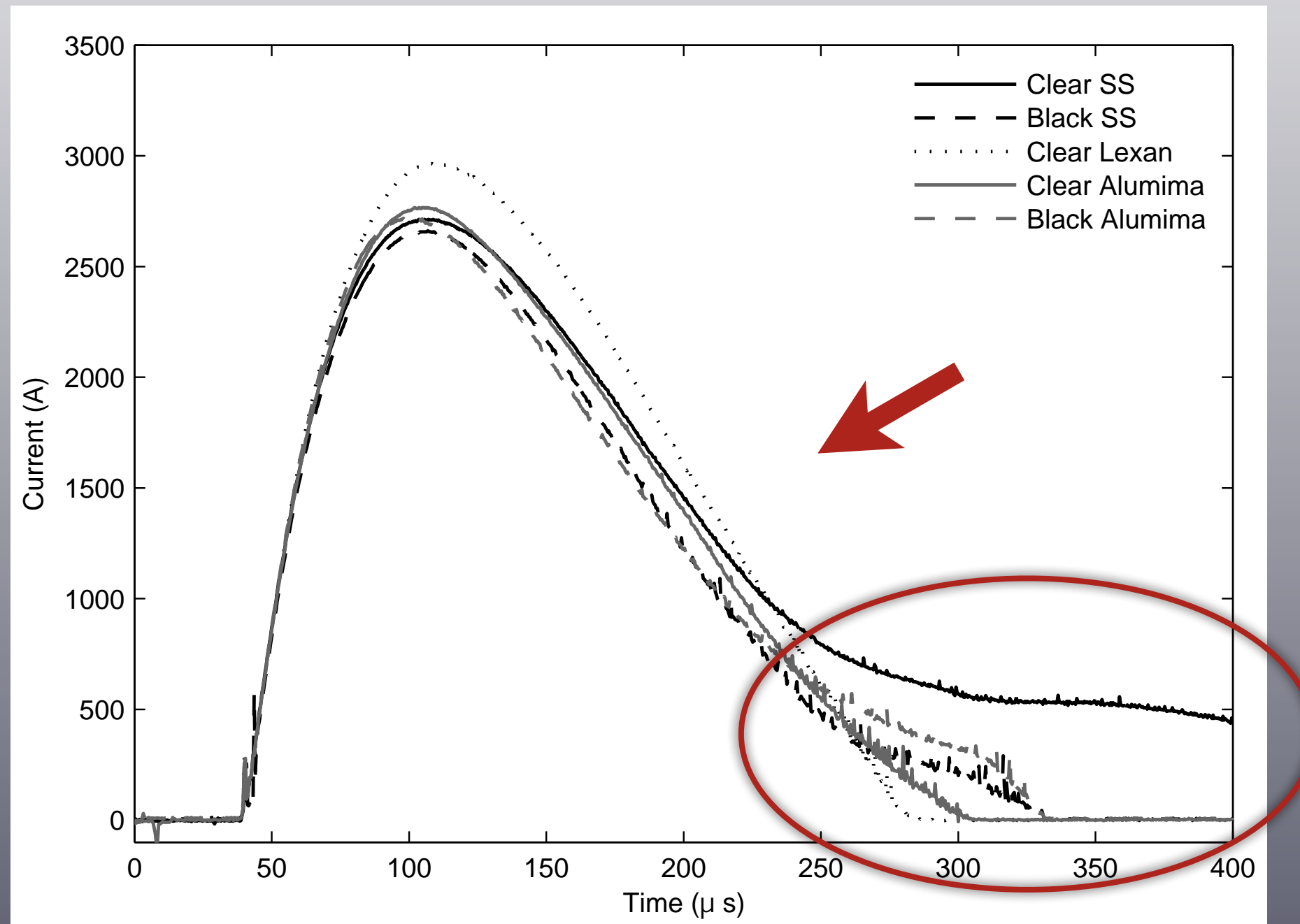
# Electron Number Density



[7] J. Ashkenazy, [33] S. A. Flih, E. Oks, and Y. Vitel. Comparison of the stark widths and shifts of the h-alpha line measured in a flash tube with theoretical results. *J. Phys. B: At. Mol. Opt. Phys.*, 36:283–296, 2003.



# Material Effects



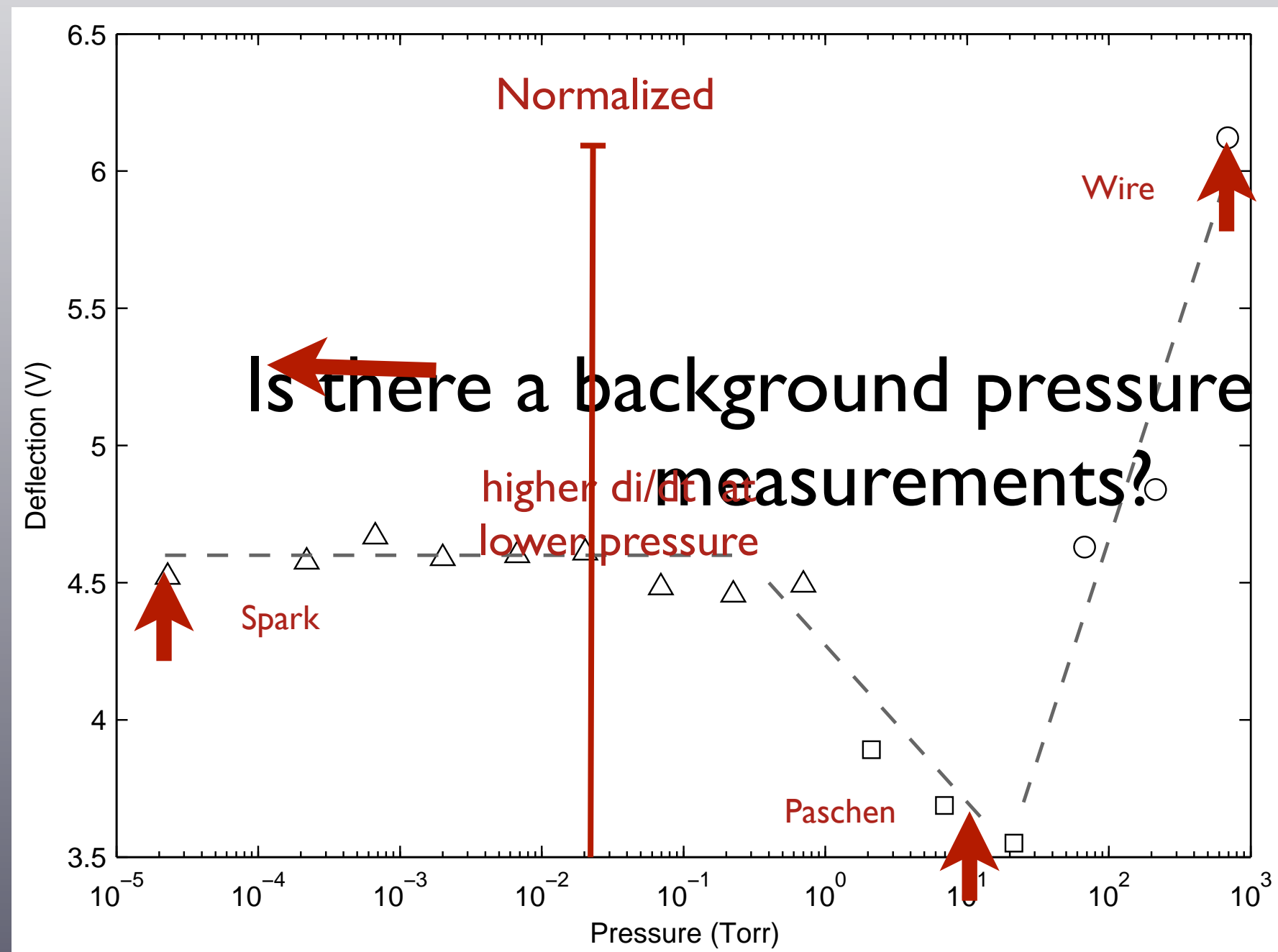
**Extinction is dependent on:**

- Tube coloration
- housing material

First discharge on new tube is different then subsequent discharges



# Background Pressure



# Wire Ignited

6 cm  
2500 V

## effect on Background pressure clearly has an effect on capillary discharges



# Conclusions

## **Viability of a capillary discharge electrothermal pulsed plasma thruster**

- A clear need was shown
- Groundwork was laid in order to achieve higher efficiencies

## **Expanded previous work**

- Understand the operating physics
  - investigated ablation process
  - role of electrode erosion
- Comparison with computer model
  - good predictability in trend
  - stressed importance of late time ablation
- Measurements
  - accurate Impulse, Specific Impulse, Efficiency measurements
  - time resolve number density measurements

## **Study of ignition on thruster performance of a capillary discharge**

- No dual mode operation seen with other methods
- Discharge was not greatly effected by ignition method
- 3 electrode operated most reliability and most applicable for future development